

Thermal Spray Coating Development of Inert Anode for
Aluminum Electrolysis Process

Vahid Jalilvand

A Thesis
In
The Department of
Mechanical, Industrial and Aerospace Engineering

Presented in Partial Fulfillment of the Requirements
For the Degree of
Doctor of Philosophy (Mechanical Engineering) at
Concordia University
Montreal, Quebec, Canada

August 2022

© Vahid Jalilvand, 2022

CONCORDIA UNIVERSITY
School of Graduate Studies

This is to certify that the thesis prepared

By: *Vahid Jalilvand*

Entitled: *Thermal Spray Coating Development of Inert Anode for Aluminum Electrolysis Process*

And submitted in partial fulfilment of the requirements for the degree of

Doctor of Philosophy (Mechanical Engineering)

Complies with the regulations of the University and meets the accepted standards with respect to originality and quality.

Signed by the final Examining Committee:

_____ Chair
Dr. Ahmed Soliman

_____ External Examiner
Dr. Philippe Bocher

_____ External to Program
Dr. Pantcho Stoyanov

_____ Examiner
Dr. Rolf Wuthrich

_____ Examiner
Dr. Mamoun Medraj

_____ Thesis Co-Supervisor
Dr. Christian Moreau

_____ Thesis Co-Supervisor
Dr. Ali Dolatabadi

Approved by: _____
Dr. Ivan Contreras, Graduate Program Director

August 16, 2022

Dr. Mourad Debbabi, Dean
Gina Cody School of Engineering and Computer Science

Abstract

Thermal Spray Coating Development of Inert Anode for Aluminum Electrolysis Process

Vahid Jalilvand, Ph.D.

Concordia University, 2022

The primary aluminum industry is an important producer of greenhouse gases (GHGs) due to the use of carbon anodes that are consumed during the Al electrolysis process to form CO₂. The most effective solution would be to replace consumable carbon anodes with so-called inert anodes that emit O₂ rather than CO₂. Among the numerous materials studied so far, Cu-Ni-Fe-based alloys appear to be the most promising metallic anode materials, due to their ability to produce a protective nickel ferrite (NiFe₂O₄) layer during Al electrolysis. However, this protective layer needs time to form at the surface of these alloys, during which fluorination can occur, causing premature degradation of the electrode. The main objective of this work is to develop a thermal spray coating of (Co,Ni)O on the Cu-Ni-Fe anodes to slow down the attack of the electrolyte and allow the formation of NiFe₂O₄ surface scale to occur.

In this thesis, a novel approach in the preparation of thick, dense, homogenous and single phase (Co,Ni)O coatings using suspension plasma spray (SPS) and high velocity oxygen fuel (HVOF) was studied. The effects of spraying variables on the composition and microstructure of the coatings were investigated. The coatings deposited by HVOF were single phase, while reduction of NiO to Ni was observed in the coatings prepared by SPS. The possible causes for the formation of Ni during spraying of (Co,Ni)O by SPS are discussed. Substrate temperature was identified as the most critical parameter affecting SPS coating composition. In-flight particles and splats were collected to study the melting and mixing behavior of CoO and NiO during spraying. Plasma power input was found to play a major role in determining the shape and number of the generated splats.

The influence of the HVOF sprayed coating and substrate compositions on their behavior was studied at 1000 °C under argon and air. On Cu-rich alloy, Co_xNi_{1-x}O coatings with higher nickel content slow down oxygen diffusion to the substrate, as well as copper diffusion to the

sample surface. On Ni-rich alloy, the formation of a NiFe_2O_4 scale is observed, whose thickness decreases as the Ni content of the $\text{Co}_x\text{Ni}_{1-x}\text{O}$ coatings increases. The results demonstrated that $(\text{Co},\text{Ni})\text{O}$ coatings decrease the oxidation rate of the underlying Cu-Ni-Fe alloy. However, the diffusion of alloying elements from substrates to the coatings and formation of new oxide layers in the coatings were observed after 20 h of heat treatment in air. Therefore, Ni-20Cr and CrMnFeCoNi high-entropy alloy (HEA) were used as bond coat materials to completely prevent the oxidation as well as the inter-diffusion of alloying elements between substrate and $(\text{Co},\text{Ni})\text{O}$ protective coating. The effect of HVOF-sprayed bond coat layers on the oxidation resistance of coated samples was investigated at 1000 °C in the presence of oxygen. The formation of a dense thin layer of Cr_2O_3 on both bond coats inhibits oxygen diffusion to the substrates. No diffusion of elements is observed from NiCr to $(\text{Co},\text{Ni})\text{O}$, while Mn atoms diffuse from HEA into the top coat layer during the oxidation process.

Acknowledgements

First, I would like to express my sincere appreciation to my thesis supervisors Professor Christian Moreau and Professor Ali Dolatabadi for all their support, patience, encouragement and knowledge shared with me during the course of my PhD program. Many thanks for giving me the chance to be a part of your research group and work with you for this research.

I wish to thank the entire Concordia University Thermal Spray Laboratory group members, particularly Dr. Fadhel Ben Ettouil for all the technical help during my experimental work.

This thesis was carried out in collaboration with INRS-EMT. I am grateful to Professor Daniel Guay and Professor Lionel Roué for their helpful collaboration, advice and comments throughout this study. I want to thank Saeed Mohammadkhani at Professor Guay's group for his friendly and positive attitude.

I extend my appreciation to the Fonds de Recherche du Québec-Nature et Technologies (FRQNT) for the support of my research.

Finally, I would like to thank my parents, family and friends for their unconditional support.

Contribution of Authors

This thesis is prepared in manuscript format. Chapters 1, 2 and 7 are the introduction, experimental procedures and conclusions of the thesis, respectively. The subsequent chapters are reprinted from the papers published or submitted to scientific journals. The contribution of the candidate is described below.

Chapter 3:

S. Mohammadkhani¹, V. Jalilvand¹, B. Davis, F. Ben Ettouil, A. Dolatabadi, L. Roué, C. Moreau*, D. Guay*, Suspension plasma spray deposition of $\text{Co}_x\text{Ni}_{1-x}\text{O}$ coatings. *Surface & Coatings Technology* 399 (2020) 126168.

¹ These authors contributed equally

* Co-corresponding authors

The candidate:

- involved in planning and methodology;
- performed all SPS coating experiments and collected the data;
- conducted the SEM characterization of the samples and particle size distribution tests;
- contributed to the analyses and discussions about the results;
- contributed to the writing of the initial draft and review of the manuscript.

Chapter 4:

V. Jalilvand, S. Mohammadkhani, F. Ben Ettouil, L. Roué, D. Guay*, A. Dolatabadi, C. Moreau*, Study on the formation of (Co,Ni)O solid solution and metallic Ni phases during suspension plasma spraying of CoO and NiO powders. Submitted to the *Journal of Thermal Spray Technology*.

* Co-corresponding authors

The candidate:

- created and developed the experimental plan;
- performed all of the experimental work including SPS coating and collecting in-flight particles and splats;
- conducted the optical microscopy and SEM / EDS characterization of the samples;

- contributed to the analysis the results;
- wrote the draft of the manuscript.

Chapter 5:

S. Mohammadkhani, V. Jalilvand, B. Davis, G.H. Gauthier, A. Dolatabadi, C. Moreau*, L. Roué, D. Guay*, High-temperature behaviour of HVOF (Co,Ni)O coated Cu-Ni-Fe anodes. *Corrosion Science* 189 (2021) 109563.

* Co-corresponding authors

The candidate:

- contributed to the design of experiments;
- performed all HVOF coating experiments and optimized the spray parameters;
- conducted some of the characterization tests;
- contributed to the analysis the HVOF coating results;
- contributed to the review of the manuscript.

Chapter 6:

V. Jalilvand¹, S. Mohammadkhani¹, B. Davis, L. Roué, A. Dolatabadi, D. Guay*, C. Moreau*, The effect of bond coat on high-temperature behavior of HVOF-sprayed (Co,Ni)O coating on Cu-Ni-Fe anodes. *Surface & Coatings Technology* 441 (2022) 128576.

¹ These authors contributed equally

* Co-corresponding authors

The candidate:

- contributed to the development of methodology;
- performed all HVOF coating experiments including spraying bond coats and top coats;
- conducted some of the characterization tests;
- contributed to the analysis the various results;
- wrote the draft of the manuscript.

Table of Contents

List of Figures	xii
List of Tables	xix
List of Abbreviations	xx
Chapter 1. Introduction.....	1
1.1. Current aluminum production and the Hall-Héroult process.....	1
1.2. Inert anodes	2
1.3. Literature review on coatings of inert anodes.....	4
1.3.1. Cerium oxide coated anodes	4
1.3.2. Inert anode composed of Ni–Cr alloy substrate, intermediate oxide film and α - Al ₂ O ₃ /Au (Au–Pt, Au–Pd, Au–Rh) surface composite coating.....	5
1.3.3. Cold sprayed Cu-Ni-Fe anode for Al production	6
1.3.4. De Nora oxygen evolving inert metallic anode	8
1.4. Development of inert anode by thermal spray coating	9
1.5. Thermal spray processes	10
1.5.1. Suspension plasma spray	12
1.5.2. High Velocity Oxy-Fuel (HVOF) spray	16
1.6. Objectives	17
1.7. Thesis organization	18
Chapter 2. Experimental procedures.....	20
2.1. Sprayed powder	20
2.2. Spray systems.....	20
2.2.1. Suspension plasma spray	21
2.2.2. High-velocity oxy-fuel.....	21
2.3. Measurement techniques.....	22
2.3.1. Particle size measurements	22
2.3.2. X-ray diffraction (XRD)	23

2.3.3.	Scanning electron microscopy (SEM) equipped with energy-dispersive spectroscopy (EDS)	25
2.4.	High-temperature dry oxidation tests for coatings.....	27
Preface to Chapter 3.....		28
Chapter 3.	Suspension plasma spray deposition of $\text{Co}_x\text{Ni}_{1-x}\text{O}$ coatings.....	29
3.1.	Introduction.....	29
3.2.	Experimental.....	31
3.2.1.	Materials and spray conditions	31
3.2.2.	Materials characterization.....	33
3.3.	Results.....	34
3.4.	Discussion.....	44
3.5.	Conclusions.....	46
Preface to Chapter 4.....		47
Chapter 4.	Study on the formation of $(\text{Co},\text{Ni})\text{O}$ solid solution and metallic Ni phases during suspension plasma spraying of CoO and NiO powders	48
4.1.	Introduction.....	48
4.2.	Materials and methods	50
4.3.	Results and discussion	53
4.3.1.	Collected in-flight particles.....	53
4.3.2.	Investigation of collected splats.....	54
4.3.3.	Coatings study.....	59
4.4.	Conclusions.....	68
Preface to Chapter 5.....		70
Chapter 5.	High-temperature behaviour of HVOF $(\text{Co},\text{Ni})\text{O}$ coated Cu-Ni-Fe anodes for aluminum electrolysis	71
5.1.	Introduction.....	71
5.2.	Experimental.....	73
5.3.	Results and discussion	74
5.3.1.	As-coated samples	74

5.3.2.	Heat treatment under argon.....	77
5.3.3.	Heat treatment under air.....	81
5.4.	Conclusions.....	85
Preface to Chapter 6.....		87
Chapter 6. The effect of bond coat on the high-temperature behavior of HVOF-sprayed (Co,Ni)O coating on Cu-Ni-Fe anodes.....		88
6.1.	Introduction.....	88
6.2.	Experimental procedure.....	90
6.3.	Results and discussion.....	93
6.3.1.	As-coated samples.....	93
6.3.2.	High-temperature oxidation behavior.....	98
6.4.	Conclusion.....	108
Chapter 7. Conclusions and suggestions for future.....		110
7.1.	Summary and conclusions.....	110
7.2.	Contributions.....	112
7.3.	Future work.....	113
References.....		114
Appendix A. Supplementary data for Chapter 3.....		126
Appendix B. Supplementary data for Chapter 5.....		127
Appendix C. Impact of HVOF sprayed Ni-Cr and (Co,Ni)O coatings on the behaviour of Cu-Ni-Fe anodes for green Al production.....		135
C.1.	Introduction.....	135
C.2.	Experimental.....	138
C.2.1.	(Co,Ni)O synthesis.....	138
C.2.2.	Solubility measurements.....	138
C.2.3.	High velocity oxygen fuel (HVOF) coating.....	139
C.2.4.	Dry oxidation.....	139

C.2.5.	Aluminum electrolysis	140
C.3.	Results and discussion.....	141
C.3.1.	Solubility measurements	141
C.3.2.	Heat treatment in air	143
C.3.3.	Cell voltage evolution	149
C.3.4.	Characterization of the anodes after Al electrolysis.....	151
C.4.	Conclusion.....	158
	Supplementary information	158
	References.....	159

List of Figures

Figure 1.1. Schematic of the Hall-Héroult Process [2].....	2
Figure 1.2. SEM micrographs of CeO ₂ coatings deposited with varying initial CeO ₂ concentration (a) 0.5; (b) 1.0; (c) 1.5% [14].....	5
Figure 1.3. SEM images of inert anode composed of Ni–Cr substrate, intermediate oxide film and α -Al ₂ O ₃ /Au surface coating [15].....	6
Figure 1.4. Cross section images at different zones of the cold sprayed 65Cu20Ni15Fe (A) transversal slice image, (B, C) curved top part and (D, E) longitudinal part of the anode [18]	7
Figure 1.5. Experimental oxygen over-potentials of (Co,Ni)O and Co ₃ O ₄ coatings in cryolite at 930 °C [20].....	8
Figure 1.6. Schematic view of a thermal spray process [30].....	11
Figure 1.7. Overview of particle temperature versus particle velocity for different thermal spray processes [32].....	11
Figure 1.8. Schematic of the suspension plasma spray system with axial injection [35].....	13
Figure 1.9. Schematic of the consequent events (stages) in SPS coating deposition [37].....	13
Figure 1.10. Schematic of a typical impinging gas-jet system [39].....	14
Figure 1.11. Schematic illustration of the shadowing of different-size droplets impacting on substrate asperities [41].....	15
Figure 1.12. Schematic of the Northwest Mettech Axial III central injection torch [36].....	16
Figure 1.13. A schematic of the high-velocity oxy-fuel technique [42].....	17
Figure 1.14. Schematic of the three experimental phases in this project.....	19
Figure 2.1. Suspension plasma spray with a Mettech’s Axial III gun [48]	21
Figure 2.2. Diamond Jet 2700-hybrid HVOF gun from Oerlikon Metco [48]	22
Figure 2.3. The Spraytec Wet Dispersion Accessory [51].....	23
Figure 2.4. Bragg's law reflection [52]	24
Figure 2.5. Different types of signals used by an SEM and the area from which they originate [54].....	25
Figure 2.6. Principle of generation of characteristic X-rays [55]	26

Figure 3.1. SEM micrographs of (a) CoO and (b) NiO precursor powders, and particle size distribution histograms of (c) CoO and (d) NiO precursor powders.	34
Figure 3.2. In (a) XRD patterns of coatings prepared at plasma powers ranging from 75 to 95 kW. In (b), the relative proportion of the solid solution phase, and the Ni content of the solid solution phase are plotted with respect to the plasma power.....	35
Figure 3.3. Cross-sectional SEM micrographs of coatings prepared at different plasma powers: (a) 75 kW, (b) 80 kW, (c) 85 kW, (d) 90 kW and (e) 95 kW. In (f) the same coating as (c) is shown at a lower magnification. The substrate temperature was always lower than 600 °C	37
Figure 3.4. XRD patterns of mixed CoO and NiO (50–50 mol%) precursor particles sprayed in water, and then collected and dried in an oven. Different plasma powers were used: (a) 75 kW, (b) 85 kW and, (c) 95 kW.	38
Figure 3.5. XRD patterns of coatings prepared from (a, b and c) NiO powder and (d) CoO powder. The input power was (a) 75 kW, (b and d) 85 kW and (c) 95 kW. All other spraying parameters are listed in Table 2.1.	39
Figure 3.6. XRD patterns of coatings prepared using $\text{Co}_{0.5}\text{Ni}_{0.5}\text{O}$ solid solution powder (instead of a physical mixture of CoO + NiO) as starting materials and three plasma powers: (a) 54 kW, (b) 82 kW, and (c) 93 kW. In this series of experiments, the gas mixture consisted of Ar/N ₂ /He (instead of Ar/N ₂ /H ₂) to provide a less reductive atmosphere	40
Figure 3.7. XRD patterns of coatings prepared in the second series of experiments: (a) standoff distance = 50 mm, and (b) standoff distance = 70 mm. In both cases, the plasma power was 85 kW and the substrate temperature was always lower than 300 °C. In (c and d), cross-sectional SEM images of corresponding coatings	41
Figure 3.8. XRD patterns of coatings prepared in the third series of experiments with (a) [50% mol. CoO + 50% mol. NiO] and (b) [75% mol. CoO + 25% mol. NiO] mixtures. The input power was 85 kW.....	42
Figure 3.9. Cross-sectional SEM micrographs of (a) [50% mol. CoO + 50% mol. NiO] and, (b) [75% mol. CoO + 25% mol. NiO] mixtures. The input power was 85 kW. The variation in substrate temperature with the number of passes is seen in (c)	43
Figure 4.1. SEM micrographs of the precursor powders: (a) CoO and (b) NiO.....	50
Figure 4.2: Histograms showing the particle size distributions for the (a) CoO and (b) NiO powders	51

Figure 4.3. (a and b) SEM images at different magnifications of the in-flight particles of sample S1	53
Figure 4.4. Cross-sectional SEM image and corresponding EDS mapping images of the in-flight particles of sample S1	54
Figure 4.5. (a, b and c) SEM images at different magnifications of the collected splats of sample S1	55
Figure 4.6. EDS mapping images of the collected splats of sample S1.....	56
Figure 4.7. (a, b and c) SEM images at different magnifications of the collected splats of sample S2	57
Figure 4.8. EDS mapping images of the un-melted particles along with the evaporated and re-condensed particles of sample S2	58
Figure 4.9. EDS mapping images of the collected splats of sample S2.....	59
Figure 4.10. XRD patterns of coated samples (a) S1, (b) S2 and (c) S3	60
Figure 4.11. Optical microscopy cross-sectional images of coated samples (a) S1, (b) S2 and (c) S3	61
Figure 4.12. Cross-sectional SEM image and corresponding EDS mapping image of sample S1	62
Figure 4.13. XRD pattern of the coated sample S4 [79].....	63
Figure 4.14. (a) Cross-sectional SEM micrograph of sample S4, and (b) variation in substrate temperature with the number of passes [79].....	64
Figure 4.15. Point EDS analysis results (in at.%) of the coated samples (a) S5, and (b) S6.....	65
Figure 4.16. Selected-area EDS analysis results (in at.%) of the coated samples (a) S2, (b) S5 and (c) S6.....	65
Figure 4.17. SEM image taken from bottom region of coating showing the porous structure of the metallic Ni areas in sample S1	66
Figure 4.18. XRD patterns of sample S7: (a) as-coated and (b) heat treated at 1000 °C for 1 h under argon	67
Figure 4.19. SEM and corresponded EDS mapping images of sample S7: (a and b) as-coated and (c and d) heat treated at 1000 °C for 1 h under argon.....	68
Figure 5.1. SEM micrographs (a, b and c) and particle size distribution histograms (d, e and f) of (a and d) CoO, (b and e) Co _{0.75} Ni _{0.25} O and (c and f) Co _{0.5} Ni _{0.5} O precursor powders	75

Figure 5.2. XRD patterns of coatings deposited on Cu-rich substrate (a, b and c) and Ni-rich substrate (d, e and f): CoO (a and d), Co _{0.75} Ni _{0.25} O (b and e), Co _{0.5} Ni _{0.5} O (c and f).....	76
Figure 5.3. Cross-sectional SEM micrographs of coatings deposited on Cu-rich substrate (a, b and c) and Ni-rich substrate (d, e and f): CoO (a and d), Co _{0.75} Ni _{0.25} O (b and e), Co _{0.5} Ni _{0.5} O (c and f). The EDS analysis (at.%) of as-sprayed coatings are presented as well	77
Figure 5.4. XRD patterns of samples S1-S6 after 20 h of heat treatment at 1000 °C under an argon flow	78
Figure 5.5. Cross-sectional SEM micrographs of samples (S1-S6) after 20 h of heat treatment at 1000 °C under an argon flow.....	79
Figure 5.6. EDS analysis results and schematic illustrations of CoO coatings deposited on (a) Cu-20Ni-15Fe (S1) and (b) Ni-25Fe-10Cu (S4) substrates after 20 h of heat treatment at 1000 °C under an argon flow. The source of carbon is the resin used for the sample.....	79
Figure 5.7. Iron content in (Co,Ni)O coatings after 20 h of heat treatment at 1000 °C under an argon flow	81
Figure 5.8. Cross-sectional SEM micrographs of coatings (sample S1-S6) after 20 h of heat treatment at 1000 °C in static air. Layers 1, 2, 3 and 4 are identified.....	82
Figure 5.9. EDS analysis results and schematic illustration of CoO coating deposited on (a) Cu-20Ni-15Fe and (b) Ni-25Fe-10Cu substrate (sample S1 and S4, respectively), after 20 h of heat treatment at 1000 °C in static air. The source of carbon is the resin used for the sample preparation	82
Figure 5.10. The oxide layer thickness below the HVOF coatings on (a) Cu-20Ni-15Fe substrates and (b) on Ni-25Fe-10Cu substrates after the heat treatment for 20 h at 1000 °C in air (samples S1-S6).	83
Figure 6.1. Histograms showing the particle size distributions of the precursor powders (a) high entropy alloy, (b) Ni-Cr and (c) Co _{0.5} Ni _{0.5} O.....	91
Figure 6.2. XRD results of the coatings prepared by HVOF, (a) samples coated with only a bond coat layer, and (b) samples coated with a bond coat and a top coat layer.	93
Figure 6.3. Cross sectional SEM micrographs of the as-sprayed bond coat layers prepared by HVOF, (a) S1, (b) S2, (c) S3 and (d) S4.....	94
Figure 6.4. EDS analysis results (in at.%) of the as-sprayed bond coats, (a) S1 (Ni-rich + HEA) and (b) S3 (Ni-rich + Ni-Cr).....	95

Figure 6.5. Cross sectional SEM micrographs of the as-sprayed bond-coat + top-coat layers prepared by HVOF, (a) S5 (Cu-rich + HEA + (Co,Ni)O), (b) S6 (Cu-rich + Ni-Cr + (Co,Ni)O), (c) S7 (Ni-rich + HEA + (Co,Ni)O), and (d) S8 (Ni-rich + Ni-Cr + (Co,Ni)O). 97

Figure 6.6. EDS analysis results (in at.%) of the as-sprayed bond coat and (Co,Ni)O layers, (a) S6 (Cu-rich + Ni-Cr + (Co,Ni)O) and (b) S7 (Ni-rich + HEA + (Co,Ni)O) 98

Figure 6.7. XRD patterns of the HVOF coatings with (a) a HEA bond coat layer and (b) a Ni-Cr bond coat layer, after a 20 h heat treatment at 1000 °C in static air atmosphere..... 99

Figure 6.8. Top-view EDS analysis results (in at.%) of (a) Cu-rich substrate and (b) Ni-rich substrate, coated with HEA + (Co,Ni)O layers (samples S5 and S7) after a 20 h heat treatment at 1000 °C in air..... 100

Figure 6.9. Cross sectional SEM micrographs of Ni-rich coated with (a) only a (Co,Ni)O layer, (b) only a HEA layer, (c) both HEA and (Co,Ni)O layers, as well as Cu-rich coated with (d) only a (Co,Ni)O layer, (e) only a HEA layer, (f) both HEA and (Co,Ni)O layers, after a 20 h heat treatment at 1000 °C in air 102

Figure 6.10. EDS analysis results (in at.%) of Ni-rich substrates coated with (a) only a HEA bond coat layer (sample S1) and (b) HEA + (Co,Ni)O layers (sample S7), after a 20 h heat treatment at 1000 °C in air 103

Figure 6.11. EDS analysis results (in at.%) of Cu-rich substrates coated with (a) only a HEA bond coat layer (sample S2) and (b) HEA + (Co,Ni)O layers (sample S5), after a 20 h heat treatment at 1000 °C in air 104

Figure 6.12. Cross sectional SEM micrographs of (a) bare Ni-rich, (b) Ni-rich coated with only Ni-Cr, (c) Ni-rich coated with Ni-Cr and (Co,Ni)O, (d) bare Cu-rich, (e) Cu-rich coated with only Ni-Cr, (f) Cu-rich coated with Ni-Cr and (Co,Ni)O, after a 20 h heat treatment at 1000 °C in static air atmosphere 105

Figure 6.13. EDS analysis results (in at.%) of Ni-rich substrates coated with (a) only a Ni-Cr bond coat layer (sample S3) and (b) Ni-Cr + (Co,Ni)O layers (sample S8) after a 20 h heat treatment at 1000 °C in air 107

Figure 6.14. EDS analysis results (in at.%) of Cu-rich substrates coated with (a) only a Ni-Cr bond coat layer (sample S4) and (b) Ni-Cr + (Co,Ni)O layers (sample S6), after a 20 h heat treatment at 1000 °C in air..... 108

Figure S3.1. Typical examples of XRD experimental data and Rietveld refinement fitting results: a) sample S2 that contains two phases and b) sample S8 that contains a single phase	126
Figure S5.1. XRD patterns of coatings prepared in the first series of experiments using different HVOF gas compositions ranging.....	129
Figure S5.2. Cross-sectional SEM micrographs of coatings prepared in the first series of experiments using different HVOF gas compositions ranging.....	130
Figure S5.3. EDS analysis results and schematic illustrations of $\text{Co}_{0.75}\text{Ni}_{0.25}\text{O}$ coatings deposited on (a) Cu-20Ni-15Fe and (b) Ni-25Fe-10Cu substrates (sample S2 and S5, respectively), after 20 h of heat treatment at 1000 °C under an argon flow. The source of carbon is the resin used for the sample preparation.....	133
Figure S5.4. EDS analysis results and schematic illustrations of $\text{Co}_{0.5}\text{Ni}_{0.5}\text{O}$ coatings deposited on (a) Cu-20Ni-15Fe and (b) Ni-25Fe-10Cu substrates (sample S3 and S6, respectively), after 20 h of heat treatment at 1000 °C under an argon flow. The source of carbon is the resin used for the sample preparation	133
Figure S5.5. EDS analysis results and schematic illustration of $\text{Co}_{0.75}\text{Ni}_{0.25}\text{O}$ coating deposited on (a) Cu-20Ni-15Fe and (b) Ni-25Fe-10Cu substrate (sample S2 and S5, respectively), after 20 h of heat treatment at 1000 °C in static air. The source of carbon is the resin used for the sample preparation	134
Figure S5.6. EDS analysis results and schematic illustration of $\text{Co}_{0.5}\text{Ni}_{0.5}\text{O}$ coating deposited on (a) Cu-20Ni-15Fe and (b) Ni-25Fe-10Cu substrate (sample S3 and S6, respectively), after 20 h of heat treatment at 1000 °C in static air. The source of carbon is the resin used for the sample preparation	134
Figure C.1. Schematic illustration of aluminum electrolysis cell.....	141
Figure C.2. Concentration of (a) Co and (b) Ni in cryolite-alumina bath at 1000 °C for $\text{Co}_x\text{Ni}_{1-x}\text{O}$ (with $x = 0, 0.75, 0.5, 0.25$ and 1) as a function of time and (c) as a function of x for $t = 9$ h..	142
Figure C.3. Cross-sectional SEM micrographs of (a) (Co,Ni)O coating on Ni-25Fe-10Cu substrate, (b) (Co,Ni)O coating on Cu-20Ni-15Fe substrate, (c) [Ni-Cr + (Co,Ni)O] coatings on Ni-25Fe-10Cu substrate , and (d) [Ni-Cr + (Co,Ni)O] coatings on Cu-20Ni-15Fe substrate ...	143
Figure C.4. Cross-sectional SEM images and EDS elemental mappings of Ni-25Fe-10Cu coated by (a) (Co,Ni)O and (b) [Ni-Cr + (Co,Ni)O], after 20 h heat-treatment at 1000 °C in air	144

Figure C.5. Schematic representation of the oxidation stages of Ni-25Fe-10Cu coated by (a) (Co,Ni)O and (b) [Ni-Cr + (Co,Ni)O], during the 20 h heat-treatment at 1000 °C in air	146
Figure C.6. Cross-sectional SEM images and EDS mappings of Cu-20Ni-15Fe coated by (a) (Co,Ni)O and (b) [Ni-Cr + (Co,Ni)O], after 20 h heat-treatment at 1000 °C in air.....	147
Figure C.7. Schematic representation of oxidation stages of (a) Cu-20Ni-15Fe coated by (Co,Ni)O and (b) Cu-20Ni-15Fe coated by [Ni-Cr + (Co,Ni)O], during the 20 h heat-treatment at 1000 °C in air	149
Figure C.8. Cell voltage vs. electrolysis time performed at 1000 °C for (a) Ni-rich anode coated with (Co,Ni)O, (b) Ni-rich anode coated with [Ni-Cr + (Co,Ni)O], (c) Cu-rich anode coated with (Co,Ni)O and (d) Cu-rich anode coated with [Ni-Cr + (Co,Ni)O].	150
Figure C.9. Cross-sectional SEM images and EDS analyses and mappings of Ni-25Fe-10Cu anodes (a) uncoated part, (b) coated with (Co,Ni)O and (c) coated with (Co,Ni)O + Ni-Cr after aluminum electrolysis at 1000 °C for 5 h	151
Figure C.10. Cross-sectional SEM images and EDS analyses and mappings of Cu-20Ni-15Fe anodes (a) uncoated part, (b) coated with (Co,Ni)O and (c) coated with (Co,Ni)O + Ni-Cr after aluminum electrolysis at 1000 °C for 5 h	152
Figure C.11. Schematic representation of oxidation stages during Al electrolysis at 1000 °C of (a) Cu-20Ni-15Fe anode (a) without coating and (b) coated by (Co,Ni)O.....	156

List of Tables

Table 1.1. Performance targets for inert anodes [6].....	3
Table 3.1. Spray process parameters.....	32
Table 3.2. Parameters extracted from the Rietveld analysis and the mass balance analysis of samples S1–S9. Note that the Co, Ni and O contents in the powder used for samples S1 to S8 were 39.2, 39.4 and 21.4 wt%, respectively. For sample S9, the Co, Ni and O contents were 59.0, 19.6 and 21.4 wt.%, respectively.	36
Table 3.3. Spray parameters of a complementary series of experiments. A powder made of a $\text{Co}_{0.5}\text{Ni}_{0.5}\text{O}$ solid solution was used as starting material and helium was used instead of hydrogen in the plasma gas mixture.	39
Table 4.1. Spray process parameters.....	52
Table 5.1. Structural parameters of (Co,Ni)O coatings	76
Table 6.1. HVOF spray process parameters	91
Table 6.2. List of the samples prepared by HVOF	92
Table S5.1. HVOF Spray process parameters	127

List of Abbreviations

APS	Atmospheric Plasma Spray
CR	Cryolite Ratio
CTE	Thermal Expansion Coefficient
EDS/EDX	Energy Dispersive X-ray Spectroscopy
EPD	Electrophoretic Deposition
FE-SEM	Field Emission Scanning Electron Microscopy
GHG	Greenhouse Gas
HEA	High Entropy Alloy
HVAF	High Velocity Air Fuel
HVOF	High Velocity Oxygen Fuel
ICP-AES	Inductively Coupled Plasma Atomic Emission Spectroscopy
OM	Optical Microscopy
PVA	Polyvinyl Alcohol
PVP	Polyvinylpyrrolidone
SEM	Scanning Electron Microscopy
SOFC	Solid Oxide Fuel Cell
SPS	Suspension Plasma Spray
VPS	Vacuum Plasma Spray
XRD	X-ray Diffraction
YSZ	Yttria Stabilized Zirconia

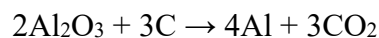
Chapter 1

Introduction

1.1. Current aluminum production and the Hall- Héroult process

Aluminum represents about eight percent of the Earth's crust composition, which makes it the most abundant metal on the planet. Nevertheless, it is always found combined with other elements, never in a pure state, mainly alum ($KAl(SO_4)_2 \cdot 12H_2O$) and alumina state (Al_2O_3). The production of aluminum begins with bauxite ore. Bauxites are refined to obtain alumina through the Bayer process. In the next step, alumina is smelted into pure aluminum metal. The melting point of alumina (Al_2O_3) is 2072 °C, which generally is so high for commercial production. To produce aluminum more efficiently at a lower operating temperature, scientists in the 19th century looked for identifying a chemical compound that acted as a solvent for Al_2O_3 . In 1886, Paul Louis Toussaint Héroult and Charles Martin Hall apart from each other found and patented the procedure which is still in use today, i.e. the electrolysis of Al_2O_3 dissolved in cryolite (Na_3AlF_6) melt. The working temperature of their melts was nearly 1010 °C, which is the melting point of cryolite. The Hall-Héroult procedure is the only process by which aluminum is produced industrially today [1]. The schematic of Hall-Héroult process is shown in the Fig. 1.1.

In the Hall-Héroult method, liquid aluminum is produced by electrolytic reduction of alumina which is dissolved in an electrolyte mostly containing molten cryolite. The oxygen from alumina is electrolytically discharged on the anode and reacts with the carbon anode and therefore consumes it by the formation of mostly gaseous carbon dioxide (CO_2) and small amounts of carbon monoxide (CO). Under the electrolyte bath, there is a pool of molten aluminum, contained in a carbon lining with insulation materials inside a steel shell. The aluminum is deposited at the bottom of the carbon-lined bath, which acts as the cathode. Thus, the overall chemical reaction can be written [1]:



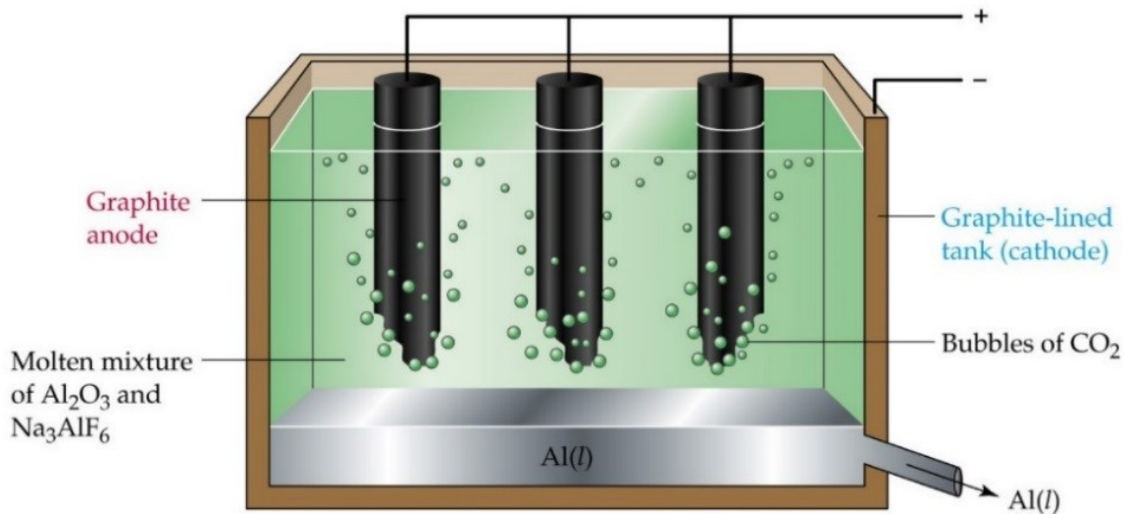
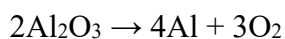


Figure 1.1. Schematic of the Hall-Héroult Process [2].

Current technology uses carbon anodes that consume during the electrolysis of the aluminum to form CO₂. Other greenhouse gases (GHGs) may also be formed during electrolysis, such as perfluorocarbons. Although it is essentially produced from hydroelectricity, Canadian aluminum production is an important source of (GHG). Over the past 20 years, the modernization of aluminum smelters and improved process control have significantly improved the environmental performance of this industry. Despite this, with an average of 2 tons of CO₂ emitted per ton of Al in 2020 [3], the production of Al is the main industrial process emitter of GHG in Quebec with 38.3% (4.7 Mt CO₂ eq.) of emissions in this sector in 2018 [4].

1.2. Inert anodes

Substitution of consumable carbon anodes by inert (O₂-evolving) anodes in the Hall-Héroult process has both environmental and economic benefits. In contrast to the traditional carbon anode, which reacts with the cryolite bath producing carbon dioxide (CO₂), the inert anode serves as a catalyst for the reduction of alumina into gaseous oxygen (O₂) and metallic aluminum. Here is the reaction at the inert anode.



This would allow GHG reductions of 75 to 100% depending on the type of emissions (CO₂, CF_x, NO_x, SO_x ...) [5]. Furthermore, the purity, availability and cost of the carbon is becoming a

concern for producers. It is therefore not surprising that the development of inert anodes is a primary R&D priority of the primary aluminum industry.

Table 1.1. Performance targets for inert anodes [6].

Essential (1 st Tier)		Beneficial (2 nd Tier)
Criterion	Target for Inert Anode	Criterion
Electrochemical and thermodynamic stability	Erosion rate of <10 mm/yr with current density (0.8 amps/cm ²)	Health and Safety
Electrochemical behavior (Current density)	Polarization voltage of <0.5 volts at 0.8 amps/cm ²	Economics
Electrical conductivity	Voltage (continuous) drop no worse than with carbon anode - bus to electrolyte	Net Energy
Mechanical properties	Sufficiently robust to survive in normal plant conditions - must withstand cell vibrations - must support its own weight - must maintain mechanical integrity - must not suffer from thermal shock - must survive in normal bath - must handle heat-up from room to operating temperature range of 930 °C- 1100 °C	Opportunity for Retrofit
Oxidation	Stability in oxygen at 1,000 °C - should not spall - may be a higher/lower operating temperature	Potential for Bath Chemistry Modification
Metal quality	No worse than today's quality - 0.1% Fe, 0.2% Si - meets today's market standards	Other Cell Construction Materials
Environmental and safety acceptability of the material	Eliminate beryllium, chromium, radioactive and EPA-defined hazardous materials	Thermal Conductivity
		Porosity
		Positive Influence on Cathode life

The quest for a stable material in contact with cryolite and electrolysis temperatures, which must also have good electrical conductivity is not simple. There are several challenges to the

development of inert anodes. In this context, US Department of Energy published an “Inert Anode Roadmap” in 1998 in which the expected and required potential benefits from inert anodes were established [6]. In the “Inert Anode Roadmap”, different performance criteria were defined for inert anodes. These performance criteria were categorized into two sets, Essential (first tier) targets and Beneficial (second tier) targets, as presented in Table 1.1.

To date, the efforts have focused on three possible materials classes: ceramics, cermets and metals. Among these materials classes, metals appear to be the most promising material for inert anodes [7]. They have the advantage of having a high electrical conductivity, good thermomechanical resistance and easy to manufacture. However, most metals being soluble in a cryolite medium, their resistance to corrosion rests on the formation of a surface oxide layer which must remain sufficiently conductive, stable, dense and adherent during electrolysis.

Among several possible metals, alloys with different compositions based on Ni, Fe, Cu, Co or Al elements have been widely studied. Cu-Al alloys have been used as inert anode in studies by Hyrn et al. [8,9]. Shi et al. [10] used Ni-Fe alloys as inert anodes and Simakov et al. [11] studied Ni-based anodes containing Fe, Cu and Al. With the obtained results, these alloys seemed to be promising inert anodes, however, the purity of produced aluminum was relatively low due to its contamination with iron or copper.

To address this issue, coatings have been proposed as a means of protecting the underlying material. While there is a vast literature on the inert anode materials [7,12,13], there is very limited published work on the coating of inert anodes. In the following section, previous works on coatings on inert anodes for aluminum electrolysis are reviewed.

1.3. Literature review on coatings of inert anodes

In this section, a brief review of what has been investigated so far on coatings of inert anodes is provided.

1.3.1. Cerium oxide coated anodes

In 1982, researchers discovered that cerium oxide coatings could be deposited anodically from the cryolite melt on different substrates [14]. This discovery resulted in the concept of a CeO₂ self-forming anode technology. The self-forming anode technology assumes that the addition of

cerium oxide to the bath of molten cryolite under controlled conditions allows the formation of a protective coating on a proper conducting substrate.

In this research, the deposition of CeO_2 on tin oxide substrate has been done using a commercial molten cryolite [14]. Generally, the thickness of coating and average size of the pores increased with increasing cerium oxide concentration (Fig. 1.2). For measuring the corrosive attack on the tin oxide anode, the cryolite bath and aluminum pool were analyzed for tin. In all cases, the impurity amounts in the cryolite melt were very low. Additionally, the tin levels were decreased by the presence of Ce in the bath.

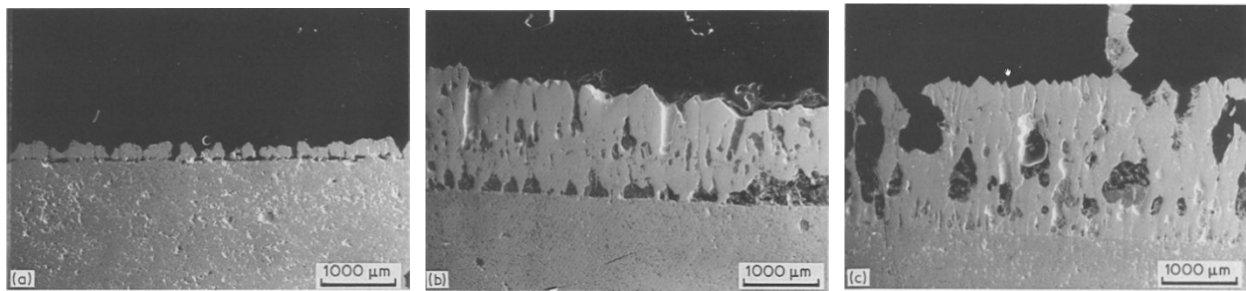


Figure 1.2. SEM micrographs of CeO_2 coatings deposited with varying initial CeO_2 concentration (a) 0.5; (b) 1.0; (c) 1.5% [14].

Although addition of Ce to the molten cryolite reduces the levels of substrate impurities in the aluminum electrolysis, appreciable cerium levels in the aluminum product were observed. Another limitation of this work is the mismatch between the substrate and coating which may lead to crack that permit electrolyte penetration.

1.3.2. Inert anode composed of Ni–Cr alloy substrate, intermediate oxide film and $\alpha\text{-Al}_2\text{O}_3/\text{Au}$ (Au–Pt, Au–Pd, Au–Rh) surface composite coating

The Ni85Cr15 alloy was used in this research as substrate material of the inert anode [15]. The intermediate oxide film consisting $\text{ZrO}_2/\text{Y}_2\text{O}_3$ was prepared by electrochemical deposition. Also, electrophoretic deposition (EPD) and hot press were applied to prepare the surface composite coating consisting $\alpha\text{-Al}_2\text{O}_3$ particles embedded in Au (Au–Pt, Au–Pd, Au–Rh). The intermediate oxide film provides good adhesion and mutual diffusion resistance between the surface composite coating and substrate material. The surface composite coating is supposed to improve the erosion and corrosion resistance of inert anode. The SEM images of inert anode are shown in Fig. 1.3.

All the inert anodes used in this research showed excellent high temperature oxidation resistance [15]. In addition, no F^- or Na^+ was detected in the substrate, intermediate oxide film and surface coating after 10 hours' electrolysis test. It means that surface composite coating could prevent the corrosion of molten electrolyte.

It was shown that decreasing the bath temperature from 960°C to 800°C leads to the slower anode corrosion [15]. So, the inert anodes have an excellent future of industrial application to manufacture high purity aluminum in low temperature Al electrolysis.

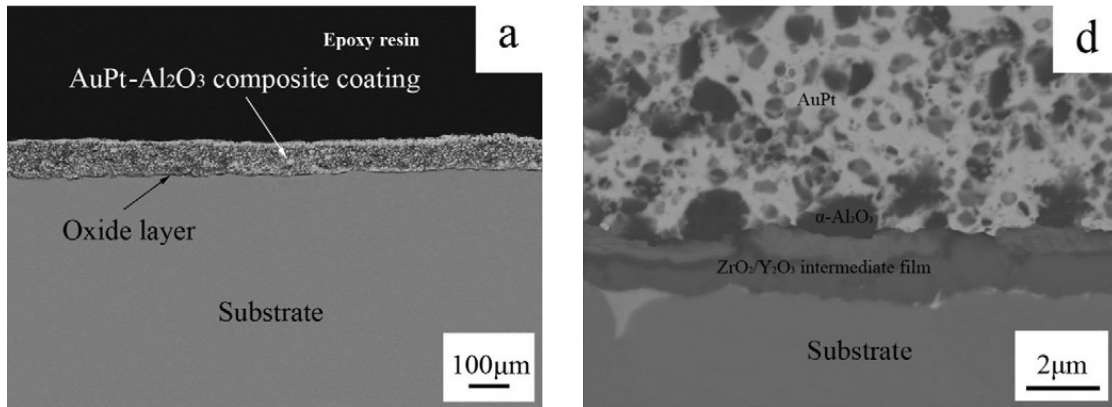


Figure 1.3. SEM images of inert anode composed of Ni–Cr substrate, intermediate oxide film and α - Al_2O_3 /Au surface coating [15].

The limitation of this work is that the electrolysis test duration was only 10 h. Longer test time might reduce the stability of the structure of intermediate oxide film.

1.3.3. Cold sprayed Cu-Ni-Fe anode for Al production

In this research, cold spray deposition of $Cu_{65}Ni_{20}Fe_{15}$ powder on the copper-based alloy C63000 substrate has been studied. Among the many metallic materials studied to date, Cu-Ni-Fe base alloys appear to be the most promising due to their ability to form a layer of nickel ferrite ($NiFe_2O_4$) at the surface of the anode which is known to have low solubility in cryolite [16]. It has been demonstrated that $Cu_{65}Ni_{20}Fe_{15}$ material manufactured by mechanical alloying has a good corrosion resistance in a $KF-AlF_3$ electrolyte medium at 700 °C [17].

The coating adhesion is very dependent of substrate geometry. As can be seen in Fig. 1.4, no porosity in the coatings and a very good interface are apparent in the vertical zone of the anode. While, on the curved section of the anode, porosities in the coating and poor-quality interface are

clearly observed. This can be explained by some factors like the temperature of substrate and particle impact angle during spraying [18]. The impacting angle of 90° is optimum, and any change to this amount reduces the velocity vector perpendicular to the surface and leads to less particle deformation and its resulting adherence [18].

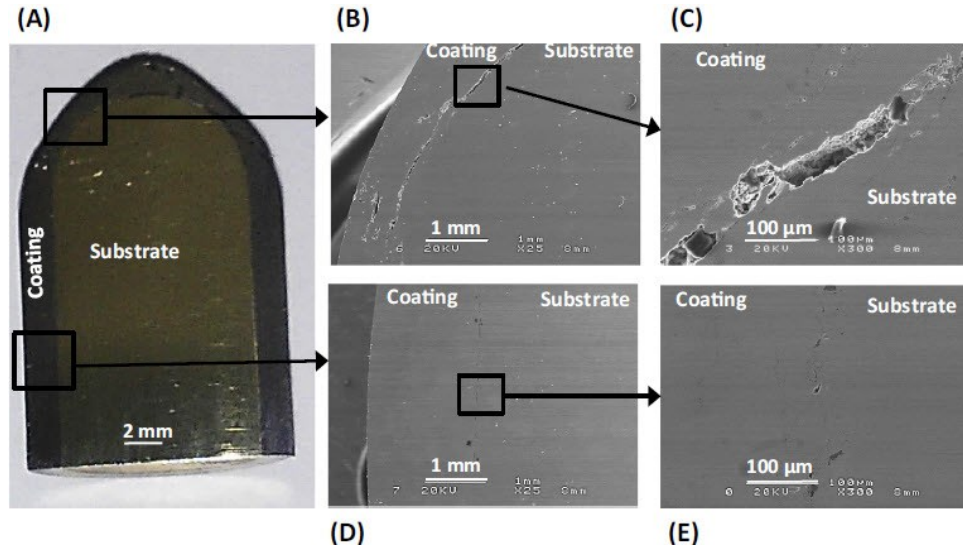


Figure 1.4. Cross section images at different zones of the cold sprayed 65Cu20Ni15Fe (A) transversal slice image, (B, C) curved top part and (D, E) longitudinal part of the anode [18].

Goupil et al. [18] showed that after 50 hours of electrolysis test, the outmost layer of the anode was composed of a Ni-Fe-O rich layer (NiFe_2O_4) with a reducing amount of Cu to the oxide/electrolyte interface. Also, major electrolyte penetration occurred in the oxide scale and accumulates in the Cu-depleted region. In addition, many FeF_2 precipitates were detected in the bulk alloy up to a depth of about 500 microns. The formation of these precipitates in the bulk alloy induces a reduction of electrical conductivity of the inert anode, resulting in an increase of the cell voltage. This increase of the cell voltage would increase the energy cost of aluminum electrolysis procedure and hence, it must be prevented [18].

Recently, Jucken et al. [19] investigated the anodic behavior of cold-sprayed $\text{Cu}_{65}\text{Ni}_{20}\text{Fe}_{15}$ anode in low temperature potassium based cryolite and compared to uncoated C63000 anode. They showed that a NiFe_2O_4 -rich layer is progressively formed in the cold-sprayed $\text{Cu}_{65}\text{Ni}_{20}\text{Fe}_{15}$ coating that is more effective in protecting the anode than the CuO-rich layer formed on the uncoated C63000 anode. As a result, a lower anode wear rate and a higher produced Al purity were observed with the $\text{Cu}_{65}\text{Ni}_{20}\text{Fe}_{15}$ -coated anode compared to the bare C63000 anode [19].

1.3.4. De Nora oxygen evolving inert metallic anode

In the work of Nguyen and Nora [20], the inert anode was constituted by a Ni-Fe base metal structure, having an active semi-conductor coating of Ni-Co mixed oxide. The Ni-Fe based metals, should be a proper material for the oxygen evolving anode because of its protective and stable mixed oxide layer of nickel ferrite (NiFe_2O_4). However, it has been proved that the Ni element in the alloy is sensitive to the fluorination reaction with aluminum fluoride, forming an insulating nickel fluoride layer at the interface of metal and oxide. Thus, the presence of an aluminum fluoride barrier is essential to protect the Ni-Fe metal of the anode substrate [20].

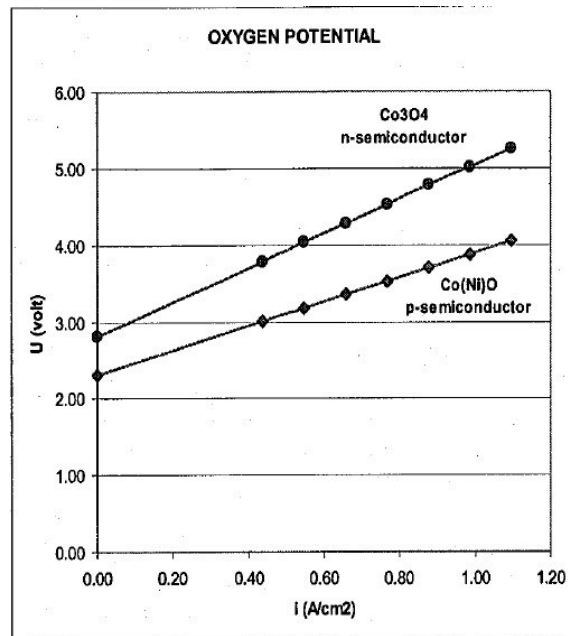


Figure 1.5. Experimental oxygen over-potentials of $(\text{Co},\text{Ni})\text{O}$ and Co_3O_4 coatings in cryolite at 930 °C [20].

An interactive external coating can produce the protective layer playing the role of the fluorination barrier. The CoO phase is very stable against the corresponding fluoride. In addition, cobalt oxides are considered as electronic semi-conductors. For the oxygen evolving anode application, the CoO form is more appropriate than the Co_3O_4 form since the electrical conductivity of CoO phase under anode operating conditions in cryolite bath is much higher than that of Co_3O_4 phase under similar conditions. Indeed, the Co_3O_4 is an n-type semiconductor that displays a significantly higher O_2 evolution overpotential than p-type semiconductor CoO. The

oxygen overpotentials of CoO and Co₃O₄ coatings measured at 930 °C in molten cryolite is shown in Fig. 1.5 [20].

The transformation equilibrium of CoO \leftrightarrow Co₃O₄ depends on the temperature and oxygen pressure. The CoO is stable at high temperature and low oxygen pressure and the Co₃O₄ is stable at low temperature and high oxygen pressure. To maintain the CoO form under the electrolysis conditions ($p_{O_2} = 1$ bar), the presence of a stabilizing element is essential. It has been found that about 15 wt% of nickel (Ni) stabilizes the CoO phase and makes it possible to avoid its transformation into Co₃O₄ phase [20].

In this work, (Co, Ni) O layer was obtained by electrodeposition of a metal layer of Ni-Co at the surface of the alloy followed by oxidation in air at a temperature of 920 °C [20]. However, due to the change of density upon oxidation of the metallic Co-Ni alloy, this manner of producing the cohesive, crack-free oxide layer required for industrial Al production may be challenging. Moreover, considering the limited thickness of the (Co,Ni)O layer (typically ~ 200 μm) and its estimated dissolution rate at 8 $\mu\text{m}/\text{day}$, its life in electrolysis conditions is ~ 1 month. It is therefore less than the minimum duration of inert anodes set by the industry (≥ 1 year) [21]. This layer of (Co,Ni)O must therefore be able to pass a certain amount of oxygen into the underlying alloy so that there is formation of a protective layer of NiFe₂O₄ before the complete dissolution of (Co,Ni)O.

1.4. Development of inert anode by deposition processes

Mechanically alloyed Cu-Ni-Fe materials with various compositions have been investigated as non-consumable anodes in KF-AlF₃ electrolyte at 700°C [17, 22-26]. It has been found that their corrosion resistance depends critically on the alloy composition, especially the copper content [23]. The Cu₆₅Ni₂₀Fe₁₅ (wt. pct.) has been identified as the optimum anode composition due to its higher ability to form a protective NiFe₂O₄-rich layer during aluminum electrolysis. The Cu-Ni-Fe alloys are produced by casting method. The production of a single-phase Cu-Ni-Fe alloy is challenging because Cu-Ni-Fe alloys tend to decompose into Cu-rich and Fe-Ni-rich phases during cooling [27], which is detrimental for their corrosion resistance during electrolysis [28]. However, it has demonstrated that single phase Cu-Ni-Fe alloys can be obtained using a suitable post-casting heat treatment [29].

Based on the current state of the industrial research developments, carbon-free Al electrolysis process with inert anodes will inevitably replace the traditional carbon anode in the future. However, there are no inert anodes fully meet the prerequisites of the aluminum industry to date [30]. Cu-Ni-Fe alloys have shown promising properties as inert anodes in low temperature electrolyte due to their ability to form a low-soluble NiFe_2O_4 surface scale upon Al electrolysis. However, the limitation for these alloys is the penetration of electrolyte in the oxide scale and the formation of insulating FeF_2 precipitates in the bulk alloy. Thus, further effort must be paid to develop appropriate strategies to improve the corrosion resistance of the Cu-Ni-Fe alloys.

Therefore, development of a surface coating treatment for preventing penetration of electrolyte into the nickel ferrite layer formed during the electrolysis and transport of fluorides in the underlying Cu-Ni-Fe alloy can meet the aluminum industry requirements. This layer must have a low porosity, good adhesion, good electrical conductivity, Low solubility in the electrolyte and low affinity for fluorides. The most suitable material is the mixed oxide $(\text{Co,Ni})\text{O}$. Indeed, the work of Nguyen and Nora [20] demonstrated the effectiveness of $(\text{Co,Ni})\text{O}$ as a barrier for fluorination of Ni-Fe metal anodes in cryolite at 930 °C. This is due to the fact that the CoO phase is very stable versus the fluorides. However, as indicated above, this work presents some limitations.

In order to meet these limitations, it can be proposed to provide protective coatings of $(\text{Co,Ni})\text{O}$ on the Cu-Ni-Fe anodes by thermal spraying.

1.5. Thermal spray processes

In thermal spray processes, a heat source, which can be a combustion or a non-combustion source such as an electric arc or a plasma, is used to fully or partially melt the feedstock materials that are pushed at high velocities toward a substrate by a stream of gas or an atomization liquid jet. The feedstock material is typically in powder, wire or rod form. Upon impact, the molten or semi-molten droplets form splats, rapidly cool down and solidify. Thus, a layer of coating is formed by the collection of these splats on the surface of the substrate. Fig. 1.6 depicts a schematic of thermal spray process [31].

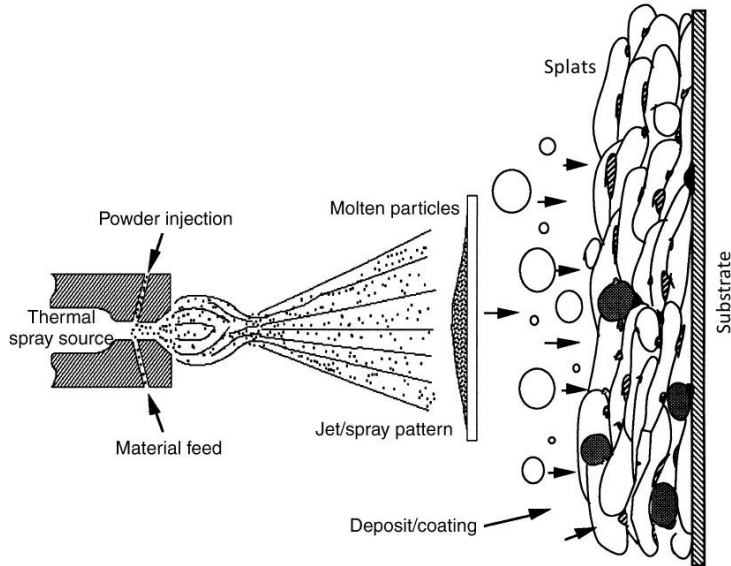


Figure 1.6. Schematic view of a thermal spray process [30].

Using thermal spray techniques, the surface morphology, microstructure and characteristics of the coatings can be governed by controlling the spray parameters [32]. Different thermal spray processes include flame spray, wire arc spray, plasma spray, high velocity oxygen-fuel (HVOF), and cold spray. Fig. 1.7 [33] presents a comparison between different thermal spray techniques based on the temperature and velocity ranges of the particles. This range of temperatures and velocities allows the deposition of almost any type of materials (metals, refractory alloys, ceramics, cermets, ...).

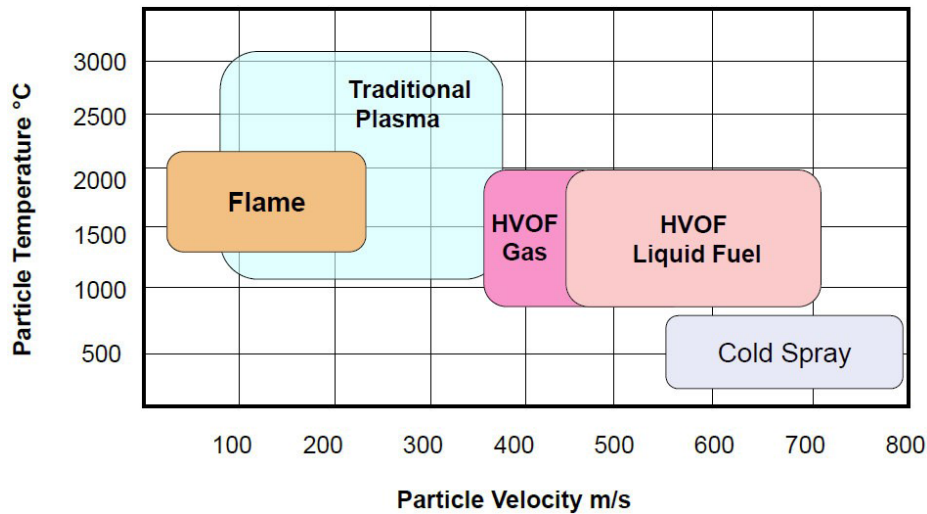


Figure 1.7. Overview of particle temperature versus particle velocity for different thermal spray processes [32].

The first benefit expected from the thermal spray method is the possibility of obtaining direct deposits of Co-Ni oxides in contrast to the current method of electrodeposition-thermal oxidation. In fact, the variation in volume associated with the transformation of (Co,Ni) into (Co,Ni)O and its problems (creation of porosity and delamination) will be eliminated. There will also be better chemical homogeneity of the deposit with no oxygen concentration gradient. Thermal spray processes will also make it possible to easily vary the composition of the deposit by changing the composition of the spray powders. They will allow us to obtain thick deposits (> 200 μm) with deposition rates 1-10 kg/h, which is essential from the industrial point of view. Such high deposition rates make this process suitable for large scale production. In addition, rapid spray rates and high deposit efficiencies result in relatively low processing costs. Finally, it is used on site for the restoration of eroded anodes.

In this study, two approaches are used for producing (Co,Ni)O coatings: suspension plasma spray and HVOF.

1.5.1. Suspension plasma spray

In recent years, the interest for producing plasma sprayed coatings using nanosized materials has increased since they can provide unique properties and superior performances [34]. However, the difficulties associated with injection and low flowability of nanosized particles through the conventional powder plasma spray process such as atmospheric plasma spray (APS), raise the need for a relatively new variety of plasma spraying called suspension plasma spray (SPS) to overcome these problems.

In plasma spraying, the plasma plume is generated by an electric arc between an anode and a cathode. The plasma gas injected in the torch is heated and accelerated by the arc and exits the nozzle as a plasma jet with high temperature and high velocity. The feedstock suspension is basically made of mixing the solvent (most of the time water or ethanol), the powder (with particle sizes ranging from tens of nanometers to a few micrometers), and a dispersing agent that helps stabilize the suspension. The injection of liquid suspension to the plasma jet can be either radial or axial. The schematic of SPS process with axial injection is shown in Fig. 1.8 [35].

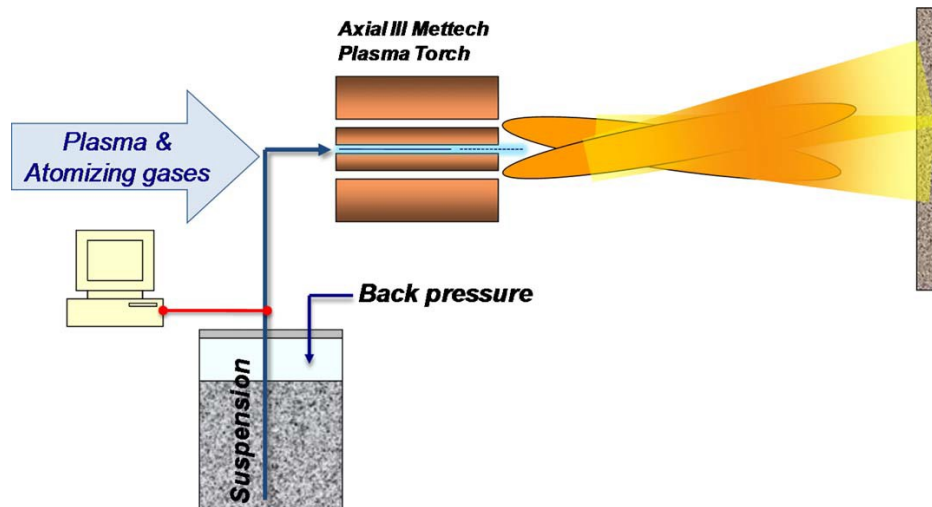


Figure 1.8. Schematic of the suspension plasma spray system with axial injection [35].

In a SPS process, the suspension is injected to the plasma plume and undergoes fragmentation of the liquid stream into droplets. Then the solvent evaporates due to the heat from the plasma, and the accelerated particles fully, or partially, melt depending on the condition and temperature and impact onto the substrate to form layers of splats and eventually the coating [36]. The coating formation stages in the SPS process are schematically presented in Fig. 1.9 [37]. The spray distance in SPS has to be rather short, between 4 and 6 cm, as smaller particles decelerate faster and undergo highly rapid heating and cooling rates [31,38].

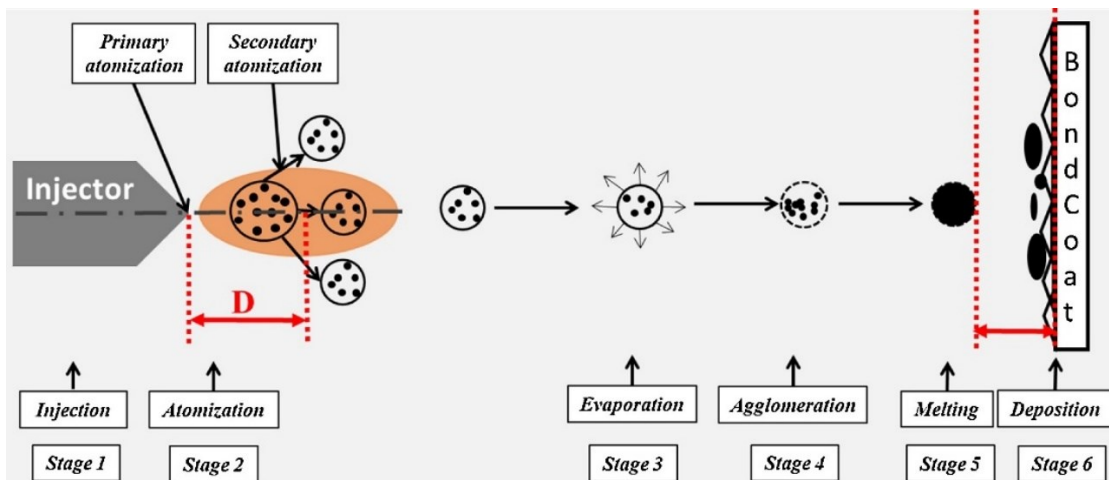


Figure 1.9. Schematic of the consecutive events (stages) in SPS coating deposition [37].

An important thing to be noted in SPS is its unique columnar microstructure. The formation of columnar structures in SPS coatings can be described by the shadowing effect that influences the deposition of individual particles or droplets on the surface. When the plasma jet encounters the surface of the substrate, the molten particles or droplets follow various trajectories, depending on their size and, thus, momentum. The smaller and lighter particles with low momentum are entrained by the plasma flow, following trajectories almost parallel to the surface of the substrate and attaching at a shallow angle on the surface asperities, not impacting on top of them. Unlike those small particles, the larger ones with higher momentum continue on their initial trajectory and impinge on the substrate, as shown in Fig. 1.10 [39].

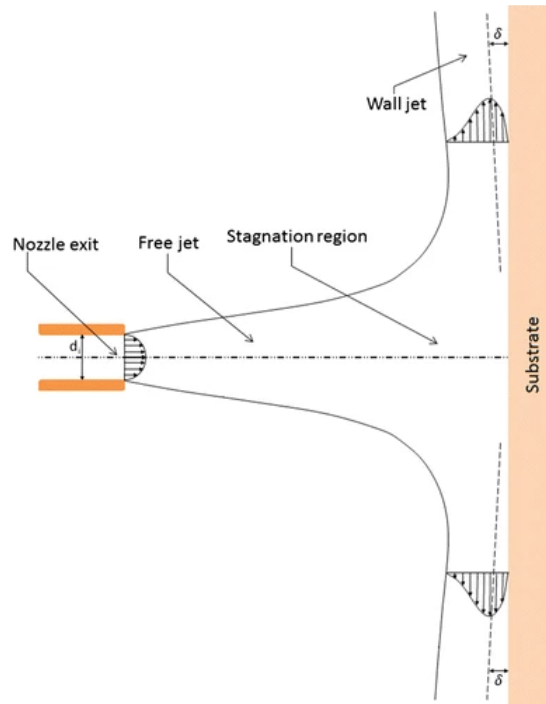


Figure 1.10. Schematic of a typical impinging gas-jet system [39].

The particle shadowing effect, explained by VanEvery et al. [40], is depicted schematically in Fig. 1.11 [41]. According to the authors, there are three major possible types of coating microstructures in SPS. Shadowing effect is largest if the suspension droplet size is extremely small ($< 1 \mu\text{m}$), which can produce a columnar type microstructure. Suspension droplets with diameters ranging from 1 to 5 μm are still small enough to be influenced by the plasma jet, hence, they can generate a feathery columnar microstructure, which contains some porosity bands within

the columns. Finally, droplets with significantly larger size ($> 5 \mu\text{m}$) are less affected by the plasma flow, therefore, they impact normally on the substrate to form a lamellar (similar to the conventional APS method) or vertically cracked structure.

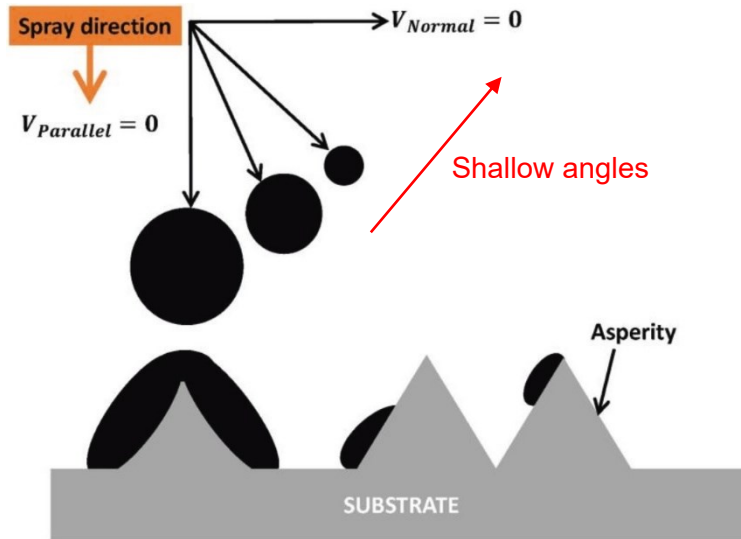


Figure 1.11. Schematic illustration of the shadowing of different-size droplets impacting on substrate asperities [41].

Obtaining a dense protective coating is necessary to improve the corrosion resistance of the inert anode. Therefore, a Mettech Axial III torch is used in this work. With this plasma gun, it is possible to form dense coatings, due to the high particle velocity that can be achieved. This torch consists of three cathodes and three anodes operated by three independent power supplies (see Fig. 1.12). The suspension liquid is injected axially in between the three plasma jets converging within an interchangeable water-cooled nozzle. Since the three plasma jets fluctuate quite independently, voltage fluctuations have lower effects on the axially injected liquid [36].

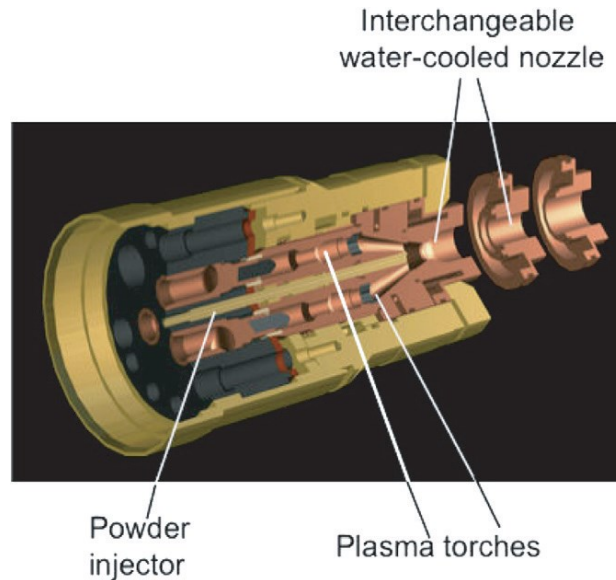


Figure 1.12. Schematic of the Northwest Mettech Axial III central injection torch [36].

The difference in the extent of melting and mixing phenomena may be recognized as a fundamental characteristic of thermal spray processes in deposition of composite materials [42]. In-flight mixing of particles in the composite coatings has been already reported in the literature. Toma et al. [43] sprayed Cr_2O_3 -15% TiO_2 coatings using suspension-HVOF process. They used two routes to produce suspensions: (a) mixture of two stable suspensions in the desired ratio, and (b) dispersion of an appropriate alloyed material in the solvent. Both routes resulted in single phase coatings confirming that in-flight mixing was occurred during spraying. Tarasi et al. [42] reported that in-flight melting followed by mixing are crucial processes for the formation of an amorphous phase during suspension plasma spraying of the alumina-zirconia composite. It was found that the particle velocity has an important role in amorphous phase formation. They reported that longer exposure at high temperature (lower in-flight particle velocity) results in higher amorphous contents due to more complete melting and mixing.

1.5.2. High Velocity Oxy-Fuel (HVOF) spray

High velocity oxy-fuel technique was commercially introduced at the beginning of the 1980s. In this process, the fuel gas or liquid (hydrogen, kerosene, propylene, ethylene, acetylene, etc.) and pure oxygen are introduced into the combustion chamber and subsequently ignited and combusted [44,45]. The exhausted gas accelerates in a converging-diverging nozzle, which is

connected to the chamber, where a supersonic gas velocity can be achieved. As the high velocity flow (500–1200 m/s) exits the nozzle, shock diamonds are formed because of the pressure difference between the high velocity flow and ambient atmosphere. The coating material in the form of powder (size range nominally 5–45 μm) can be injected radially or axially into the gas by nitrogen or argon as the carrier gas. The powder feedstock melts or partially melts in the flame and deposits on the substrate. This process is usually used to produce not only metal and cermet coatings whose melting points are relatively low, but also ceramic coatings such as alumina. A schematic of a typical HVOF system is shown in Fig. 1.13 [46].

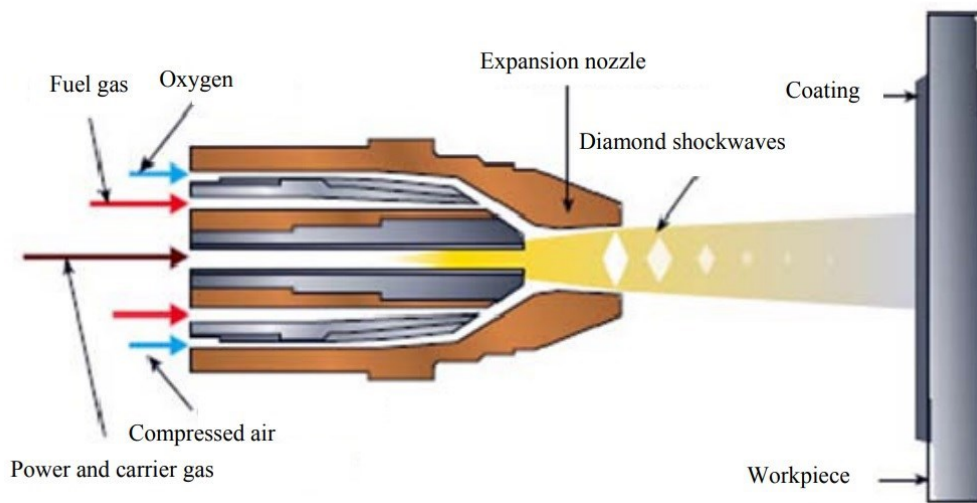


Figure 1.13. A schematic of the high-velocity oxy-fuel technique [46].

As the process temperature in HVOF is much lower than in plasma spray, (see Fig.1.6), the particles are usually not completely melted during the deposition by HVOF. Nevertheless, the high particles velocity leads to the formation of a dense stack of flattened droplets on the substrate, which results in smooth and uniform coatings with good adhesion to the substrate. Using HVOF process, the shorter residence time of the powder in the flame and also lower flame temperature as compared to plasma spray methods, leads to decrease the possibility of reduction, oxidation or decomposition of powder particles during spraying [47].

1.6. Objectives

Previous works show that, the results obtained to date with inert anodes based on Cu-Ni-Fe alloys are encouraging but still insufficient to fully meet the industrial requirements of aluminum

production. In this context, the **main objective** of this research is to develop a thermal spray coating of mixed oxide (Co,Ni)O which will significantly improve the corrosion resistance of Cu-Ni-Fe anodes. In order to achieve this main objective, the following sub-objectives are considered,

- To produce a dense, single phase, coherent and crack-free oxide coating as required for industrial aluminum production;
- To investigate the effect of coating structure on the electrolytic performance of coated anodes;
- To make an assessment of durability of the coating under anode operating conditions in electrolysis process.

1.7. Thesis organization

This thesis is divided into seven chapters. The first chapter provides a brief introduction about inert anodes for Al production, including a general literature review of the coatings on inert anodes for Al electrolysis process. A short description of the thermal spray processes used in this study (SPS and HVOF) is also given in this chapter. Finally, the objectives and organization of the thesis are presented.

In Chapter 2, the materials, experimental procedures for tests and measurement techniques are explained in detail. Basic background and the principles of operation are given for the characterization methods that are used.

Chapter 3 presents a study on the suspension plasma spray deposition of (Co,Ni)O coatings. This chapter focuses on optimization of the spray parameters to achieve uniform and dense coatings made of a single solid solution phase. The effects of SPS process parameters (plasma power, standoff distance, gas mixture, and substrate temperature) on the structure and composition of coatings are investigated.

Chapter 4 presents more details on the formation of different phases during spraying of CoO and NiO powders by SPS process. In-flight particles and splats are collected to study the melting and mixing behavior of CoO and NiO during spraying. Furthermore, the effect of heat treatment on the coating's microstructure is investigated at 1000 °C under argon to study the possibility of obtaining a single-phase coating.

In Chapter 5, high velocity oxy-fuel is introduced as a promising method for producing (Co,Ni)O coatings. The spray parameters are optimized for obtaining single phase coatings with

smooth morphology. (Co,Ni)O coatings are deposited on both Cu-rich and Ni-rich CuNiFe alloy substrates using CoO, Co_{0.75}Ni_{0.25}O and Co_{0.5}Ni_{0.5}O powders as starting materials. The effect of the coating and substrate compositions on their behavior is studied at 1000 °C under argon and air.

In Chapter 6, the influence of bond coat on high-temperature behavior of (Co,Ni)O coatings sprayed by HVOF on Cu-Ni-Fe anodes is investigated. Top coat of Co_{0.5}Ni_{0.5}O is deposited on CrMnFeCoNi high entropy alloy (HEA) and Ni-20Cr bond coats with Cu-rich and Ni-rich CuNiFe as substrate materials. The effect of bond coat layers on the oxidation resistance of coated samples is investigated at 1000 °C in air.

Chapter 7 summarizes the main achievements, conclusions and contributions of this research, and provides a list of recommendations for the future work.

Appendices A and B include the supplementary data for chapters 3 and 5, respectively.

Appendix C presents a work on the solubility of (Co,Ni)O in molten cryolite and anodic behavior of (Co,Ni)O coated Cu-Ni-Fe electrodes.

The experimental procedure of this project is divided into four phases which are listed in Fig. 1.14.

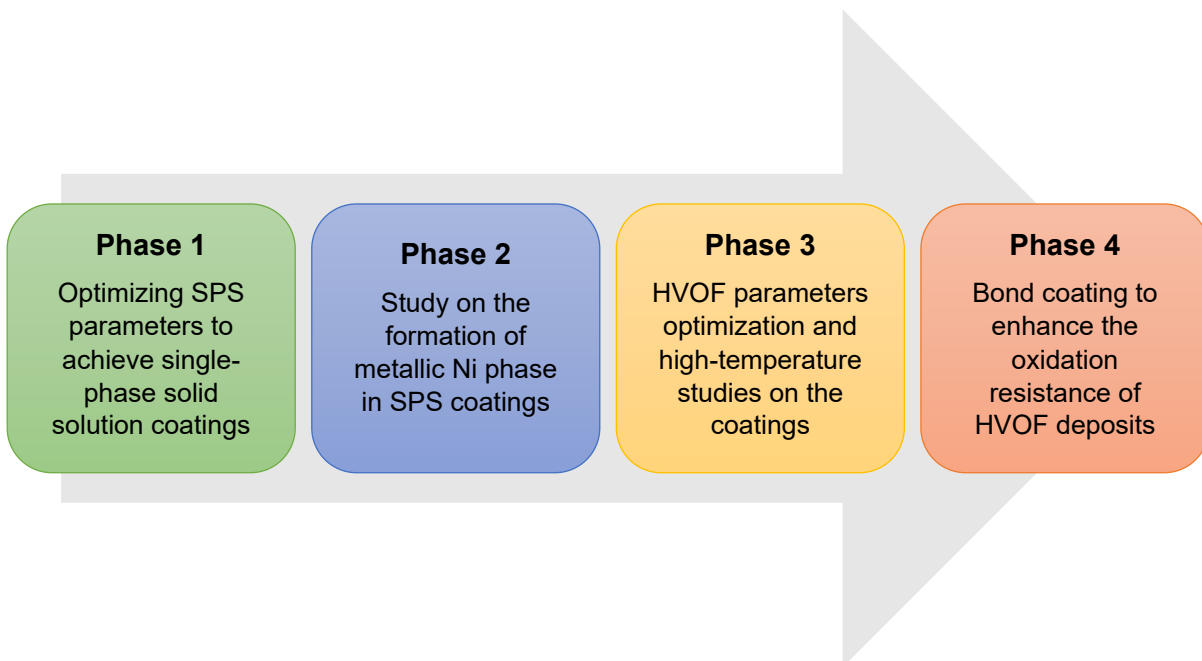


Figure 1.14. Schematic of the four experimental phases in this project.

Chapter 2

Experimental procedures

This chapter aims to introduce and provide details on the used materials and systems, as well as measurement techniques, experimental procedures and the experiments that were executed for this work.

2.1. Sprayed powders

For deposition by SPS, mixtures of as-received CoO and NiO powders with different ratios were used as feedstock materials. For a series of SPS depositions, a $\text{Co}_{0.5}\text{Ni}_{0.5}\text{O}$ solid solution powder was prepared by a three-step process involving: (i) 12 min ball milling of a mixture of Co_3O_4 and NiO with the targeted 50–50 mol% of Co and Ni in an attritor, (ii) heating at 1000 °C for 10 h, and (iii) reducing the powder particle size to less than 3 μm to meet the SPS requirements.

For HVOF depositions, $\text{Co}_{0.75}\text{Ni}_{0.25}\text{O}$ and $\text{Co}_{0.5}\text{Ni}_{0.5}\text{O}$ powders were synthesized by mixing Co_3O_4 and NiO followed by a 12 h heat treatment at 1200 °C. CoO powder was also prepared by heat treating of Co_3O_4 at 1200 °C for 12 h under argon flow, then a rapid cooling to prevent the transformation of CoO to Co_3O_4 during cooling. All powders were sieved with a mesh size of -35 μm to remove large particles and avoid clogging the HVOF gun. They were also sieved with a +20 μm mesh screen to remove small particles and improve the flowability of powders.

2.2. Spray systems

Two different thermal spray processes including suspension plasma spray (SPS) and high-velocity oxy-fuel (HVOF) were used in this investigation to deposit (Co,Ni)O coatings.

2.2.1. Suspension plasma spray

(Co,Ni)O coatings were deposited on stainless steel substrates by spraying mixtures of CoO and NiO powders or $\text{Co}_{0.5}\text{Ni}_{0.5}\text{O}$ solid solution powder using suspension plasma spray. The suspensions were prepared by mixing 10 wt.% of oxide powders with the intended CoO and NiO ratio with 1 wt.% of polyvinylpyrrolidone (PVP) as a dispersant in ethanol. Stirring of suspensions was done magnetically and ultrasonically to breakup the agglomerates and to avoid reagglomeration of particles. For the SPS coating deposition, stainless steel substrates of $25\text{ mm} \times 25\text{ mm} \times 5\text{ mm}$ were grit blasted and then cleaned by rinsing in acetone prior to their use.

A Mettech's Axial III torch (Northwest Mettech, North Vancouver, Canada), illustrated in Fig. 2.1, was used to deposit SPS coatings in this work. The injection nozzle was incorporated in the center of this torch that would allow the axial injection of the feed, in the form of liquid suspension, into the plasma jet. The Mettech plasma gun consists of three cathodes and three anodes operating on three independent power supplies that can reduce the plasma fluctuations as compared to typical radial injection plasma torches. The square-shaped stainless steel substrates were fixed on a sample holder while the torch traversed horizontally across the substrates to cover them with a uniform coating. The substrate temperature was monitored during spraying by a FLIR A320 infrared camera (FLIR Systems Inc., USA).



Figure 2.1. Suspension plasma spray with a Mettech's Axial III gun [48].

2.2.2. High-velocity oxy-fuel

(Co,Ni)O and CoO coatings were deposited on Cu-Ni-Fe alloys using HVOF process. Two compositions of Cu-Ni-Fe alloy, Cu-20Ni-15Fe and Ni-25Fe-10Cu (in wt.%), were used as substrates. Mono-phased Cu-Ni-Fe alloys were produced by the casting method and then homogenized by a post-casting heat treatment to avoid the formation of a two-phase structure (a Cu-rich phase and a Fe-Ni-rich phase) during their solidification [49,50]. These alloys were cut into disk shaped coupons with 15 mm diameter and ~7 mm thickness. (Co,Ni)O and CoO powders were prepared by a heat treatment process as explained above. All powders were dried in an oven at 75 °C for at least 24 h prior to deposition.

HVOF coatings in this thesis were generated using a propylene-fueled Diamond Jet 2700-hybrid gun (Oerlikon Metco, Westbury, NY). The HVOF gun used in this work is presented in Fig. 2.2. A FLIR A320 infrared camera was used to monitor substrate temperature during the HVOF coating process.



Figure 2.2. Diamond Jet 2700-hybrid HVOF gun from Oerlikon Metco [48].

2.3. Measurement techniques

2.3.1. Particle size measurements

Particle size analyses for CoO, NiO and (Co,Ni)O powders were performed using a Malvern Panalytical Spraytec instrument. The functioning of this system is based on the technique of laser diffraction and the fact that the intensity of light scattered by the particles depends on the size of the particles.

For particle size measurements, powders were suspended in a liquid dispersant (water or ethanol) and then were analyzed using a Malvern Wet Dispersion Accessory instrument (shown in Fig. 2.3). The suspensions were continuously recirculated using the dispersion unit's pump and stirrer system in order to keep the sample suspended and homogenized. The particle size measurement was performed by pumping the suspension through a measurement cell that is positioned between the Spraytec transmitter and receiver units. Light scattering data for the dispersed particles is then analyzed to calculate the size of particles that created the scattering pattern.



Figure 2.3. The Spraytec Wet Dispersion Accessory [51].

2.3.2. X-ray diffraction (XRD)

X-ray diffraction (XRD) is a well-established characterization technique to determine the constituent phases in a material as well as their crystal structure. In order to fully characterize the crystalline structure of a material, X-rays of a fixed wavelength and at certain incident angles are directed through the material. The incident X-rays interact with the crystal lattice with repeating structure and produce constructive interference (also diffracted rays) only if the Bragg's law is satisfied (Fig. 2.4). According to Bragg Equation:

$$n\lambda = 2d \sin\theta$$

Where λ is the wavelength of the incident X-rays, d is the inter-planar distance and θ is the incident angle of the beam. X-ray detector moves radially around the sample and measures the intensity and position (angle of X-ray diffraction: 2θ) of the peaks. The intensity of the highest peak is set to 100, and the intensity of all other peaks are scaled with respect to this.

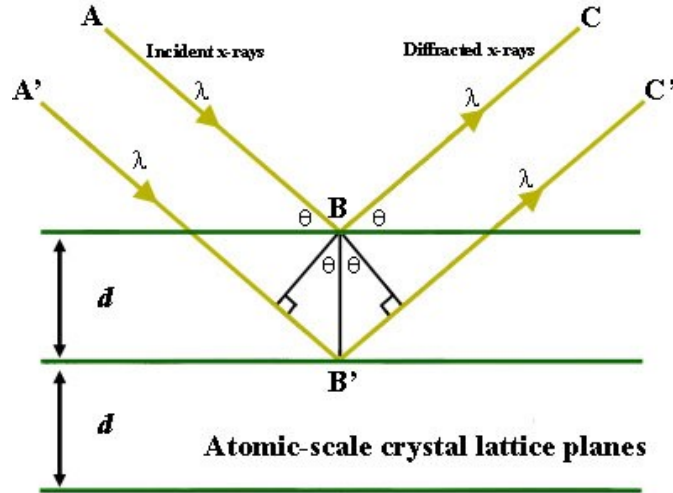


Figure 2.4. Bragg's law reflection [52].

In this work, the X-ray diffraction analysis of powders, alloys and coatings was carried out using a Bruker D8 diffractometer (available at INRS) with Cu K α ($\lambda = 0.15406$ nm) monochromatic radiation in a θ - 2θ configuration. The samples were scanned at the step size of 0.02 to 0.1° for the step duration of 2 to 30 seconds. EVA software was used to identify the phases present and index the diffraction peaks. Measuring the position and the FWHM (Full Width at Half Maximum) of the peaks were carried out by simulating the peaks by a function of the Pseudo-Voigt type. Rietveld refinement technique was used to collect further diffraction data such as structural information and quantitative phase analysis.

Rietveld refinement is a multiparameter curve fitting methodology to reveal crystal structure knowledge concealed in the XRD data. Rietveld refinement is conducted by fitting of an experimental diffraction pattern with reference or calculated patterns and backgrounds. The FULLPROF Suite program was employed for Rietveld refinement.

In our studies, the crystalline structure and unit cell dimensions of (Co,Ni)O powders and (Co,Ni)O coatings deposited by thermal spray methods were identified using Rietveld refinement

analysis. In these analyses, lattice parameters of (Co,Ni)O solid solutions were derived and then a quantitative analysis was performed to obtain relative proportions of solid solution and metallic Ni phases in SPS coatings. The exact composition of solid solution was derived based on the existing linear relationship between the lattice parameter and the NiO molar fraction of the (Co,Ni)O solid solution [53].

2.3.3. Scanning electron microscopy (SEM) equipped with energy-dispersive spectroscopy (EDS)

Scanning electron microscope (SEM) is a powerful and versatile tool for materials characterization. A SEM projects and scans a focused beam of high-energy electrons to form an image. The emitted electrons in the beam interact with atoms in the material, thereby generating a variety of signals at the surface that can be used to obtain information about the surface's topography and chemical composition.

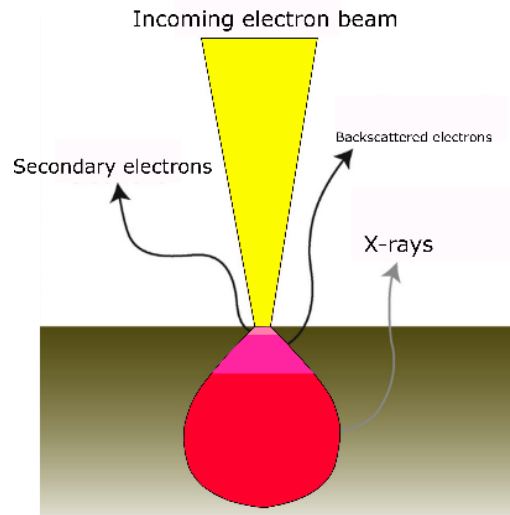


Figure 2.5. Different types of signals used by an SEM and the area from which they originate [54].

The interaction of electrons within a sample can produce several signals including secondary electrons (SE), back-scattered electrons (BSE) and characteristic X-rays as illustrated in Fig. 2.5. These signals are collected by various detectors. Secondary (SE) and back-scattered electrons (BSE) are the signals most commonly used for imaging. SEs are a result of inelastic scattering of the electron beam with the atoms of the sample. By contrast, BSEs are reflected back

after elastic interactions between the primary electrons and the sample material. The energy of SEs is relatively low and they originate from surface regions (see Fig. 2.5) and are most valuable for illustrating morphology and topography on the samples. Whereas, BSEs consist of high-energy electrons arising from deeper regions of the sample (see Fig. 2.5) and are most valuable for showing contrasts in composition in multiphase samples.

For elemental analysis, emitted X-rays with corresponding characteristic energies can be detected by an appropriate detector for EDS. Characteristic X-rays are produced by inelastic collisions of the incident electrons with electrons in lower energy levels (shells) of atoms in the sample material, as illustrated in Fig. 2.6. When the electrons from higher levels return to lower energy states, they generate X-rays that are of exactly the same energy as the difference between the respective energy levels. As the energy of these X-rays is specific for each element of the periodic table, EDS allows the elemental composition of the sample to be measured.

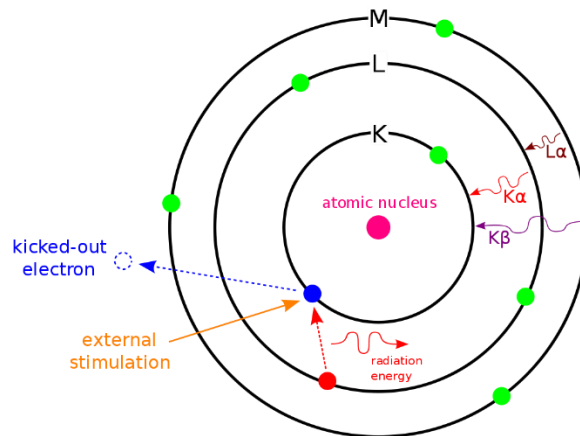


Figure 2.6. Principle of generation of characteristic X-rays [55].

In this project, a Regulus 8230 field-emission scanning electron microscope (FE-SEM), a Tescan Vega3 scanning electron microscope, and a Hitachi S-3400N scanning electron microscope were used for imaging in both secondary electron (SE) and back-scattered electron (BSE) modes at an energy of 5-20 kV. These microscopes, in addition, were used for energy-dispersive spectroscopic (EDS) chemical analysis and compositional mapping. All as-sprayed and heat-treated coatings were cut using a precision cut-off machine (Secotom-15, Struers A/S, Denmark), then mounted and polished using standard metallographic procedures to a final finish of 0.4 μm before being analyzed with SEM-EDS.

2.4. High-temperature dry oxidation tests of coatings

High-temperature behavior of coated Cu-Ni-Fe alloys was investigated at 1000 °C in dry inert and oxidizing atmospheres. Heat treatment of as-coated samples was carried out at 1000 °C for 20 h in static air and under an argon flow in a muffle furnace and a tubular furnace, respectively. The heating rate was 5 °C.min⁻¹. The heat-treated samples were then analyzed with XRD and SEM-EDS.

Preface to Chapter 3.

As it was discussed in the previous chapters, one of the main objectives of this work is to investigate the capability of thermal spray processes to generate (Co,Ni)O coatings that improve the corrosion resistance of inert anodes for Al electrolysis process. In view of that, the suspension plasma spraying (SPS) was the first technique that was investigated. Obtaining a dense protective coating is necessary to improve the corrosion resistance of the inert anode. Therefore, a Mettech Axial III torch is used in this work. With this plasma torch, it is possible to form dense coatings, due to the high particle velocities that can be achieved. Additionally, achieving a homogeneous and single-phase coating is desired for corrosion protection application. As a result, the next chapter in this thesis is entirely devoted to investigating the potential of SPS process to create dense and single phase (Co,Ni)O coatings and how the process parameters can affect on the composition and structure of the resulting coatings.

Chapter 3

Suspension plasma spray deposition of $\text{Co}_x\text{Ni}_{1-x}\text{O}$ coatings¹

Abstract

Suspension Plasma Spray (SPS) process was used for the deposition of cobalt-nickel oxide solid solutions as potential coatings for inert anodes in primary aluminum production. The effects of SPS process parameters (plasma power, standoff distance, gas mixture, and substrate temperature) on the structure and composition of coatings were investigated. X-ray diffraction measurements, coupled with Rietveld refinement analysis, and scanning electron microscope (SEM) coupled with energy-dispersive X-ray spectroscopy (EDX) analyses were performed. It was shown that substrate temperature is the single most important parameter affecting the nature of the coating, and that uniform, adherent and non-porous $\text{Co}_x\text{Ni}_{1-x}\text{O}$ coatings made of a single solid solution phase are obtained when the substrate temperature is above 950 °C. Metallic Ni is observed in coatings prepared at lower temperatures and, in that case, the composition of the solid solution phase deviates from that of the starting materials. This work also discusses possible causes for the formation of metallic nickel during spraying.

Keywords: (Co,Ni)O solid solution, Suspension plasma spray, Al electrolysis

3.1. Introduction

Aluminum is the second most widely used metal in the world. However, primary Al production by electrolysis results in heavy CO₂ emissions [56]. Actually, the aluminum industry is contributing around 1% of the carbon footprint generated by the industrial sector, and 0.21% of

¹ This chapter has been published as an article in the *Surface & Coatings Technology*: S. Mohammadkhani, V. Jalilvand, B. Davis, F. Ben Ettouil, A. Dolatabadi, L. Roué, C. Moreau, D. Guay. *Surface & Coatings Technology* 399 (2020) 126168.

global carbon greenhouse gas (GHG) emissions [57]. A relevant approach to produce Al in a greener way is to substitute consumable carbon (CO_2 evolving) anodes by inert (O_2 evolving) anodes. Among the numerous materials studied so far, Cu-Ni-Fe-based alloys appear to be promising, due to their ability to produce a protective nickel ferrite (NiFe_2O_4) layer in low-temperature ($700\text{ }^\circ\text{C}$) potassium-based cryolite [18,19,58]. However, these Cu-Ni-Fe alloys may fluorinate during electrolysis to form non-conductive nickel or iron fluoride, resulting in an increased cell voltage and a decreased energy efficiency of the electrolysis process [49].

To protect the CuNiFe alloy from corrosion and prevent the formation of metallic fluorides, the use of (Co,Ni)O-based protective coatings appears promising. Indeed, the work of Nguyen and de Nora [20] demonstrated the effectiveness of this oxide as a fluorination barrier for Ni-Fe metal anodes in a cryolitic medium at $930\text{ }^\circ\text{C}$. This is because the CoO phase is very stable with respect to fluorination. However, according to the phase diagram of the Co-O system [59], CoO is likely to be converted to Co_3O_4 under Al electrolysis conditions, which is undesirable since Co_3O_4 is an n-type semiconductor that displays a significantly higher O_2 evolution overpotential than p-type semiconducting CoO [20].

Adding Ni atoms to the CoO phase and forming a (Co,Ni)O solid solution makes it possible to avoid the transformation of CoO to Co_3O_4 [20,60]. The impact of the Ni content on the thermal stability and electrical conductivity of the Co-Ni-O system was highlighted by Moore and White [61]. The thermal stability of $\text{Co}_x\text{Ni}_{1-x}\text{O}$ solid solutions produced by ball milling and calcination has also been studied in our previous work [53].

To make a (Co,Ni)O-based protective coating, a Co-Ni alloy was first electrodeposited onto the anode, followed by an oxidation treatment in air at high temperature to favor the formation of a (Co,Ni)O solid solution [20]. However, due to the change of densities upon oxidation of the metallic Co-Ni alloy, this manner of producing a cohesive, crack-free oxide layer on the inert anode may be challenging.

A potentially relevant method to produce (Co,Ni)O-coated inert anodes is through the direct deposition of (Co,Ni)O oxide compounds, or a mixture of CoO and NiO, *via* thermal spray deposition techniques. Thermal spraying is a promising, fast and efficient method to deposit thick coatings for various applications in a single step [47]. Various thermal spray techniques exist, including high-velocity oxygen fuel (HVOF), high-velocity air fuel (HVOF), atmospheric plasma spray (APS), and suspension plasma spray (SPS). The latter process was invented in the mid-1990s

[62] and has demonstrated its ability to deposit oxide coatings that are usually challenging when using other conventional methods such as electrodeposition, sintering and vacuum-based deposition methods [63]. APS is mainly used for powders that flow easily, and sub-micrometer size powders cannot be used directly due to their low flowability. On the contrary, SPS is ideal for sub-micrometer size particles since they are dispersed and transported by a liquid medium. Also, the main purpose of this study was to prepare coatings made of (Co,Ni)O solid solutions starting from physical mixtures of NiO and CoO powders. During SPS, thinner splats are formed than in APS, which increases the probability that an alloy will form between the two powders.

During SPS, submicron solid particles are injected into a plasma jet from a suspension. The atomization and evaporation of the liquid phase occurs first, followed by the acceleration and melting of particles that travel to and impact the substrate on which they are deposited [38,64,65]. SPS has been widely used to deposit coatings for a variety of applications; these include biomaterials coatings, wear- and corrosion resistant coatings, thermal barrier coatings, ceramic filtration membranes, and abradable coatings [66–68]. This method's advantages include a relatively high deposition rate, versatility, high scalability, moderate operating cost, and controlled thermal input into substrates [63,69]. With SPS, thick coatings (from 10 to 500 μm) with sub-micrometer or nanometer scale structures can be produced [70]. Therefore, the ability to create different distinct types of microstructures (columnar-grown, segmented, dense, and porous), the use of fine particles of single or multiphase composition, and even the capability of combining different processes, presents multiple possibilities in terms of thermal spray engineering [71].

In the current study, a novel approach in the preparation of thick, dense, uniform, and single phase (Co,Ni)O coatings using the SPS process is presented. The effects of spraying parameters on the composition and structure of the coatings were studied.

3.2. Experimental

3.2.1. Materials and spray conditions

Cobalt oxide (CoO, Skyspring Nanomaterials, USA) and nickel oxide (NiO, Fuelcellmaterials, USA) were used as starting powders. The particle size distribution was analyzed by laser diffraction using a Malvern Panalytical Spraytec instrument after dispersing the powder in ethanol using a Malvern wet dispersion accessory.

Table 3.1. Spray process parameters.

Part 1. Powder suspension of 50% CoO + 50% NiO								
Sample #	Total gas (slm), Ar/N ₂ /H ₂ (slm), Current (amps)	Power (kW)	Air cooling	Water cooling	Preheating to 200 °C	Inter-pass pauses	Standoff distance (mm)	Substrate temperature
S1	180, 45/45/10, 155	75	Yes	No	Yes	Yes	50	< 600 °C
S2	180, 45/45/10, 167	80	Yes	No	Yes	Yes	50	< 600 °C
S3	180, 45/45/10, 180	85	Yes	No	Yes	Yes	50	< 600 °C
S4	180, 45/45/10, 192	90	Yes	No	Yes	Yes	50	< 600 °C
S5	180, 45/45/10, 210	95	Yes	No	Yes	Yes	50	< 600 °C
Part 2. Powder suspension of 50% CoO + 50% NiO								
S6	180, 45/45/10, 180	85	Yes	Yes	Yes	Yes	50	< 300 °C
S7	180, 45/45/10, 180	85	Yes	Yes	Yes	Yes	70	< 300 °C
Part 3. Powder suspension of 50% CoO + 50% NiO (S8) and 75% CoO + 25% NiO (S9)								
S8	180, 45/45/10, 180	85	No	No	Yes	No	50	ca 950 °C
S9	180, 45/45/10, 180	85	No	No	No	No	50	ca 950 °C

The plasma spraying parameters used for SPS are listed in Table 3.1. A first series of tests was performed to explore the deposition parameters space (Part 1, samples S1 to S5). Then, a series of three complementary tests were performed. In the first one, a 50–50 mol% CoO + NiO powder mixture was sprayed into water using different plasma powers. The particles were collected, dried in an oven, and analyzed *via* XRD and SEM. In the second one, NiO and CoO powders were deposited separately on a substrate using the spray conditions listed in Part 1 of Table 3.1. Finally, in the third complementary test, a Co_{0.5}Ni_{0.5}O solid solution powder was used as starting material to prepare coatings. The Co_{0.5}Ni_{0.5}O solid solution was prepared through a

three-step process that involves 12 min ball milling step of a mixture of NiO and Co₃O₄ with the targeted 50–50 mol% of Co and Ni, followed by a heat treatment at 1000 °C for 10 h and a final 3 h ball milling step to reduce the powder particle size to under 3 μm to meet the SPS requirements. Following these complementary tests, a second and a third series of tests (S6–S7 and S8–S9 samples, respectively) were performed to obtain a single-phase coating with low porosity and good adhesion. Square-shaped AISI 304 Stainless steel substrates (2.5 * 2.5 cm² and 0.5 cm thickness) were grit blasted and then rinsed with acetone prior to their use. All substrates have been prepared using the same conditions resulting in a surface roughness, R_a , of 1.3 ± 0.2 μm.

Suspensions of CoO and NiO were prepared by mixing 10 wt% of oxide powders with the intended CoO and NiO ratio with 1 wt% of polyvinylpyrrolidone (PVP) as a dispersing agent in ethanol. The injection setup for SPS was developed in-house, and has been described in detail in our previous work [42]. A Mettech's Axial III Plasma Spray System was used in all experiments. This is a high-power, high-efficiency deposition device with axial injection capability (injection of feedstock materials directly into the center of the plasma plume). A FLIR A320 infrared camera (FLIR Systems Inc., USA) was used to monitor substrate temperature during SPS.

3.2.2. Materials Characterization

The crystalline structure of coatings was determined by X-ray diffraction (XRD) using a Bruker D8 diffractometer with Cu K α radiation. The crystalline structure and unit cell dimensions were obtained through the Rietveld refinement technique, a multi-parameter curve-fitting procedure to extract structural information from the XRD pattern. Refinements of lattice parameters were carried out using the FULLPROF program [72]. The background was removed in the XRD patterns shown below.

As-sprayed specimens were cut using a precision cut-off machine (Secotom-15, Struers A/S, Denmark), then mounted and polished using standard metallographic procedures to a final finish of 0.4 μm. A scanning electron microscope (SEM) coupled with an energy-dispersive X-ray spectroscopy (EDX) elemental analyser (S-3400N, Hitachi High Technologies America, Inc., USA) operating at 15 kV was used for metallographic observation of the deposited samples.

3.3. Results

SEM micrographs of precursor powders are shown in Fig. 3.1. CoO and NiO powders consist of spherical particles. Figures 3.1c and d shows the corresponding particle size distribution histograms. The particle diameters of CoO powder are centered along a single mode (maximal frequency) at 3 μm , while those of NiO powder are spread over two modes located at 0.5 and 6 μm . The D10, D50, and D90 values are 0.73, 2.3, and 6.1 μm for CoO powder and 0.20, 0.65 and 5.3 μm for NiO powder, respectively.

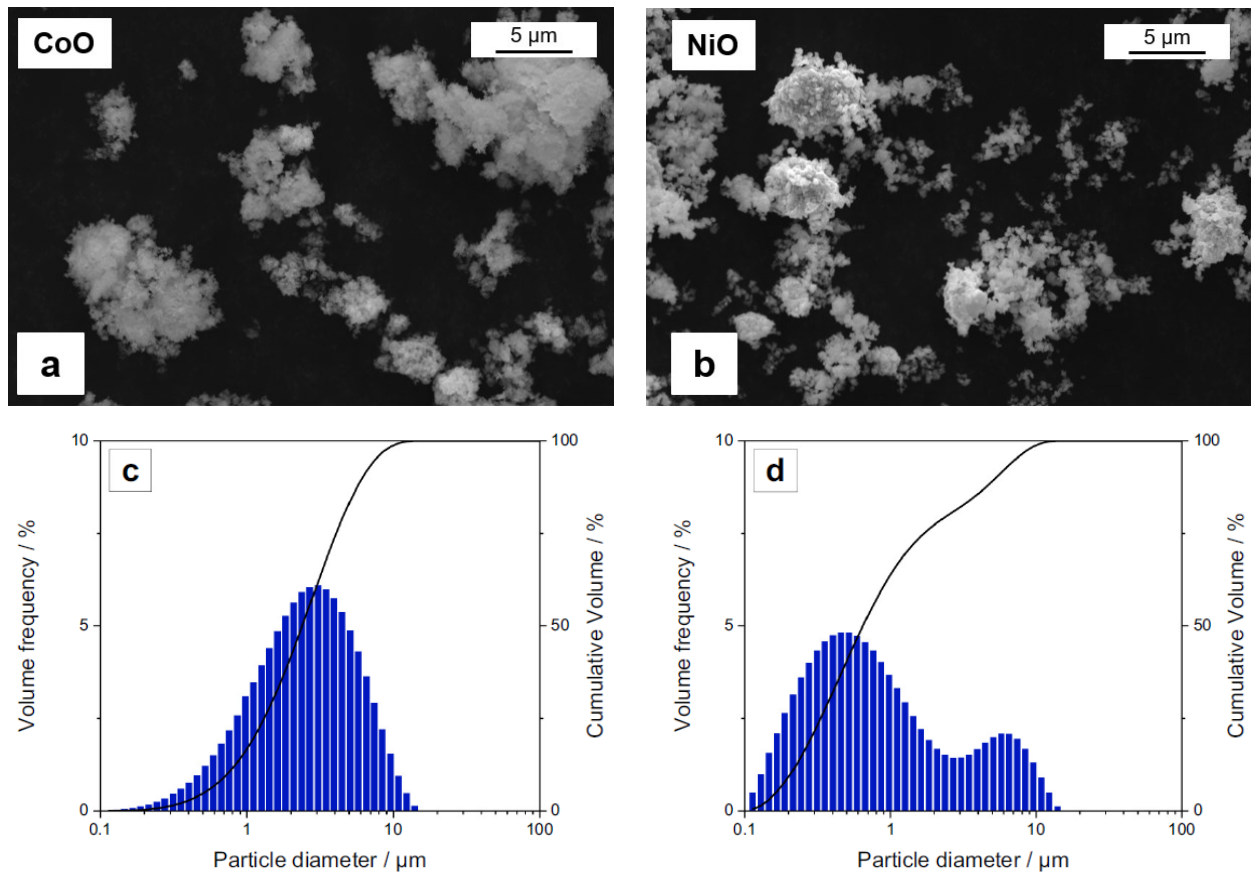


Figure 3.1. SEM micrographs of (a) CoO and (b) NiO precursor powders, and particle size distribution histograms of (c) CoO and (d) NiO precursor powders.

In the first series of experiments, the suspensions prepared by mixing CoO and NiO powders with 50–50 mol% were sprayed using five different input powers ranging from 75 to 95 kW, with all other spray parameters kept constant (see Table 3.1). The substrate was maintained below 600 $^{\circ}\text{C}$ by applying inter-pass pauses and air jet cooling to prevent overheating during

spraying. Fig. 3.2a presents the XRD patterns of the prepared coatings. Two sets of peaks appear in the XRD patterns. The main diffraction peaks occur at *ca.* $2\theta = 37^\circ, 43^\circ, 62^\circ, 75^\circ$ and 78° and are assigned to a *fcc* (Co,Ni)O solid solution. The diffraction peaks of this *fcc* phase are slightly displaced toward larger 2θ value compared to CoO, suggesting that NiO is dissolved in CoO to form a (Co,Ni)O solid solution. A second set of peaks observed at *ca.* $2\theta = 44.4^\circ, 51.7^\circ$ and 76.1° are attributed to metallic Ni, indicating that a fraction of the NiO particles are reduced to metallic nickel.

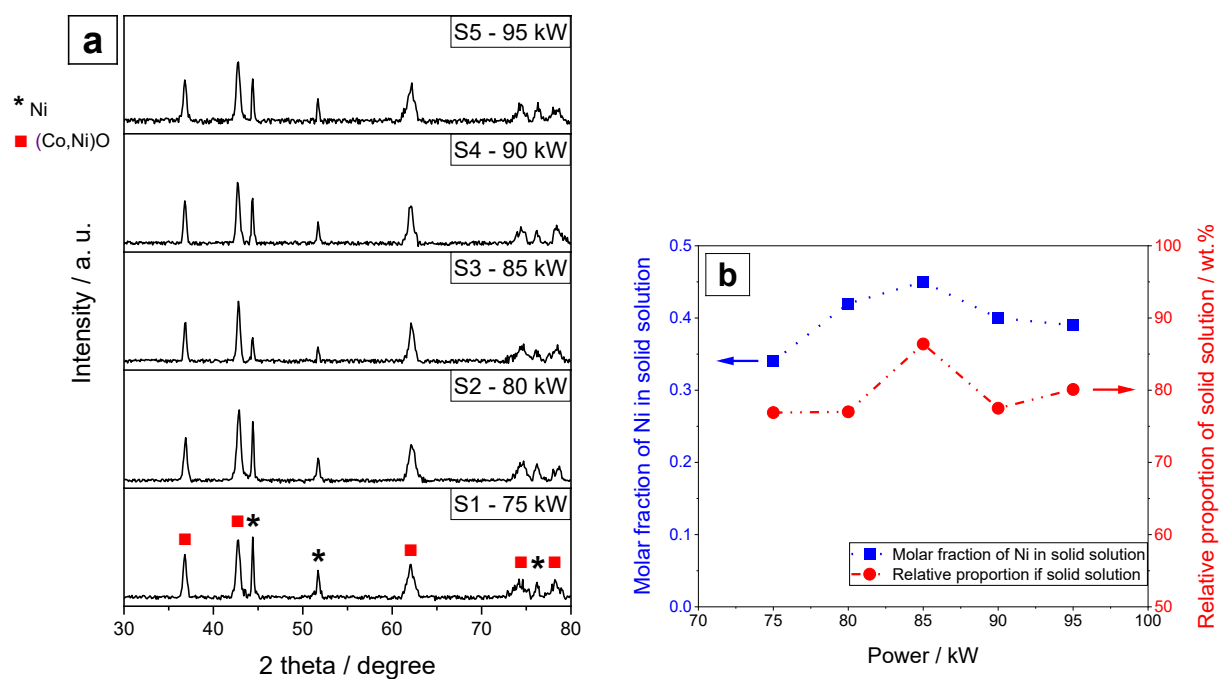


Figure 3.2. In (a) XRD patterns of coatings prepared at plasma powers ranging from 75 to 95 kW. In (b), the relative proportion of the solid solution phase, and the Ni content of the solid solution phase are plotted with respect to the plasma power.

A quantitative analysis was conducted *via* the Rietveld refinement technique to establish the lattice parameters as well as the Co and Ni contents of the solid solutions, and the relative proportions of solid solution and metallic Ni phases. Typical examples of the correspondence between the experimental data and the fitted curve are shown in Fig. S3.1. Based on the existing linear relationship between the lattice parameter and the NiO molar fraction of the $\text{Co}_x\text{Ni}_{1-x}\text{O}$ solid solution [53], the latter's composition can be ascertained from the lattice parameter value obtained

through Rietveld analysis. The coating's total Co and Ni contents may be calculated by considering the relative proportions of solid solution and metallic Ni phases extracted from the Rietveld analysis, and the weight percent of Co and Ni in the solid solution phase. These values were compared to those of the starting materials in Table 3.2. Both sets of data (mass balance) are in reasonably good agreement.

Table 3.2. Parameters extracted from the Rietveld analysis and the mass balance analysis of samples S1–S9. Note that the Co, Ni and O contents in the powder used for samples S1 to S8 were 39.2, 39.4 and 21.4 wt%, respectively. For sample S9, the Co, Ni and O contents were 59.0, 19.6 and 21.4 wt%, respectively.

Sample	wt.% (Co,Ni)O from Rietveld	wt.% Ni from Rietveld	Lattice parameter of (Co,Ni)O phase from Rietveld	Composition of (Co,Ni)O phase (based on lattice parameter)	wt.% Co in SS phase	wt.% Ni in SS phase	Total wt.% Co in coating	Total wt.% Ni in coating
S1	76.9	23.1	4.230	Co _{0.66} Ni _{0.34} O	52.0	26.7	40.0	43.6
S2	77.0	23.0	4.222	Co _{0.58} Ni _{0.42} O	44.9	33.7	34.6	48.9
S3	86.1	13.9	4.219	Co _{0.55} Ni _{0.45} O	42.5	36.1	36.6	45.0
S4	77.5	22.5	4.225	Co _{0.60} Ni _{0.40} O	47.2	31.4	36.6	46.8
S5	82.1	17.9	4.226	Co _{0.61} Ni _{0.39} O	48.0	30.6	39.4	43.0
S6	47.8	52.2	4.253	Co _{0.93} Ni _{0.07} O	73.2	5.5	35.0	54.8
S7	51.3	48.7	4.250	Co _{0.90} Ni _{0.10} O	70.8	7.8	36.3	52.7
S8	100	0	4.216	Co _{0.48} Ni _{0.52} O	37.8	40.8	37.8	40.8
S9	100	0	4.241	Co _{0.77} Ni _{0.23} O	60.6	18.0	60.6	18.0

The Ni content of the Co_xNi_{1-x}O solid solution varied with the input power (Fig. 3.2b). It was maximal at 85 kW, although not as large as expected based on the composition of the injected powder. This is consistent with the variation in the relative proportions of solid solution and

metallic Ni phases, which show a maximum at the same power. Thus, NiO and CoO were reacting together to form a $\text{Co}_x\text{Ni}_{1-x}\text{O}$ solid solution phase, but this process was not complete.

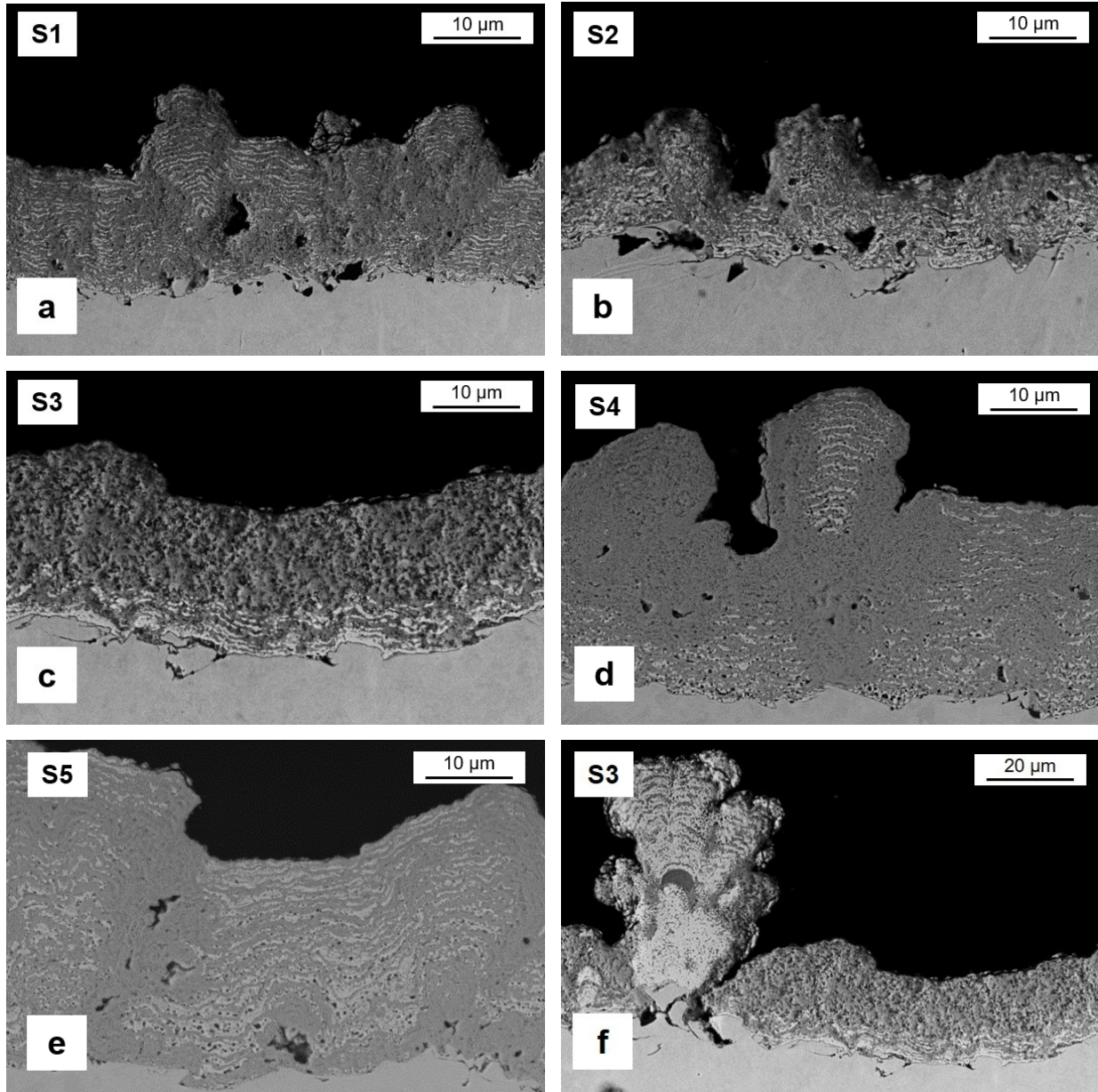


Figure 3.3. Cross-sectional SEM micrographs of coatings prepared at different plasma powers: (a) 75 kW, (b) 80 kW, (c) 85 kW, (d) 90 kW and (e) 95 kW. In (f) the same coating as (c) is shown at a lower magnification. The substrate temperature was always lower than 600 °C.

Fig. 3.3 shows the cross-sectional SEM micrographs of SPS coatings. After 25 deposition passes, these cross-sectional micrographs displayed an approximate coating thickness of 20 to 50

μm, with good adherence to the substrate. All coatings except S3 were composed of light and dark grey areas, parallel to the substrate. The EDX analyses (not presented here) reveal that the light grey areas did not contain any Co, while the dark grey areas contained both Co and Ni atoms. For sample S3, the light grey areas were observed only at the interface between the coating and the substrate as well as in a few areas where columnar growth is observed (Fig. 3.3f). From this point forward, the input power was set at 85 kW, and the spraying parameters were varied to identify the deposition conditions that would give a coating made of a single $\text{Co}_x\text{Ni}_{1-x}\text{O}$ solid solution phase.

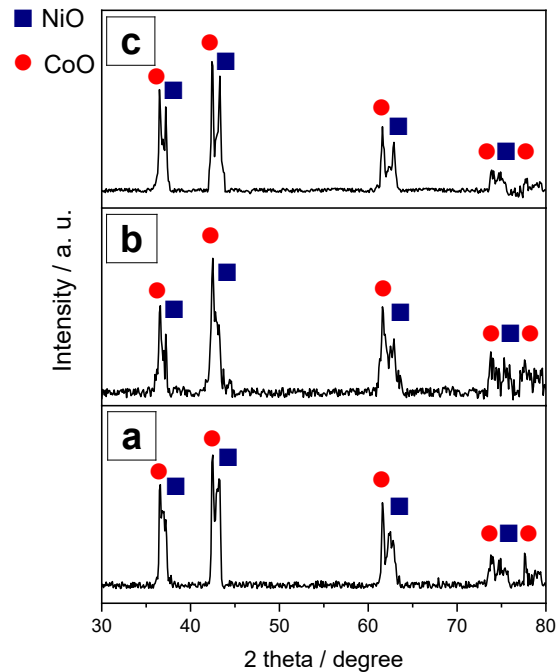


Figure 3.4. XRD patterns of mixed CoO and NiO (50–50 mol%) precursor particles sprayed in water, and then collected and dried in an oven. Different plasma powers were used: (a) 75 kW, (b) 85 kW and, (c) 95 kW.

Fig. 3.4 shows the XRD patterns of the sprayed particles collected from water. Two sets of peaks appear in the XRD patterns, attributed to CoO and NiO phases. Interestingly, the XRD peaks of the solid solution were not observed. This suggests that the formation of the solid solution occurred mostly on the substrate. The XRD peaks of metallic Ni were not observed either, although it is possible that metallic Ni particles were reoxidized upon contact with water. This must be the case since spraying only NiO particles on a substrate using the spray parameters given in Part 1 of

Table 3.1 produced a coating that contains both NiO and metallic nickel phases (Fig. 3.5a, b and c). In contrast, spraying only CoO particles using the same spray parameters produced a coating that contains only CoO (Figure 3.5d).

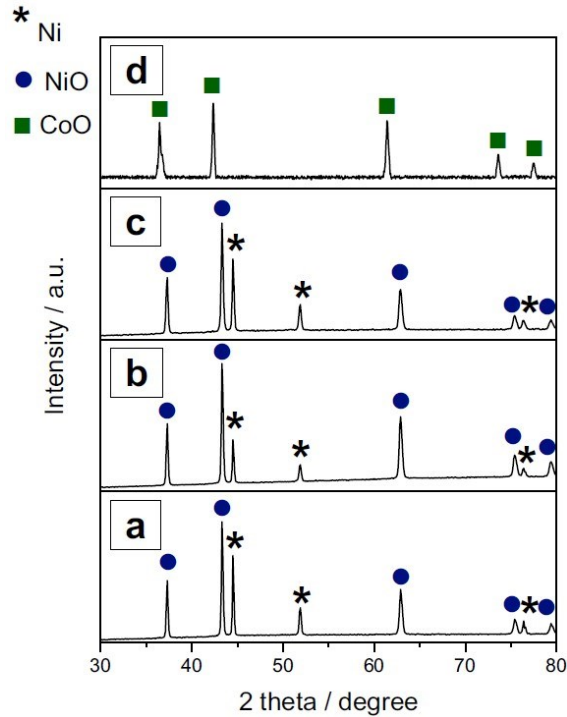


Figure 3.5. XRD patterns of coatings prepared from (a, b and c) NiO powder and (d) CoO powder. The input power was (a) 75 kW, (b and d) 85 kW and (c) 95 kW. All other spraying parameters are listed in Table 2.1.

Table 3.3. Spray parameters of a complementary series of experiments. A powder made of a $Co_{0.5}Ni_{0.5}O$ solid solution was used as starting material and helium was used instead of hydrogen in the plasma gas mixture.

Suspension $Co_{0.5}Ni_{0.5}O$ solid solution								
Sample #	Total gas (slm), Ar/N ₂ /He (slm), Current (amps)	Power (kW)	Air cooling	Water cooling	Preheating to 200 °C	Inter-pass pauses	Standoff distance (mm)	Substrate temperature
1	180, 75/10/15, 240	54	Yes	No	Yes	Yes	50	< 600 °C
2	180, 45/45/10, 245	82	Yes	No	Yes	Yes	50	< 600 °C
3	225, 45/45/10, 245	93	Yes	No	Yes	Yes	50	< 600 °C

Then, a powder made of a $\text{Co}_{0.5}\text{Ni}_{0.5}\text{O}$ solid solution was used as starting material (instead of the previous 50–50 mol% physical mixture of $\text{CoO} + \text{NiO}$.) The $\text{Co}_{0.5}\text{Ni}_{0.5}\text{O}$ solid solution was prepared through a three-step process outlined in our previous work [53]. To provide a less reductive atmosphere, helium rather than hydrogen was used in the plasma gas mixture, and the spraying parameters are listed in Table 3.3. Independently of the input power, the XRD pattern showed the characteristic peaks of both the solid solution and the metallic nickel phases (Fig. 3.6). So, metallic Ni is formed even if a solid solution is used as starting material and, most importantly, in the absence of a reductant in the plasma gas mixture.

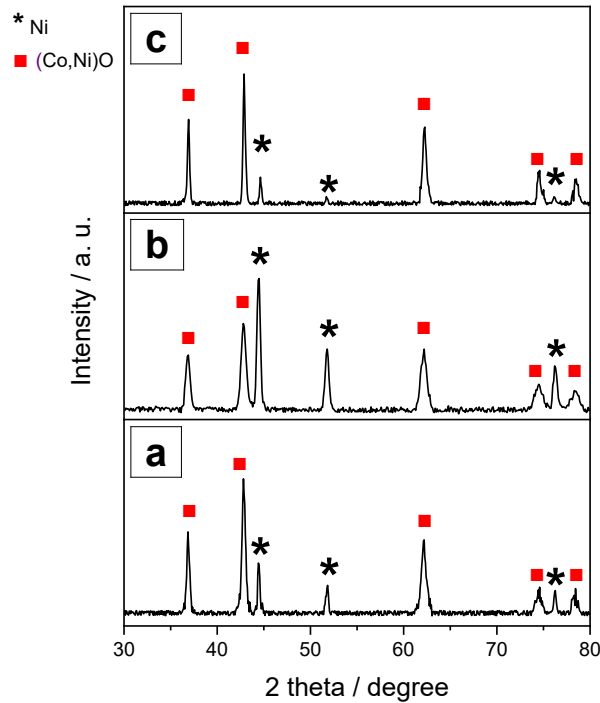


Figure 3.6. XRD patterns of coatings prepared using $\text{Co}_{0.5}\text{Ni}_{0.5}\text{O}$ solid solution powder (instead of a physical mixture of $\text{CoO} + \text{NiO}$) as starting materials and three plasma powers: (a) 54 kW, (b) 82 kW, and (c) 93 kW. In this series of experiments, the gas mixture consisted of $\text{Ar}/\text{N}_2/\text{He}$ (instead of $\text{Ar}/\text{N}_2/\text{H}_2$) to provide a less reductive atmosphere.

At 600 °C, the lowest substrate temperature recorded in the previous experiments, NiO is not stable and decomposes to form metallic Ni when the O_2 pressure is less than 10^{-18} bar according to the Ni-O phase diagram [73]. The stability domain of Ni-O varies with the temperature. For example, at 300 °C, the decomposition of NiO to Ni occurs when the O_2 pressure is lower than

10^{-32} bar. It was inferred from this observation that a lower substrate temperature would decrease the amount of metallic Ni in the coating. Accordingly, in a second series of experiments, the plasma power was set at 85 kW, and a water-cooled substrate holder and longer inter-pass pauses were introduced to maintain the substrate temperature below 300 °C. The same mixture of CoO and NiO powders (with 50–50 mol%) was used. The spraying parameters used for this series of experiments (S6 and S7) are listed in the second part of Table 3.1.

Fig. 3.7a and b displays XRD patterns of samples S6 and S7 that were prepared at two standoff distances (50 and 70 mm) and with the substrate temperature maintained below 300 °C. Increasing the standoff distance may allow the coating to be exposed to more O₂ molecules from the surroundings. For both coatings, two series of peaks were observed, assigned to the solid solution and metallic nickel phases. There was no significant difference between the two XRD patterns, indicating the distance between the nozzle and the substrate is not a critical factor in the formation of metallic Ni. The cross-sectional SEM micrographs in Fig. 3.7c and d indicate that compared to sample S6, increasing the standoff distance (sample S7) made the coating slightly less porous and more uniform.

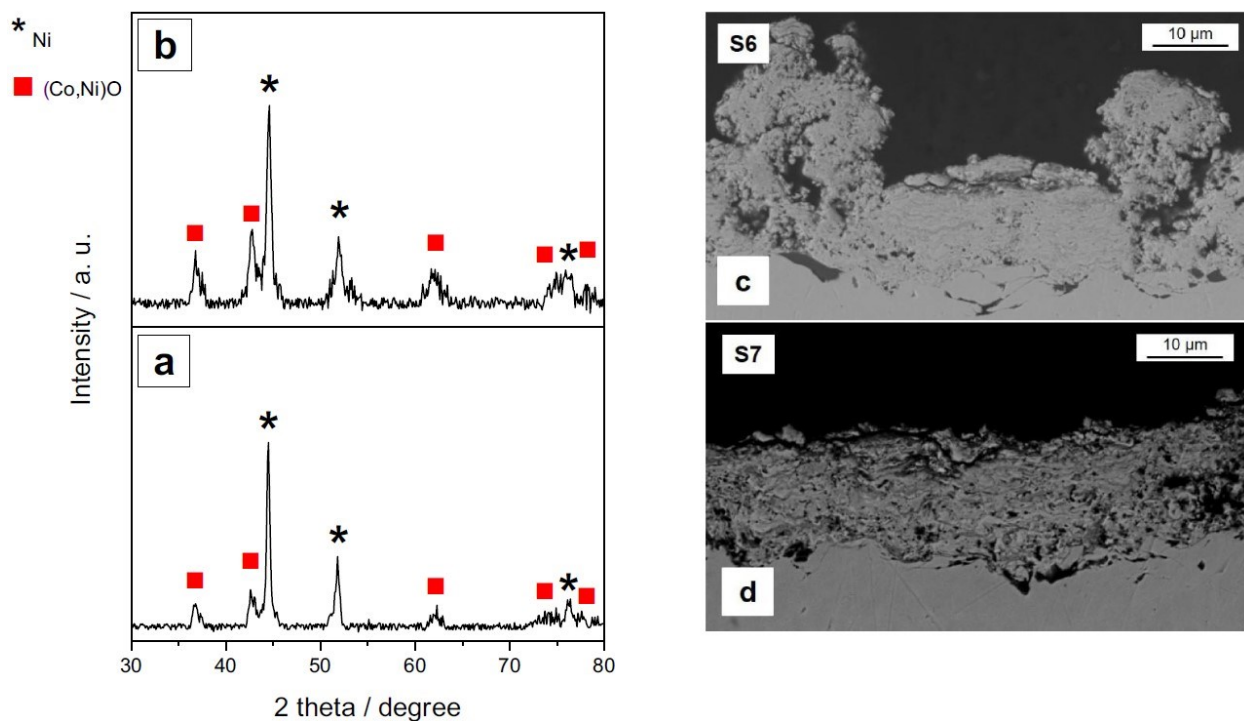


Figure 3.7. XRD patterns of coatings prepared in the second series of experiments: (a) standoff distance = 50 mm, and (b) standoff distance = 70 mm. In both cases, the plasma power was 85 kW and the substrate temperature was always lower than 300 °C. In (c and d), cross-sectional SEM images of corresponding coatings.

Interestingly, the metallic Ni phase content of sample S3 was 14 wt%, much lower than sample S6 at 52 wt%, even if the maximal temperature of sample S3 (600 °C) was higher than S6 (300 °C). Based on the thermodynamics of the Ni-O system, one would expect decomposition of NiO to metallic Ni to be favored at higher temperature, contrary to what was observed.

Thus, no inter-pass pause or additional cooling were applied, and the substrate temperature was allowed to increase to *ca.* 950 °C in the third series of experiments (see Table 3.1). Fig. 3.8 exhibits the XRD pattern of samples S8 and S9. These samples were prepared from powder mixtures consisting of (50% mol. CoO and 50% mol. NiO) and (75% mol. CoO and 25% mol. NiO), respectively. Both XRD patterns have only a single set of peaks attributed to $\text{Co}_x\text{Ni}_{1-x}\text{O}$ solid solutions, with no trace of metallic Ni. The $\text{Co}_x\text{Ni}_{1-x}\text{O}$ composition was $x = 0.48$ and 0.77 for samples S8 and S9, respectively, which is in agreement with the starting powders' compositions.

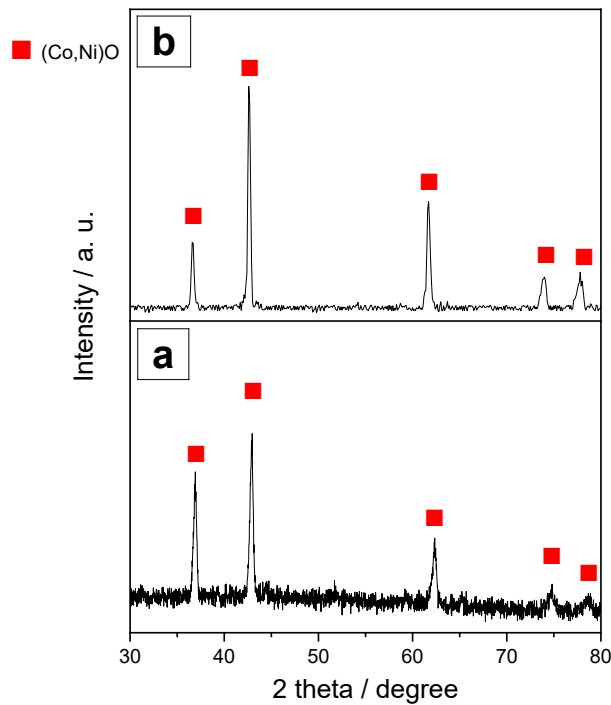


Figure 3.8. XRD patterns of coatings prepared in the third series of experiments with (a) [50% mol. CoO + 50% mol. NiO] and (b) [75% mol. CoO + 25% mol. NiO] mixtures. The input power was 85 kW.

The cross-sectional SEM images of these two samples are presented in Fig. 3.9. For sample S8, the substrate was pre-heated at 200 °C and the coating is uniform and dense. Its surface has a

dome-shaped structure and dark grey appearance. Sample S9 has a relatively flat surface. Coating S9 exhibits a light grey area close to the substrate/coating interface, while its upper portion (close to the coating/air interface) has a dark grey appearance. From previous observations, the darker areas and lighter areas were attributed to the solid solution and metallic Ni phases, respectively. The metallic nickel phase in sample S9 is not detected by XRD most probably because it is buried underneath a thicker layer (*ca.* 50 μm thick) made of only the solid solution phase. The EDX analysis results showed that the cobalt, nickel and oxygen contents in sample S8 were 37, 39 and 24 wt%, while these of sample S9 were 60, 16 and 24, respectively. The EDX results are in good agreement with the quantitative results obtained from Rietveld refinement of the XRD patterns and presented in Table 3.2. Based on the EDX analysis results, there was no trace of iron or chromium in the coating, confirming that there was no diffusion of these elements from the substrate.

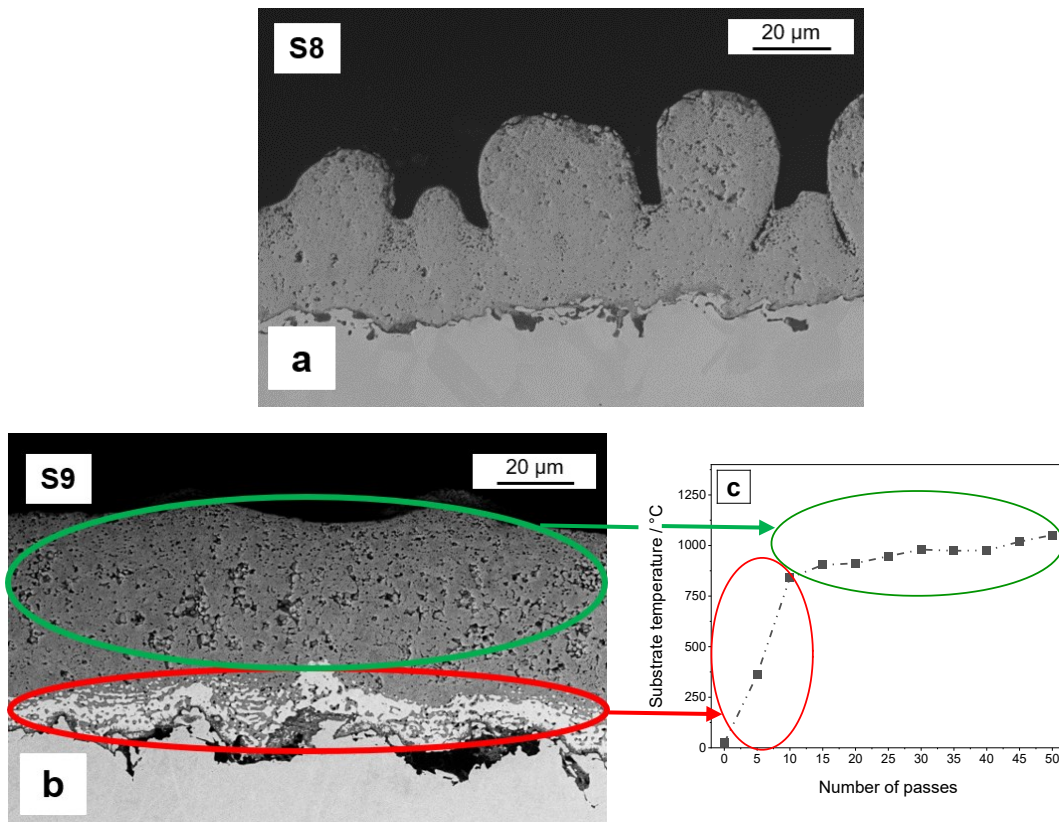


Figure 3.9. Cross-sectional SEM micrographs of (a) [50% mol. CoO + 50% mol. NiO] and, (b) [75% mol. CoO + 25% mol. NiO] mixtures. The input power was 85 kW. The variation in substrate temperature with the number of passes is seen in (c).

Variations in substrate temperature with the number of passes are depicted in Fig. 3.9c. The substrate temperature rose to 950 °C in the first ten passes, and remained nearly unchanged over the following 40 passes. The metallic nickel phase in sample S9 was formed in the first few passes of spraying, when the temperature was below 950 °C. Sample S8 does not exhibit a light grey region at the coating/substrate interface. Note that sample S8's substrate was preheated to 200 °C before beginning the coating process. As a result, it is hypothesized that the substrate reached its maximum temperature faster, which would explain why these light grey strata are not observed in sample S8.

3.4. Discussion

Using a mixture of CoO and NiO as starting materials, it was shown it is possible to use SPS as a deposition technique to prepare $\text{Co}_x\text{Ni}_{1-x}\text{O}$ coatings that are relatively dense, adherent, and made of a single phase. Our investigation has shown that substrate temperature is the most important parameter affecting the nature of the coating. At low substrate temperature, metallic Ni is formed and the composition of the solid solution phase deviates from that of the starting powders. In contrast, only a single phase is observed in coatings prepared at high temperature, and the composition of the solid solution thus formed is the same as that of the starting materials.

The mechanisms leading to the formation of metallic nickel in the sprayed coatings is not fully understood, and the different factors that can contribute are going to be discussed. One hypothesis to explain the formation of metallic Ni might be that CoO acts as a reducing agent and is further oxidized to Co_3O_4 . However, Co_3O_4 's characteristic diffraction peaks were never detected in XRD traces. Also, from the Ni-O and Co-O phase diagrams [59,73], one would not expect CoO to reduce NiO and form Co_3O_4 . Moreover, as presented in Fig. 3.5, the reduction of NiO to metallic Ni occurs even in the absence of CoO.

Reduction of NiO to metallic Ni was observed in several studies dealing with plasma-spraying of NiO/yttria-stabilized zirconia (NiO/YSZ) anode coatings for solid oxide fuel cells (SOFCs) [74–76]. In most cases, H_2 was used in the plasma jet, and reduction of NiO by H_2 was even used as a strategy to increase the porosity of the coating due to the volume shrinkage between NiO and Ni [76]. Also, oxide reduction of ZrO_2 to Zr_2O_3 in yttria-zirconia thermal barrier coatings prepared by plasma spraying and low-pressure plasma-spraying with a plasma jet consisting of Ar

and H₂ have been observed in the past [77]. The interaction between ceramic particles and the reducing plasma gas was thought to be responsible for the reduction of ZrO₂ to Zr₂O₃. Partial reduction of TiO₂ to Ti_nO_{2n-1} (Magnéli phases, where *n* is an integer) has also been observed during the spraying of TiO₂ particles in a mixture of Ar and H₂ [78].

The occurrence of metallic Ni in coatings prepared by plasma spraying of NiO – nanoagglomerate was also observed in the absence of H₂ in the plasma jet [75,79], which raises the question of the nature of the reducing agent. It was claimed that collisions of energetic plasma ions with the sprayed material could be responsible for the observed reduction of NiO during spraying.

NiO can be reduced to metallic Ni at high temperatures through a solid-solid reaction (carbothermal reduction) using coal. NiO can also be reduced through solid-gas reactions using H₂ [80] and CH₄ [81,82]. It was shown recently through a thermodynamic analysis and a series of experimental results that ethanol can be used to reduce NiO to metallic Ni and full conversion of NiO to Ni was observed between *ca* 375–825 °C [83]. This is because the decomposition products of ethanol (H₂, CO and C_xH_y) are strong reducing agents [84].

The occurrence of C and H species in the plasma (mixture of Ar and He) formed in suspension plasma spraying of YSZ particles dispersed in ethanol was nicely confirmed using optical emission spectra [85]. Indeed, Michaux et al. attributed the occurrence of metallic Ni in coatings prepared by solution plasma spraying of an ethanolic suspension of NiO and Y₂O₃/ZrO₂ powder to reduction of NiO by reducing species resulting from the vaporization/decomposition/ionization of the liquid phase, although H₂ was used as secondary plasma forming gas in their study [75]. So, even in the absence of H₂ in the plasma gas mixture, extensive formation of metallic Ni in coatings prepared at low substrate temperature should not come as a surprise in our SPS experiments since an ethanolic suspension of NiO and CoO powders was used. At high substrate temperature, metallic Ni is oxidized to NiO. This is most particularly evident in sample S9, where metallic Ni is exclusively observed at the substrate/coating interface while the substrate temperature was not high enough for Ni to oxidize to NiO before the next pass. Upon reaching a stable substrate temperature of *ca.* 950 °C, oxidation of metallic Ni to NiO is fast compared to the transverse motion of the nozzle, allowing the formation of Co_xNi_{1-x}O coating made of a single solid solution phase.

In summary, different powder mixtures (50% mol CoO + 50% mol NiO) and (75% mol CoO and 25% mol NiO) were used to prepare coatings. The results showed that coatings made of a single phase $\text{Co}_x\text{Ni}_{1-x}\text{O}$ solid solution were obtained as long as the substrate temperature is above 950 °C. It is known from the literature that $\text{Co}_x\text{Ni}_{1-x}\text{O}$ solid solution can be prepared with $0 \leq x \leq 1$ at temperature higher than *ca.* 900 °C [53]. Thus, it is inferred that $\text{Co}_x\text{Ni}_{1-x}\text{O}$ coatings with $0 \leq x \leq 1$ can be obtained starting from an initial powder mixture with the right composition.

3.5. Conclusions

$\text{Co}_x\text{Ni}_{1-x}\text{O}$ coatings were deposited by SPS using CoO and NiO as starting materials. The effects of spraying variables - including input power, standoff distance, and substrate temperature - on coating composition were studied. Substrate temperature was identified as the most critical parameter affecting coating composition. Uniform, adherent and non-porous $\text{Co}_x\text{Ni}_{1-x}\text{O}$ coatings made of a single solid solution phase were obtained when the substrate temperature was above 950 °C. In the future, the use of inert metallic anodes protected by $\text{Co}_x\text{Ni}_{1-x}\text{O}$ coatings will be further investigated for the primary production of aluminum.

Preface to Chapter 4.

In the previous chapter, it was demonstrated that NiO can be reduced to metallic Ni during the SPS coating of (Co,Ni)O at lower temperatures. Although the effects of the SPS process parameters on the structure and composition of the (Co,Ni)O coatings were studied, the mechanism leading to the formation of metallic nickel in the SPS-sprayed coatings was not fully investigated. Therefore, the following chapter is devoted to investigating the sources of the formation of the metallic Ni phase within as-sprayed (Co,Ni)O coatings. In addition, it is important to understand whether the mixing of NiO and CoO particles occurs on the substrate surface or in-flight during spraying. Thus, collecting of in-flight particles into water along with capturing of splats formed on heated smooth metal substrates are used to gain further insight into the melting and mixing phenomena of the NiO and CoO powders during spraying.

Chapter 4

Study on the formation of (Co,Ni)O solid solution and metallic Ni phases during suspension plasma spraying of CoO and NiO powders²

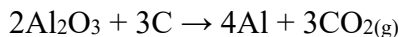
Abstract

SPS-sprayed (Co,Ni)O coating was investigated as a potential material for inert anode applications in Al production. In-flight particles were collected in water and splats formed on heated smooth metal substrates were captured to gain further insight into the melting and mixing of NiO and CoO powders during spraying. SEM, EDS, and X-ray diffraction analyses contributed to understanding the formation of different crystalline phases within the as-sprayed coatings. The metallic nickel phase could be formed in the coatings prepared at low temperatures. Accordingly, this study discussed in detail the possible causes for the formation of metallic Ni during spraying.

Keywords: Suspension plasma spray, (Co,Ni)O solid solution, Metallic Ni, Al electrolysis

4.1. Introduction

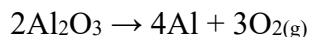
Aluminum is the second most widely used metal in the world, but the aluminum industry is a major emitter of greenhouse gases (GHGs) and accounts for ~1.0% of the emissions [56,57,86]. This is mainly due to the use of carbon anodes consumed during the aluminum electrolysis to form CO₂ according to the overall reaction:



Substitution of carbon anodes with inert materials which emit O₂ instead of CO₂, accompanied with the use of wettable TiB₂ cathodes and reducing the anode-to-cathode distance

² This chapter has been submitted as an article in the *Journal of Thermal Spray Technology*: V. Jalilvand, S. Mohammadkhani, F. Ben Ettouil, L. Roué, D. Guay, A. Dolatabadi, C. Moreau.

will have significant environmental benefits as the emission of contaminants during the electrolysis process would be eliminated according to the overall electrochemical reaction [13,87,88]:



Among possible inert anode materials (metals, ceramics and cermets), metal-based anodes have the advantages of high electrical conductivity, excellent thermal shock resistance, mechanical robustness, and ease of manufacture [12]. However, the major challenge for metal-based anodes is to obtain a material having a very low dissolution rate and an excellent high-temperature corrosion resistance under Al electrolysis conditions.

Among the many materials studied so far, Cu–Ni–Fe-based alloys appear to be one of the most promising metallic anode materials thanks to their ability to produce a protective nickel ferrite (NiFe_2O_4) layer during Al electrolysis [17,23,28]. Nevertheless, these alloys might fluorinate during electrolysis and form non-conductive nickel or iron fluoride which increases cell voltage and decreases the energy efficiency of the electrolysis process [19,49]. This limitation can be circumvented by protecting metallic anodes, such as Cu–Ni–Fe-based ones, with an appropriate coating method.

Using CoO-based protective coating for metal-based anodes seems to be promising as shown by Nguyen and de Nora [20]. Indeed, the CoO phase is highly stable against the fluorination of metallic anodes in cryolite. However, CoO is likely to be converted into Co_3O_4 under Al electrolysis conditions according to the phase diagram of the Co–O system, showing that the dissociation of CoO to Co_3O_4 occurs at ~ 960 °C in 1-bar O_2 [53,59]. For the inert anode application, the p-semiconductor CoO form is more appropriate than the n-semiconductor Co_3O_4 form since the oxygen evolution overpotential is much lower with the former one. About 15 wt.% of nickel stabilizes the CoO phase to form a (Co,Ni)O solid solution [20].

The coating process used in this study is suspension plasma spray (SPS). SPS spraying involves the injection within the thermal plasma flow of a suspension made of feedstock particles, a liquid phase, and a dispersant. This suspension can be injected either as a continuous liquid stream or as atomized drops of a few tens of micrometers [89]. Upon penetration within the plasma flow, the liquid stream or drops encounter two mechanisms, fragmentation and vaporization [90]. After the fragmentation followed by the evaporation of the liquid in the plasma jet, the accelerated particles must be melted to form the coating when impacting the substrate [36]. SPS is a well-

established technology for producing protective oxide coatings for various industrial applications. Additionally, thermal spray could be used in Al production sites to restore protective (Co,Ni)O coating on end-of-life inert anodes.

In our previous works [91-93], (Co,Ni)O coatings with various compositions were successfully deposited by SPS and high-velocity oxygen fuel (HVOF) techniques. Adherent and non-porous (Co,Ni)O coatings were achieved using both SPS and HVOF methods; however, a reduction of NiO to metallic Ni was observed in the SPS coatings prepared at lower temperatures which causes the composition of the (Co,Ni)O solid solution phase to deviate from that of the starting materials [91]. Although the effects of the SPS process parameters on the structure and composition of the (Co,Ni)O coatings were elucidated, the mechanism leading to the formation of metallic nickel in the SPS-sprayed coatings was not fully investigated.

Therefore, this study aimed to identify the sources of the formation of the metallic Ni phase within as-sprayed (Co,Ni)O coatings. The SPS coatings were deposited using an ethanol-based suspension with varying some process parameters to study how these changes are reflected in the coating structure and the intermediate products such as the in-flight particles and splats. The effect of heat treatment at 1000 °C under argon on the phases present in the coatings was then studied to investigate the possibility of dissolving the metallic Ni into the (Co,Ni)O solid solution phase.

4.2. Materials and methods

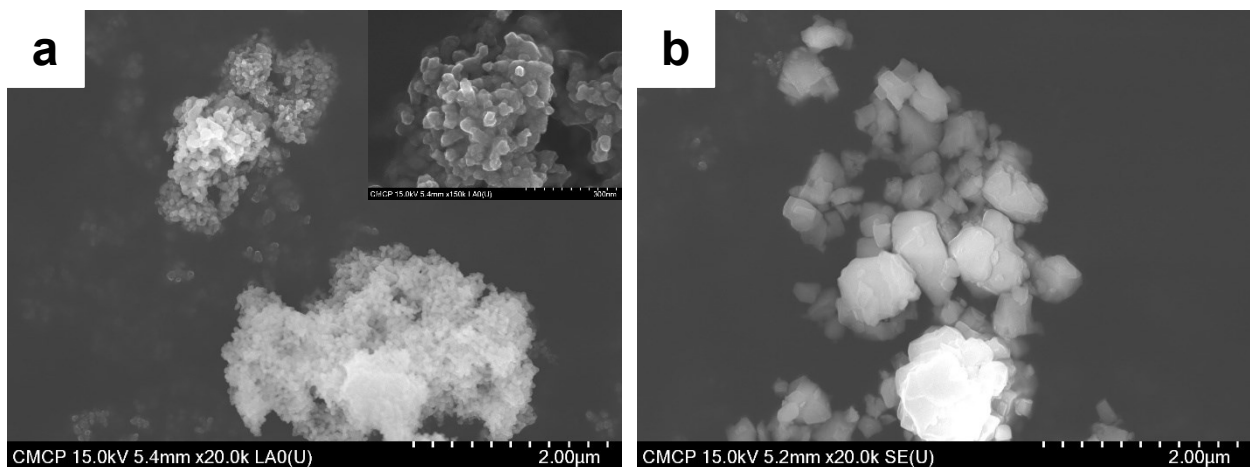


Figure 4.1. SEM micrographs of the precursor powders: (a) CoO and (b) NiO.

The starting powders used to deposit the coatings included cobalt oxide (CoO, Skyspring Nanomaterials, USA) and nickel oxide (NiO, Fuelcellmaterials, USA). Fig. 4.1 shows the particle morphology of both powders. The high-magnification micrograph in the insert of Fig. 4.1a indicates that the CoO particles are actually agglomerates of a large number of CoO nanoparticles.

The particle size distribution was determined by laser diffraction using a Malvern Panalytical Spraytec instrument after dispersing the powder in ethanol using a Malvern wet dispersion accessory. Fig. 4.2 depicts the particle size distribution test results of precursor powders. The D10, D50, and D90 of the size distributions were measured to be 0.73, 2.3, and 6.1 μm for CoO and 0.20, 0.65, and 5.3 μm for NiO powders, respectively.

The CoO and NiO suspensions were prepared by mixing 10 wt.% of oxide powders with the intended CoO and NiO ratio with 1 wt.% of polyvinylpyrrolidone (PVP) as a dispersing agent in ethanol. Mirror-polished AISI 304 stainless steel substrates of 25 mm \times 25 mm \times 3 mm were used for splat collection. For the SPS coating deposition, AISI 304 stainless steel substrates of 25 mm \times 25 mm \times 5 mm were grit-blasted and then cleaned by rinsing in acetone prior to their use.

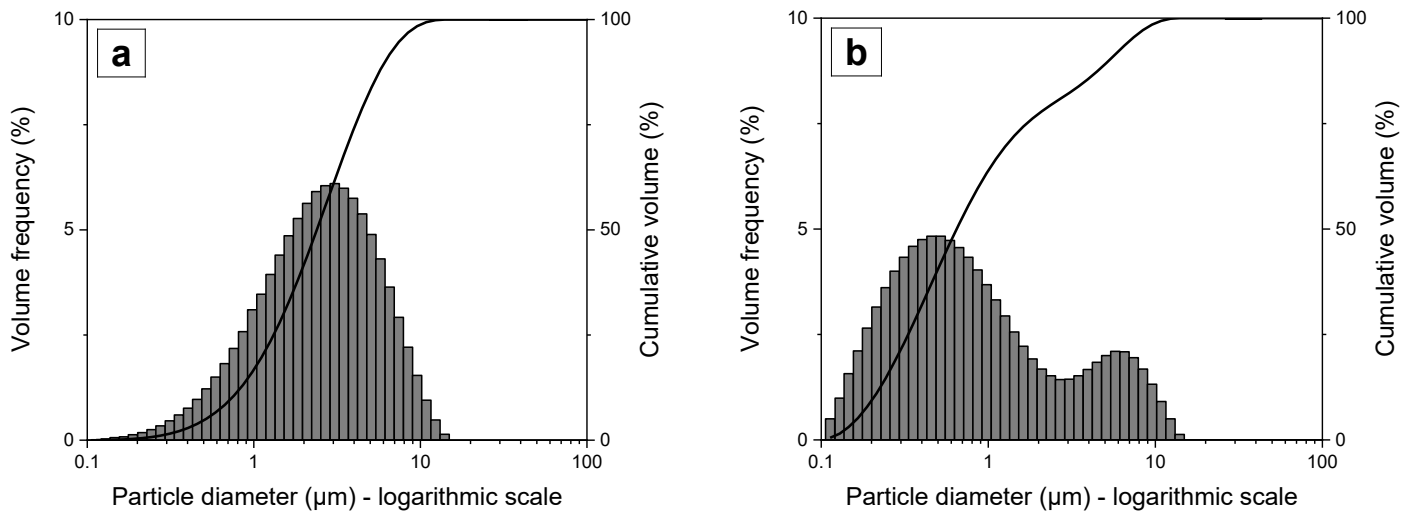


Figure 4.2: Histograms showing the particle size distributions for the (a) CoO and (b) NiO powders.

The suspensions were axially injected into a Mettech's Axial III (Northwest Mettech, North Vancouver, Canada) plasma torch and sprayed under the conditions summarized in Table 4.1. The Axial III torch consists of three cathodes and three anodes operating on three independent power supplies that can reduce plasma fluctuations as compared to typical radial injection plasma torches.

The spray distance was kept constant at 50 mm for all the samples. The in-flight particle temperature (T_p) and velocity (V_p) were measured at the spray distance using an AccuraSpray G3 (Tecnar Automation, St. Bruno, Canada). A FLIR A320 infrared camera (FLIR Systems Inc., USA) was used to monitor substrate temperature during spraying.

Table 4.1. Spray process parameters.

Sample #	Powder weight ratio	Total gas (slm), Ar/N ₂ /H ₂ (slm), Current (A)	Power (kW)	Preheating to 200 °C	Air cooling	Water cooling	Number of passes
S1	50 CoO/50 NiO	180, 75/10/15, 220	77	Yes	No	No	50
S2	50 CoO/50 NiO	180, 45/45/10, 180	85	Yes	No	No	50
S3	50 CoO/50 NiO	225, 45/45/10, 180	97	Yes	No	No	50
S4	75 CoO/25 NiO	180, 45/45/10, 180	85	No	No	No	50
S5	50 CoO/50 NiO	180, 75/10/15, 220	77	No	Yes	Yes	10
S6	50 CoO/50 NiO	180, 45/45/10, 180	85	No	Yes	Yes	10
S7	50 CoO/50 NiO	180, 45/45/10, 180	85	No	Yes	No	50

Splat depositions were performed on substrates preheated over 200 °C to improve the adhesion of the deposited material. The scanning speed of the plasma torch was set at 1.5 m s⁻¹ to collect isolated splats and particles on the substrate surface.

To collect the in-flight particles, the injected suspension feed was sprayed into a water vessel (instead of deposition on a substrate). The torch was held at a distance of 30–50 cm above the water surface for approximately 2 min. The collected particles were next dried in an oven at 75 °C and analyzed via a scanning electron microscope.

Heat treatment of sample S7 was carried out at 1000 °C for 1 h under an argon flow in a tubular furnace. X-ray diffraction (XRD) measurements were conducted using a Bruker D8 diffractometer with Cu K_α radiation. The as-sprayed specimens were cut using a precision cut-off machine (Secotom-15, Struers A/S, Denmark), then mounted and polished using standard metallographic procedures to a final finish of 0.4 μm. An optical microscope (OM) and a field-emission scanning electron microscope (FE-SEM, Regulus 8230, Hitachi Co, Japan) equipped with an energy dispersive spectroscopy (EDS) were employed to study the specimen cross-sections and particle morphology.

4.3. Results and discussion

4.3.1. Collected in-flight particles

Fig. 4.3a and b displays the SEM micrographs of the in-flight particles produced under the spray condition of sample S1 and collected in water. Two types of particles can be distinguished: spherical-shaped large ones about 1 to 4 μm in diameter, and small nano-sized particles. The higher magnification of the small particles in Fig. 4.3b reveals that their size is as fine as 50 nm or less. Evidently, the smaller sprayed particles remained un-melted at the end of their travel in the plasma. It seems that many of these particles have traveled within the colder periphery of the plasma jet and were not melted. In contrast, the larger particles are completely round, which indicates their full melting during the in-flight phase.

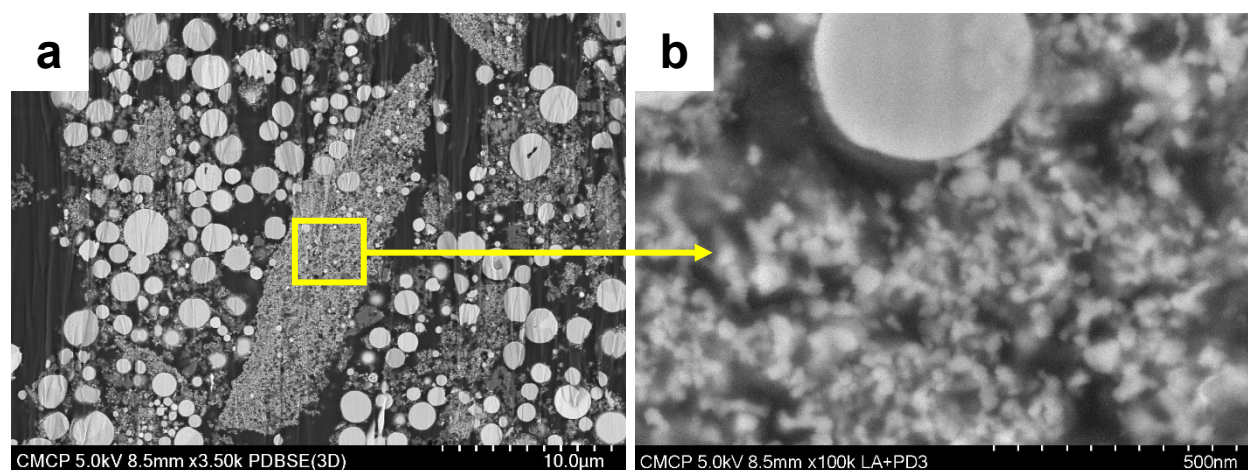


Figure 4.3. (a and b) SEM images at different magnifications of the in-flight particles of sample S1.

The EDS elemental mapping in Fig. 4.4 illustrates that the large spherical particles have been completely melted during spraying, but with a variety of mixing behaviors. These particles can be classified as fully un-mixed single-components and fully mixed particles. However, the un-mixed particles were the more common category observed. The un-mixed single-component particle is either a NiO or a CoO particle. Based on Fig. 4.4, the size of the CoO in-flight particles is larger than that of the NiO in-flight ones, although the accurate ratio of large-to-small ones was

not analyzed. This means that the larger particle size before spraying ended up with the larger sprayed particles.

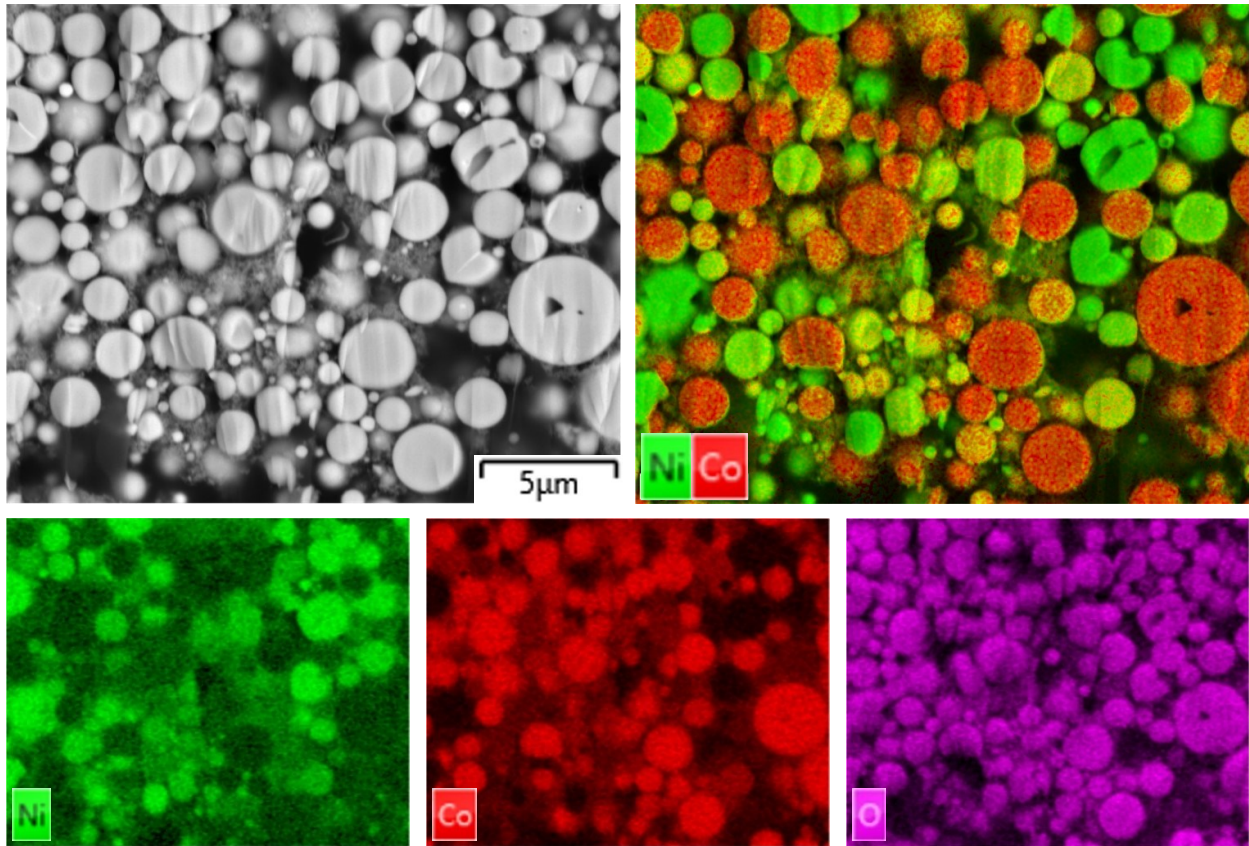


Figure 4.4. Cross-sectional SEM image and corresponding EDS mapping images of the in-flight particles of sample S1.

4.3.2. Investigation of collected splats

It is known from the literature [94,95] that the velocity and melting degree of the particles before their impact play an important role in the flattening behavior and final shape of the splats. When the in-flight particles impact the substrate surface with appropriate melting degree and velocity, they spread while cooling down and solidify rapidly on the substrate to form splats. Otherwise, the particles impinge on the surface of the substrate in the solid state (cold particles) either as un-melted or melted and re-solidified particles.

The smooth stainless steel substrates were preheated over 200 °C before splats' collection. Fig. 4.5 depicts the SEM images of splats collected under the spray condition of sample S1 with a plasma power of 77 kW. Most of the splats present here are well-spread and disk-shaped with

diameters between 1 and 10 μm , showing a good melting of the particles (see Fig. 4.5a). In general, disk-shaped splats are preferred as they present better contact with the underlying surface than irregular-shaped splats, resulting in better adhesion-cohesion of the sprayed coatings [96]. Higher magnification in Fig. 4.5b reveals the presence of many fine and spherical particles below 0.5 μm around the splats, indicating that these fine particles have been melted and solidified before the impact on the substrate. It is believed that due to their small size and lack of momentum quantity, such particles could not be spread on the surface. Ultra-high magnification at 200kX by FE-SEM in Fig. 4.5c demonstrates the presence of numerous small particles (below 20 nm) resulting from the re-condensation of evaporated particles. The formation of such nano-sized particles during suspension plasma spraying has been reported by other researchers, too [38,97].

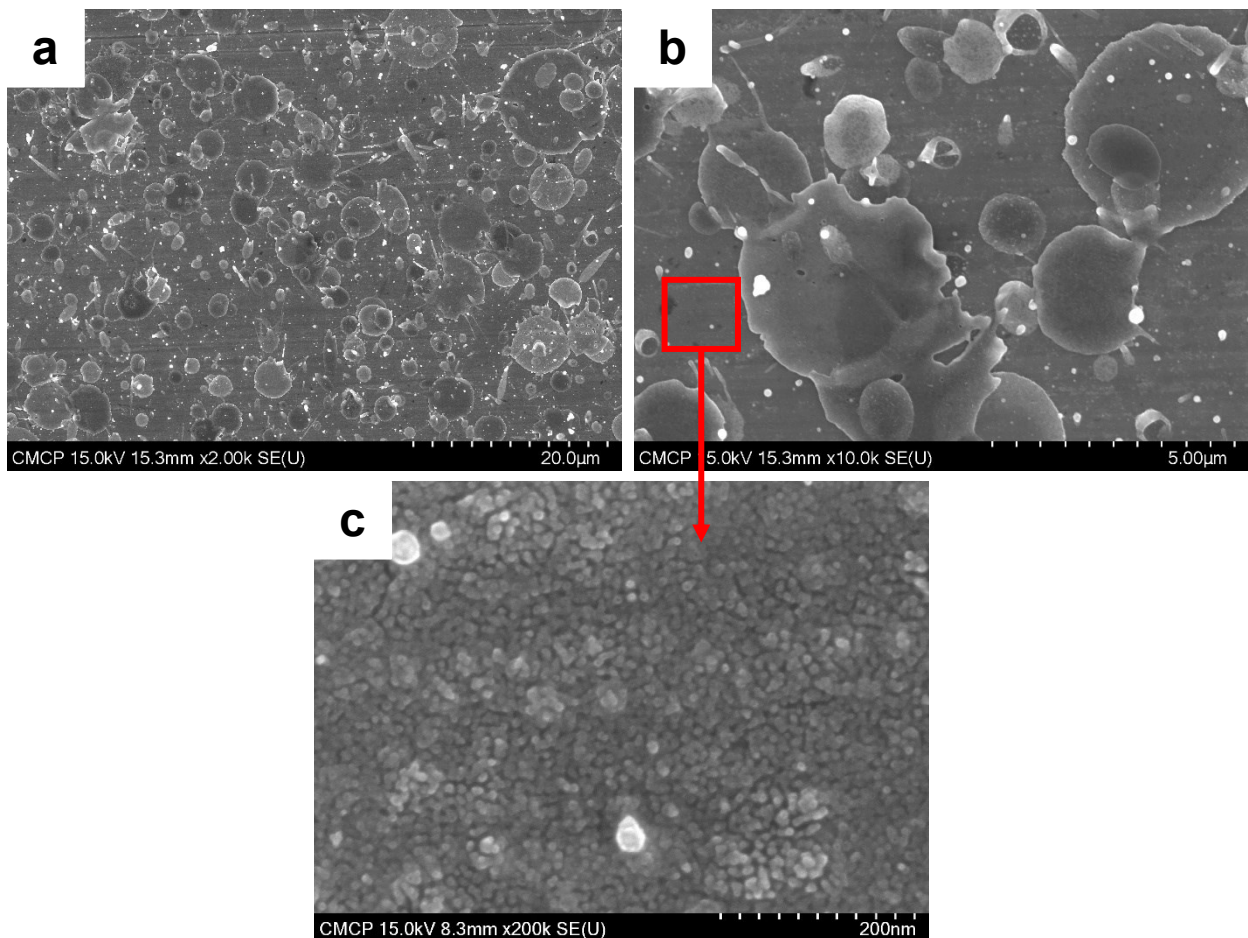


Figure 4.5. (a, b and c) SEM images at different magnifications of the collected splats of sample S1.

The EDS mapping analysis results of the splats collected under the spray condition of sample S1 are displayed in Fig. 4.6. It can be seen that most of the splats and particles are either Ni-rich or Co-rich, while only a small part of them contains both Ni and Co atoms. This is consistent with the findings from the collected in-flight particles. This observation indicates a relatively low mixing of NiO and CoO particles in-flight during spraying. Moreover, the oxygen elemental map shows that a number of splats seem to have lost their oxygen (shown by arrows in the SEM image), which means they undergo partial reduction to form sub-stoichiometric oxide splats. This will be discussed in detail later in this paper.

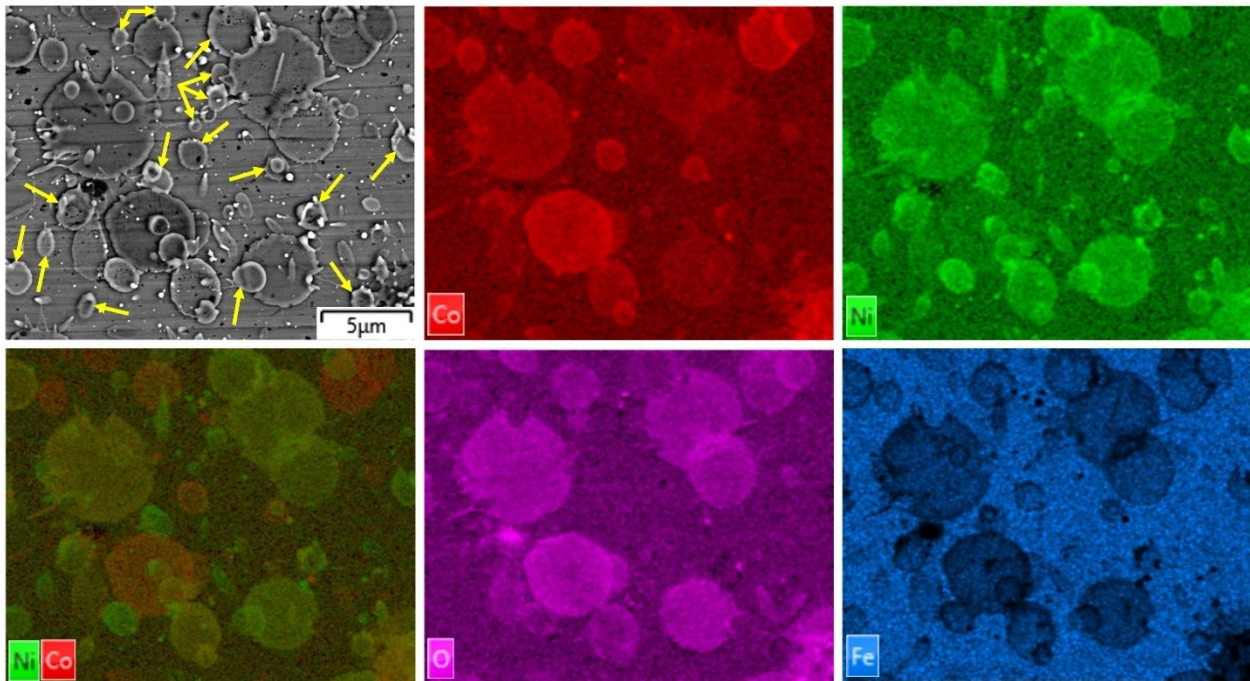


Figure 4.6. EDS mapping images of the collected splats of sample S1.

Figure 4.7 illustrates the SEM images of splats collected under the spray condition of sample S2 with a plasma power of 85 kW. Flower-like splats with fine spreads are observed with the increment of spraying power (see Fig. 4.7a). This splat type has a flower-like shape and is similar to the disk-like splat except for the little splashing and fingering around the periphery of the splat that forms the flower shape. This is possibly caused by the minor instability of the liquid flow during spreading. In general, the splats tend to be more irregular under higher spraying power. The higher level of splashing could be associated with the higher temperature and velocity of in-flight particles when the spraying power increased from 77 kW ($T_p = 2450$ °C, $V_p = 640$ m/s) to

85 kW ($T_p = 3500$ °C, $V_p = 880$ m/s). Spreading time and thickness decrease with increasing droplet velocity and temperature, resulting in the de-stabilization of liquid at the edges of the spreading droplet [98].

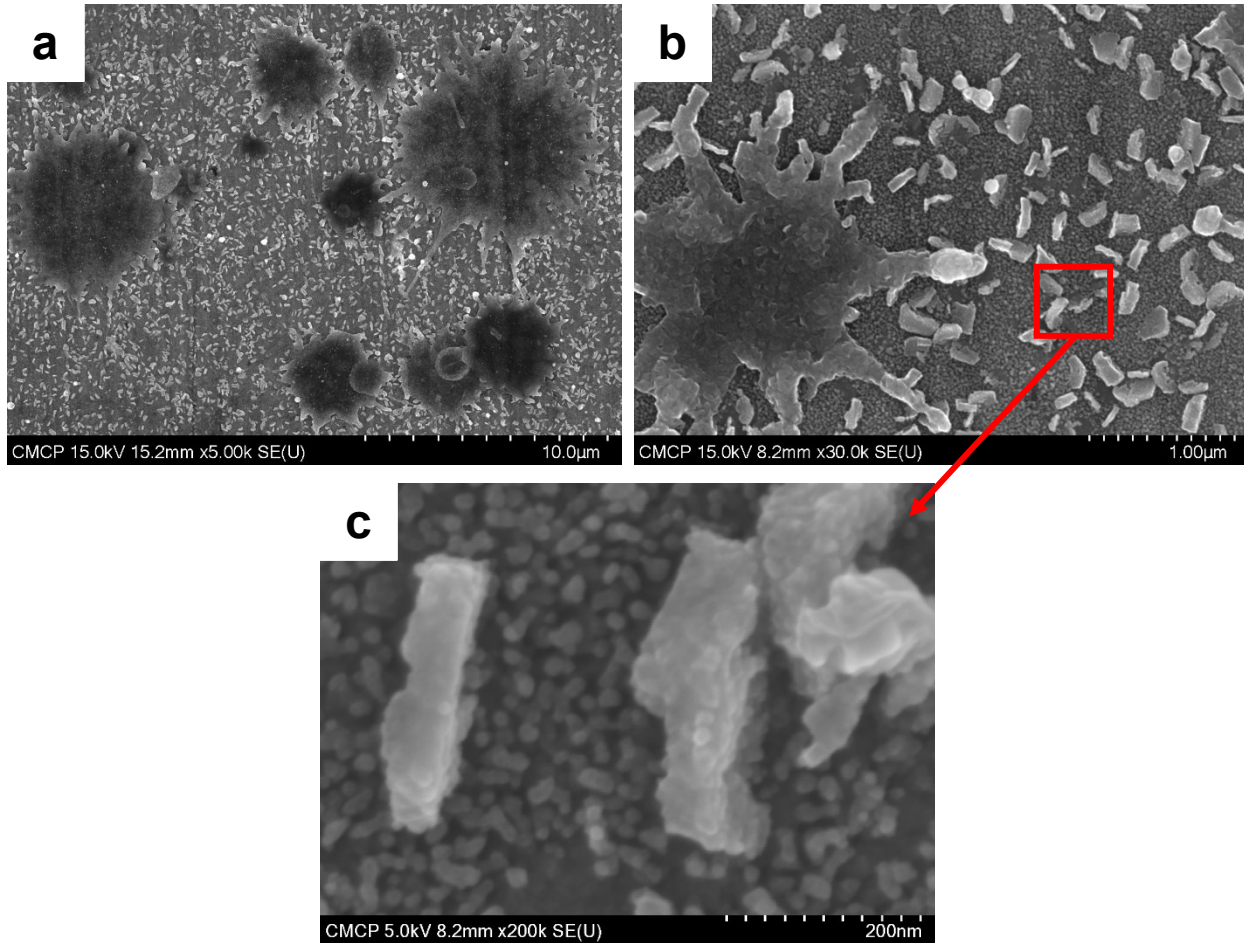


Figure 4.7. (a, b and c) SEM images at different magnifications of the collected splats of sample S2.

A large amount of angular-shaped particles (below 0.3 μm) which are identical to those in the NiO feedstock powder is observed in Fig. 4.7b, indicating that these particles might have remained un-melted during their passage in the plasma plume. This can be attributed to the higher particle velocity causing shorter particle residence at the high temperature of the plasma jet and, thus, less time for melting. Another hypothesis to explain these small angular particles may be that they are debris of the broken fingers radiating from the periphery of the splats. However, one would not expect these particles to be debris of the fingers, as they appear quite uniformly

distributed on the substrate surface. Besides splats and angular un-melted particles, evaporated and re-condensed small particles (below 20 nm) can be observed in Fig. 4.7b and c. Ultra-high magnification at 200kX by FE-SEM in Fig. 4.7c reveals that these nano-sized particles cover the surface of un-melted particles. The EDS mapping analysis results of these particles are exhibited in Fig. 4.8. It is noteworthy that the un-melted particles are not thick enough to be clearly revealed by the EDS technique. However, the results demonstrate an obvious distribution of oxygen atoms in these angular particles which are most likely to be NiO. The Co elemental map shows the presence of Co atoms on the un-melted particles, which is possibly associated with the presence of evaporated and re-condensed particles containing CoO and NiO that cover the surface of un-melted particles. Note that the Ni elemental map would not provide reliable distribution of this element in the particles since the substrate material contains a significant concentration of Ni which is also detected during the analysis.

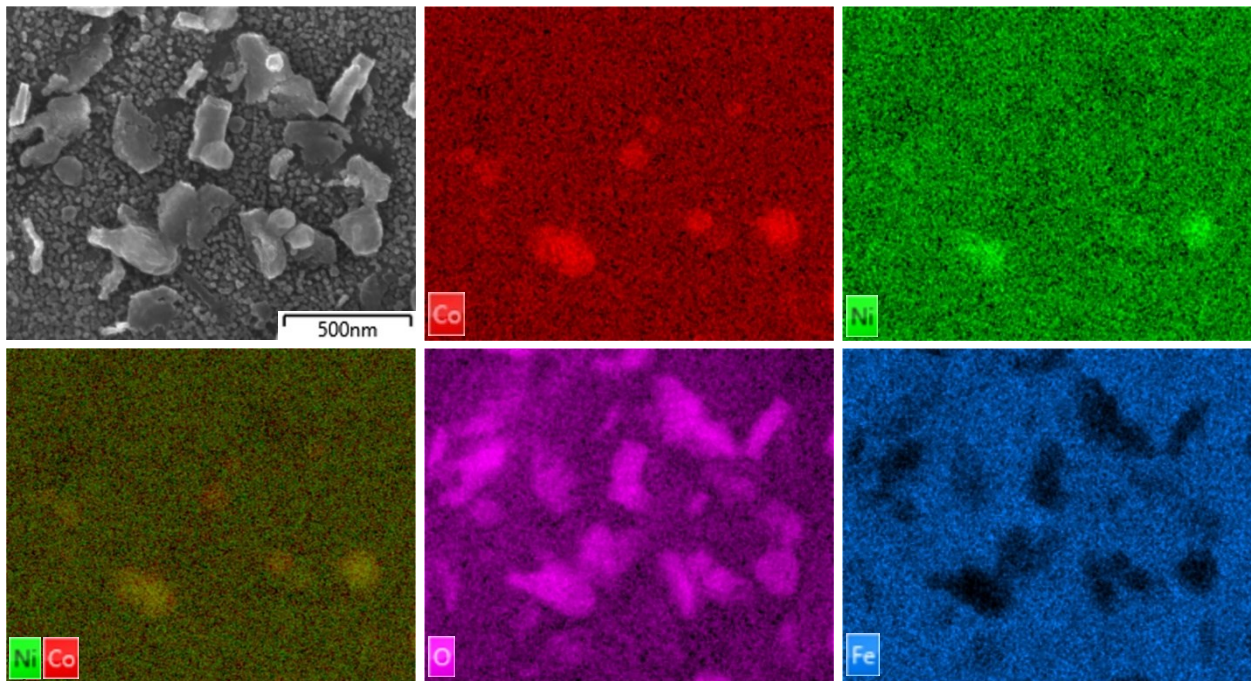


Figure 4.8. EDS mapping images of the un-melted particles along with the evaporated and re-condensed particles of sample S2.

Fig. 4.9 presents the EDS mapping analysis results of the splats collected under the spray condition of sample S2. Similar to those observed in the splats collected under the spray condition of sample S1 (Fig. 4.6), also in this case, only a limited mixing of NiO and CoO particles occurs

in-flight during the deposition process, and so most of the splats are either Ni-rich or Co-rich. Furthermore, the oxygen elemental map confirms the formation of some partially reduced oxide splats (shown by arrows in the SEM image) in this sample as well.

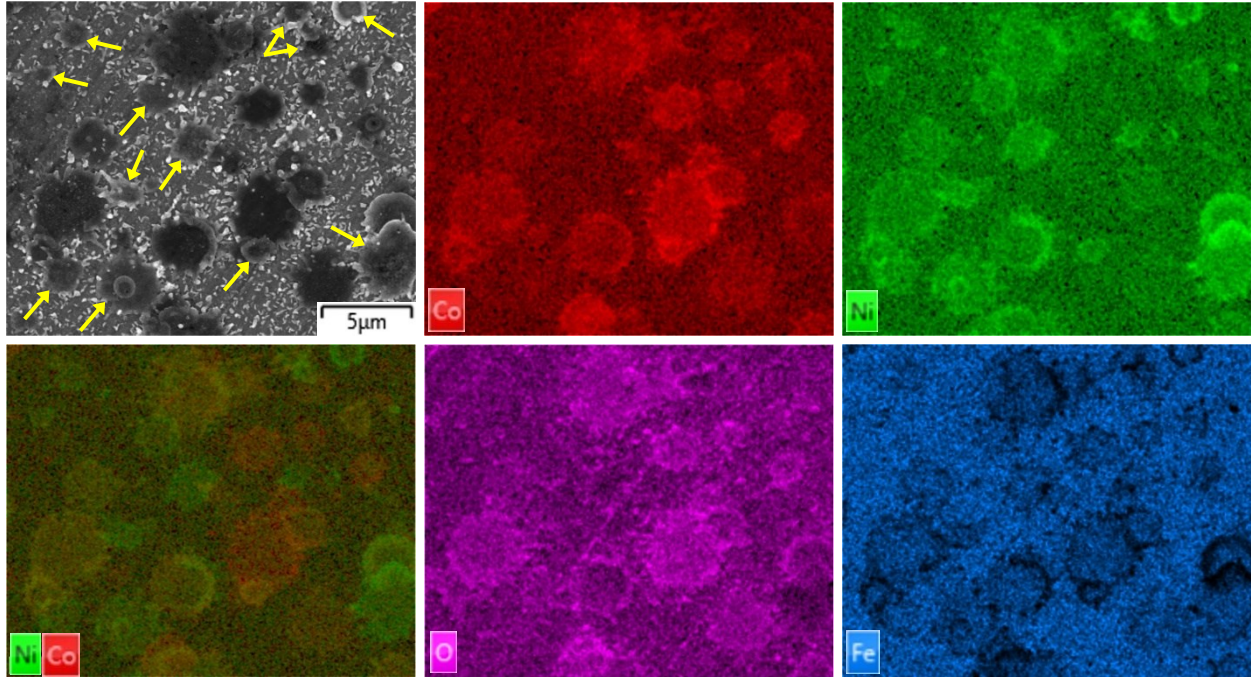


Figure 4.9. EDS mapping images of the collected splats of sample S2.

4.3.3. Coatings study

For coating of the samples S1–S3, the suspensions prepared by mixing CoO and NiO powders with 50–50 mol% were sprayed using three different spray conditions (see Table 4.1). Fig. 4.10 depicts the XRD patterns of the prepared coatings. Two sets of peaks appear in the XRD pattern of samples S1 and S3, indicating that a fraction of the NiO particles is reduced to metallic nickel in them. In contrast, the XRD pattern of sample S2 shows only one set of peaks assigned to the (Co,Ni)O solid solution phase.

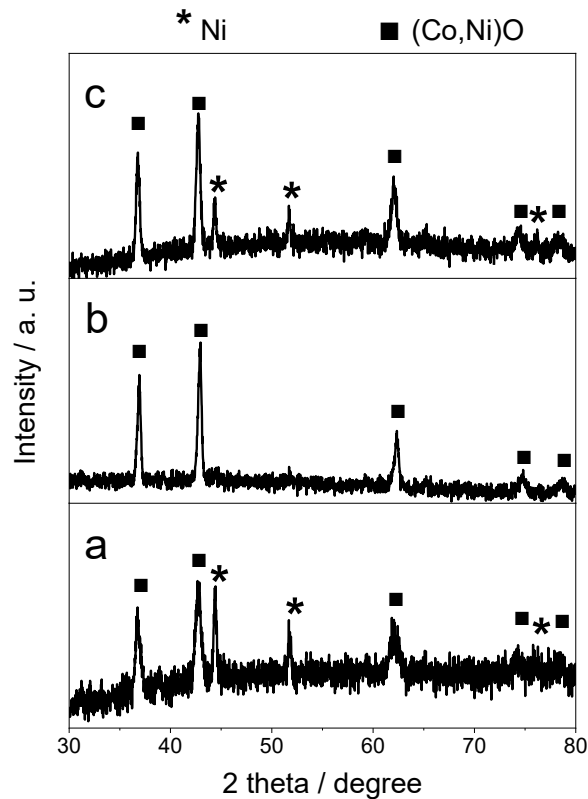


Figure 4.10. XRD patterns of coated samples (a) S1, (b) S2 and (c) S3.

Fig. 4.11 displays the OM cross-section of coated samples S1–S3 sprayed according to Table 4.1. A typical lamellar structure consisting of overlapped splats is observed in the coating of sample S1 (Fig. 4.11 a) resulting from well-melted and flattened particles. Evidently, this coating consists of distinct lamellar splats of two grey levels in the cross-section. Fig. 4.12 shows the SEM and EDS map pictures of sample S1. Based on the EDS map picture, the bright splats contain only nickel without any cobalt or oxygen atoms indicating that they are metallic nickel phase, while the dark splats contain cobalt, nickel, and oxygen atoms to form a (Co,Ni)O solid solution. For sample S2, the coating contains only one phase which corresponds to the (Co,Ni)O solid solution (Figs. 4.11b and 4.10b). However, this coating features many dome-shaped bumps which increase the surface roughness. The formation of such bumps is likely attributed to shadowing effects during deposition. On the other hand, the average coating thickness of samples S1 and S2 deposited with the same number of passes was about 90 and 40 μm , respectively. This means the coating thickness per pass for sample S2 is more than twice smaller than that of sample S1. The smaller thickness obtained for sample S2 is probably associated with the splat formation behavior explained in

Section 4.3.2. From Fig. 4.7, it is clearly noted that a significantly smaller number of splats have been collected under the spray condition of sample S2 as compared to those of sample S1 (see Fig. 4.5). This may be associated with the fact that a fairly large percentage of the particles remain unmelted in sample S2, which are more likely not to adhere to the surface, thereby leading to lower coating thickness and deposition efficiency.

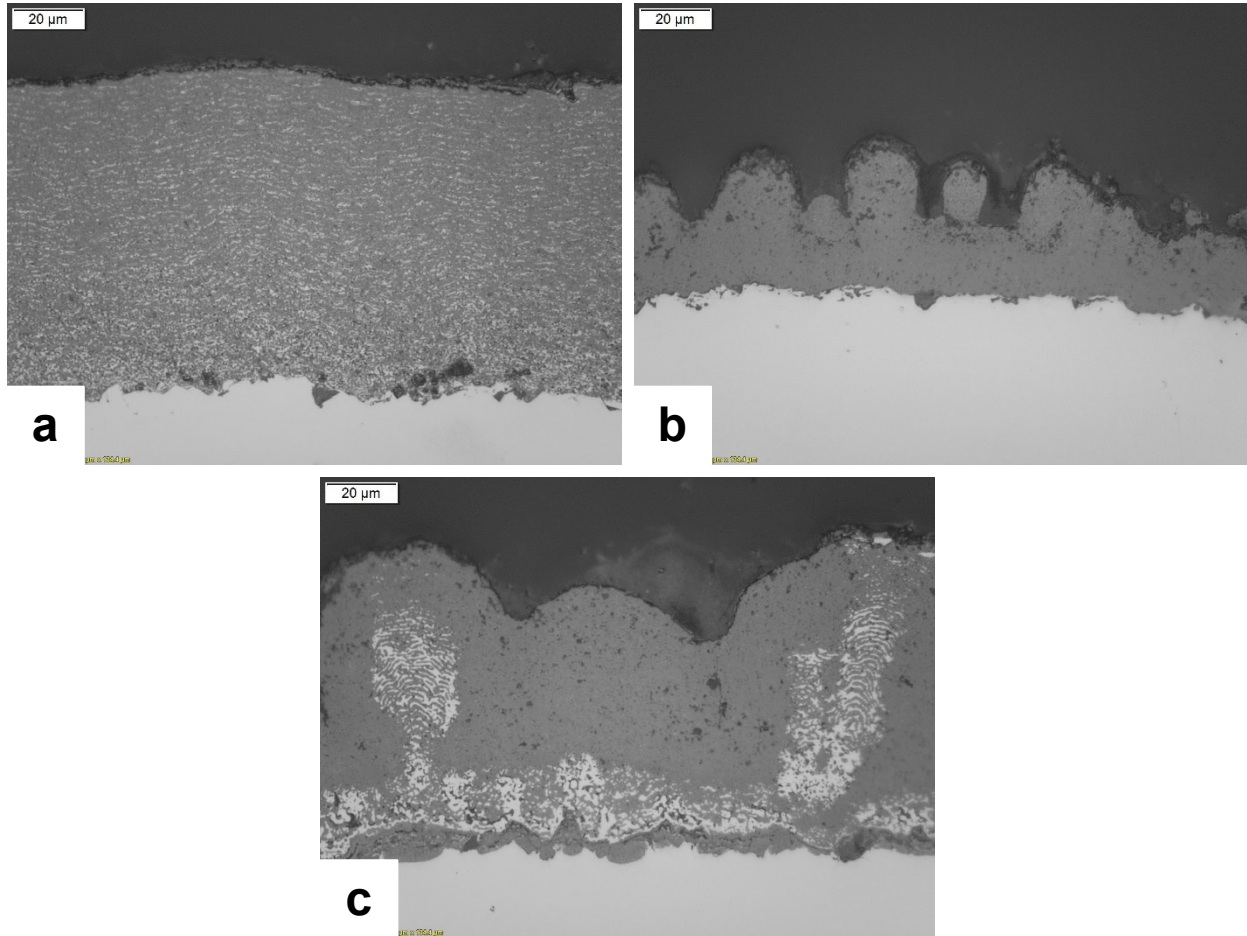


Figure 4.11. Optical microscopy cross-sectional images of coated samples (a) S1, (b) S2 and (c) S3.

Based on Fig. 4.11c, Ni-rich columns have been formed in the sample S3 coating. The formation of this unique structure is possibly related to the feedstock particle size. Note that the submicron-sized NiO powder used in this study was much smaller than CoO powder. As a result, the smaller NiO particles follow the deflecting gas flow parallel to the surface of the substrate in the stagnation region during spraying. In this context, very fine NiO particles with low inertia tend

to travel laterally almost parallel to the substrate surface and possibly attach on asperities on the coating surface, not impacting their top. The growing columns further shadow the surrounding area, causing the incoming particles to attach to the surface of these columns and preventing the formation of a continuous coating.

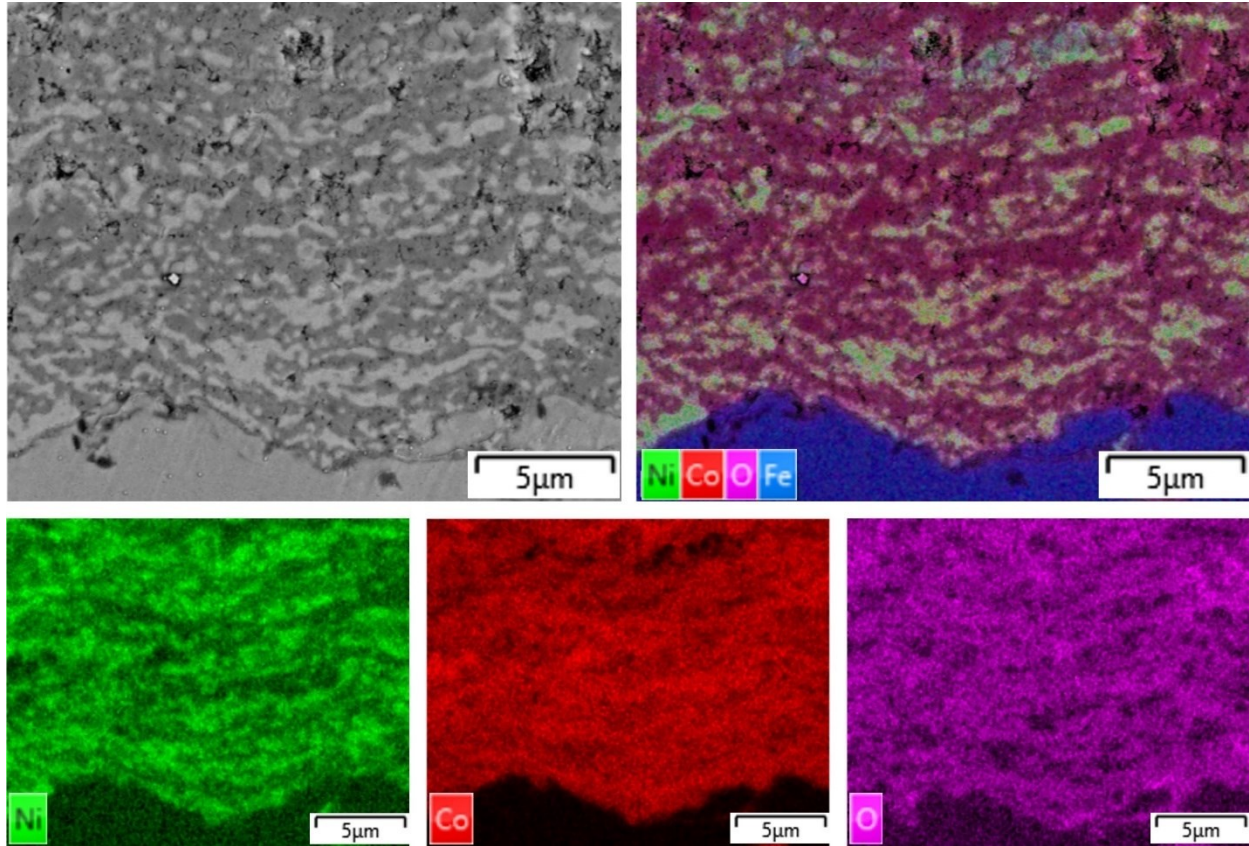


Figure 4.12. Cross-sectional SEM image and corresponding EDS mapping image of sample S1.

In our previous study [91], an experiment was devised to investigate the effect of substrate temperature on the formation of metallic nickel in the prepared coating. Accordingly, the coated sample S4 was prepared from a powder mixture consisting of 75% mol. CoO and 25% mol. NiO and sprayed under the same spray conditions as sample S2. The XRD pattern of sample S4 can be seen in Fig. 4.13. The XRD pattern depicts only one set of peaks assigned to the (Co,Ni)O solid solution, with no trace of metallic nickel. The cross-sectional SEM micrograph of this sample is presented in Fig. 4.14a. It can be seen that metallic nickel is formed only close to the substrate/coating interface. The XRD diffraction pattern did not reveal diffraction peaks of metallic Ni since it is completely covered with a thick layer (*ca.* 50 μm thick) made of only the solid

solution phase. The evolution of the substrate temperature during spraying with the number of passes is illustrated in Fig. 4.14b. The substrate temperature increased up to 950 °C in the first 10 passes and remained almost unchanged in the following 40 passes. The metallic Ni phase in sample S4 was formed in the first few passes of spraying when the substrate temperature was below 950 °C. Note that the substrate in sample S2 was preheated to 200 °C before starting the coating process. Thus, it can be assumed that the substrate reached its maximum temperature faster than that of sample S4 in which the coating started when the substrate was at room temperature. These results can explain why metallic Ni layers are not observed in sample S2.

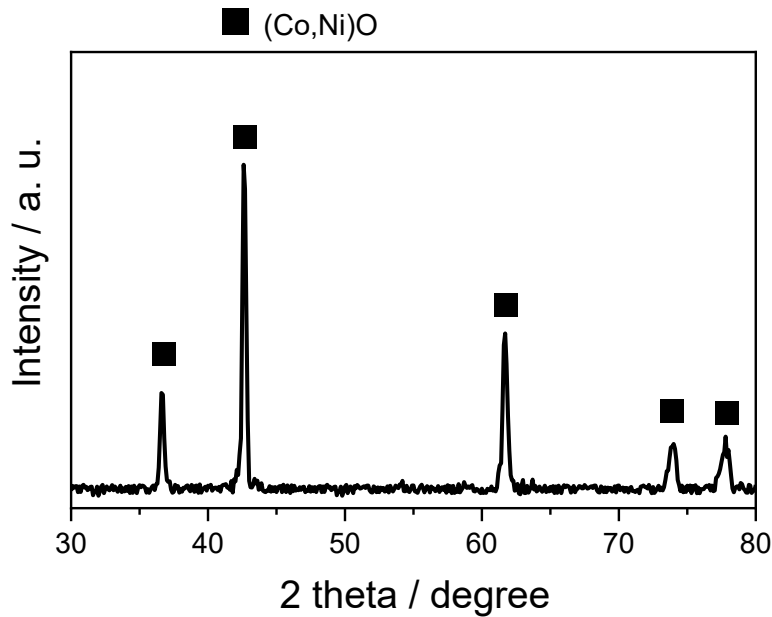


Figure 4.13. XRD pattern of the coated sample S4 [91].

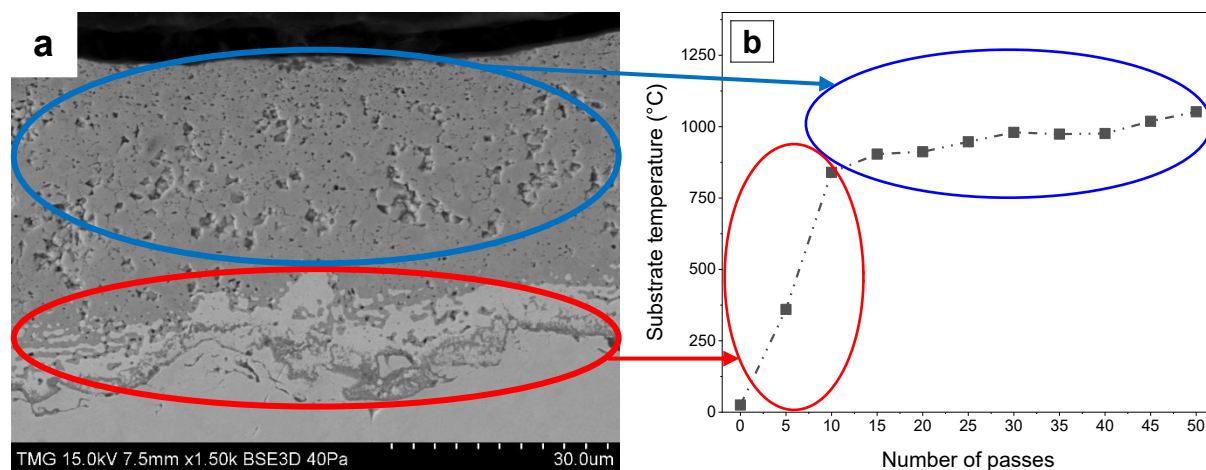


Figure 4.14. (a) Cross-sectional SEM micrograph of sample S4 and (b) variation in substrate temperature with the number of passes [91].

As reported in different NiO plasma spraying studies, the presence of metallic nickel was observed and attributed to NiO reduction during spraying with hydrogen gas [74,99]. Poon et al. [79] reported the partial reduction of stoichiometric NiO to NiO_{1-x} after air plasma spraying of NiO–YSZ powder and the change in appearance from a green powder feedstock to a black plasma spray coating.

To further investigate the formation of metallic Ni at low substrate temperature during the first few passes of spraying, samples S5 and S6 were prepared by spraying 10 passes while maintaining the substrate temperature below 200 °C by using a water-cooled sample holder and an air jet impinging on the front surface of the samples (see Table 4.1). Fig. 4.15 displays the SEM images and EDS composition analyses on the coating splats in samples S5 and S6. As can be observed, the splats formed in these coatings are mostly either Ni-rich or Co-rich, confirming the quite low mixing of NiO and CoO particles in-flight during deposition. This is in agreement with those results obtained for collected particles and splats. Fig. 4.16 depicts the selected-area EDS analysis results obtained on the coatings in samples S2, S5 and S6. It can be seen that the composition of coating in sample S2 is almost the same as that of the starting material, in agreement with the XRD results. Nevertheless, the composition results of coatings in samples S5 and S6 reveal that the oxygen has partially depleted from the deposited splats in these samples to form sub-stoichiometric oxides, expressed as NiO_{1-x} and CoO_{1-x}. The formation of such sub-

stoichiometric oxides is common in air plasma spray and SPS [77,78]. Based on these findings, the possible explanation for the formation of metallic Ni at low temperatures is proposed below.

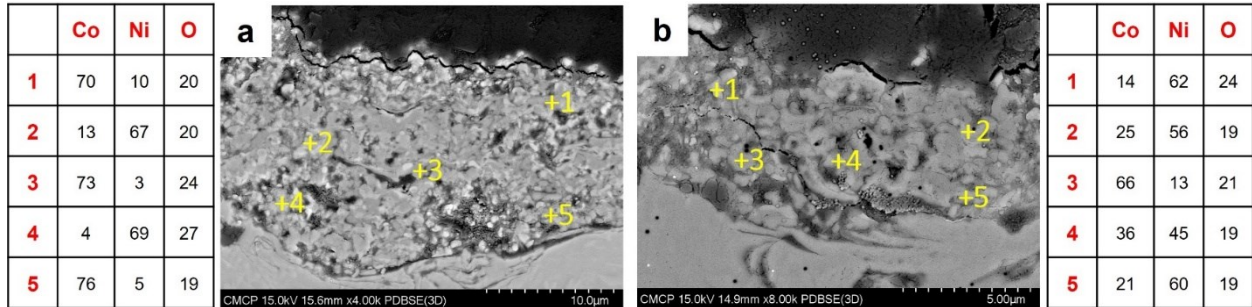


Figure 4.15. Point EDS analysis results (in at.%) of the coated samples (a) S5 and (b) S6.

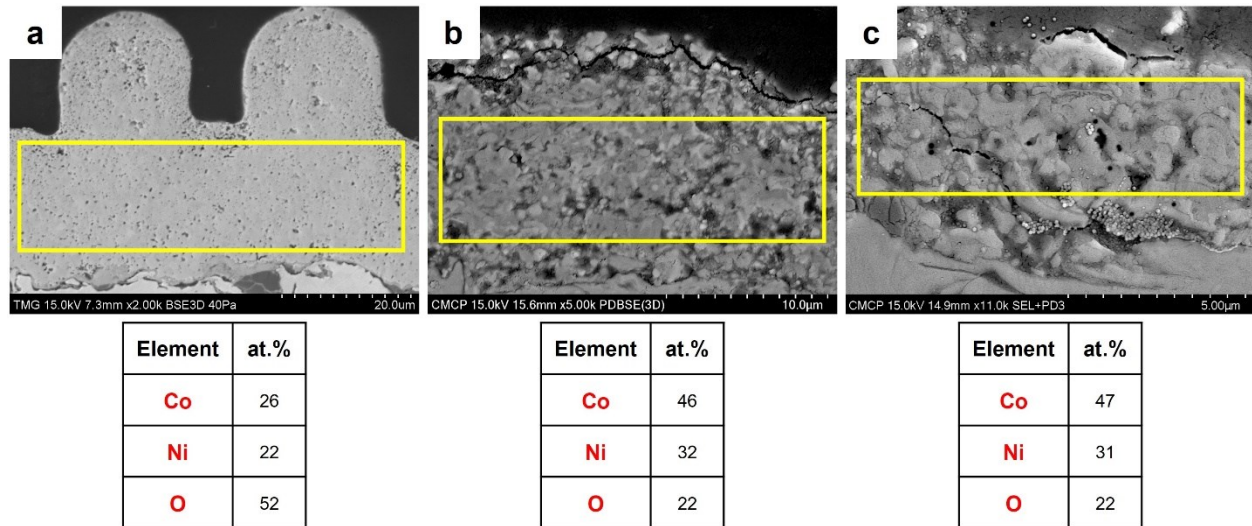


Figure 4.16. Selected-area EDS analysis results (in at.%) of the coated samples (a) S2, (b) S5 and (c) S6.

According to Ellingham's diagram, the Gibbs free energy of CoO is more negative than NiO, and the driving force for Co oxidation is larger than Ni [100]. Therefore, sub-stoichiometric NiO_{1-x} is expected to be less stable than sub-stoichiometric CoO_{1-x}. Consequently, when the temperature is high enough, the oxygen can move from NiO_{1-x} to CoO_{1-x} splats and metallic Ni is formed when no additional oxygen is available. Such a reaction can occur close to the substrate. For sample S4 (Fig. 4.14b), the substrate temperature was relatively low during the deposition of the first passes but increased to about 950 °C after 10 passes. Meanwhile, the top layers can be gas-tight not permitting oxygen from the air to reach the region close to the substrate. Thus, the

elemental inter-diffusion between the NiO_{1-x} and CoO_{1-x} splats occurred at a high temperature without the presence of oxygen, leading to the formation of the $(\text{Co,Ni})\text{O}$ solid solution and metallic Ni. The coating top layers in sample S4 (Fig. 4.14a) do not show the presence of metallic Ni as the top surface of the coating was heated at a high temperature and exposed to air during deposition so that both the Co and Ni are fully oxidized.

Fig. 4.17 shows the region close to the substrate in sample S1 at high magnification. One can see that the first layers of the coating have a sponge-like structure containing many rounded pores, clearly indicating a transformation of the lamellar structure normally observed in an SPS coating. These pores are believed to have formed during the reduction of the NiO_{1-x} splats due to the associated large volume decrease, which is around 40% for fully reduced NiO.

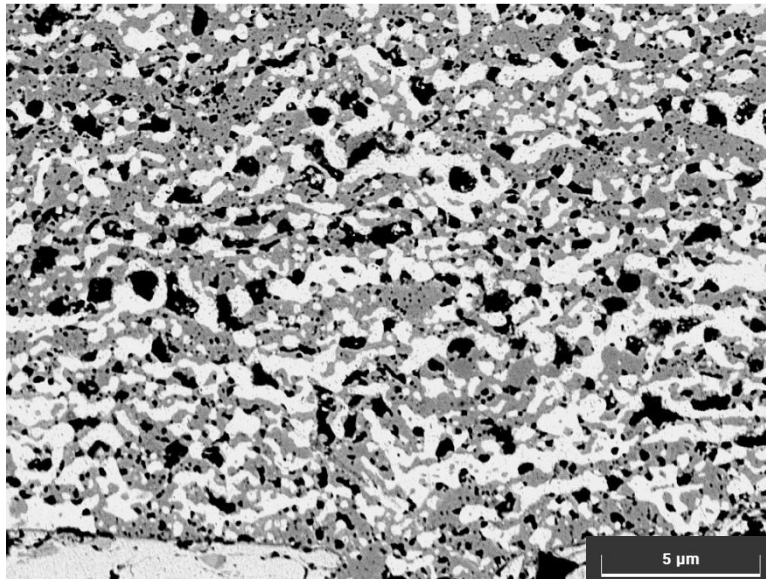


Figure 4.17. SEM image taken from the bottom region of the coating showing the porous structure of the metallic Ni areas in sample S1.

Heat treatment of sample S7, which was sprayed according to the spray condition given in Table 4.1, was carried out at 1000 °C for 1 h under argon with the aim to homogenize the coating microstructure. The XRD patterns of the as-coated and heat-treated samples are presented in Fig. 4.18. Two sets of peaks appear in the XRD pattern of the as-coated sample, attributed to the $(\text{Co,Ni})\text{O}$ solid solution and metallic Ni phases, while only a single set of peaks assigned to $(\text{Co,Ni})\text{O}$ solid solution is detected in the XRD pattern of the heat-treated sample. Fig. 4.19 exhibits the cross-sectional SEM images and the corresponding EDS mapping pictures of as-

coated and heat-treated samples. Evidently, the as-coated sample is composed of (Co,Ni)O, and metallic Ni layers overlapped each other across the coating (Fig. 4.19a and b). According to Fig. 4.19(c) and (d), the metallic Ni phase has been dissolved at the upper region of the coating into a (Co,Ni)O phase after heat treatment. Note that although an argon atmosphere was used to prevent substrate oxidation, a small fraction of oxygen remains in the furnace atmosphere during heat treatment, inducing some oxidation reactions with the coating. Based on Fig. 4.19(c) and (d), there is still a metallic Ni phase present at the region close to the substrate after 1 h of heat treatment at 1000 °C. Longer heating time at the same temperature may dissolve metallic Ni in the inner parts of the coating. These findings confirm the possibility of obtaining a single-phase solid solution by dissolving the metallic Ni phase into (Co,Ni)O phase during the post-heat treatment of the coatings.

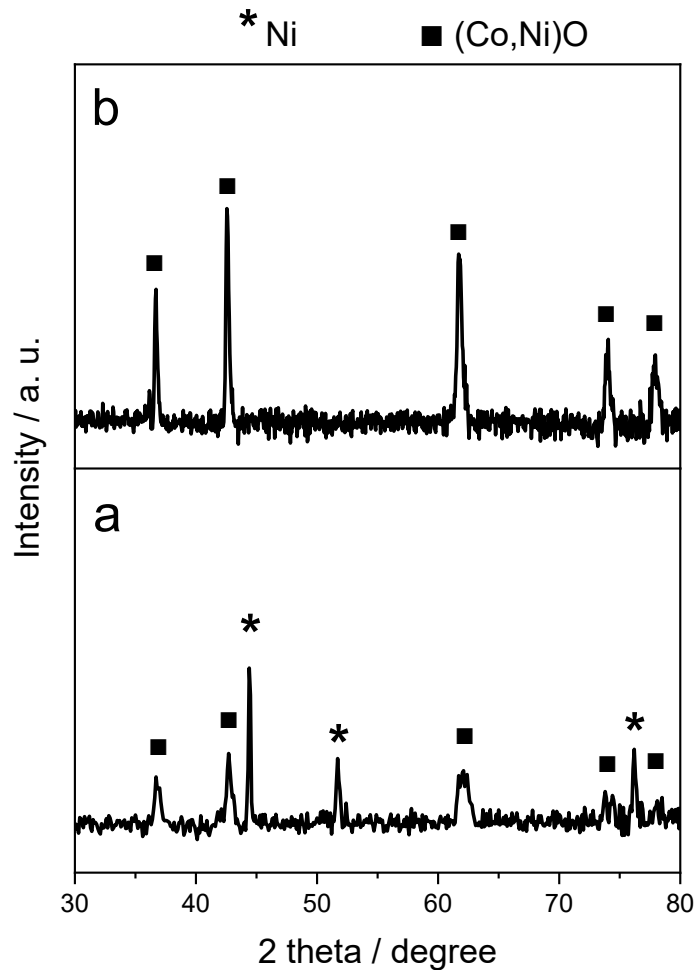


Figure 4.18. XRD patterns of sample S7: (a) as-coated and (b) heat treated at 1000 °C for 1 h under argon.

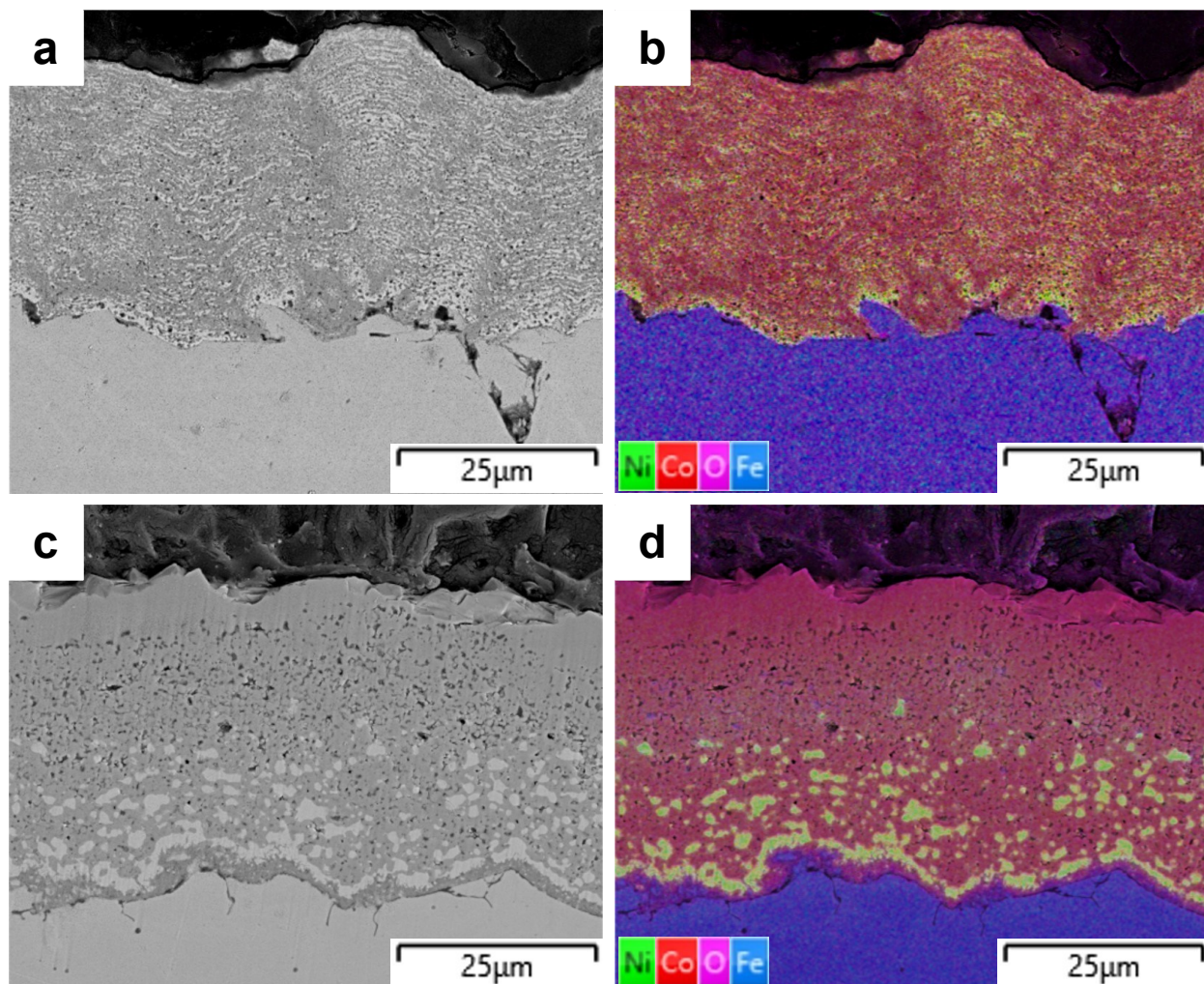


Figure 4.19. SEM and corresponded EDS mapping images of sample S7: (a and b) as-coated and (c and d) heat treated at 1000 °C for 1 h under argon.

4.4. Conclusions

(Co,Ni)O suspension containing CoO and NiO starting powders was deposited using the SPS process. The in-flight collected particle studies revealed that these particles are mostly either NiO or CoO, indicating a quite low mixing of NiO and CoO particles in-flight during spraying. In fact, the mixing of NiO and CoO may only occur on the substrate surface, not in-flight, while keeping the substrate temperature high. Plasma power input was found to play a major role in determining the shape and number of the generated splats. An increase in plasma power resulted in a splat morphology change from disk-like to flower-like, as well as the formation of un-melted

particles and drastic decline of the number of splats, which were responsible for decreasing the coating thickness. In addition to the (Co,Ni)O solid solution phase, the formation of metallic nickel was noticed in the coated samples. Investigation of coatings revealed that the substrate temperature was a major determining factor affecting coating composition. It is suggested that the elemental diffusion between NiO_{1-x} and CoO_{1-x} splats formed in the first few passes of spraying leads to the formation of a (Co,Ni)O solid solution, metallic nickel, and rounded pores in the region close to the substrate at high temperatures without the presence of oxygen. On the other hand, a single (Co,Ni)O solid solution phase is formed in the top region of the coating due to the high temperature and exposure to air during spraying which leads to the oxidation of splats. A well-homogenized coating can be achieved by heat treatment under argon flow, leading to the complete dissolution of metallic Ni into the (Co,Ni)O solid solution phase.

Preface to Chapter 5.

In the chapters 3 and 4, it was demonstrated that the suspension plasma spray (SPS) technique with Axial III Mettech torch is capable of producing (Co,Ni)O protective coatings with a dense and crack-free structure which is necessary to prevent the infiltration of electrolyte into the anode surface during electrolysis process. However, undesired reduction of NiO to metallic Ni was observed in coatings deposited with SPS. Therefore, high-velocity oxy-fuel (HVOF) method was selected as an alternative. In the HVOF process, the flame temperature is lower than in SPS method, which further decreases the possibility that the powder is reduced or decomposed. Furthermore, the high particle velocity in HVOF method enables generating dense, smooth and uniform coatings with good adhesion to the substrate. The next chapter in this thesis is devoted to investigating the capability of the HVOF process in generating dense, coherent and single-phase (Co,Ni)O coatings on both Ni-rich and Cu-rich Cu-Ni-Fe substrates and studying the high-temperature behavior of coated samples at 1000 °C in dry inert and oxidizing atmospheres.

Chapter 5

High-temperature behaviour of HVOF (Co,Ni)O coated Cu-Ni-Fe anodes for aluminum electrolysis ³

Abstract

Cu-Ni-Fe alloys are promising inert anodes for green Al production but their corrosion resistance must be improved. Here, protective (Co,Ni)O coatings are deposited by high velocity oxygen fuel (HVOF) process on Cu-Ni-Fe alloys. The influence of the coating and substrate compositions on their behavior is studied at 1000 °C under argon and air. On Cu-rich alloy, $\text{Co}_x\text{Ni}_{1-x}\text{O}$ coatings with higher nickel content slow down oxygen diffusion to the substrate, as well as copper diffusion to the sample surface. On Ni-rich alloy, the formation of a NiFe_2O_4 scale is observed, whose thickness decreases as the Ni content of the $\text{Co}_x\text{Ni}_{1-x}\text{O}$ coatings increases.

Keywords: (Co,Ni)O solid solution, high velocity oxygen fuel, high-temperature oxidation, inert anode, Al electrolysis.

5.1. Introduction

The substitution of consumable carbon anodes emitting CO_2 with inert O_2 -evolving anodes for the primary production of aluminum would reduce considerably the emissions of carbon dioxide and perfluorocarbons from this industry. This substitution would eliminate about 6 Mt of CO_2 eq produced annually by Canadian aluminum smelters, which is equivalent to the amount of CO_2 generated annually by about 2 million cars [56,57]. However, the design of inert anodes is a major challenge because of the severe Al electrolysis conditions that require materials with

³ This chapter has been published as an article in the *Journal of Corrosion Science*: S. Mohammadkhani, V. Jalilvand, B. Davis, G.H. Gauthier, A. Dolatabadi, C. Moreau, L. Roué, D. Guay. *Corrosion Science* 189 (2021) 109563.

excellent resistance to corrosion and thermal shock, as well as adequate electrochemical properties. Single phase Cu-Ni-Fe alloys are promising materials for inert anodes due to their ability to form a protective NiFe_2O_4 layer upon Al electrolysis [18,19,23]. However, this protective layer needs time to form at the surface of Cu-Ni-Fe alloys, during which fluorination can occur, causing premature degradation of the electrode [49].

In this context, the use of (Co,Ni)O-based protective coatings for metallic anode appears promising. In fact, CoO can work as a barrier for the fluorination of Ni-Fe alloys and the transformation of CoO to CoF_2 occurs only at very low oxygen pressure in cryolite medium [20]. In addition, it has been shown that adding Ni atoms to CoO and forming (Co,Ni)O solid solutions helps in preventing the decomposition of CoO to Co_3O_4 at elevated temperatures [20,53,60,61]. The formation of Co_3O_4 , which is a n-type semiconductor, should be avoided as it would translate into higher overpotential during Al electrolysis due to its lower conductivity in comparison with p-type semiconductor (Co,Ni)O solid solution [20].

Preparing a single phase, adherent and crack-free oxide layer at the surface of a substrate is challenging. For example, in the work of Nguyen and de Nora [20], (Co,Ni)O coatings were prepared following a two-step procedure that first involved the electrodeposition of a metallic Co-Ni alloy, followed by an oxidation treatment in air. However, producing a crack-free and cohesive oxide layer on an electrode using this approach is challenging as a drastic change in density occurs upon oxidation of the metallic Co-Ni alloy. One alternative is to use thermal spraying of an oxide powder to deposit oxide coatings in a single step and with a relatively high efficiency [47]. Thermal spray methods can be divided into several categories that include high velocity thermal spraying (high velocity oxy fuel (HVOF) and high velocity air fuel (HVOF)), plasma spraying (suspension plasma spray (SPS), vacuum plasma spray (VPS) and atmospheric plasma spray (APS)), combustion flame spraying, detonation gun spraying and arc spraying. However, high velocity thermal spraying techniques are preferred to form coatings with low porosity and good adhesion to the substrate. In these methods, a mixture of oxygen and fuel such as hydrogen, propylene, ethylene or propane is used to produce a supersonic jet through a Laval nozzle. Powdered materials are injected into the flame, where the particles begin to melt while being accelerated towards a substrate. The high velocity of the particles causes them to form a dense stack of flattened droplets on the substrate, resulting in smooth, uniform coatings with good adhesion to the substrate. Usually, the residence time of the powder in the flame is shorter and the flame temperature is lower

than in other thermal spray methods, which further reduces the possibility that the powder is reduced, oxidized or decomposed, or that undesired phase transformation occurs during spraying [47]. Different types of materials, including dense and porous metals, cermets and ceramics have been deposited by HVOF and HVAF, and the targeted applications are diverse such as wear and corrosion resistant coatings, and coatings acting as thermal barrier for high-temperature applications [45,101-108].

In our previous work, (Co,Ni)O coatings have been prepared by SPS of (Co,Ni)O powders [91]. However, an undesired reduction of NiO to Ni has been observed during the SPS process that causes the composition of the (Co,Ni)O solid solution of the coating to deviate from that of the starting materials. This is thought to occur because of the vaporization/decomposition/ionization of ethanol used as liquid phase in the SPS process to disperse oxide powders. Accordingly, it would be best to use a thermal spraying process where the oxide powder is injected directly.

In the current study, dense, uniform, and single phase $\text{Co}_x\text{Ni}_{1-x}\text{O}$ coatings, with $x = 1, 0.75$ and 0.5 , are deposited on CuNiFe substrates using the HVOF process. Substrates with two different alloy compositions are investigated, namely Cu-20Ni-15Fe (in wt.%) (Cu-rich alloy) and Ni-25Fe-10Cu (in wt.%) (Ni-rich alloy), which were previously studied as O_2 -evolving anodes for Al production [6]. The behaviour at $1000\text{ }^\circ\text{C}$ of the coating/substrate ensembles is investigated in dry inert and oxidizing atmospheres.

5.2. Experimental

$\text{Co}_x\text{Ni}_{1-x}\text{O}$ with $x = 0.75$ and 0.5 was synthesized by mixing Co_3O_4 (purity $\geq 99.7\%$, -325 mesh, from Alfa Aesar) and NiO powders (purity $\geq 99\%$, -325 mesh, from Cerac) followed by a 12 h heat treatment at $1200\text{ }^\circ\text{C}$ in air. Cobalt oxide (CoO) was also prepared by heating Co_3O_4 at $1200\text{ }^\circ\text{C}$ for 12 h under an argon flow, with a subsequent rapid cooling to prevent the conversion of CoO to Co_3O_4 upon cooling. All powders were prepared in kg quantity. They were sieved with -35 and $+20\text{ }\mu\text{m}$ screens to remove large particles and avoid clogging the HVOF gun. To determine the particle size, CoO and (Co,Ni)O powders were dispersed in water and analyzed by a Malvern Panalytical Spraytec instrument.

A Diamond Jet 2700-hybrid HVOF gun with a convergent-divergent nozzle from Oerlikon Metco (Westbury, NY, USA) was used to deposit coatings. Propylene and nitrogen were used as

fuel and powder carrier gas, respectively. The substrate temperature was monitored during the HVOF coating process by a FLIR A320 infrared camera. The HVOF spraying parameters were first optimized by varying the deposition conditions (H1, H2 and H3 in Table S5.1). Based on the porosity and adherence of the coating on the substrate, the deposition conditions H2 were selected. A detailed description of the optimization procedure is given in the supplementary section.

Two compositions of CuNiFe alloy, Cu-20Ni-15Fe and Ni-25Fe-10Cu (in wt.%), were used as substrates. CuNiFe alloys were produced by the casting method and were further homogenized by a heat treatment under argon as explained in our previous work [49,50]. Substrates were cut into disc-shaped specimens of 15 mm diameter and ~7 mm thickness. Then, they were grit-blasted and cleaned by several rinsing in distilled water and acetone. Only one side of the disc-shaped samples was coated by HVOF. All substrates were preheated to 200 °C by performing 5 passes of HVOF jet on the substrate surface before injecting the powder.

CoO, Co_{0.75}Ni_{0.25}O and Co_{0.5}Ni_{0.5}O powders were dried in an oven at 75 °C for at least 24 h prior to deposition. HVOF was used to deposit CoO, Co_{0.75}Ni_{0.25}O and Co_{0.5}Ni_{0.5}O powders on Cu-20Ni-15Fe (Cu-rich) and Ni-25Fe-10Cu (Ni-rich) substrates using the spray conditions denoted S1 to S6 in Table S5.1. The number of deposition passes was varied from 50 to 55 to achieve coatings with ~100–125 μm thickness.

Coatings were heated at 1000 °C for 20 h in static air and under an argon flow in a muffle furnace and a tubular furnace, respectively. Scanning Electron Microscopy / Energy Dispersive X-ray Spectroscopy (SEM-EDS) observations of as-sprayed and heat-treated specimens were undertaken by use of a Tescan Vega3 scanning electron microscope equipped with a Bruker XFlash® 6 | 10 Detector energy dispersive X-ray spectroscope. The crystalline structure of the starting powders and as-sprayed and heat-treated coatings was determined by X-ray diffraction (XRD) using a Bruker D8 diffractometer equipped with Cu K α radiation.

5.3. Results and discussion

5.3.1. As-coated samples

SEM micrographs of the starting powders are shown in Fig. 5.1a-c. CoO, Co_{0.75}Ni_{0.25}O and Co_{0.5}Ni_{0.5}O powders consist of spherical or near-spherical primary particles that are formed from the agglomeration of smaller particles. The particle size distribution curves of these powders are

also shown in Fig. 5.1d-f. The particle diameters of CoO, Co_{0.75}Ni_{0.25}O and Co_{0.5}Ni_{0.5}O powders are centered along a single mode, with maximal volume frequency at 21, 19 and 16 μm, respectively. The D50 and D90 values are 22 and 35 μm for CoO, 20 and 32 μm for Co_{0.75}Ni_{0.25}O and 15 and 27 μm for Co_{0.5}Ni_{0.5}O, respectively.

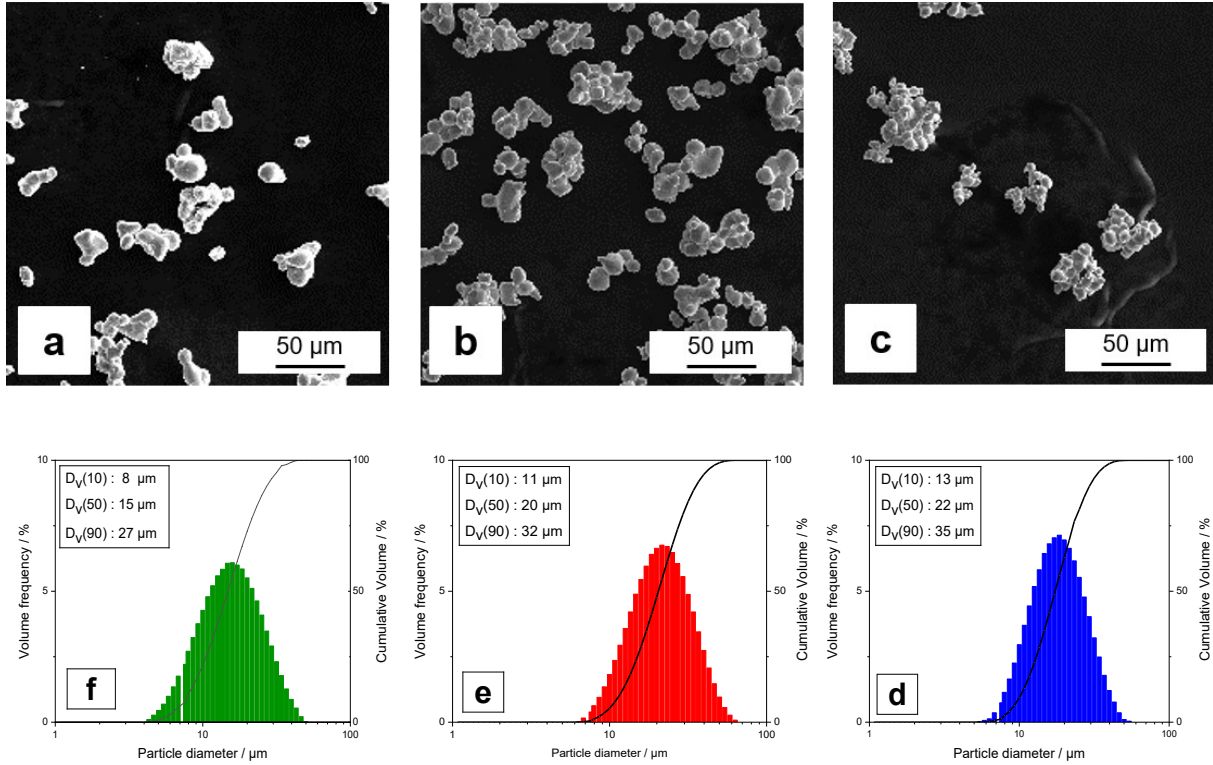


Figure 5.1. SEM micrographs (a, b and c) and particle size distribution histograms (d, e and f) of (a and d) CoO, (b and e) Co_{0.75}Ni_{0.25}O and (c and f) Co_{0.5}Ni_{0.5}O precursor powders.

Fig. 5.2 displays the XRD patterns of samples S1-S6. For all coatings, only one set of peaks are observed that are assigned to a *fcc* Co_xNi_{1-x}O solid solution. The *a* lattice parameter of the Co_xNi_{1-x}O solid solution was calculated from the position of the diffraction peaks of each coating. The value of *x* was then calculated using the known relationship between *a* and the composition of the Co_xNi_{1-x}O solid solution [53]. As shown in Table 5.1, the lattice parameters of the Co_xNi_{1-x}O coatings and corresponding powders are similar, and their values are in accordance with the nominal composition of the starting powders.

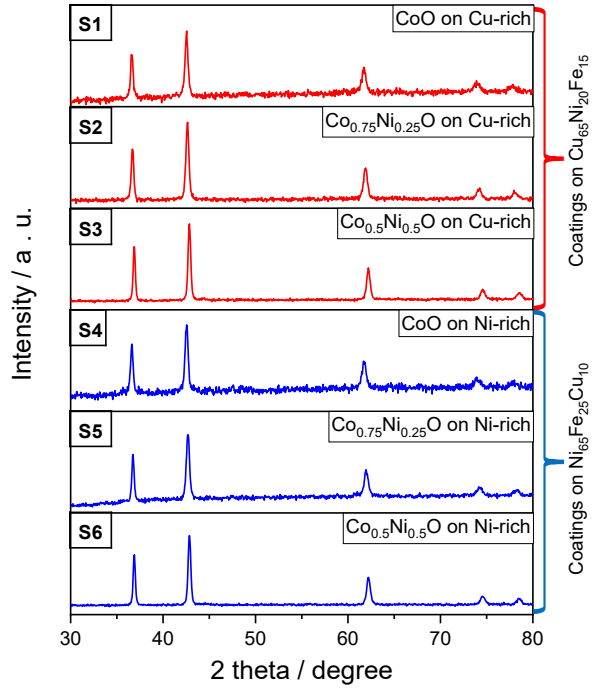


Figure 5.2. XRD patterns of coatings deposited on Cu-rich substrate (a, b and c) and Ni-rich substrate (d, e and f): CoO (a and d), $\text{Co}_{0.75}\text{Ni}_{0.25}\text{O}$ (b and e), $\text{Co}_{0.5}\text{Ni}_{0.5}\text{O}$ (c and f).

Table 5.1. Structural parameters of (Co,Ni)O coatings.

Sample	Coating composition	Lattice parameter of (Co,Ni)O powders (Å)	Lattice parameter of (Co,Ni)O coatings (Å)	(Co,Ni)O lattice parameter after heat treatment under argon flow (Å)	$\Delta a / a$ after heat treatment under argon flow	(Co,Ni)O lattice parameter after heat treatment in air (Å)
On Cu-20Ni-15Fe substrates						
S1	CoO	4.264	4.263	4.274	0.011	n/a
S2	$\text{Co}_{0.75}\text{Ni}_{0.25}\text{O}$	4.239	4.238	4.251	0.013	n/a
S3	$\text{Co}_{0.5}\text{Ni}_{0.5}\text{O}$	4.221	4.222	4.235	0.013	n/a
On Ni-25Fe-10Cu substrates						
S4	CoO	4.264	4.263	4.273	0.010	4.262
S5	$\text{Co}_{0.75}\text{Ni}_{0.25}\text{O}$	4.239	4.239	4.250	0.011	4.238
S6	$\text{Co}_{0.5}\text{Ni}_{0.5}\text{O}$	4.221	4.221	4.231	0.010	4.223

Fig. 5.3 presents the cross-sectional SEM micrographs of coatings. All coatings are uniform and crack-free with very low porosity. The surface of coatings is smooth, and their thickness varies between 110 and 125 μm . The composition of all coatings, as determined by EDS, is very close to that of their respective starting powders, in accordance with the previous XRD data.

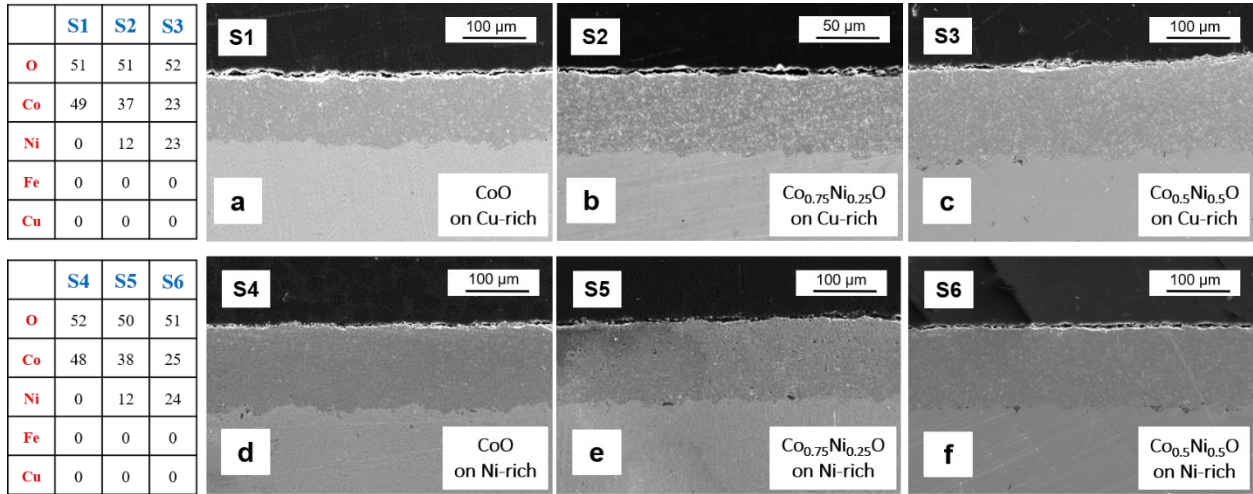


Figure 5.3. Cross-sectional SEM micrographs of coatings deposited on Cu-rich substrate (a, b and c) and Ni-rich substrate (d, e and f): CoO (a and d), $\text{Co}_{0.75}\text{Ni}_{0.25}\text{O}$ (b and e), $\text{Co}_{0.5}\text{Ni}_{0.5}\text{O}$ (c and f). The EDS analysis (at.%) of as-sprayed coatings are presented as well.

5.3.2. Heat treatment under argon

One of the main issues of coating metal alloys with oxide layers is the difference in thermal expansion coefficients between the substrate and the coating. At high temperatures in an inert atmosphere, this difference can lead to the formation of cracks in the coating, and even its partial or complete detachment from the substrate. In an oxidizing atmosphere, this problem can be exacerbated due to the formation of new oxides or changes in the oxidation state of the coating. Thus, it is important to study the behavior of coatings at high temperatures in inert and oxidizing atmospheres in order to separate these two effects and thus understand the complex behavior of coatings.

Fig. 5.4 shows the XRD patterns of sample S1-S6 after a 20 h heat treatment at 1000 $^{\circ}\text{C}$ under argon. Only one set of diffraction peaks can be observed in the XRD patterns, indicating that no new phase is formed during heat treatment. However, the XRD peaks of all coatings are

shifted to smaller angles, indicating that the lattice parameter of the fcc phase has increased and thus a change in the composition of the coatings has occurred. The relative change of the lattice parameter, which is given by $\Delta a / a$, of coatings deposited on Cu-rich substrates are larger than on Ni-rich substrates (see Table 5.1), indicating that the final composition of the coatings varies with the nature of the substrate. This issue will be discussed in more detail later.

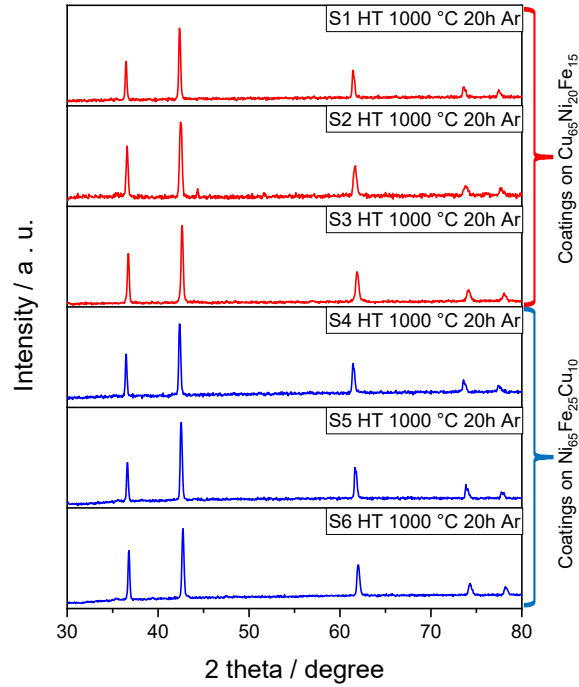


Figure 5.4. XRD patterns of samples S1-S6 after 20 h of heat treatment at 1000 °C under an argon flow.

The cross-sectional SEM micrographs of samples after heat treatment in argon are shown in Fig. 5.5. For coatings deposited on Cu-rich substrates, pores are observed at the coating/substrate interface, especially for the CoO coating. In contrast, coatings deposited on nickel-rich substrates are dense and homogeneous and no porosities are observed at the coating/substrate interface.

Fig. 5.6 shows the EDS quantitative and mapping results of CoO coatings on Cu-rich and Ni-rich substrates after heat treatment in argon. Schematic representations of the different compounds formed resulting from heat treatment are also shown. In both cases, three layers are observed, denoted by L1, L2 and L3. Layers 1 and 3 correspond to the coating and substrate, respectively, while L2 is located on the substrate side of the coating/substrate interface.

Quantitative EDS analysis was performed in 5 different zones. In Layer 1, EDS results show that diffusion of iron from the substrate to the coating, and that diffusion of cobalt from the coating to the substrate, have occurred. Diffusion of nickel and copper from the substrate to the coating is not observed to any significant extent. On both substrates, zones 1 and 2 in Layer 1 contain the same amount of Fe, indicating there is no Fe concentration gradient in the coating following 20 h of heat treatment. From the EDS results, the atomic ratio $M / (M + O)$, where M is the sum of all metallic elements and O is oxygen, is 0.47 and 0.49 in zones 1 and 2, respectively, almost identical to the value measured on as-deposited coatings. This suggests that the average oxidation state of the metallic elements in the coating was not altered during heat treatment.

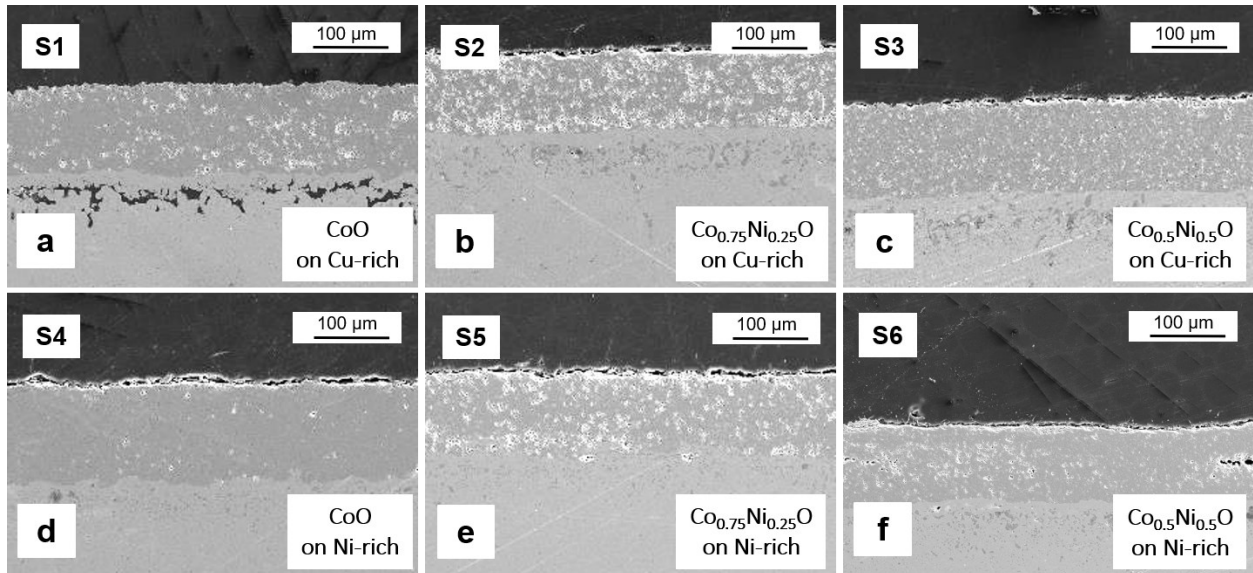


Figure 5.5. Cross-sectional SEM micrographs of samples (S1-S6) after 20 h of heat treatment at 1000 °C under an argon flow.

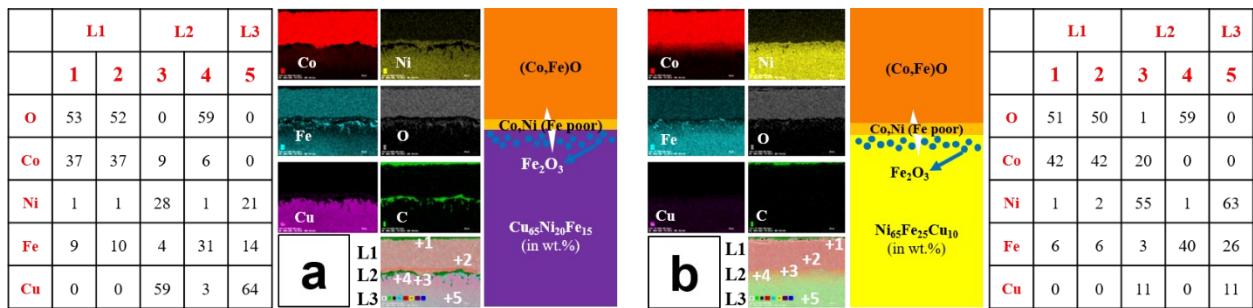


Figure 5.6. EDS analysis results and schematic illustrations of CoO coatings deposited on (a) Cu-20Ni-15Fe (S1) and (b) Ni-25Fe-10Cu (S4) substrates after 20 h of heat treatment at 1000 °C under an argon flow. The source of carbon is the resin used for the sample.

As noted above, diffusion of Fe atoms to the coating and Co atoms to the substrate is more important on Cu-rich than on Ni-rich substrate. The Fe^{2+} and Co^{2+} ionic radii are 0.77 and 0.74 Å, respectively [109]. Accordingly, this should translate into a larger relative change of the lattice parameter of coatings deposited on Cu-rich than on Ni-rich substrates, which is consistent with what was observed previously in Table 5.1.

Following Fe diffusion to the coating, a Fe-poor region is formed at the coating/substrate interface of both substrates, where cobalt atoms that have diffused from the coating are concentrated (zone 3 of Layer 2), along with Ni and Cu atoms. Iron atoms in Layer 2 are essentially present as iron oxide inclusions (zone 4 of Layer 2) dispersed in a metallic matrix mainly composed of Cu, Ni and Co atoms (zone 3 of Layer 2). The standard Gibbs free energy of formation, ΔG°_f (at 1300 K) of FeO, Fe_2O_3 and Fe_3O_4 are -188 , -487 and -702 kJ mol $^{-1}$ of oxide, respectively, compared to -74 , -41 and -123 kJ mol $^{-1}$ for Cu_2O , CuO and NiO [110,111]. Based on these data, iron is the most oxidizable element, and the formation of iron oxides, instead of copper and nickel oxide, is not surprising. It is difficult to ascertain the exact nature of the iron oxide compounds formed, but based on the O and Fe stoichiometry, Fe_2O_3 and Fe_3O_4 are the most probable.

A mass balance calculation was performed to determine the total amount of Fe and O atoms in Layers 1 and 2. Details of these calculations are given in the supplementary section. Of the total number of Fe atoms initially contained in Layer 2 of the substrate, about 85 % are diffusing to the coating (Layer 1) during heat treatment. As mentioned earlier, there is almost no diffusion of Ni and Cu atoms from the substrate to Layer 1. The preferential diffusion of Fe atoms can be understood based on Cu – O, Fe – O and Ni – O phase diagrams [112–114]. During heat treatment in the presence of 99.999 % pure Ar, the O_2 partial pressure must be below 10^{-10} atm. At this pressure, Cu_2O is more stable than CuO, Ni is more stable than NiO, and FeO is more stable than either Fe_2O_3 or Fe_3O_4 . It is hypothesized that diffusion of Fe^{+2} cations in CoO is favored over diffusion of Ni° and Cu^{+1} . Also, both CoO and FeO have a *fcc* rock-salt crystal structure, and they are known to form a (Co,Fe)O solid solution at high temperature and low oxygen pressure [115]. It is inferred that both factors contribute to promote the diffusion of iron atoms from the substrate to the coating, where they can dissolve homogeneously in the CoO coating to form a (Co,Fe)O phase.

Heat treatment of these samples was conducted in Ar with limited contamination by oxygen (99.999 % pure). Accordingly, O atoms found in Layer 2 must originate from the oxide coating

(Layer 1). Extending on the previous mass balance calculation (see the supplementary section), the total amount of O atoms in Layer 2 after heat treatment corresponds to only 2–3 % of those initially present in the coating (Layer 1). Such a small variation is within the uncertainty of the EDS measurements and would go unnoticed.

The same analysis was conducted for $\text{Co}_{0.75}\text{Ni}_{0.25}\text{O}$ and $\text{Co}_{0.5}\text{Ni}_{0.5}\text{O}$ coatings deposited on Cu-rich and Ni-rich substrates, and the results are depicted in Figs. S5.3 and S5.4. All samples exhibit the same structure, with three well-distinct regions (L1, L2 and L3). However, as shown in Fig. 5.7, the Fe content in Layer 1 varies with the nature of the substrate and the composition of the coating. Interestingly, the iron content in coatings deposited on Cu-rich substrate decreases steadily as the molar fraction of Ni in the $(\text{Co},\text{Ni})\text{O}$ coating is increased. This is because the diffusion coefficient of Fe atoms at 1000 °C is smaller in NiO than in CoO ($2.3 \cdot 10^{-11}$ vs. $1.59 \cdot 10^{-9} \text{ cm}^2 \text{ s}^{-1}$) [109]. As a result, increasing the Ni content of the $(\text{Co},\text{Ni})\text{O}$ coating decreases the iron diffusivity. On Ni-rich substrates, the Fe content in Layer 1 is almost constant at about 5 at.% and independent of the coating composition. In that case, the diffusion of iron atoms from the Ni-rich substrate is limiting. This is thought to reflect on the smaller diffusion coefficient of Fe atoms in metallic nickel compared to metallic Cu ($7 \cdot 10^{-12}$ vs. $2 \cdot 10^{-9} \text{ cm}^2 \text{ s}^{-1}$) [116,117].

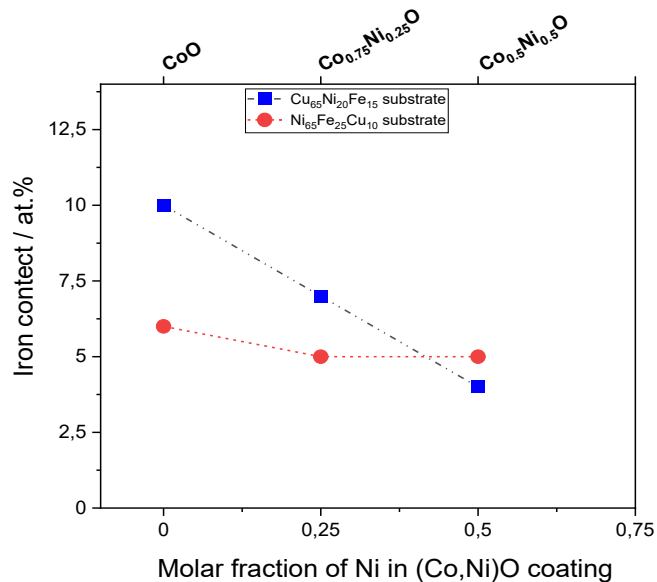


Figure 5.7. Iron content in $(\text{Co},\text{Ni})\text{O}$ coatings after 20 h of heat treatment at 1000 °C under an argon flow.

5.3.3. Heat treatment under air

Fig. 5.8 illustrates cross-sectional SEM micrographs of HVOF coatings heat-treated in air at 1000 °C during 20 h. For comparison, cross-sectional SEM micrographs of bare Cu-rich and Ni-rich substrates after the same heat treatment are shown as well. Samples heated in air show very different behaviours according to the composition of the substrate. All coatings on Cu-rich substrate (Figure 5.8b-d) exhibit a thick oxide layer (L2, ~500–1000 μm) that grows underneath the (Co,Ni)O layer. This oxide layer does not have good adhesion to either the CuNiFe substrate (L3) or the (Co,Ni)O coating (L1) and has been delaminated from both coating and substrate. On Ni-rich substrates (Fig. 5.8f-h), this oxide layer is thinner (L2, ~30–35 μm) and it is still attached to the HVOF coatings while it has been delaminated from the Ni-rich substrate. Understanding these variations calls for a detailed analysis of the composition of each layer.

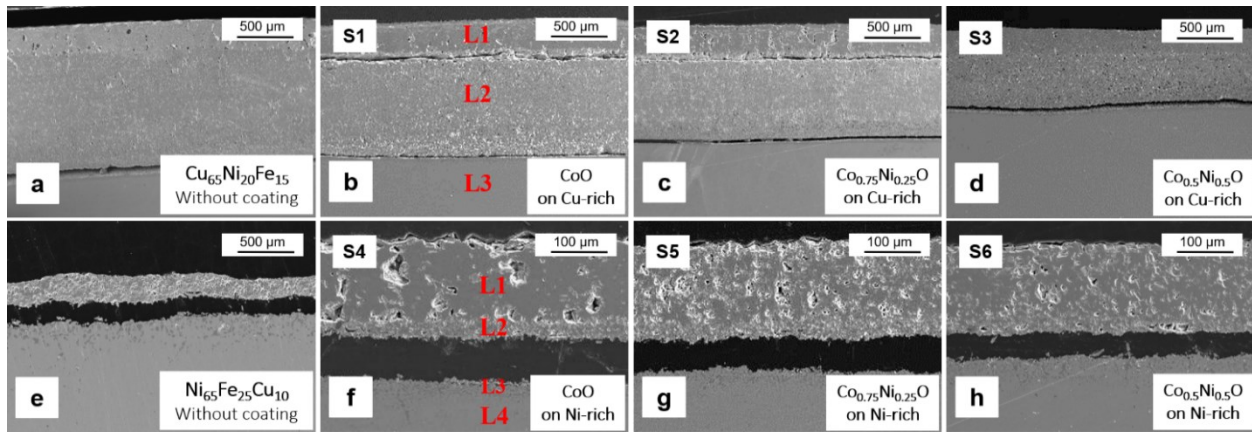


Figure 5.8. Cross-sectional SEM micrographs of coatings (sample S1-S6) after 20 h of heat treatment at 1000 °C in static air. Layers 1, 2, 3 and 4 are identified.

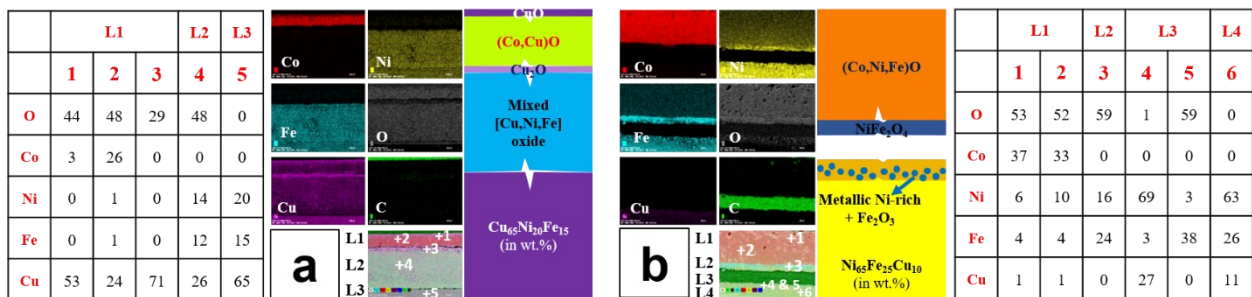


Figure 5.9. EDS analysis results and schematic illustration of CoO coating deposited on (a) Cu-20Ni-15Fe and (b) Ni-25Fe-10Cu substrate (sample S1 and S4, respectively), after 20 h of heat treatment at 1000 °C in static air. The source of carbon is the resin used for the sample preparation.

Detailed EDS analysis reveals that the structure and composition of these layers is complex. As shown in Fig. 5.9a, a thin layer of CuO is formed on the outer side (Zone 1) of the CoO coating sprayed on Cu-rich substrate, while a thin layer of Cu₂O is formed on its inner side (Zone 3). Also, EDS analysis reveals that Cu atoms are dispersed homogeneously in the CoO coating (Zone 2). Unlike heat treatment in argon, no evidence of Fe in the CoO coating was observed. The composition of the (Co,Ni)O coating does not have any drastic effect on the structure of the L1 oxide scale (Figs. S5.5 and S5.6). Indeed, in all cases, the HVOF coating is sandwiched between a top CuO and a bottom Cu₂O layer, and Cu atoms are found in the HVOF coating, although there is a gradual decrease of the CuO and Cu₂O oxide scales as the Ni content of the (Co,Ni)O coatings is increased. According to the Cu–O stability diagram [113,118], the equilibrium O₂ pressure for CuO/Cu₂O is around 10⁻² atm at 1000 °C. Accordingly, CuO is formed next to the sample surface, where the O₂ pressure is large, whereas Cu₂O is stable under the CoO oxide coating. The same CuO and Cu₂O layered structure was observed in our previous work, where as-cast and homogenized Cu-20Ni-15Fe alloys were used as O₂-evolving anodes for Al production in KF-based cryolite at 700 °C [49].

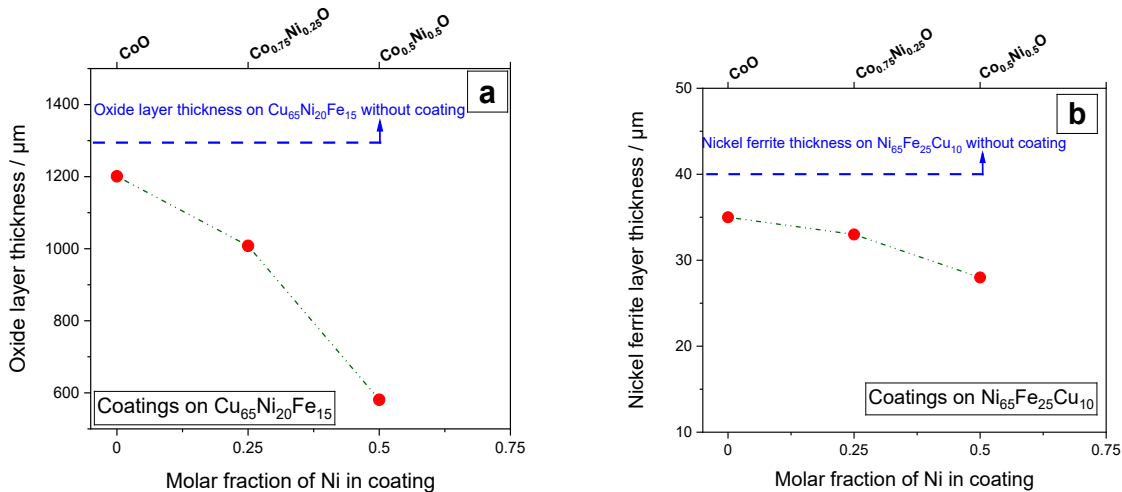


Figure 5.10. The oxide layer thickness below the HVOF coatings on (a) Cu-20Ni-15Fe substrates and (b) on Ni-25Fe-10Cu substrates after the heat treatment for 20 h at 1000 °C in air (samples S1-S6).

The formation of CuO and Cu₂O follows from the diffusion of Cu atoms from the substrate. Accordingly, Layer 2 is poorer in Cu (Zone 4) in comparison with the substrate (Zone 5). Oxygen atoms are present in Zone 4, along with Cu, Ni and Fe atoms, resulting in the formation of a thick

oxide layer. Figs. S5.5 and S5.6 show that the composition of Layer 2 does not change with the composition of (Co,Ni)O coating. However, as the nickel content in the (Co,Ni)O coating increases, the thickness of L2 decreases significantly (from $\sim 860 \mu\text{m}$ beneath CoO to $\sim 400 \mu\text{m}$ beneath $\text{Co}_{0.5}\text{Ni}_{0.5}\text{O}$) (Fig. 5.10a). In comparison, following the same heat treatment process, the thickness of L2 is $1300 \mu\text{m}$ on bare Cu-rich substrate. Clearly, the (Co,Ni)O coating acts as a semipermeable barrier for the diffusion of O atoms, and this effect is emphasized by the presence of Ni in the coating.

In argon, it was shown previously that Fe atoms from the substrate diffuse preferentially to the coatings, and that Cu atom was almost absent. The situation is very different when the heat treatment is performed under air, where Cu atoms are clearly observed in the coatings. According to the Cu – O and Fe – O phase diagrams, CuO and Fe_2O_3 are the more stable phases at $1000 \text{ }^\circ\text{C}$ and high oxygen pressure. In these conditions, it is inferred that Cu^{+2} diffuses preferentially in the CoO coating to react with oxygen at the coating/air interface to form CuO. The presence of both Co and Cu atoms in the HVOF coating is consistent with a previous report showing that (Co,Cu)O has a *fcc* rock-salt crystal structure similar to CoO and is stable at $1000 \text{ }^\circ\text{C}$ in the presence of oxygen [119]. The thickness of the CuO oxide scale is about 70, 45 and $5 \mu\text{m}$ on CoO, $\text{Co}_{0.75}\text{Ni}_{0.25}\text{O}$ and $\text{Co}_{0.5}\text{Ni}_{0.5}\text{O}$ coated Cu-rich substrate. This is a clear indication that the diffusion of Cu atoms from the substrate to the top of the HVOF coating is slowed down considerably as the Ni content of the coating is increased. The same holds true for the diffusion of O atoms to reach the substrate through the coating as the thickness of the Cu_2O oxide scale decreases from about 90 to 70 and then to $45 \mu\text{m}$ as the fraction of Ni in the coating is increased from 0 to 50 %. This is consistent with the previously observed thickness decrease of L2 as the Ni content of (Co,Ni)O coatings is increased.

Under the same conditions, the behaviour of Ni-rich substrate coated with (Co,Ni)O coatings is totally different. For example, with CoO-coated Ni-rich substrate heat-treated in air at $1000 \text{ }^\circ\text{C}$ during 20 h, copper diffusion and subsequent oxidation are not the predominant phenomena, and the CoO coating is not sandwiched between CuO and Cu_2O oxide layers (Fig. 5.9b). Also, the Cu content of the CoO coating is negligible (1 at.%, Zones 1 and 2). This is because, in CuNiFe alloys, the diffusion and mobility of Cu, Fe and Ni atoms depends strongly on the alloy composition, and thus copper concentration. In Cu-rich alloy, copper is the most mobile element with a diffusion coefficient a hundred-time higher than nickel or iron. However, the

diffusion coefficient of copper is decreased significantly in Cu-poor alloy, varying from $\sim 10^{-11}$ to $10^{-9} \text{ cm}^2 \text{ s}^{-1}$ [120]. Instead, both nickel (6–10 at.%) and iron (4 at.%) are found in the coating (Zones 1 and 2). Iron atoms are dispersed homogeneously in the coating, while there is a gradient of nickel, with 6 at.% in the upper section of the coating (Zone 1) and 10 at. % near the substrate (Zone 2).

A thin layer of nickel ferrite (less than $30 \mu\text{m}$) is formed under the HVOF coating (zone 3 in L2). The formation of a nickel ferrite layer significantly decreases the oxidation rate of Ni-rich substrate. Between the NiFe_2O_4 layer and the Ni-rich substrate, there is a layer (L3) made of iron oxide particles dispersed in a metallic matrix made of Cu and Ni. The iron oxide particles have a spherical shape with a few microns diameter. Indeed, the formation of iron oxide is the primary stage for the formation of the nickel ferrite phase that formed once the ratio between iron, nickel and oxygen atoms has the right value [6]. The composition of the (Co,Ni)O coating does not have any significant effect on the structure of L3.

As a summary, Fig. 5.10 shows the thickness of the oxide layer (L2 + L3) as a function of the coating composition. On both Cu-rich and Ni-rich substrates, the oxide layer thickness decreases as the nickel content of the (Co,Ni)O coating increases. This is because the oxygen diffusion coefficient in NiO is much lower than in CoO at $1000 \text{ }^\circ\text{C}$ [121]. The thickness of the oxide layer formed on uncoated Cu-rich substrate is $1300 \mu\text{m}$ (Fig. 5.10a). Increasing the nickel content of the (Co,Ni)O coating decreases the diffusivity of oxygen, which results in thinner oxide layers that decreases from 1200 to $600 \mu\text{m}$ between CoO and $\text{Co}_{0.5}\text{Ni}_{0.5}\text{O}$. In comparison, the thickness of the NiFe_2O_4 oxide layer formed on uncoated Ni-rich substrate is only $40 \mu\text{m}$. This is because the formation of a nickel ferrite layer slows down the further oxidation of the underlying substrate [26,49]. In that case, increasing the nickel content of the (Co,Ni)O coating results in a less marked effect on the thickness of the oxide layers, although it decreases from 35 to $28 \mu\text{m}$ between CoO and $\text{Co}_{0.5}\text{Ni}_{0.5}\text{O}$.

5.4. Conclusions

CuNiFe alloy substrates could be used as inert anodes for aluminum electrolysis. However, they are very severely corroded before a protective layer of NiFe_2O_4 can form under the aluminum electrolysis conditions, thus slowing down the attack of the electrolyte. In an effort to circumvent

this limitation, we have investigated the use of (Co,Ni)O coatings as protective layers to slow down the formation of copper oxide known to readily dissolved in the cryolithic medium at high temperature.

So, (Co,Ni)O coatings have been deposited by HVOF on both Cu-rich and Ni-rich CuNiFe alloy substrates using CoO, Co_{0.75}Ni_{0.25}O and Co_{0.5}Ni_{0.5}O powders as starting materials. Using optimized deposition conditions, all coatings are single phase and have a smooth morphology. The oxidation behavior of these samples was investigated at 1000 °C in the presence of oxygen to assess the effect of the coatings on the diffusion of Cu and O atoms. Comparison with their high temperature behaviour in inert atmosphere was also performed. After 20 h of heat treatment in air, HVOF coatings on Cu-rich substrates are sandwiched between a top CuO and a bottom oxide layer. However, increasing the nickel content of the (Co,Ni)O coating from 0 to 0.5 decreases the Cu and O diffusivity, which results in thinner CuO and bottom oxide scales. In the case of Ni-rich CuNiFe alloy, Cu diffusion to react with O and form CuO and Cu₂O is less of an issue because the diffusion of Cu atoms in Ni-rich CuNiFe alloys is considerably slowed down. In that case, a nickel ferrite scale is formed between the HVOF coating and the substrate. As expected, the thickness of the NiFe₂O₄ layer decreases slightly (~ 15 %) as the Ni content of the (Co,Ni)O coating is increased from 0 to 0.5. These coated samples will be used as anodes in Al production and their anodic behaviour in severe aluminum electrolysis conditions will be presented in the near future.

Preface to Chapter 6.

In the previous chapter, (Co,Ni)O coatings were deposited by HVOF on Cu-Ni-Fe alloy substrates and the dry oxidation behavior of the coatings was investigated at 1000 °C in the presence of oxygen. Although (Co,Ni)O coatings decreased the oxidation rate of the underlying Cu-Ni-Fe alloy, the diffusion of alloying elements from the substrates to the coatings and the formation of new oxide layers in the coatings were observed after 20 h of heat treatment in air. Application of an appropriate bond coat, such as CrMnFeCoNi high entropy alloy (HEA) or NiCr, can completely prevent the oxidation as well as the inter-diffusion of alloying elements between the substrate and the (Co,Ni)O protective coating. This is due to an oxide layer formation at the interface between the bond coat and top coat at high temperatures. Therefore, the following chapter is devoted to investigating the potential of CrMnFeCoNi HEA and NiCr bond coats as a barrier to oxidation and diffusion of elements between the substrate and the protective coating at 1000 °C in air atmosphere.

Chapter 6

The effect of bond coat on the high-temperature behavior of HVOF-sprayed (Co,Ni)O coating on Cu-Ni-Fe anodes ⁴

Abstract

The high-temperature behavior of Cu-Ni-Fe-coated materials is evaluated as inert anodes for zero-carbon Al production. $\text{Co}_{0.5}\text{Ni}_{0.5}\text{O}$ top coat is deposited on CrMnFeCoNi high entropy alloy (HEA) and Ni-20Cr bond coats with Cu-rich and Ni-rich CuNiFe as the substrate materials. The bond coats as well as the top coat are deposited by high velocity oxy fuel (HVOF) process. The effect of the bond coat layers on the oxidation resistance of coated samples is investigated at 1000 °C in air. The formation of a dense thin layer of Cr_2O_3 on both bond coats inhibits oxygen diffusion to the substrates. No diffusion of elements is observed from NiCr to (Co,Ni)O, while Mn atoms diffuse from HEA into the top coat layer during oxidation process.

Keywords: Bond coat, (Co,Ni)O solid solution, HVOF, Oxidation, Inert anode, Al electrolysis

6.1. Introduction

Carbon is still used as anode material in the Hall-Héroult process, developed in 1886, which results in carbon consumption and emission of carbon dioxide and perfluorocarbon during the primary production of aluminum. One of the main challenges in the aluminum industry is to substitute the release of greenhouse gases by environment-friendly O_2 gas on an inert anode with the following requirements: high electrical conductivity ($>200 \text{ S cm}^{-1}$), prominent oxidation resistance at high temperature and an erosion rate lower than 1 cm year^{-1} for 0.8 A cm^{-2} [6]. To

⁴ This chapter has been published as an article in the *Surface & Coatings Technology*: V. Jalilvand, S. Mohammadkhani, F. Ben Ettouil, L. Roué, A. Dolatabadi, D. Guay, C. Moreau. *Surface & Coatings Technology* 441 (2022) 128576.

fulfil these conditions, three kinds of inert anodes for Al electrolysis process were investigated: ceramics, cermets and metals, of which the last are the most promising [7,120,122-126].

Among the metallic materials studied so far, Cu-Ni-Fe based alloys have received particular attention, due to their ability to produce a protective nickel ferrite (NiFe_2O_4) layer upon Al electrolysis [18,19,23]. However, this protective layer needs time to form at the surface of Cu-Ni-Fe alloys, during which the fluorination reaction can occur, resulting in the premature degradation of the electrode [49]. It is therefore essential to protect the Cu-Ni-Fe anodes from corrosion and prevent the formation of metallic fluorides during the period needed for the protective NiFe_2O_4 layer to form. In this context, using (Co,Ni)O-based protective coatings for Cu-Ni-Fe metal-based anodes appears promising as shown by Nguyen and de Nora [20]. Indeed, the CoO phase is very stable versus the fluorination of metallic anodes in cryolite medium. In addition, it has been found that about 15 wt.% of Ni stabilizes the CoO phase, forming a (Co,Ni)O solid solution and helping in preventing the decomposition of CoO to Co_3O_4 at high temperatures [20,53,60,61]. The formation of Co_3O_4 should be avoided since Co_3O_4 is an n-type semiconductor that displays a significantly higher O_2 evolution overpotential owing to its lower conductivity than p-type semiconductor (Co,Ni)O solid solution [20].

Thermal spraying processes are widely used to produce coatings for corrosion, wear and erosion protection applications. The first benefit expected from thermal spray technology is the possibility of obtaining direct deposits of (Co,Ni)O in contrast to the current two-step method of electrodeposition–thermal oxidation, which was used by Nguyen and de Nora [20]. In fact, the change of densities upon oxidation of the metallic Co-Ni alloy and its possible consequences such as the creation of cracks and delamination would be eliminated. Thermal spray processes would also make it possible to easily vary the composition of the deposit by changing the composition of the spray powders. In addition, they can be used on-site for the restoration of eroded anodes.

Among the different thermal spraying techniques, high-velocity oxy-fuel (HVOF) spraying appeared to be one of the most viable options to prepare a single phase and low-porosity adherent coating. In this process, the fuel gas or liquid and pure oxygen are introduced into the combustion chamber together with the spray powder. The combustion of gases produces a high temperature and pressure in the chamber, which creates a supersonic gas flow through the nozzle exit [44,45]. The powder feedstock melts or partially melts in the flame and deposits on the substrate. High flame velocity, low flame temperature and short dwell time in HVOF process can suppress the

undesired oxidation, decomposition or reduction which have been reported in numerous plasma spraying works [47,79,91,127].

In our previous work [92], (Co,Ni)O coatings have been deposited by HVOF on both Cu-rich and Ni-rich Cu-Ni-Fe alloy substrates and the dry oxidation behavior of the coatings have been investigated at 1000 °C in the presence of oxygen. (Co,Ni)O coatings decreased the oxidation rate of the underlying Cu-Ni-Fe alloy. However, the diffusion of alloying elements from the substrates to the coatings and the formation of new oxide layers in the coatings have been observed after 20 h of heat treatment in air. Accordingly, it would be best to use a bond coat to completely prevent the oxidation as well as the inter-diffusion of alloying elements between the substrate and the (Co,Ni)O protective coating.

The bond coating is widely used to obtain coatings resistant to high-temperature oxidation and corrosion [128-132]. When a coating system consisting of a metallic bond coat and a ceramic top coat is exposed to high temperatures, oxygen molecules penetrate from the top coat and, then, react with the bond coat elements. Subsequently, they form an oxide layer at the interface between the bond coat and top coat. Various types of oxides can be created in this layer depending on the bond coat chemical composition and diffusion kinetics. The formation of this oxide layer can prevent the inward diffusion of oxygen and the outward diffusion of metallic elements [133,134].

In this study, Ni-20Cr and CrMnFeCoNi high-entropy alloy (HEA) were selected as the bond coat materials, which are likely to act as a barrier to diffusion of elements between the substrate and the protective coating. The bond coat powders and the $\text{Co}_{0.5}\text{Ni}_{0.5}\text{O}$ powders are deposited on Cu-Ni-Fe substrates using HVOF process. Their dry oxidation behaviors are evaluated under air atmosphere at 1000 °C.

6.2. Experimental Procedure

A commercially available Ni-20Cr alloy powder (Metco 43VF-NS, Oerlikon Metco) and an equiatomic CrMnFeCoNi HEA powder supplied by Castolin Eutectic were used as starting powders for bond coats. The $\text{Co}_{0.5}\text{Ni}_{0.5}\text{O}$ powder for the top coat was synthesized by mixing Co_3O_4 (purity $\geq 99.7\%$, from Alfa Aesar) and NiO powders (purity $\geq 99\%$, from Cerac) followed by 12 h heat treatment at 1200 °C in air.

The particle size distribution was analyzed by laser diffraction using a Malvern Panalytical Spraytec instrument after dispersing the powder in water using a Malvern wet dispersion accessory. The D10, D50 and D90 values are 6, 25 and 48 μm for CrMnFeCoNi HEA, 7, 18 and 38 μm for Ni-20Cr and 4, 16 and 32 μm for $\text{Co}_{0.5}\text{Ni}_{0.5}\text{O}$, respectively. Fig. 6.1a-c shows the corresponding particle size distribution histograms.

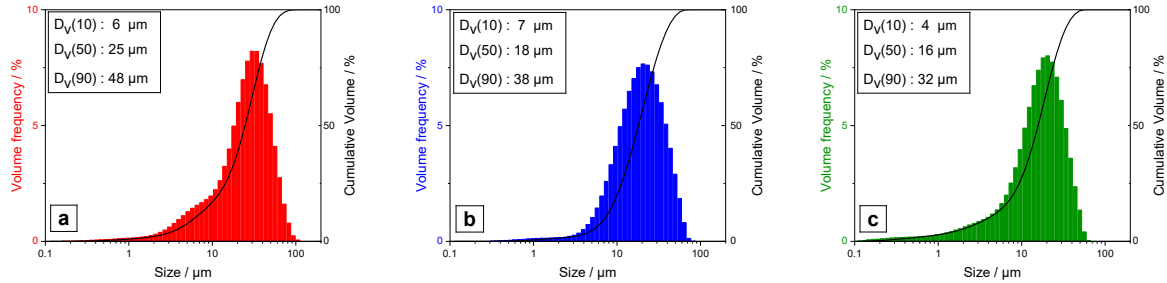


Figure 6.1. Histograms showing the particle size distributions of the precursor powders (a) high entropy alloy, (b) Ni-Cr and (c) $\text{Co}_{0.5}\text{Ni}_{0.5}\text{O}$.

Two compositions of Cu-Ni-Fe alloy, Cu-20Ni-15Fe and Ni-25Fe-10Cu (in wt.%), were used as substrates. Mono-phased Cu-Ni-Fe alloys were produced by the casting method and, then, homogenized by a post-casting heat treatment to avoid the formation of a two-phase structure (a Cu-rich phase and a Fe-Ni-rich phase) during their solidification, which is detrimental for their corrosion resistance in cryolytic medium [49,50]. Cu-20Ni-15Fe (Cu-rich) and Ni-25Fe-10Cu (Ni-rich) substrates were cut into disk shaped coupons with 15 mm diameter and ~ 7 mm thickness. Then, they were grit-blasted and rinsed with acetone prior to their utilization.

Table 6.1. HVOF spray process parameters.

	Oxygen flow (lpm)	Propylene flow (lpm)	Air flow (lpm)	N_2 carrier gas flow (lpm)	Powder feed rate (g/min)	Number of passes	Spray distance (mm)
Bond coat	164	93	413	15	50	2	150
Top coat	217	70	167	15	10	80	180

HVOF coatings were generated using a propylene-fueled Diamond Jet 2700-hybrid gun (Oerlikon Metco, Westbury, NY). All the powders were dried in an oven at 75 °C for at least 24 h prior to deposition. Air jet directed to the substrate surface was used as cooling media during the spraying of bond coats. The HVOF spraying parameters used during the deposition of bond coats and top coats are listed in Table 6.1. Same spray parameters were used for both bond coat powders. The list of samples prepared is displayed in Table 6.2.

Table 6.2. List of the samples prepared by HVOF.

Sample #	Substrate	Coating
S1	Ni-rich	HEA
S2	Cu-rich	HEA
S3	Ni-rich	NiCr
S4	Cu-rich	NiCr
S5	Cu-rich	HEA + Co _{0.5} Ni _{0.5} O
S6	Cu-rich	NiCr + Co _{0.5} Ni _{0.5} O
S7	Ni-rich	HEA + Co _{0.5} Ni _{0.5} O
S8	Ni-rich	NiCr + Co _{0.5} Ni _{0.5} O

The substrate temperature was measured during the HVOF coating process using a FLIR A320 infrared camera. The substrates were preheated to about 150 °C and 200 °C by performing two and five passes of HVOF flame without powder before starting the deposition of bond coat and top coat layers, respectively. The maximum surface temperature during deposition was 210 °C and 280 °C for bond coats and top coats, respectively.

The oxidation experiments were conducted at 1000 °C for 20 h in static air in a muffle furnace. Scanning electron microscopy / energy dispersive X-ray spectroscopy (SEM-EDS) observations of the coatings were done using a Tescan Vega3 scanning electron microscope equipped with a Bruker XFlash® 6 | 10 Detector energy dispersive X-ray spectroscope. X-ray

diffraction (XRD) measurements were conducted by a Bruker D8 diffractometer equipped with Cu K_{α} radiation.

6.3. Results and discussion

6.3.1. As-coated samples

The XRD patterns of samples S1-S8 are presented in Fig. 6.2. For all the coatings, only the diffraction peaks of one phase are observed. Cr-Mn-Fe-Co-Ni and Ni-Cr were detected in the XRD patterns of the samples with only bond coats of HEA and NiCr, respectively. For the samples with both bond coat and $\text{Co}_{0.5}\text{Ni}_{0.5}\text{O}$ top coat, only a single set of peaks is observed that are assigned to a *fcc* (Co,Ni)O solid solution. The HEA and Ni-Cr bond coats are not detected by XRD because they are buried underneath a thick (*ca.* 100 μm thick) (Co,Ni)O top coat layer. These confirm the presence of original feedstock constituents with no additional phases in the deposited coatings.

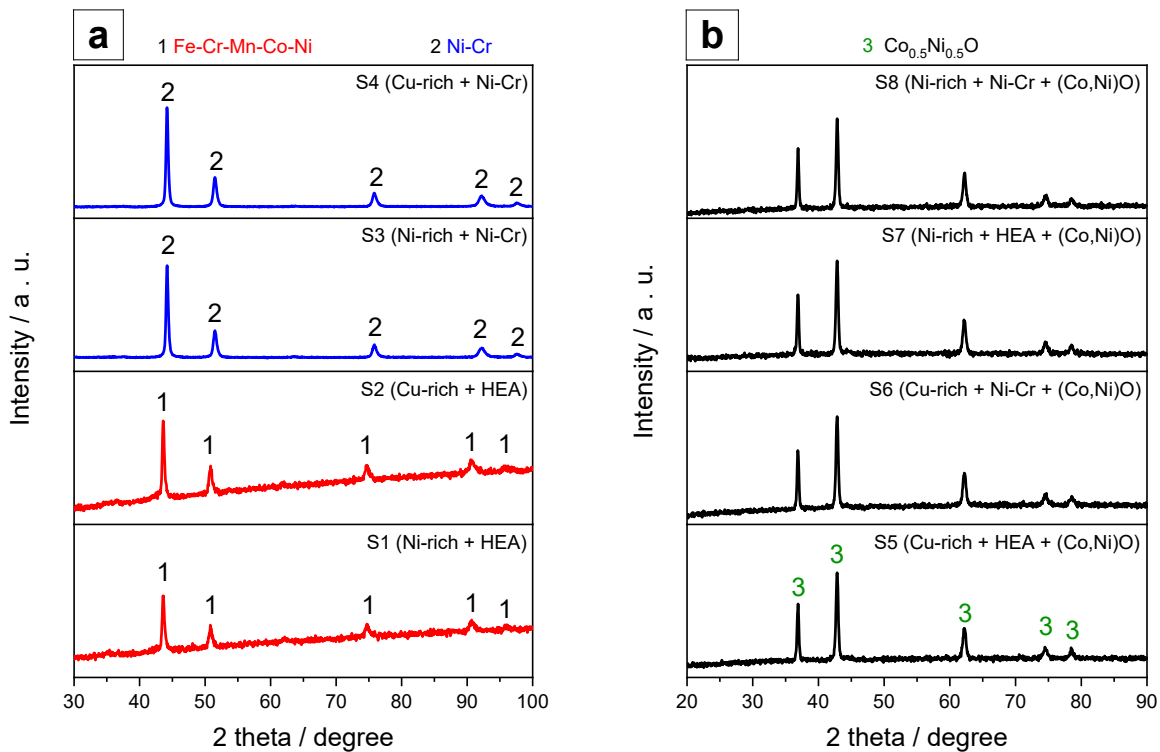


Figure 6.2. XRD results of the coatings prepared by HVOF, (a) samples coated with only a bond coat layer, and (b) samples coated with a bond coat and a top coat layer.

Fig. 6.3 depicts the cross-sectional SEM micrographs of the bond coat layers. The coatings show high density and almost no porosity. The darker areas (shown by arrows in this figure) are regions of high oxygen content showing inter-lamellar oxidation between two passes in both HEA and NiCr bond coats. This can be attributed to the heat input from the flame. Heating of the substrate and already deposited coating layer by the spray flame would increase the oxidation of previously deposited coating during spraying. The XRD diffraction patterns did not reveal any diffraction peaks that could be attributed to oxides, most probably because of their low concentration in the near-surface region.

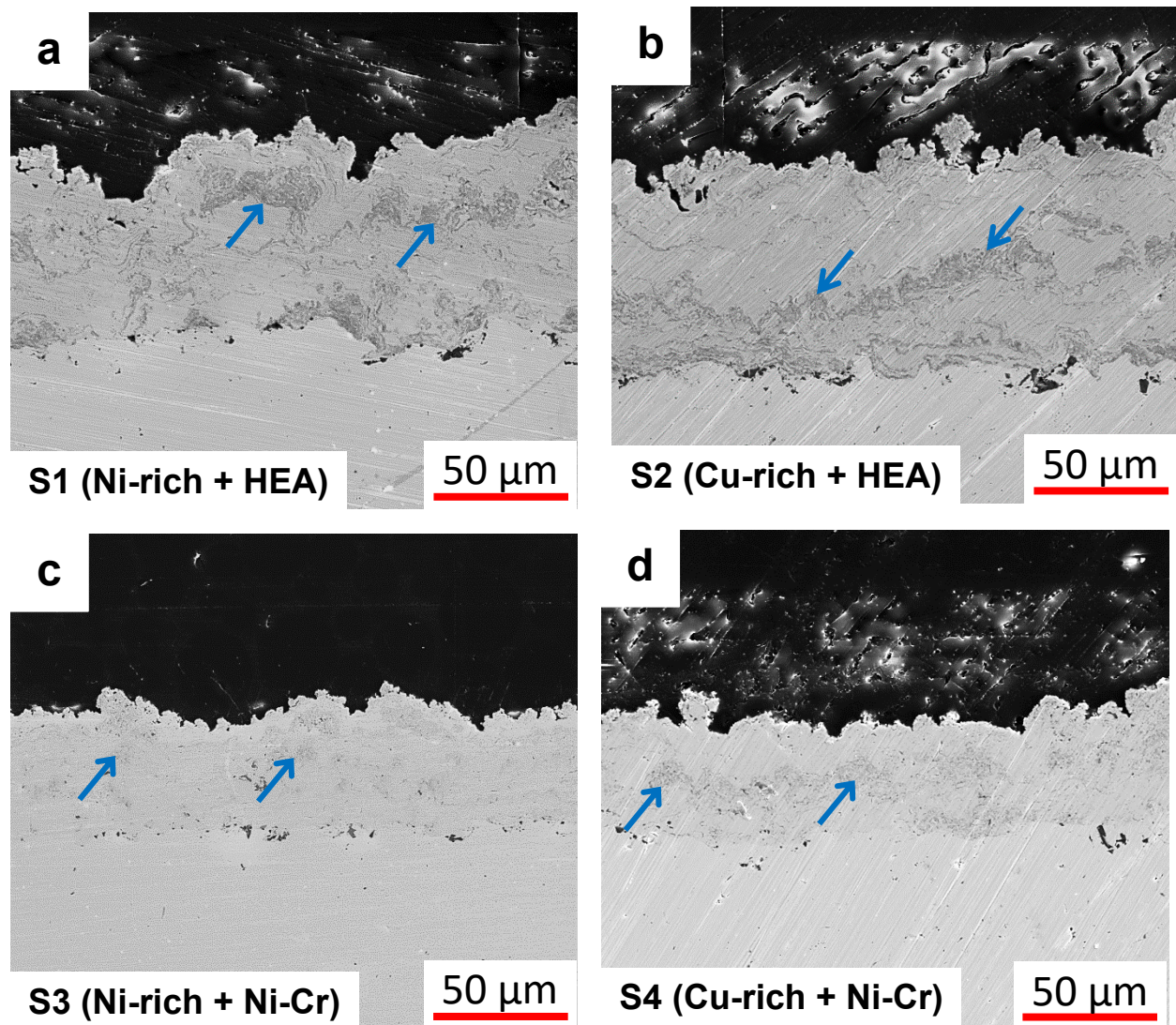


Figure 6.3. Cross-sectional SEM micrographs of the as-sprayed bond coat layers prepared by HVOF, (a) S1, (b) S2, (c) S3 and (d) S4.

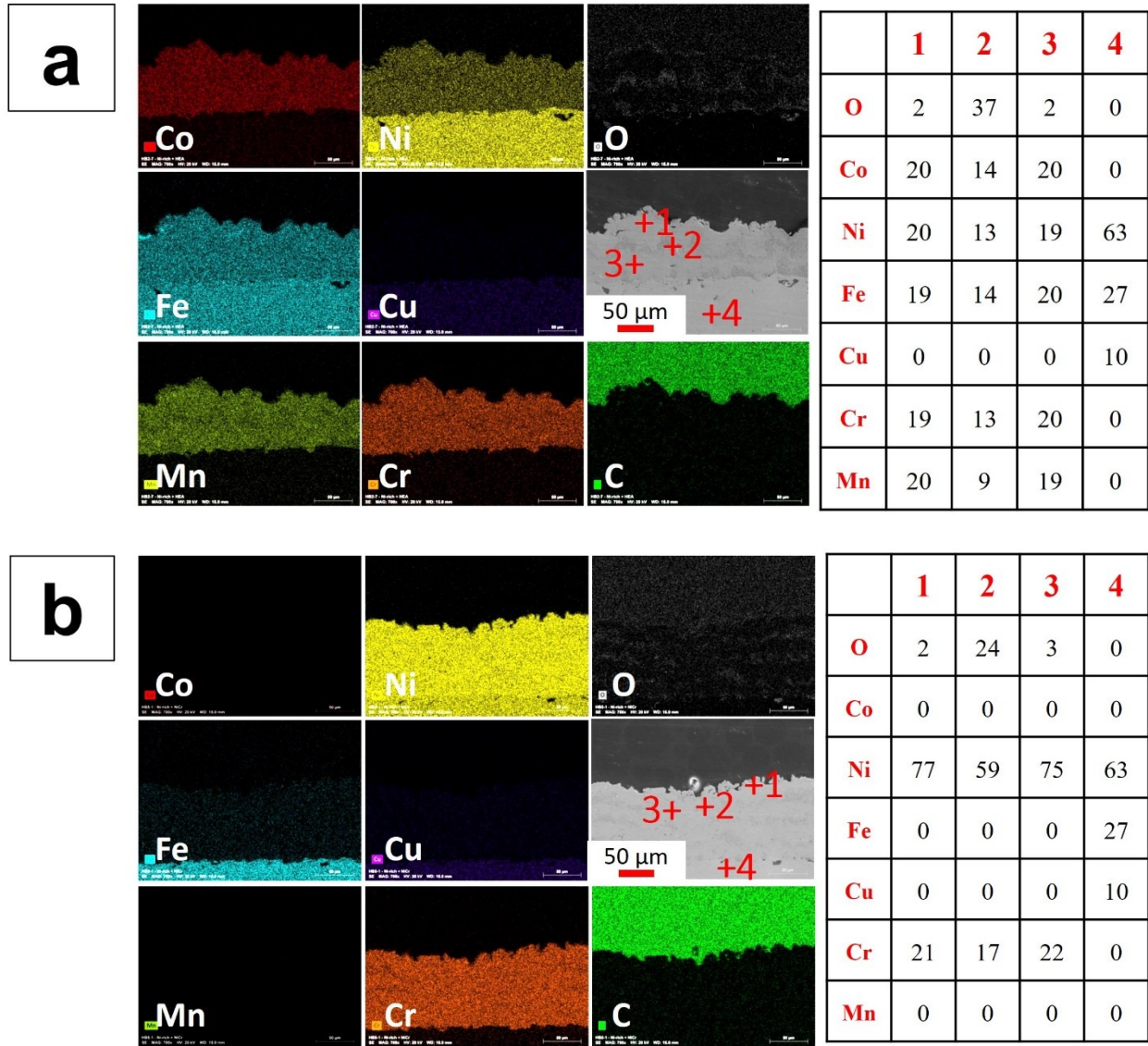


Figure 6.4. EDS analysis results (in at.%) of the as-sprayed bond coats, (a) S1 (Ni-rich + HEA) and (b) S3 (Ni-rich + Ni-Cr).

Fig. 6.4 shows the EDS quantitative (in at.%) and mapping results of the as-sprayed HEA and NiCr coatings on the Ni-rich substrate. The oxygen concentration in the dark grey areas is clearly higher than the background, confirming that these regions with a different texture in the bond coats are oxides. Apart from the presence of oxygen, the results show that the chemical composition of metallic phases is very close to that of their respective feedstock powders, in accordance with the previous XRD data. As shown in Fig. 6.4a, the Co, Ni, Fe, Cr and Mn elements with equal at.% (~20 at.% for each element) are homogeneously distributed in the metallic phase

of HEA coating (Zone 1 and Zone 3), while the O element is enriched in the dark grey oxide phase (Zone 2). EDS results indicate these oxides are composed of a mixture of partially oxide phases. The formation of Fe_2O_3 , CoO , NiO , Cr_2O_3 and Mn_2O_3 has also been reported in the air plasma spray and HVOF coatings of CrMnFeCoNi HEA [135,136]. Similarly, from the EDS results of NiCr coating (Fig. 6.4b), the contents of Ni and Cr elements in the metallic phase (Zone 1 and Zone 3) are around 80 at.% and 20 at.%, respectively, maintaining the same content as the raw powder. It is noted that the dark regions (Zone 2) with higher content of O element are presumed to be oxides. Literature [137,138] has reported the presence of NiO , NiCr_2O_4 and Cr_2O_3 as the oxide phase present when spraying NiCr powders. In the present work, EDS results show that the oxide phase present in the NiCr deposited layer contains high content of Ni. The same analysis was conducted for HEA and NiCr coatings deposited on Cu-rich substrates (not shown here) and the results are similar. Therefore, the above given discussion is representative of other two samples.

Fig. 6.5 presents the cross-sectional SEM images of the as-sprayed samples comprised bond coats and top coats. All $\text{Co}_{0.5}\text{Ni}_{0.5}\text{O}$ top coats are uniform, continuous and free of cracks with low porosity. The average thickness of HEA, NiCr and $\text{Co}_{0.5}\text{Ni}_{0.5}\text{O}$ deposited layers is about 70, 50 and 100 μm , respectively. The roughness of a coating surface is an important factor in corrosion protection applications, as lower surface roughness leads to a lower surface area exposed to a corrosive solution, which can result in lower susceptibility to corrosion [139]. As can be observed from Fig. 6.5, the surface of all $\text{Co}_{0.5}\text{Ni}_{0.5}\text{O}$ top coatings is smooth, even on HEA or NiCr bond coats that have rough surfaces and whose thickness varies in different areas. In any case, the coating roughness is a property linked mainly to the powder particle size. As a rule, a lower size of the feedstock powder will involve a decrease of the superficial coating roughness. Thus, the lowest roughness of the $\text{Co}_{0.5}\text{Ni}_{0.5}\text{O}$ coatings can be explained on the basis that $\text{Co}_{0.5}\text{Ni}_{0.5}\text{O}$ powder used in this study had the finest particle size.

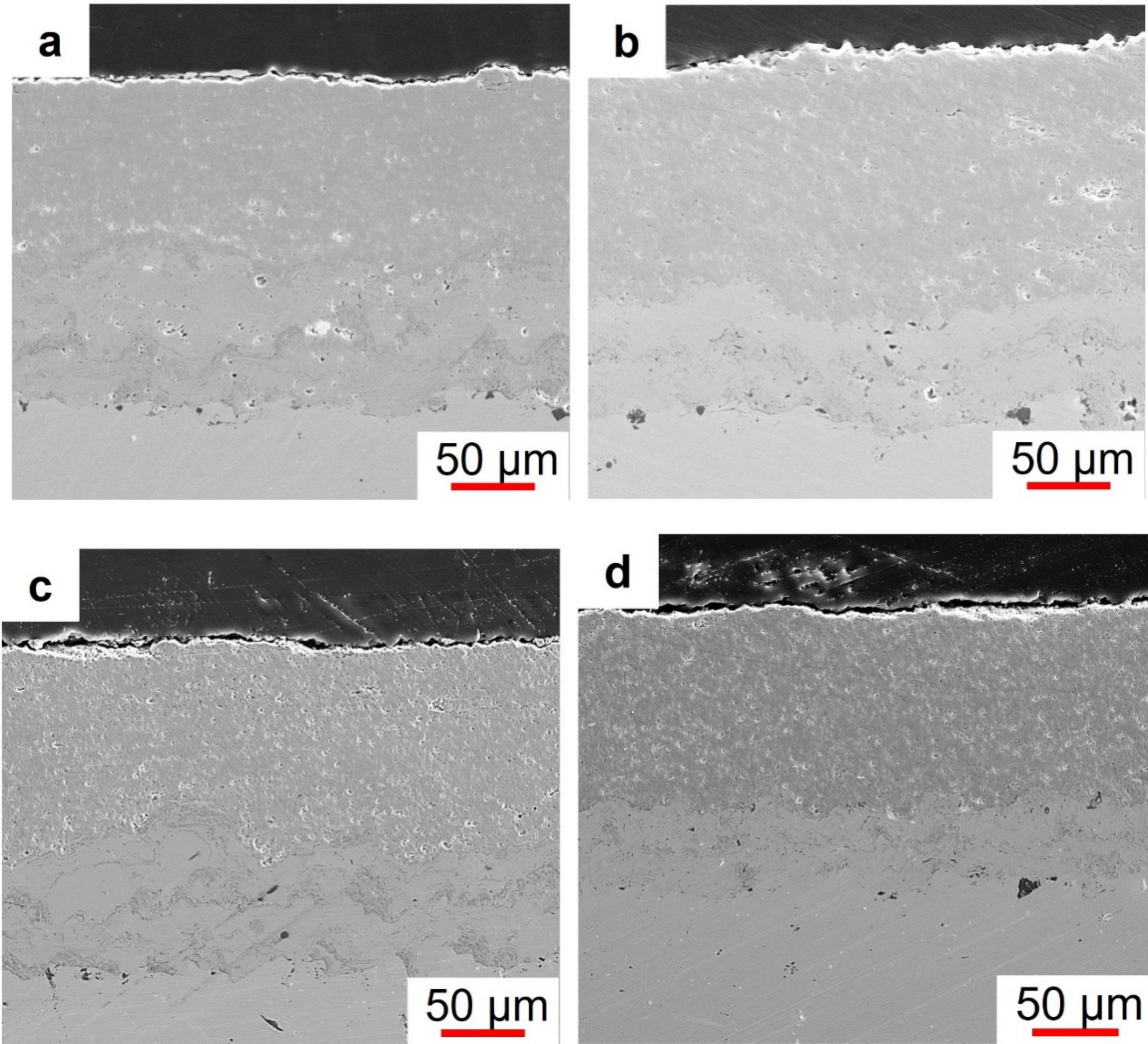


Figure 6.5. Cross-sectional SEM micrographs of the as-sprayed bond-coat + top-coat layers prepared by HVOF, (a) S5 (Cu-rich + HEA + (Co,Ni)O), (b) S6 (Cu-rich + Ni-Cr + (Co,Ni)O), (c) S7 (Ni-rich + HEA + (Co,Ni)O), and (d) S8 (Ni-rich + Ni-Cr + (Co,Ni)O).

EDS analysis results of as-coated samples S6 and S7 comprised NiCr and HEA bond coats and $\text{Co}_{0.5}\text{Ni}_{0.5}\text{O}$ top coat layers are shown in Fig. 6.6. It can be seen that the elementary composition of different areas of HEA and NiCr bond coats was not altered after spraying the $\text{Co}_{0.5}\text{Ni}_{0.5}\text{O}$ top coat. In addition, the composition of $\text{Co}_{0.5}\text{Ni}_{0.5}\text{O}$ top coats is the same as that of the starting material, in agreement with the XRD results. The same analysis was performed for the samples S5 and S8 (not shown here), the results of which are similar. Thus, the obtained results could be representative of other two samples.

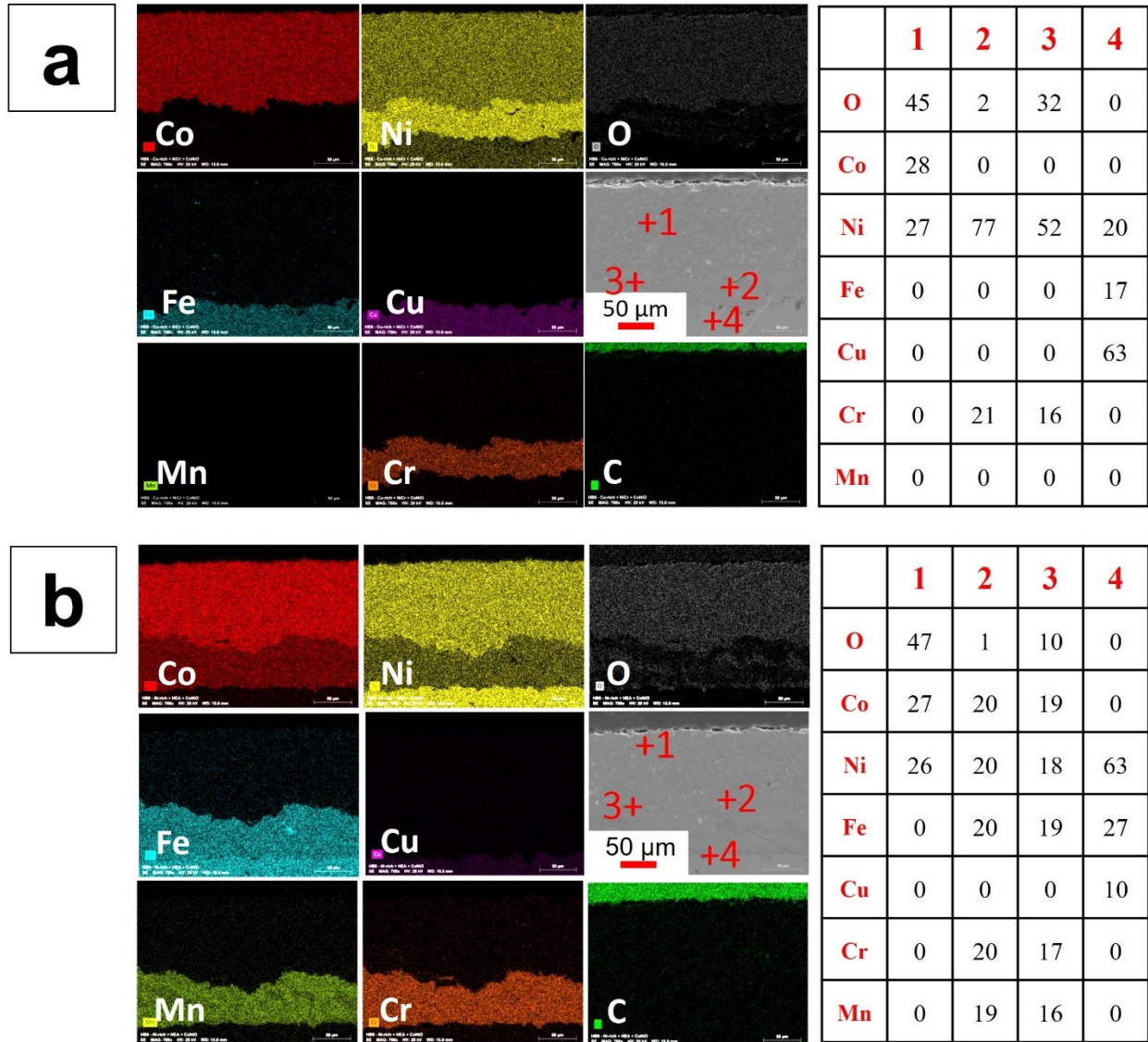


Figure 6.6. EDS analysis results (in at.%) of the as-sprayed bond coat and (Co,Ni)O layers, (a) S6 (Cu-rich + Ni-Cr + (Co,Ni)O) and (b) S7 (Ni-rich + HEA + (Co,Ni)O).

6.3.2. High-temperature oxidation behavior

Fig. 6.7 illustrates the XRD patterns of samples S1-S8 after 20 h heat treatment at 1000 °C in air. It is noteworthy that all Cu-oxide peaks are detected from uncoated edges of Cu-rich substrate. These oxides grow on the bare Cu-rich substrate surfaces. Based on our previous studies [92], it is known that CuO and Cu₂O oxide scales are formed on uncoated Cu-rich substrate after the same heat treatment in air. Besides, as will be shown later by SEM/EDS analysis, no Cu-oxide

phases are formed in the deposited coatings. Accordingly, the Cu-oxide phases in the XRD patterns are detected from the edges of the samples with Cu-rich substrate.

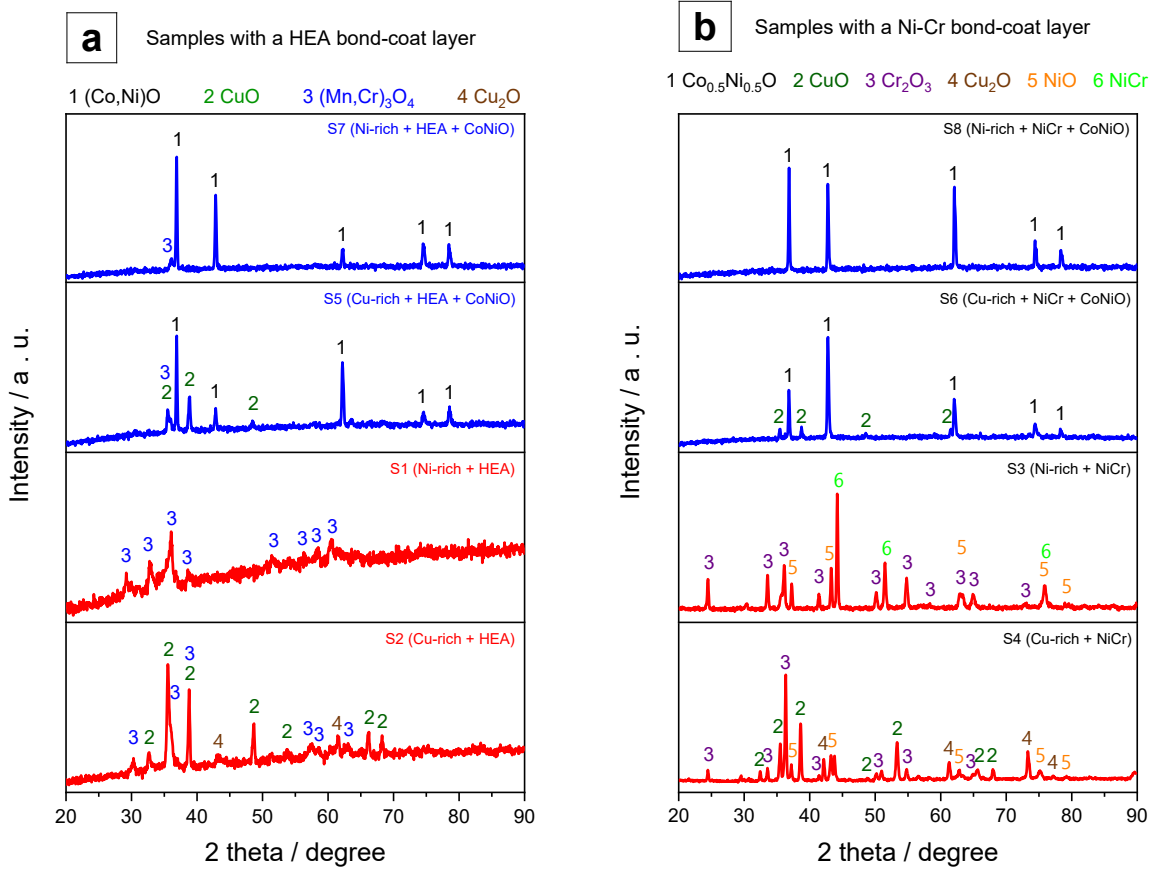


Figure 6.7. XRD patterns of the HVOF coatings with (a) a HEA bond coat layer and (b) a Ni-Cr bond coat layer, after a 20 h heat treatment at 1000 °C in static air atmosphere.

From the XRD results in Fig. 6.7, the main oxide layer growing in the HEA coatings (Sample S1 and S2) is (Mn,Cr)₃O₄. According to the Mn-O and Cr-O phase diagrams, Mn₃O₄ could be stable from 877 to 1160 °C [140]. Besides, Cr₂O₃ is the only stable crystalline phase in the Cr-O system. The standard Gibbs free energy of formation, ΔG°_f (in kJ.mol⁻¹) of Mn₃O₄ (-949) and Cr₂O₃ (-793) is much lower than that of Fe₃O₄ (-702), Fe₂O₃ (-487), FeO (-188), CoO (-142) and NiO (-123) at 1300 K [110], while the value of (Mn,Cr)₃O₄ has not been reported in the literature. However, the ternary (Mn,Cr)₃O₄ oxide is possibly a solid solution between Cr₂O₃ and MnO/Mn₃O₄. Therefore, the formation of (Mn,Cr)₃O₄ is thermodynamically favorable because of its lower dissociation partial pressure of oxygen [141]. The HEA's *fcc* phase is not detected due to

the formation of a thick oxide scale on the surface of these coatings. In contrast, *fcc* NiCr phase along with Cr₂O₃ and NiO phases is detected in the heat-treated sample S3, suggesting that the oxide layer grown on this coating is thin. Chromium exhibits higher affinity for oxygen as compared to nickel and forms more stable oxides. Thus, predominant external layer of Cr₂O₃ is expected to develop on the NiCr coatings in this study. The same peaks of Cr₂O₃ and NiO are observed in the XRD result of sample S4.

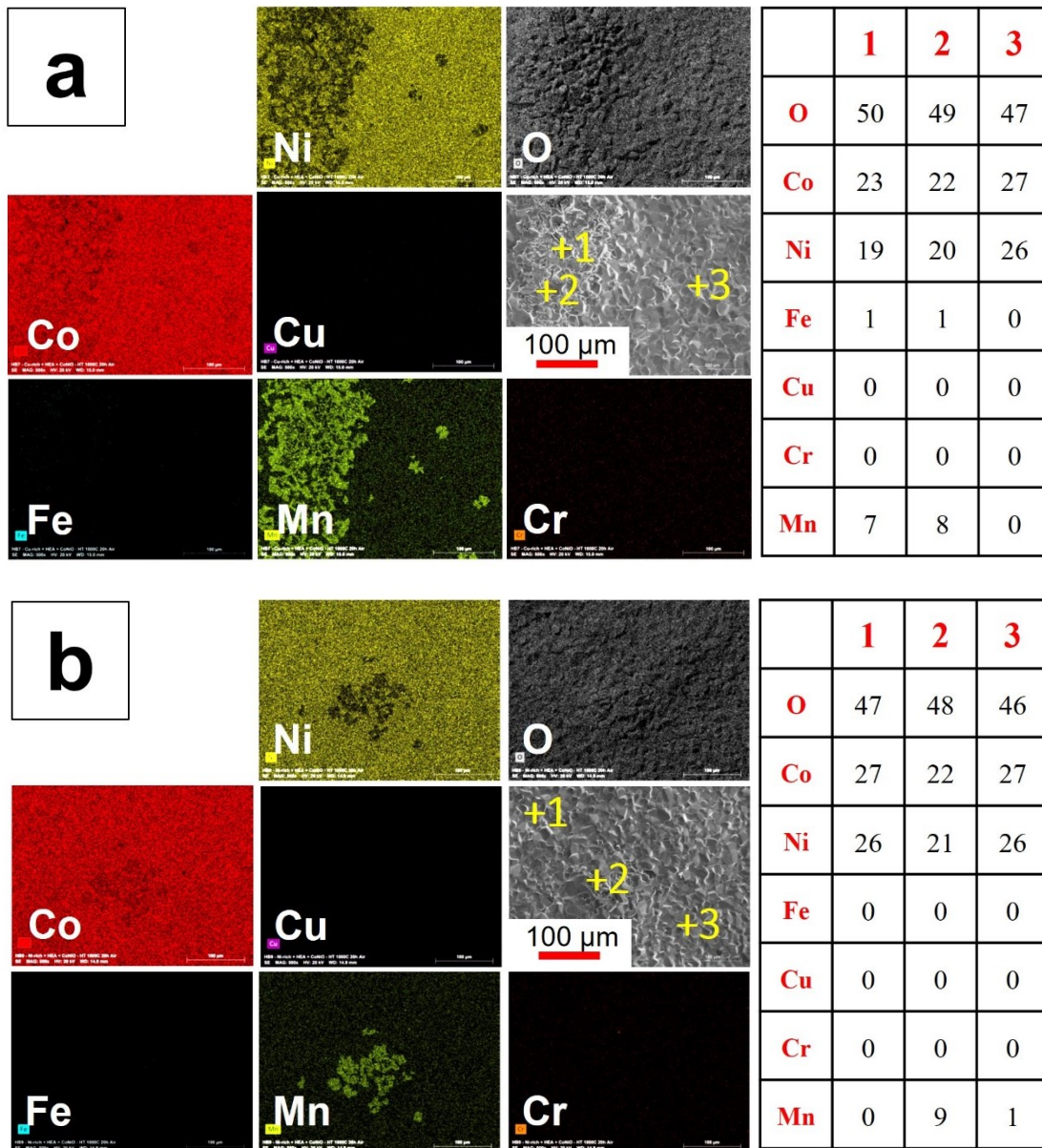


Figure 6.8. Top-view EDS analysis results (in at.%) of (a) Cu-rich substrate and (b) Ni-rich substrate, coated with HEA + (Co,Ni)O layers (samples S5 and S7) after a 20 h heat treatment at 1000 °C in air.

The XRD patterns of samples S5-S8 (see Fig. 6.7) indicate the peaks are mainly responsible for (Co,Ni)O solid solution phase in top coats. The small XRD peak of Mn-rich in samples S5 and S7 is linked to diffusion of Mn from HEA bond coat to the top coat, which will be discussed in more details later, and then formation of Mn-rich oxide phase during heat treatment in air. Fig. 6.8 shows a top view EDS analysis of oxidized [HEA + (Co,Ni)O] coatings sprayed on Cu-rich and Ni-rich substrates. Such EDS analysis along with XRD confirms the presence of Mn-rich oxide in some parts of the surface.

Fig. 6.9 depicts cross-sectional SEM micrographs of HVOF coated samples including HEA bond coat, with and without (Co,Ni)O top coat heat treated in air at 1000 °C during 20 h. For comparison, cross-sectional SEM micrographs of substrates coated with only a HVOF deposited (Co,Ni)O layer after the same heat treatment are shown as well. Figs. 6.9a and d have lower magnification than Figs. 6.9b, c, e and f. The samples without bond coat exhibit varied behaviors based on the composition of the substrate. The (Co,Ni)O layer deposited on a Ni-rich substrate (Fig. 6.9a) demonstrates a 25- μm -thick oxide layer that grows beneath the (Co,Ni)O layer. This oxide layer is attached to the (Co,Ni)O coating while it has been delaminated from the Ni-rich substrate. On Cu-rich substrate (Fig. 6.9d), this oxide layer is thicker ($\sim 400 \mu\text{m}$) and has been delaminated from substrate. From SEM images, it is apparent that the oxidation resistance of coated samples is increased by applying the bond coat as no evident oxidation can be observed underneath the bond coat layers.

The heat-treated HEA coatings (Figs. 6.9b and e) are composed of two layers with $\sim 50 \mu\text{m}$ of thickness each: An irregular oxide scale (L1) formed on the deposited layer of coating (L2). Large-area cracks occurred in some parts of the L1 oxide layer. The variation in thermal expansion coefficients (CTEs) of different oxides creates relatively high thermal stresses in the oxide layer during cooling of the sample, which can lead to the formation of cracks. Likewise, the HEA bond coat layer of heat-treated sample S5 is delaminated from the substrate (Fig. 6.9f). The delamination has been occurred during cooling process after heat treatment since no trace of oxidation is found beneath the bond coat layer. The average thickness of the heat-treated HEA and (Co,Ni)O deposited layers in samples S5 and S7 were measured to be approximately 90 and 120 μm , respectively.

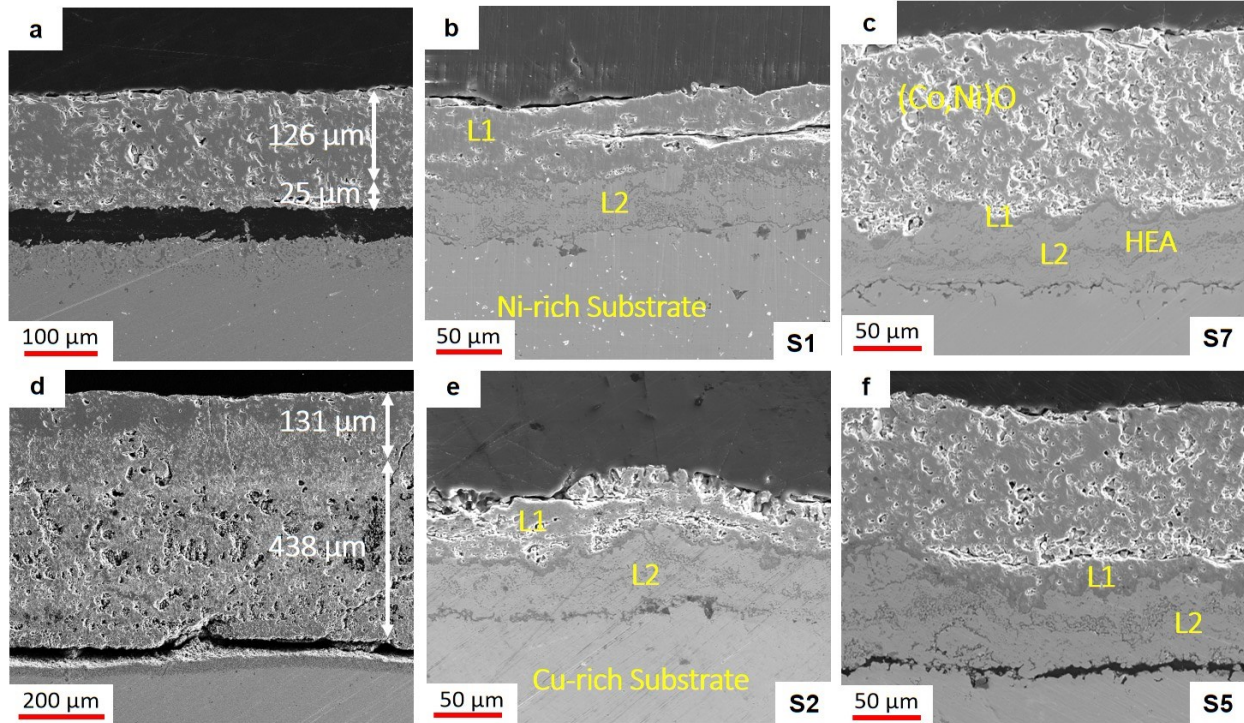


Figure 6.9. Cross sectional SEM micrographs of Ni-rich coated with (a) only a (Co,Ni)O layer, (b) only a HEA layer, (c) both HEA and (Co,Ni)O layers, as well as Cu-rich coated with (d) only a (Co,Ni)O layer, (e) only a HEA layer, (f) both HEA and (Co,Ni)O layers, after a 20 h heat treatment at 1000 °C in air.

Detailed EDS analysis of the oxidized HEA coated layer deposited on Ni-rich substrate (Fig. 6.10a) reveals that the L1 oxide scale is enriched in Mn, O and Cr, while Ni, Co and Fe are barely detected. This oxide scale can be divided into two layers, including a manganese-rich outer layer and a thinner chromium-rich inner layer right above the HEA matrix/oxide scale interface. The distribution of elements is related to the oxygen affinities of Mn and Cr along with the outward diffusion rates of their cations in the oxide scale [142,143]. The diffusion rate of manganese through the first-formed scale is almost two orders of magnitude faster than that of chromium [144], which leads to the formation of Mn-rich oxide in the outer layer of the oxide scale. Based on these results and the XRD patterns, $(\text{Mn,Cr})_3\text{O}_4$ and Cr_2O_3 are likely present in the outer and inner layers, respectively. It is important to note that the thin Cr-oxide layer could not be detected by XRD because of the large thickness of the outer Mn-rich oxide layer. Due to the large outward dispersion of the Mn and Cr, the HEA matrix is correspondingly partially depleted in these elements. The alloying elements Fe, Ni and Co are enriched underneath the oxide scale.

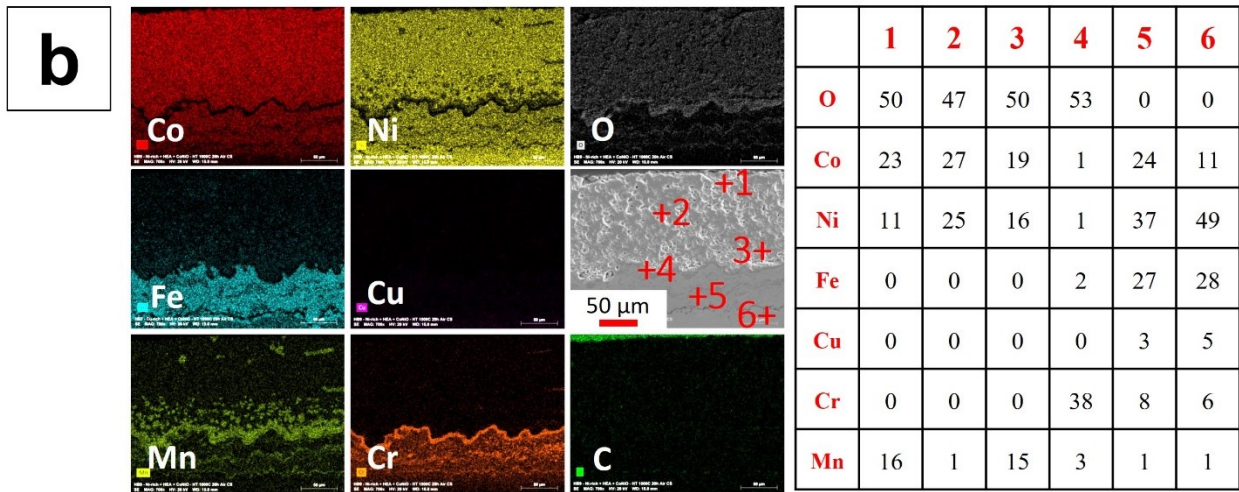
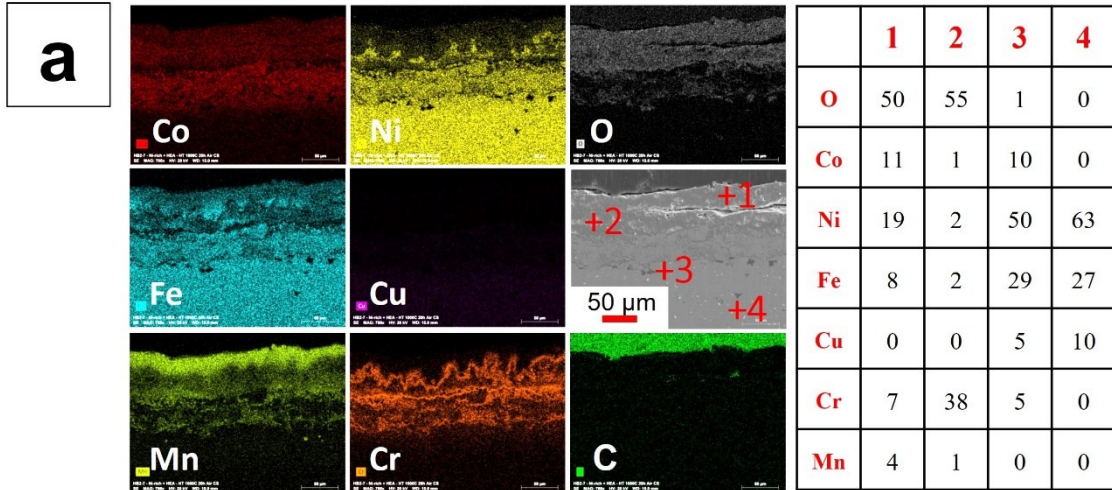


Figure 6.10. EDS analysis results (in at.%) of Ni-rich substrates coated with (a) only a HEA bond coat layer (sample S1) and (b) HEA + (Co,Ni)O layers (sample S7), after a 20 h heat treatment at 1000 °C in air.

When comparing the distribution of elements in the heat-treated HEA coated sample on Ni-rich substrate (Fig. 6.10a), it can be noticed that there is no diffusion of oxygen into the substrate material, so one can say that the dense Cr-rich oxide beneath the Mn-rich layer can effectively hinder the diffusion of O atoms, thereby protecting the substrate from further oxidation. Evidently, diffusion of copper from the substrate to the coating, as well as diffusion of cobalt and chromium from the coating to the substrate, have occurred across the bond coat/substrate interface. As can be observed from Fig. 6.10b, there is no diffusion of cobalt and chromium from HEA bond coat into the (Co,Ni)O top coat. However, the Mn elemental map showed that manganese diffused outward from bond coat toward the top coat layer and the extent of diffusion decreased as the

distance from the bond coat/top coat interface increased. The present HEA has a typically sluggish diffusion behavior and the diffusion coefficient sequence of foreign cations in the Cr_2O_3 sublattices is: $D_{\text{Mn}^{2+}} > D_{\text{Fe}^{2+}} > D_{\text{Ni}^{2+}} > D_{\text{Cr}^{3+}}$ [145]. Thus, it can be expected that outward diffusion rate of Mn ions is much faster than that of other cations, thereby forming Mn-rich ternary oxide scale on the Cr_2O_3 layer, as well as further diffusion of Mn into the (Co,Ni)O top coat layer.

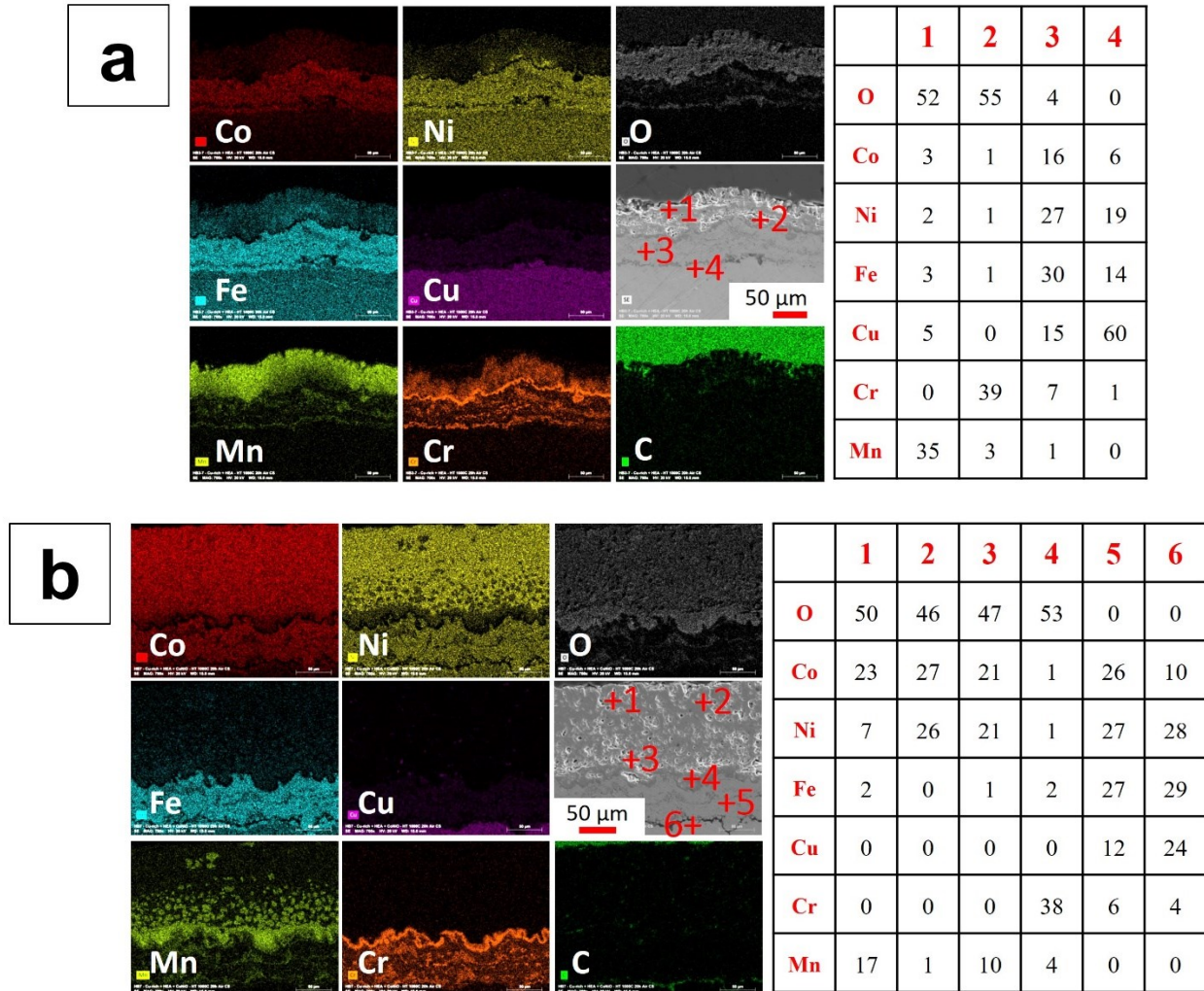


Figure 6.11. EDS analysis results (in at.%) of Cu-rich substrates coated with (a) only a HEA bond coat layer (sample S2) and (b) HEA + (Co,Ni)O layers (sample S5), after a 20 h heat treatment at 1000 °C in air.

The same analysis was conducted for Cu-rich substrate coated with HEA bond coat and (Co,Ni)O top coat layers and the results are presented in Fig. 6.11. These samples exhibit the same structure as the coated Ni-rich substrate samples, which means there is no significant influence

from the substrate. Similar to those observed in the coated Ni-rich substrate samples (see Fig. 6.10), also in this case the formation of oxide scale containing the outermost Mn-rich oxide layer and the inner Cr_2O_3 layer on top of the HEA bond coat, as well as the gradient diffusion of Mn atoms from bond coat into the $(\text{Co,Ni})\text{O}$ top coat are present. Moreover, the same diffusion of Co and Cr atoms from bond coat into the $(\text{Co,Ni})\text{O}$ top coat are present. However, the same diffusion of Co and Cr atoms from the HEA bond coat to the substrate and the diffusion of Cu from substrate to the bond coat has taken place near the interface. However, the amount of diffused copper increases in the coated Cu-rich substrate. The reason for this is that, in the Cu-Ni-Fe system, the alloy composition and, thus, copper concentration play a very important role in the diffusion and mobility of Cu, Fe and Ni atoms. Copper is the most mobile component in Cu-rich alloys and its diffusion rate is a hundred-time higher than nickel or iron. Nevertheless, the diffusion rate of copper is decreased considerably in Cu-poor alloy [92,120].

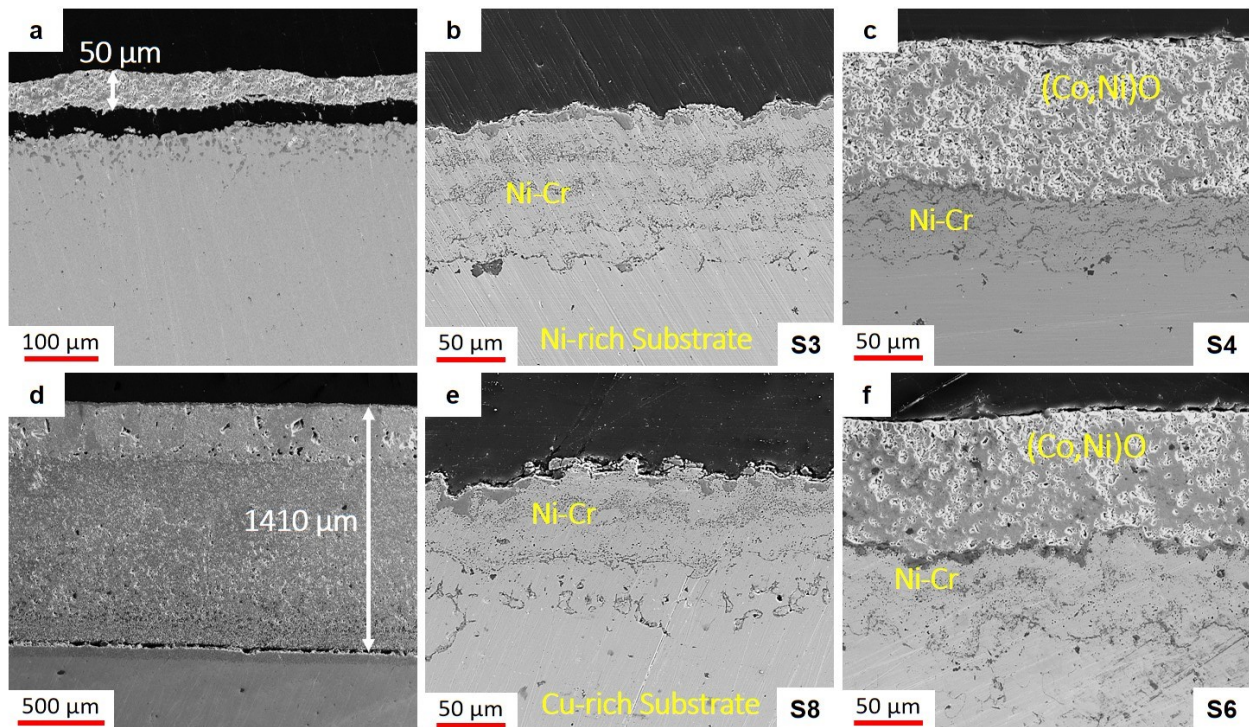


Figure 6.12. Cross sectional SEM micrographs of (a) bare Ni-rich, (b) Ni-rich coated with only Ni-Cr, (c) Ni-rich coated with Ni-Cr and $(\text{Co,Ni})\text{O}$, (d) bare Cu-rich, (e) Cu-rich coated with only Ni-Cr, (f) Cu-rich coated with Ni-Cr and $(\text{Co,Ni})\text{O}$, after a 20 h heat treatment at 1000 °C in static air atmosphere.

Fig. 6.12 illustrates cross-sectional SEM images of HVOF coated samples comprised NiCr bond coat, with and without $(\text{Co,Ni})\text{O}$ top coat heat treated in air at 1000 °C during 20 h. For

comparison, cross-sectional SEM images of bare Ni-rich and Cu-rich substrates following the same heat treatment process are shown as well. Note that Figs. 6.12a and d have lower magnification than Figs. 6.12b, c, e and f. A thick oxide layer ($\sim 1400\ \mu\text{m}$) is formed on uncoated Cu-rich substrate (Fig. 6.12d), while the oxide layer formed on uncoated Ni-rich substrate is much thinner ($\sim 50\ \mu\text{m}$) (Fig. 6.12a), in which due to the formation of a NiFe_2O_4 layer, further oxidation of the underlying Ni-rich substrate has been significantly decelerated [92]. In contrast, all the coated samples exhibit neither delamination from the substrate, nor oxide scale initiation at the bond coat/substrate interface after oxidation test. This confirms the excellent oxidation resistance of NiCr bond coats on both Ni-rich and Cu-rich substrates. The average thickness of heat-treated NiCr and (Co,Ni)O deposited layers in samples S6 and S8 were determined to be around 60 and 110 μm , respectively.

EDS analysis of the heat-treated NiCr bond coat layer deposited on Ni-rich substrate (Fig. 6.13a) demonstrates the chromium enrichment at the surface of the coating. The oxygen mapping also shows an enrichment at this region, indicating that the chromium-rich oxide layer with the thickness of 5–10 μm is formed at the surface of the NiCr coating. Combining with the XRD results in Fig. 6.7, the oxidized product is Cr_2O_3 . It is worth recalling that chromium has stronger affinity for oxygen than nickel and develops more stable oxide layer. This is in line with existing literature [130,133], suggesting that the formation of Cr_2O_3 is favored in the oxidation of NiCr coating. In the NiCr bond coat, the elemental mapping for Cu and Fe displayed a slightly amount of outward diffusion from the substrate to the coating. Correspondingly, the Cr elemental map exhibited that the Cr present in the bond coat diffused to the substrate adjacent to the coating. However, no diffusion of oxygen content was noticed into the substrate material. Furthermore, the EDS results of the heat-treated [NiCr + (Co,Ni)O] coating layers deposited on Ni-rich substrate (Fig. 6.13b) confirms that no diffusion of atoms has taken place into the (Co,Ni)O top coat during oxidation process. As can be seen, the chemical composition corresponding to the oxidized (Co,Ni)O top coat layer is very similar to that of as-sprayed (Co,Ni)O coating. This is in agreement with the corresponding XRD data (Fig. 6.7) that show the presence of only a single phase (Co,Ni)O solid solution in the heat-treated top coats deposited on NiCr bond coats. Indeed, the continuous thin layer of Cr-rich oxide on the bond coat can work as a barrier to inhibit the diffusion of atoms into the top coat, in addition to protecting the substrate from further oxidation.

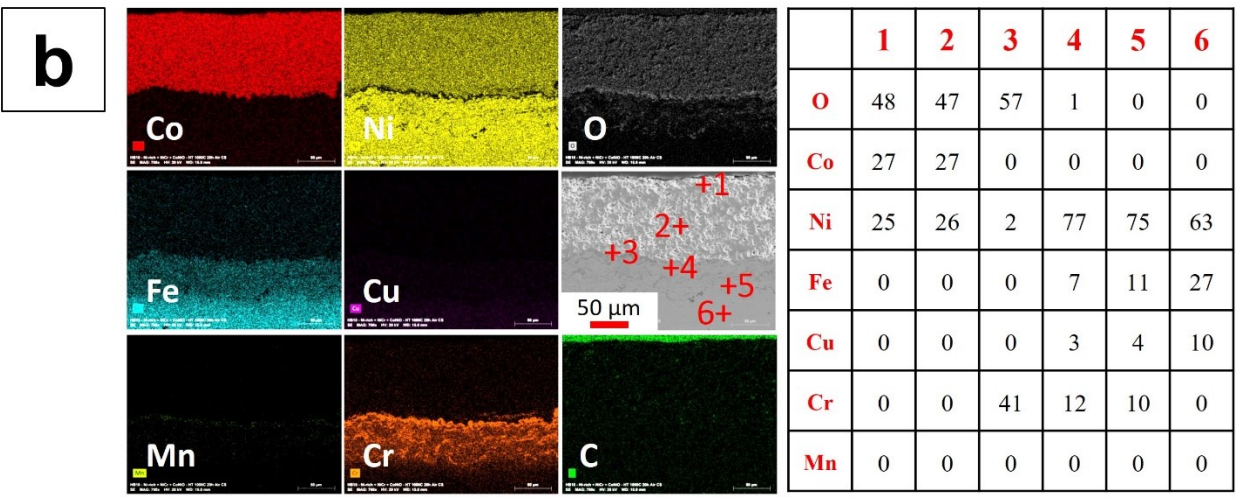
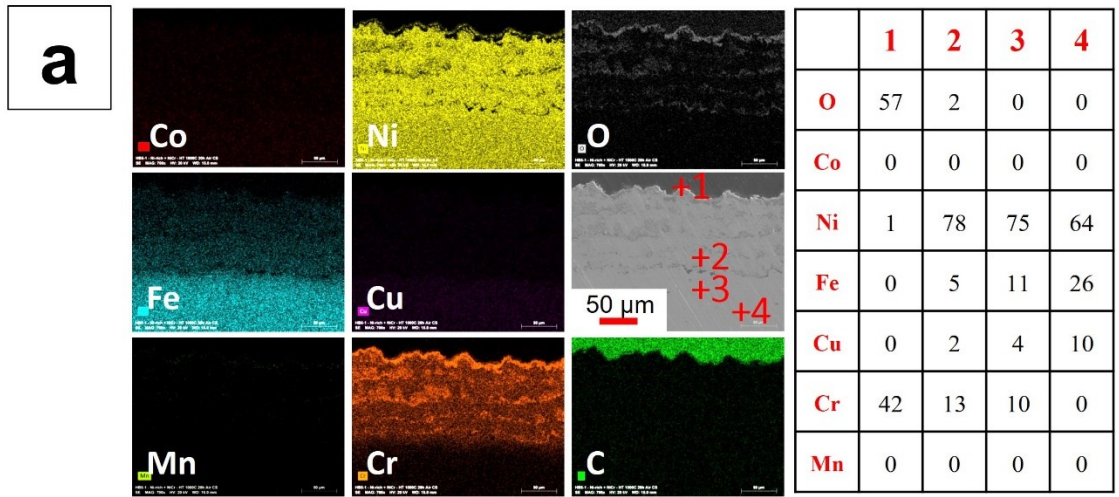


Figure 6.13. EDS analysis results (in at.%) of Ni-rich substrates coated with (a) only a Ni-Cr bond coat layer (sample S3) and (b) Ni-Cr + (Co,Ni)O layers (sample S8) after a 20 h heat treatment at 1000 °C in air.

The EDS results in Fig. 6.14 indicate that the behavior of heat-treated Cu-rich substrate coated with [NiCr + (Co,Ni)O] layers is totally comparable to the one of coated Ni-rich samples. Resembling those observed in the coated Ni-rich substrates, due to the formation of protective Cr-rich oxide layer on the NiCr bond coat, diffusion of elements into the (Co,Ni)O top coat and also oxidation of substrate surface are prevented following heat treatment of coated Cu-rich samples. Additionally, the same diffusion of copper and iron elements is observed from the Cu-rich substrate to the NiCr bond coat. Nonetheless, the diffusion extent of Cu and Fe atoms in the coated Cu-rich sample is obviously higher than that in the coated Ni-rich sample. In general, Cu is the

fastest component in the CuNiFe alloys, while Ni is the most sluggish element. The diffusivities of each element also increase with the Cu concentration.

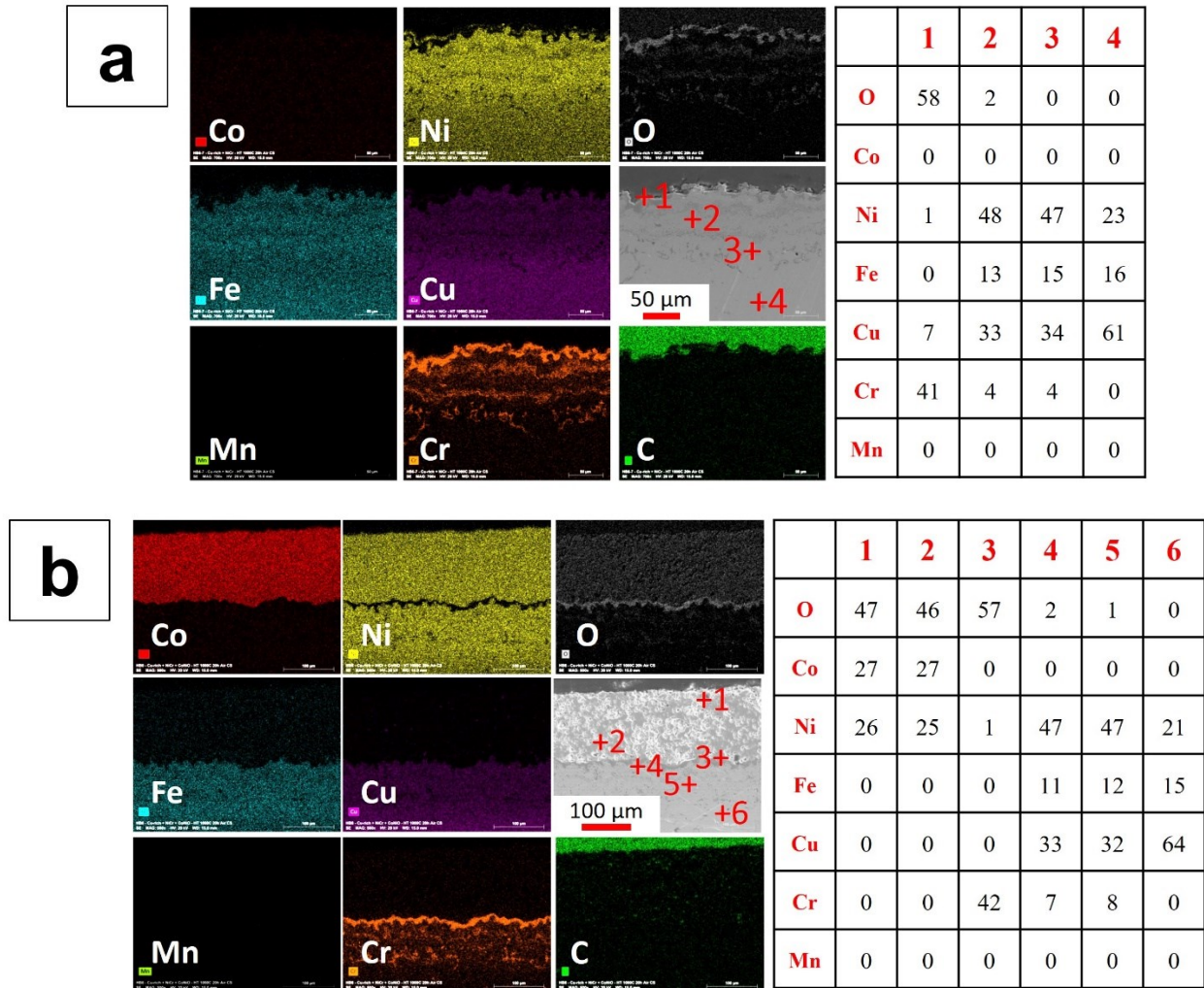


Figure 6.14. EDS analysis results (in at.%) of Cu-rich substrates coated with (a) only a Ni-Cr bond coat layer (sample S4) and (b) Ni-Cr + (Co,Ni)O layers (sample S6), after a 20 h heat treatment at 1000 °C in air.

6.4. Conclusion

In this article, CrMnFeCoNi HEA and Ni-20Cr as the bond coats and $\text{Co}_{0.5}\text{Ni}_{0.5}\text{O}$ as the top coat were deposited by HVOF on both Cu-rich and Ni-rich CuNiFe alloy substrates. These samples were subjected to oxidation experiments at 1000 °C in the presence of oxygen. The bond coat composition was found to exhibit a remarkable influence on the oxidation-resistance performance of the coatings. The most promising results were achieved with the [NiCr +

(Co,Ni)O] coating, in which no diffusion of alloying elements into each layer was observed after 20 h of heat treatment in air. A continuous thin layer of Cr_2O_3 is formed at the surface of the bond coats which protects the samples from further oxidation, in addition to preventing the diffusion of Cu or Fe elements (diffused from substrate to the bond coat during oxidation process) into the (Co,Ni)O top coat layer. In the case of [HEA + (Co,Ni)O] coating, a double oxide layer composed of an outer Mn-rich oxide followed by an inner Cr_2O_3 layer is developed at the bond coat/top coat interface. Moreover, the undesired diffusion of Mn atoms takes place from HEA bond coat into the top coat layer. The results indicated that, the composition of the CuNiFe substrate has no significant effect on the oxidation behavior of the coatings. These coated samples will be investigated as inert anodes in aluminum production and their anodic behavior in severe electrolysis conditions will be presented in the near future.

Chapter 7

Conclusions and suggestions for future

7.1. Summary and conclusions

The main objective of this work was to develop a surface treatment for Cu-Ni-Fe inert anodes to slow down the attack of the molten electrolyte and allow the formation of nickel ferrite (NiFe_2O_4) surface scale to occur. This protective layer should thus have good adhesion, low solubility in the electrolyte, low affinity for fluorides, low porosity and good electrical conductivity. $(\text{Co,Ni})\text{O}$ seems to be the most promising material. Therefore, selected $(\text{Co,Ni})\text{O}$ compositions were deposited on Cu-Ni-Fe alloys by suspension plasma spray (SPS) and high velocity oxy-fuel (HVOF) techniques. The thermal spray variables were optimized to achieve dense, thick and single phase coatings.

In a first step, $\text{Co}_x\text{Ni}_{1-x}\text{O}$ coatings were deposited by SPS using $(\text{Co,Ni})\text{O}$ solid solution powders or mixture of CoO and NiO powders as feedstock materials. The influences of spraying parameters including plasma power, spray distance and substrate temperature on the coating composition were investigated. Substrate temperature is identified as the most important parameter affecting coating composition. In some of the coatings deposited by SPS, undesired reduction of NiO to metallic nickel was observed. Uniform, adherent and non-porous $\text{Co}_x\text{Ni}_{1-x}\text{O}$ coatings made of a single solid solution phase were obtained when the substrate temperature was above $950\text{ }^\circ\text{C}$.

A further step was then taken to identify the sources of the formation of metallic Ni phase within the $(\text{Co,Ni})\text{O}$ coated samples by SPS. It was suggested that, the reduction of NiO_{1-x} by CoO_{1-x} splats formed in the first few passes of spraying leads to the formation of metallic nickel at the region close to the substrate. In-flight particles and splats were collected to study the melting and mixing behavior of CoO and NiO during spraying. Plasma power input was found to play a major role in determining the shape and number of the generated splats. An increase in plasma power resulted in a splat morphology change from disk-like to flower-like; as well as the formation of unmelted particles and drastically decrease of the number of splats, which were responsible for

decreasing the coating thickness. Furthermore, the effect of heat treatment on the coating's microstructure was investigated at 1000 °C under argon to study the possibility of obtaining a single-phase coating. A well-homogenized coating can be achieved by heat treatment under argon flow, leading to completely dissolved metallic Ni into (Co,Ni)O solid solution phase.

Since deposition of a single phase (Co,Ni)O coating was challenging with SPS, (Co,Ni)O coatings were prepared by HVOF process. In HVOF, powder particles are sprayed with a relatively lower temperature and higher velocity compared to plasma spray. Using HVOF process, the shorter residence time of the powder in the flame and also lower flame temperature as compared to plasma spray methods, leads to decrease the possibility of reduction, oxidation or decomposition of powder particles during spraying. Thus, (Co,Ni)O coatings were deposited by HVOF method on both Ni-rich and Cu-rich Cu-Ni-Fe alloy substrates using CoO, Co_{0.75}Ni_{0.25}O and Co_{0.5}Ni_{0.5}O powders as feedstock materials. Using optimized deposition conditions, all coatings were single phase and have a dense and smooth morphology. The oxidation behavior of these samples was studied at 1000 °C in the presence of oxygen to assess the effect of the coatings on the diffusion of Cu and O atoms. Comparison with their high temperature behavior in inert atmosphere was also performed. After 20 h of heat treatment in air, HVOF coatings on Cu-rich substrates are sandwiched between a top CuO and a bottom oxide layer. However, increasing the nickel content of the (Co,Ni)O coating from 0 to 0.5 decreases the Cu and O diffusivity, which results in thinner CuO and bottom oxide scales. In the case of Ni-rich CuNiFe alloy, Cu diffusion to react with O and form CuO and Cu₂O is less of an issue because the diffusion of Cu atoms in Ni-rich CuNiFe alloys is considerably slowed down. In that case, a nickel ferrite scale is formed between the HVOF coating and the substrate. As expected, the thickness of the NiFe₂O₄ layer decreases slightly (~ 15 %) as the Ni content of the (Co,Ni)O coating is increased from 0 to 0.5.

In the last step, bond coats were used in order to completely prevent the oxidation as well as the inter-diffusion of alloying elements between substrate and (Co,Ni)O protective coating. Accordingly, the effect of CrMnFeCoNi high entropy alloy (HEA) and Ni-20Cr bond coat layers on the high temperature behavior of (Co,Ni)O coated samples by HVOF was studied at 1000 °C in air. No inter-diffusion of elements between the NiCr bond coat and (Co,Ni)O top coat layers was observed after 20 h of heat treatment in air. In the case of HEA + (Co,Ni)O coatings, Mn atoms diffuse from bond coat into the top coat layer. A continuous thin layer of Cr-rich oxide is formed at the surface of both NiCr and HEA bond coats which protects the samples from further

oxidation, in addition to preventing the diffusion of Cu or Fe elements (diffused from substrate to the bond coat during oxidation process) into the (Co,Ni)O top coat layer. A thicker Mn-rich oxide scale is also formed on top of the Cr-rich oxide layer in the samples coated with HEA. It was found that, the composition of the CuNiFe substrate does not have any significant effect on the oxidation behavior of the coatings.

7.2. Contributions

The main contributions of this research can be summarized as follows.

- A detailed study was conducted to optimize the coating parameters used in suspension plasma spray and HVOF methods to produce a dense, single phase, coherent and crack-free (Co,Ni)O coating as required for industrial aluminum production.
- Suspension plasma spray was used for the first time to manufacture inert anodes for Al electrolysis by deposition of sub-micron particles.
- The developed SPS (Co,Ni)O coatings showed that metallic nickel phase can be formed in the coatings. It was determined that substrate temperature is the most critical parameter affecting the SPS coating composition. Spraying on the substrate with high temperature (above 950 °C) can result in uniform, adherent and non-porous (Co,Ni)O coatings made of a single solid solution phase.
- Unlike SPS coatings in which the undesired reduction of NiO to Ni was observed, all HVOF coatings were single phase and had a very dense and smooth morphology.
- The high-temperature oxidation studies of the HVOF (Co,Ni)O coatings showed the diffusion of alloying elements from the substrates to the coatings as well as the formation of new oxide layers in the coatings. Applying HEA and NiCr bond coats completely avoided the dry oxidation of Cu-Ni-Fe substrates. Moreover, no interdiffusion was taken place between (Co,Ni)O top-coat and NiCr bond-coat.
- The electrolysis results at 1000 °C revealed that HVOF (Co,Ni)O layer increases the corrosion resistance of Cu-Ni-Fe anode and it is effective in providing required time for the formation of nickel ferrite layer as well as in preventing Cu-Ni-Fe anode from fluorination.

7.3. Future work

The effect of (Co,Ni)O and [Ni-Cr + (Co,Ni)O] HVOF coatings on the degradation resistance of Cu-Ni-Fe anodes (Cu-rich and Ni-rich alloys) upon Al electrolysis at 1000 °C was evaluated and the results are presented in Appendix C. Although the coated anodes have been examined in short time electrolysis, the obtained results are encouraging. However, these results must be validated with prolonged electrolysis tests (e.g., 100 h) at pilot scales to confirm the potential of these anodes for industrial usage. Large area Cu-Ni-Fe anodes can be coated with a layer of (Co,Ni)O using HVOF technique and then used as anodes under electrolysis conditions closer to the current conditions of industrial primary aluminum production.

Another approach to improve the corrosion resistance of the anodes, and in particular to decrease the contamination of electrolyte, would be to deposit a layer of nickel ferrite (NiFe₂O₄) using thermal spray methods. A single layer of nickel ferrite or a double layer coating composed of nickel ferrite and (Co,Ni)O can be deposited on Cu-Ni-Fe anodes and the anodic behavior of coated anodes must be studied to confirm the utility of this approach for application in industrial aluminum production.

References

- [1] O.A. Lorentsen, Behavior of nickel, iron and copper by application of inert anodes in aluminum production. PhD Thesis, Norwegian University of Science and Technology, 2000.
- [2] Website: http://wps.prenhall.com/wps/media/objects/602/616516/Chapter_18.html
- [3] Aluminum Association of Canada, Sustainable development report, 2020.
- [4] Ministry of the Environment, and the Fight against Climate Change, Quebec inventory of greenhouse gas emissions in 2018 and their evolution since 1990.
- [5] Environment Canada. Evaluation of Feasibility and Roadmap for Implementing Aluminum Production Technologies that Reduce/Eliminate Greenhouse Gas and Other Emissions, 2002.
- [6] The Aluminum Association, Inert anode roadmap: A framework for technology development, Washington, 1998.
- [7] D.R. Sadoway, Inert anodes for the Hall–Héroult cell: the ultimate materials challenge, *JOM – J. Miner. Met. Mater.* 53 (2001) 34–35.
- [8] J.N. Hryn, D.R. Sadoway, Cell testing of metal anodes for aluminum electrolysis, *Light Met.* (1993) 475.
- [9] J.N. Hryn, M.J. Pellin, E.S. Division, M. Society, S. Diego, Dynamic inert metal anode, *Light Met.* (1999) 377.
- [10] Z. Shi, J. Xu, Z. Qiu, An Iron-Nickel metal anode for aluminum electrolysis, *Light Met. TMS (The Miner. Met. Mater. Soc.)* (2004) 1–5.
- [11] V.M.D. D.A. Simakov, E.V. Antipov, M.I. Borzenko, S.Y. Vassiliev, Y.A. Velikodny, Nickel and nickel alloys electrochemistry in cryolite-alumina melts, *Light Met. TMS (The Miner. Met. Mater. Soc.)* (2007) 489–493.
- [12] R.P. Pawlek, Inert anodes: an update. *Light Metals* (2014) 1309.
- [13] I. Galasiu, R. Galasiu, J. Thonstad, *Inert Anodes for Aluminium Electrolysis*. Aluminium-Verlag, Dusseldorf, 2007.
- [14] J. K. Walker, J. Kinkoph, C. K. Saha, The development of cerium oxide coatings from cryolite melts. A self-forming anode for aluminum electrowinning, *Journal of applied electrochemistry* 19 (1989) 225–230.

- [15] X.X. Ma, Y.D. He, D.R. Wang, Inert anode composed of Ni–Cr alloy substrate, intermediate oxide film and α -Al₂O₃/Au (Au–Pt, Au–Pd, Au–Rh) surface composite coating for aluminium electrolysis, *Corr. Sci.* 53 (2011) 1009–1017.
- [16] D.H. DeYoung. Solubilities of oxides for inert anodes in cryolite-based melts. *Light Met.* (1986) 299.
- [17] S. Helle, M. Pedron, B. Assouli, B. Davis, D. Guay, L. Roué, Structure and high-temperature oxidation behavior of Cu–Ni–Fe based alloys prepared by high-energy ball milling for application as inert anodes for aluminum electrolysis, *Corr. Sci.* 52 (2010) 3348–3355.
- [18] G. Goupil, S. Jucken, D. Poirier, J.G. Legoux, E. Irissou, B. Davis, D. Guay, L. Roué, Cold sprayed Cu–Ni–Fe anode for Al production, *Corr. Sci.* 90 (2015) 259–265.
- [19] S. Jucken, M.H. Martin, E. Irissou, B. Davis, D. Guay, L. Roué, Cold-sprayed Cu–Ni–Fe anodes for CO₂-free aluminum production, *J. Therm. Spray Technol.* 29 (2020) 670–683.
- [20] T. Nguyen, V. De Nora, oxygen evolving inert metallic anode. *Light Met.* (2006) 385–390.
- [21] Report of the American Society of Mechanical Engineers. Technical working group on inert anode technologies. ASME International, 1999.
- [22] S. Helle, B. Brodu, B. Davis, D. Guay, and L. Roué, Influence of the iron content in Cu–Ni based inert anodes on their corrosion resistance for aluminium electrolysis, *Corr. Sci.*, 53 (2011) 3248–3253.
- [23] E. Gavrilova, G. Goupil, B. Davis, D. Guay, and L. Roué, On the key role of Cu on the oxidation behavior of Cu–Ni–Fe based anodes for Al electrolysis, *Corr. Sci.*, 101 (2015) 105–113.
- [24] E. Gavrilova, G. Goupil, B. Davis, D. Guay, and L. Roué, Influence of partial substitution of Cu by various elements in Cu–Ni–Fe alloys on their high-temperature oxidation behavior, *Light Met.*, M. Hyland, Ed., Springer, Cham (2015) 1187–1191.
- [25] G. Goupil, S. Helle, B. Davis, D. Guay, and L. Roué, Anodic behavior of mechanically alloyed Cu–Ni–Fe and Cu–Ni–Fe–O electrodes for aluminum electrolysis in low-temperature KF–AlF₃ electrolyte, *Electrochim. Acta*, 112 (2013) 176–182.
- [26] S. Helle, M. Tresse, B. Davis, D. Guay, and L. Roué, Mechanically alloyed Cu–Ni–Fe–O based materials as oxygen-evolving anodes for aluminum electrolysis, *J. Electrochem. Soc.* 159 (2012) E62–E68.
- [27] K.P. Gupta, S.B. Rajendraprasad, A.K. Jena, The copper-iron-nickel system, *J. Alloy Phase Diag.* 3 (1987) 116–127.

- [28] T.R. Beck, C.M. MacRae, N.C. Wilson, Metal anode performance in low-temperature electrolytes for aluminum production, *Metall. Mater. Trans. B*, 42 (2011) 807–813.
- [29] I. Gallino, S. Curiotto, M. Baricco, M.E. Kassner, R. Busch. Homogenization of highly alloyed Cu-Ni-Fe: a phase diagram study. *JPEDAV* 29 (2008) 131–135.
- [30] Y. He, K. Zhou, Y. Zhang, H. Xiong, L. Zhang, Recent progress of inert anodes for carbon-free aluminium electrolysis: a review and outlook. *J. Mater. Chem. A* 9 (2021) 25272.
- [31] J.R. Davis, *Handbook of Thermal Spray Technology*, ASM International, 2004.
- [32] P. Fauchais, Understanding plasma spraying, *J. Phys. D* 37 (2004) 1–17.
- [33] <https://www.asminternational.org/web/tss/technical/white-paper> (June 2022)
- [34] X. Zhao, Y. Ding, L. Ma, X. Shen, S. Xu, Structure, morphology and electrocatalytic characteristics of nickel powders treated by mechanical milling, *Inter. J. Hydrogen Energy*, 33 (2008) 6351-6356.
- [35] F. Tarasi, M. Medraj, A. Dolatabadi, J. Oberste-Berghaus, C. Moreau, Amorphous and crystalline phase formation during suspension plasma spraying of the alumina–zirconia composite. *J. Euro. Ceram. Soc.* 31 (2011) 2903–2913.
- [36] P. Fauchais, A. Joulia, S. Goutier, C. Chazelas, M. Vardelle, A. Vardelle, S. Rossignol, Suspension and solution plasma spraying. *J. Phys. D: Appl. Phys.* 46 (2013) 224015.
- [37] A. Ganvir, R. Calinas, N. Markocsan, N. Curry, S. Joshi, Experimental visualization of microstructure evolution during suspension plasma spraying of thermal barrier coatings, *J. Eur. Ceram. Soc.* 39 (2019) 470–481.
- [38] P. Fauchais, R. Etchart-Salas, V. Rat, J.-F. Coudert, N. Caron, K. Wittmann-Ténèze, Parameters controlling liquid plasma spraying: Solutions, sols, or suspensions, *J. Therm. Spray Technol.* 17 (2008) 31–59.
- [39] M. Jadidi, M. Mousavi, S. Moghtadernejad and A. Dolatabadi, A three-dimensional analysis of the suspension plasma spray impinging on a flat substrate, *J. Therm. Spray Technol.* 24 (2015) 11–23.
- [40] K. Vanevery, M.J.M. Krane, R.W. Trice, H. Wang, W. Porter, Column formation in suspension plasma-sprayed coatings and resultant thermal properties, *J. Therm. Spray Technol.* 20 (2011) 817–828.
- [41] A. Ganvir, Design of suspension plasma sprayed thermal barrier coatings, Doctoral dissertation, University West, 2018.

- [42] F. Tarasi, M. Medraj, A. Dolatabadi, J. Oberste-Berghaus, C. Moreau, Enhancement of amorphous phase formation in alumina–YSZ coatings deposited by suspension plasma spray process, *Surf. Coatings Technol.* 220 (2013) 191–198.
- [43] F.L.Toma, A. Potthoff, M. Barbosa, Microstructural Characteristics and Performances of Cr₂O₃ and Cr₂O₃-15%TiO₂ S-HVOF Coatings Obtained from Water-Based Suspensions, *J. Therm. Spray Technol.* 27 (2018) 344–357.
- [44] L. Pawlowski, *The science and engineering of thermal spray coatings*, John Wiley & Sons 2008.
- [45] M. Oksa, E. Turunen, T. Suhonen, T. Varis, S.-P. Hannula, Optimization and characterization of high velocity oxy-fuel sprayed coatings: techniques, materials, and applications, *Coatings*, 1 (2011) 17-52.
- [46] M. Salmanzadeh, M. Jalali Azizpour, and H. Mohammadi Majd, Evaluation of the Effect of Spray Distance on Fracture Toughness of Thermally Sprayed Coatings. *J. Appl. Sci.*,15 (2015) p. 709–714.
- [47] P. L. Fauchais, J. V. R. Heberlein, M. I. Boulos, *Thermal Spray Fundamentals*. Springer Science, New York, 2014.
- [48] <https://users.encs.concordia.ca/~dolat/tsmf/static/facilities/> (August 2022)
- [49] S. Jucken, B. Tougas, B. Davis, D. Guay, L. Roué, Study of Cu-Ni-Fe alloys as inert anodes for Al production in low-temperature KF-AlF₃ electrolyte, *Metall. Mater. Trans. B Process Metall. Mater. Process. Sci.* 50 (2019) 3103–3111.
- [50] S. Jucken, E. Schaal, B. Tougas, B. Davis, D. Guay, L. Roué, Impact of a post-casting homogenization treatment on the high-temperature oxidation resistance of a Cu-Ni-Fe alloy, *Corros. Sci.* 147 (2019) 321–329.
- [51] <https://www.malvernpanalytical.com/en/products/product-range/spraytec/accessories/wet-dispersion-accessory> (August 2022)
- [52] G.N. Eby, *Principles of environmental geochemistry*, (2004).
- [53] S. Mohammadkhani, E. Schaal, A. Dolatabadi, C. Moreau, B. Davis, D. Guay, L. Roué, Synthesis and thermal stability of (Co,Ni)O solid solutions, *J. Am. Ceram. Soc.* 102 (2019) 5063–5070.
- [54] <https://www.thermofisher.com/blog/materials/what-is-sem-scanning-electron-microscopy-explained/> (August 2022)
- [55] https://en.wikipedia.org/wiki/Energy-dispersive_X-ray_spectroscopy (August 2022)

- [56] D. Paraskevas, K. Kellens, A. Van de Voorde, W. Dewulf, J.R. Duflou, Environmental impact analysis of primary aluminium production at country level, *Procedia CIRP* 40 (2016) 209–213.
- [57] M. Gautam, B. Pandey, M. Agrawal, Carbon footprint of aluminum production, *Environ. Carbon Footprints*, Elsevier, 2018, pp. 197–228.
- [58] E. Gavrilova, G. Goupil, B. Davis, D. Guay, L. Roué, On the key role of Cu on the oxidation behavior of Cu–Ni–Fe based anodes for Al electrolysis, *Corros. Sci.* 101 (2015) 105–113.
- [59] M. Chen, B. Hallstedt, L.J. Gauckler, Thermodynamic assessment of the Co–O system, *J. Phase Equilibria* 24 (2003) 212–227.
- [60] S. Kuboon, Y.H. Hu, Study of NiO–CoO and Co_3O_4 – Ni_3O_4 solid solutions in multiphase Ni–Co–O systems, *Ind. Eng. Chem. Res.* 50 (2011) 2015–2020.
- [61] R.J. Moore, J. White, Equilibrium relationships in the system NiO–CoO– O_2 , *J. Mater. Sci.* 9 (1974) 1393–1400.
- [62] F. Gitzhofer, E. Bouyer, M.I. Boulos, Suspension Plasma Spray (SPS), US5609921A, (1994).
- [63] M. Aghasibeig, M. Mousavi, F. Ben Ettouill, C. Moreau, R. Wuthrich, A. Dolatabadi, Electrocatalytically active nickel-based electrode coatings formed by atmospheric and suspension plasma spraying, *J. Therm. Spray Technol.* 23 (2014) 220–226.
- [64] P. Fauchais, G. Montavon, R.S. Lima, B.R. Marple, Engineering a new class of thermal spray nano-based microstructures from agglomerated nanostructured particles, suspensions and solutions: an invited review, *J. Phys. D. Appl. Phys.* 44 (2011) 093001.
- [65] M. Aghasibeig, A. Dolatabadi, R. Wuthrich, C. Moreau, Three-dimensional electrode coatings for hydrogen production manufactured by combined atmospheric and suspension plasma spray, *Surf. Coat. Technol.* 291 (2016) 348–355.
- [66] F. Wu, Y. Huang, L. Song, X. Liu, Y. Xiao, J. Feng, J. Chen, Method for Preparing Porous Hydroxyapatite Coatings by Suspension Plasma Spraying, US8877283B2, (2009).
- [67] S. Mahade, N. Curry, S. Björklund, N. Markocsan, P. Nylén, R. Vaßen, Functional performance of $\text{Gd}_2\text{Zr}_2\text{O}_7/\text{YSZ}$ multi-layered thermal barrier coatings deposited by suspension plasma spray, *Surf. Coat. Technol.* 318 (2017) 208–216.
- [68] M. Aghasibeig, C. Moreau, A. Dolatabadi, R. Wuthrich, Fabrication of nickel electrode coatings by combination of atmospheric and suspension plasma spray processes, *Surf. Coat. Technol.* 285 (2016) 68–76.

- [69] E. Alebrahim, F. Tarasi, M.S. Rahaman, A. Dolatabadi, C. Moreau, Fabrication of titanium dioxide filtration membrane using suspension plasma spray process, *Surf. Coat. Technol.* 378 (2019) 124927.
- [70] N. Sharifi, M. Pugh, C. Moreau, A. Dolatabadi, Developing hydrophobic and superhydrophobic TiO₂ coatings by plasma spraying, *Surf. Coat. Technol.* 289 (2016) 29–36.
- [71] M. Aghasibeig, F. Tarasi, R.S. Lima, A. Dolatabadi, C. Moreau, A review on suspension thermal spray patented technology evolution, *J. Therm. Spray Technol.* 28 (2019) 1579–1605.
- [72] T. Roisnel, J. Rodríguez-Carvajal, WinPLOTR: a windows tool for powder diffraction pattern analysis, *Mater. Sci. Forum* 378–381 (2001) 118–123.
- [73] M. Kowalski, P.J. Spencer, Thermodynamic re-evaluation of the C-O, Fe-O and Ni-O systems: Remodelling of the liquid, BCC and FCC phases, *Calphad* 19 (1995) 229–243.
- [74] T. Grinys, S. Tamulevicius, I. Prosycevas, S. Meskinis, XRD analysis of plasma sprayed YSZ-NiO-Ni ceramic coatings, *Plasma Process. Polym.* 4 (2007) S181–S184.
- [75] P. Michaux, G. Montavon, A. Grimaud, A. Denoirjean, P. Fauchais, Elaboration of porous NiO/8YSZ layers by several SPS and SPPS routes, *J. Therm. Spray Technol.* 19 (2010) 317–327.
- [76] S. Kim, O. Kwon, S. Kumar, Y. Xiong, C. Lee, Development and microstructure optimization of atmospheric plasma-sprayed NiO/YSZ anode coatings for SOFCs, *Surf. Coat. Technol.* 202 (2008) 3180–3186.
- [77] G.M. Ingo, Origin of darkening in 8 wt% yttria-zirconia plasma-sprayed thermal barrier coatings, *J. Am. Ceram. Soc.* 74 (1991) 381–386.
- [78] P. Ctibor, R.C. Seshadri, J. Henych, V. Nehasil, Z. Pala, J. Kotlan, Photocatalytic and electrochemical properties of single- and multi-layer sub-stoichiometric titanium oxide coatings prepared by atmospheric plasma spraying, *J. Adv. Ceram.* 5 (2016) 126–136.
- [79] M. Poon, O. Kesler, The influence of pore formers on the microstructure of plasma sprayed NiO–YSZ anodes, *J. Power Sources* 210 (2012) 204–217.
- [80] T. Hidayat, M.A. Rhamdhani, E. Jak, P.C. Hayes, On the relationships between the kinetics and mechanisms of gaseous hydrogen reduction of solid nickel oxide, *Metall. Mater. Trans. B Process Metall. Mater. Process. Sci.* 40 (2009) 474–489.
- [81] M.C. Altay, S. Eroglu, Non-isothermal reduction behavior of NiO in undiluted Ar and CH₄ atmospheres, *Int. J. Miner. Process.* 149 (2016) 50–55.
- [82] R. Alizadeh, E. Jamshidi, H. Ale Ebrahim, Kinetic study of nickel oxide reduction by methane, *Chem. Eng. Technol.* 30 (2007) 1123–1128.

- [83] F. Coskun, S. Cetinkaya, S. Eroglu, Reduction of nickel oxide with ethanol, *JOM* 69 (2017) 987–992.
- [84] F. Korkmaz, S. Cetinkaya, S. Eroglu, Thermodynamic analysis and reduction of bismuth oxide by ethanol, *Metall. Mater. Trans. B Process Metall. Mater. Process. Sci.* 47 (2016) 2378–2385.
- [85] G. Mauer, A. Guignard, R. Vaßen, D. Stöver, Process diagnostics in suspension plasma spraying, *Surf. Coat. Technol.* 205 (2010) 961–966.
- [86] Z. Luo, A. Soria, Prospective study of the world aluminium industry. EUR 22951 EN, OPOCE, 2008.
- [87] É. Yvenou, A. Bily, F. Ben Ettouil, A. Dolatabadi, B. Davis, D. Guay, C. Moreau, L. Roué, TiB₂ deposited on graphite by suspension plasma spray as Al wettable cathode, *J. Therm. Spray Technol.* 30 (2021) 1535–1543.
- [88] S. Mohammadkhani, A. Bily, B. Davis, A. Dolatabadi, C. Moreau, L. Roué, D. Guay, Impact of density on the behavior of suspension plasma-sprayed TiB₂ coatings in the presence of molten aluminum, *J. Therm. Spray Technol.* 31 (2022) 1499–1507.
- [89] A. Bacciochini, F. Ben-Ettouil, E. Brousse, J. Ilavsky, G. Montavon, A. Denoirjean, S. Valette, P. Fauchais, Quantification of void networks of as-sprayed and annealed nanostructured yttria-stabilized zirconia (YSZ) deposits manufactured by suspension plasma spraying. *Surf. Coatings Technol.* 205 (2010) 683–689.
- [90] P. Fauchais, V. Rat, C. Delbos, J.F. Coudert, T. Chartier, L. Bianchi, Understanding of suspension DC plasma spraying of finely structured coatings for SOFC, *IEEE Trans. Plasma Sci.* 33 (2005), 920–930.
- [91] S. Mohammadkhani, V. Jalilvand, B. Davis, F. Ben Ettouil, A. Dolatabadi, L. Roué, C. Moreau, D. Guay, Suspension plasma spray deposition of Co_xNi_{1-x}O coatings. *Surf. Coatings Technol.* 399 (2020) 126168.
- [92] S. Mohammadkhani, V. Jalilvand, B. Davis, G.H. Gauthier, A. Dolatabadi, C. Moreau, L. Roué, D. Guay, High-temperature behaviour of HVOF (Co,Ni)O coated Cu–Ni–Fe anodes, *Corros. Sci.* 189 (2021) 109563.
- [93] V. Jalilvand, S. Mohammadkhani, B. Davis, L. Roué, A. Dolatabadi, D. Guay, C. Moreau, The effect of bond coat on high-temperature behavior of HVOF-sprayed (Co,Ni)O coating on Cu–Ni–Fe Anodes, *Surf. Coatings Technol.* 441 (2022) 128576.
- [94] W. Tillmann, O. Khalil, I. Baumann, Influence of spray gun parameters on inflight particle's characteristics, the splat-type distribution, and microstructure of plasma-sprayed YSZ coatings. *Surf. Coatings Technol.* 406 (2021) 126705.

- [95] S.Y. Chen, G.Z. Ma, H.D. Wang, P.F. He, Z. Liu, Solidification mechanism and quantitative characterization of Fe-based amorphous splat formed by plasma sprayed droplets with different in-flight status. *J. Alloys Comp.* 768 (2018) 789-799.
- [96] L. Bianchi, A. C. Leger, M. Vardelle, A. Vardelle, P. Fauchais, Splat formation and cooling of plasma-sprayed zirconia. *Thin Solid Films* 305 (1997), 35–47.
- [97] P. Fauchais, R. Etchart-Salas, C. Delbos, M. Tognonvi, V. Rat, J. F. Coudert, T. Chartier, Suspension and solution plasma spraying of finely structured layers: potential application to SOFCs. *J. Phys. D: Appl. Phys.* 40 (2007) 2394–2406.
- [98] H.R. Salimijazi, L. Pershin, T. W. Coyle, J. Mostaghimi, L. Rosenzweig, E. Moran, Effect of substrate temperature and droplet characteristics on plasma sprayed zirconia splats. *Proc. Int. Therm. Spray Conf.*, Seattle, USA, 2006.
- [99] A.A. Syed, Z. Ilhan, Nanostructured plasma sprayed anodes for solid oxide fuel cells. *Proc. Int. Therm. Spray Conf.*, Beijing, China, 2007.
- [100] L. Han, Q. Meng, D. Wang, Y. Zhu, J. Wang, X. Du, E.A. Stach, H.L. Xin, Interrogation of bimetallic particle oxidation in three dimensions at the nanoscale. *Nat. Commun.* 7 (2016) 13335.
- [101] W. Brandl, D. Toma, J. Krüger, H.J. Grabke, G. Matthäs, The oxidation behaviour of HVOF thermal-sprayed MCrAlY coatings, *Surf. Coatings Technol.* 94–95 (1997) 21–26.
- [102] J. Oberste Berghaus, J.-G. Legoux, C. Moreau, R. Hui, C. Decâes-Petit, W. Qu, S. Yick, Z. Wang, R. Maric, D. Ghosh, Suspension HVOF spraying of reduced temperature solid oxide fuel cell electrolytes, *J. Therm. Spray Technol.* 17 (2008) 700–707.
- [103] C.V. Cojocaru, D. Lévesque, C. Moreau, R.S. Lima, Performance of thermally sprayed Si/mullite/BSAS environmental barrier coatings exposed to thermal cycling in water vapor environment, *Surf. Coatings Technol.* 216 (2013) 215–223.
- [104] E. Turunen, T. Varis, J. Keskinen, T. Fält, S.P. Hannula, Improved mechanical properties by nanoreinforced ceramic composite HVOF coatings, *Adv. Sci. Technol.* 45 (2006) 1240–1245.
- [105] F. Tarasi, M. Medraj, A. Dolatabadi, J. Oberste-Berghaus, C. Moreau, High-temperature performance of alumina-zirconia composite coatings containing amorphous phases, *Adv. Funct. Mater.* 21 (2011) 4143–4151.
- [106] C.V. Cojocaru, S.E. Kruger, C. Moreau, R.S. Lima, Elastic Modulus evolution and behavior of Si/Mullite/BSAS-Based environmental barrier coatings exposed to high temperature in water vapor environment, *J. Therm. Spray Technol.* 20 (2011) 92–99.

- [107] T. Sahraoui, N.-E. Fenineche, G. Montavon, C. Coddet, Alternative to chromium: characteristics and wear behavior of HVOF coatings for gas turbine shafts repair (heavy-duty), *J. Mater. Process. Technol.* 152 (2004) 43–55.
- [108] M. Jones, A. Horlock, P. Shipway, D. McCartney, J. Wood, A comparison of the abrasive wear behaviour of HVOF sprayed titanium carbide- and titanium boride-based cermet coatings, *Wear* 251 (2001) 1009–1016.
- [109] K. Hoshino, N.L. Peterson, Cation impurity diffusion in CoO and NiO, *J. Phys. Chem. Solids* 45 (1984) 963–972.
- [110] M.W. Chase, A.I. of Physics., U. States., N.B. of Standards., A.C. Society., JANAF Thermochemical Tables, American Chemical Society and the American Institute of Physics for the National Bureau of Standards, New York, 1985.
- [111] R.D. Holmes, H.S.C. O'Neill, R.J. Arculus, Standard Gibbs free energy of formation for Cu₂O, NiO, CoO, and Fe_xO: high resolution electrochemical measurements using zirconia solid electrolytes from 900–1400 K, *Geochim. Cosmochim. Acta* 50 (1986) 2439–2452.
- [112] G. Ketteler, W. Weiss, W. Ranke, R. Schlögl, Bulk and surface phases of iron oxides in an oxygen and water atmosphere at low pressure, *Phys. Chem. Chem. Phys.* 3 (2001) 1114–1122.
- [113] J.-P. Wang, W.D. Cho, Oxidation behavior of pure copper in oxygen and/or water vapor at intermediate temperature, *ISIJ Int.* 49 (2009) 1926–1931.
- [114] R. Haugsrud, T. Norby, P. Kofstad, High-temperature oxidation of Cu–30 wt.% Ni–15 wt.% Fe, *Corros. Sci.* 43 (2001) 283–299.
- [115] I.-H. Jung, S.A. Decterov, A.D. Pelton, H.-M. Kim, Y.-B. Kang, Thermodynamic evaluation and modeling of the Fe–Co–O system, *Acta Mater.* 52 (2004) 507–519.
- [116] S.V. Divinski, F. Hisker, C. Herzig, R. Filipek, M. Danielewski, Self- and interdiffusion in ternary Cu-Fe-Ni alloys, *Defect Diffus. Forum* 237–240 (2005) 50–61.
- [117] K.J. Rönkä, A.A. Kodentsov, P.J.J. Van Loon, J.K. Kivilahti, F.J.J. Van Loo, Thermodynamic and kinetic study of diffusion paths in the system Cu-Fe-Ni, *Metall. Mater. Trans. A.* 27 (1996) 2229–2238.
- [118] E.M.M. Hiroaki Okamoto, Mark E. Schlesinger, *Alloy Phase Diagrams*, ASM International, 2016.
- [119] L.A. Zabdyr, O.B. Fabrichnaya, Phase equilibria in the cobalt oxide-copper oxide system, *J. Phase Equilibria Diffus.* 23 (2002) 149–155.

- [120] I. Gallino, M.E. Kassner, R. Busch, Oxidation and corrosion of highly alloyed Cu–Fe–Ni as inert anode material for aluminum electrowinning in as-cast and homogenized conditions, *Corros. Sci.* 63 (2012) 293–303.
- [121] G.J. Koel, P.J. Gellings, The contribution of different types of point defects to diffusion in CoO and NiO during oxidation of the metals, *Oxid. Met.* 5 (1972) 185–203.
- [122] E. Olsen, J. Thonstad, Nickel ferrite as inert anode in aluminium electrolysis: Part II – material performance and long-term testing and preliminary testing, *J. Appl. Electrochem.* 29 (1999) 301–311.
- [123] P. Zarrabian, M. Kalantar, S.S. Ghasemi, Fabrication and characterization of nickel ferrite based inert anodes for aluminum electrolysis, *J. Mater. Eng. Perform.* 23 (2014) 1656–1664.
- [124] L.C. Feng, W.Z. Shao, L. Zhen, N. Xie, V.V. Ivanov, Cu₂O/Cu cermet as a candidate inert anode for Al production, *Int. J. Appl. Ceram. Technol.* 4 (2007) 453–462.
- [125] J.Y. Liu, Z.Y. Li, Y.Q. Tao, D. Zhang, K.C. Zhou, Phase evolution of 17(Cu-10Ni)-(NiFe₂O₄-10NiO) cermet inert anode during aluminum electrolysis, *Trans. Nonferr. Met. Soc. China* 21 (2011) 566–572.
- [126] W. Wei, S.J. Geng, D.B. Xie, F.H. Wang, High temperature oxidation and corrosion behaviours of Ni–Fe–Cr alloys as inert anode for aluminum electrolysis, *Corros. Sci.* 157 (2019) 382–391.
- [127] I. Burlacov, J. Jirkovský, M. Müller, R.B. Heimann, Induction plasma sprayed photocatalytically active titania coatings and their characterisation by micro-Raman spectroscopy, *Surf. Coatings Technol.* 201 (2006) 255–264.
- [128] Y. Ozgurluk, A.C. Karaoglanli, H. Ahlatci, Comparison of calcium–magnesium–alumina–silicate (CMAS) resistance behavior of produced with electron beam physical vapor deposition (EB-PVD) method YSZ and Gd₂Zr₂O₇/YSZ thermal barrier coatings systems, *Vacuum* 194 (2021) 110576.
- [129] K.M. Doleker, Y. Ozgurluk, Y. Kahraman, A.C. Karaoglanli, Oxidation and hot corrosion resistance of HVOF/EB-PVD thermal barrier coating system, *Surf. Coatings Technol.* 409 (2021) 126862.
- [130] K.M. Doleker, Y. Ozgurluk, A.S. Parlakyigit, D. Ozkan, T. Gulmez, A.C. Karaoglanli, Oxidation behavior of NiCr/YSZ thermal barrier coatings (TBCs), *Open Chem.* 16 (2018) 876–881.
- [131] K.M. Doleker, H. Ahlatci, A.C. Karaoglanli, Investigation of isothermal oxidation behavior of thermal barrier coatings (TBCs) consisting of YSZ and multilayered YSZ/Gd₂Zr₂O₇ ceramic layers, *Oxid. Met.* 88 (2017) 109–119.

- [132] K.M. Doleker, A.C. Karaoglanli, Y. Ozgurluk, A. Kobayashi, Performance of single YSZ, $Gd_2Zr_2O_7$ and double-layered YSZ/ $Gd_2Zr_2O_7$ thermal barrier coatings in isothermal oxidation test conditions, *Vacuum* 177 (2020) 109401.
- [133] A.S. Parlakyigit, D. Ozkan, M. Oge, Y. Ozgurluk, K.M. Doleker, T. Gulmez, A.C. Karaoglanli, Formation and growth behavior of TGO layer in TBCs with HVOF sprayed NiCr bond coat. *Emerg. Mater. Res.* 9 (2020) 451–459.
- [134] J. Shi, T. Zhang, B. Sun, B. Wang, X. Zhang, L. Song, Isothermal oxidation and TGO growth behavior of NiCoCrAlY-YSZ thermal barrier coatings on a Ni-based superalloy, *J. Alloys Comp.* 844 (2020) 156093.
- [135] J.K. Xiao, H. Tan, Y.Q. Wu, J. Chen, C. Zhang, Microstructure and wear behavior of FeCoNiCrMn high entropy alloy coating deposited by plasma spraying, *Surf. Coatings Technol.* 385 (2020) 125430.
- [136] T. Li, Y. Liu, B. Liu, W. Guo, L. Xu, Microstructure and wear behavior of FeCoCrNiMo0.2 high entropy coatings prepared by air plasma spray and the high velocity oxy-fuel spray processes, *Coatings* 7 (2017) 7090151.
- [137] A. Valarezo, W.B. Choi, W. Chi, A. Gouldstone, S. Sampath, Process control and characterization of NiCr coatings by HVOF-DJ2700 System: A process map approach, *J. Therm. Spray Technol.* 19 (2010) 852–865.
- [138] J. Saaedi, T.W. Coyle, S. Mirdamadi, H. Arabi, J. Mostaghimi, Phase formation in a Ni-50Cr HVOF coating, *Surf. Coatings Technol.* 202 (2008) 5804–5811.
- [139] E. Sadeghimeresht, N. Markocsan, P. Nylén, A comparative study on Ni-based coatings prepared by HVOF, HVOF, and APS methods for corrosion protection applications, *J. Therm. Spray Technol.* 25 (2016) 1604–1616.
- [140] D.H. Speidel, A. Muan, The system manganese oxide- Cr_2O_3 in air, *J. Am. Ceram. Soc.* 46 (1963) 577–578.
- [141] W. Kai, C.C. Li, F.P. Cheng, K.P. Chu, R.T. Huang, L.W. Tsay, J.J. Kai, The oxidation behavior of an equimolar FeCoNiCrMn high-entropy alloy at 950 °C in various oxygen-containing atmospheres, *Corros. Sci.* 108 (2016) 209–214.
- [142] G. Laplanche, U.F. Volkert, G. Eggeler, E.P. George, Oxidation behavior of the CrMnFeCoNi high-entropy alloy, *Oxid. Met.* 85 (2016) 629–645.
- [143] Z. Tong, H. Liu, J. Jiao, W. Zhou, Y. Yang, X. Ren, Laser additive manufacturing of CrMnFeCoNi high entropy alloy: Microstructural evolution, high-temperature oxidation behavior and mechanism, *Optics Laser Technol.* 130 (2020) 106326.

[144] R.K. Wild, High temperature oxidation of austenitic stainless steel in low oxygen pressure, *Corros. Sci.* 17 (1977) 87–104.

[145] R.E. Lobnig, H.P. Schmidt, K. Hennesen, H.J. Grabke, Diffusion of cations in chromia layers grown on iron-base alloys, *Oxid. Met.* 37 (1992) 81–93.

Appendix A

Supplementary data for Chapter 3

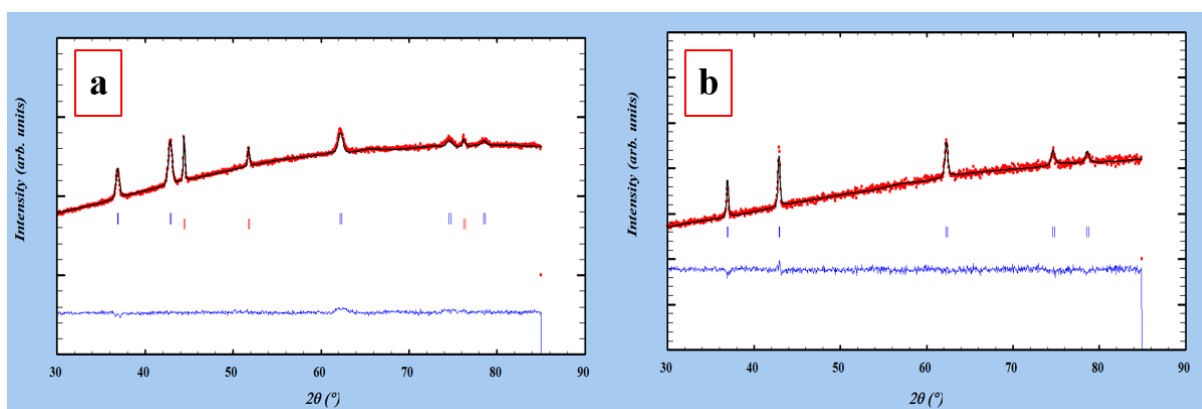


Figure S3.1. Typical examples of XRD experimental data and Rietveld refinement fitting results: a) sample S2 that contains two phases and b) sample S8 that contains a single phase.

Appendix B

Supplementary data for Chapter 5

Table S5.1. HVOF Spray process parameters.

Sample #	Oxygen flow (lpm)	Propylene flow (lpm)	Air flow (lpm)	Nitrogen (carrier gas) flow (lpm)	Substrate temperature (°C)	Number of passes	Substrate	Coating composition	Deposition efficiency (%)
Part 1									
H1	279	65	202	15	400	50	Cu-rich	Co _{0.75} Ni _{0.25} O	18
H2	217	70	167	15	450	50	Cu-rich	Co _{0.75} Ni _{0.25} O	24
H3	236	55	163	15	350	50	Cu-rich	Co _{0.75} Ni _{0.25} O	14
Part 2									
S1	217	70	167	15	450	55	Cu-rich	CoO	25
S2	217	70	167	15	450	55	Cu-rich	Co _{0.75} Ni _{0.25} O	23
S3	217	70	167	15	450	55	Cu-rich	Co _{0.5} Ni _{0.5} O	24
S4	217	70	167	15	450	55	Ni-rich	CoO	26
S5	217	70	167	15	450	55	Ni-rich	Co _{0.75} Ni _{0.25} O	29
S6	217	70	167	15	450	55	Ni-rich	Co _{0.5} Ni _{0.5} O	22

The optimum HVOF spraying conditions were determined using $\text{Co}_{0.75}\text{Ni}_{0.25}\text{O}$ powder deposited on Cu-20Ni-15Fe (Cu-rich) substrate. Three different sets of spray parameters were tested and they are listed in Table S5.1. No inter pass pauses, air or water cooling was applied during the deposition process. The substrate temperature for sample H1, H2 and H3 was about 350, 450 and 400 °C, respectively. The deposition efficiency for sample H1, H2 and H3 was 18, 24 and 14%, respectively. The XRD patterns of H1, H2 and H3 coatings are shown in Figure S5.1. In all cases, only one set of peaks appears in the XRD patterns. The diffraction peaks occur at $2\theta = 36.7^\circ, 42.7^\circ, 61.9^\circ, 74.2^\circ$ and 78.1° and are assigned to *fcc* (Co,Ni)O solid solution. The composition of the solid solutions was obtained by calculating the *a* lattice parameter of the *fcc* phase based on the position of the XRD peaks. The composition of the (Co,Ni)O solid solution was $\text{Co}_{0.73}\text{Ni}_{0.27}\text{O}$ for samples H1, H2 and H3, very close to the starting powder.

The cross-sectional SEM micrographs of H1, H2 and H3 coatings are presented in Figure S5.2. The coating thickness is between 60 to 85 μm after 50 deposition passes. The SEM images show a uniform microstructure, low porosity, very low surface roughness and good bonding to the substrate. However, sample H2 has the lowest porosity. While layers of melted splats can still be seen in sample H1 and H3, the splats observed in sample H2 formed a uniform structure, most probably because the particles were better accelerated/melted during the deposition process.

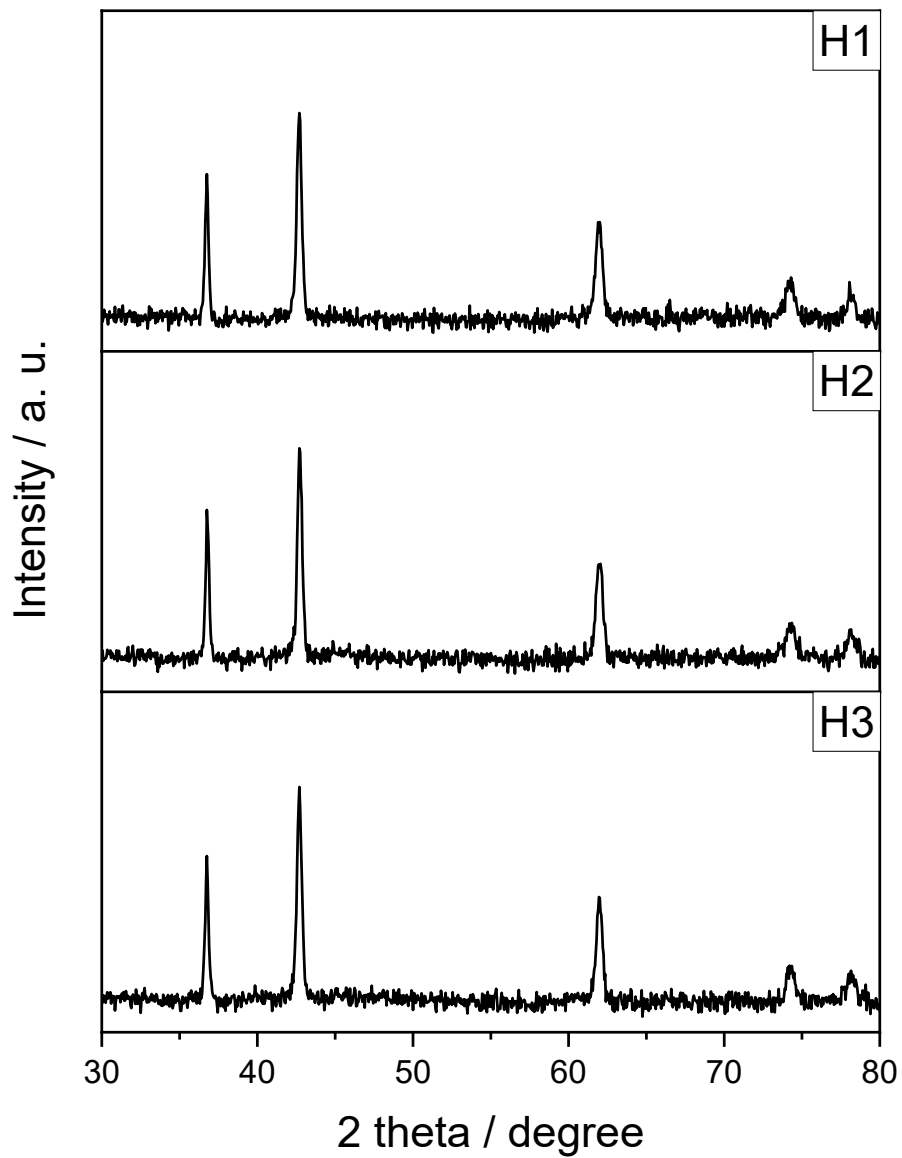


Figure S5.1. XRD patterns of coatings prepared in the first series of experiments using different HVOF gas compositions ranging.

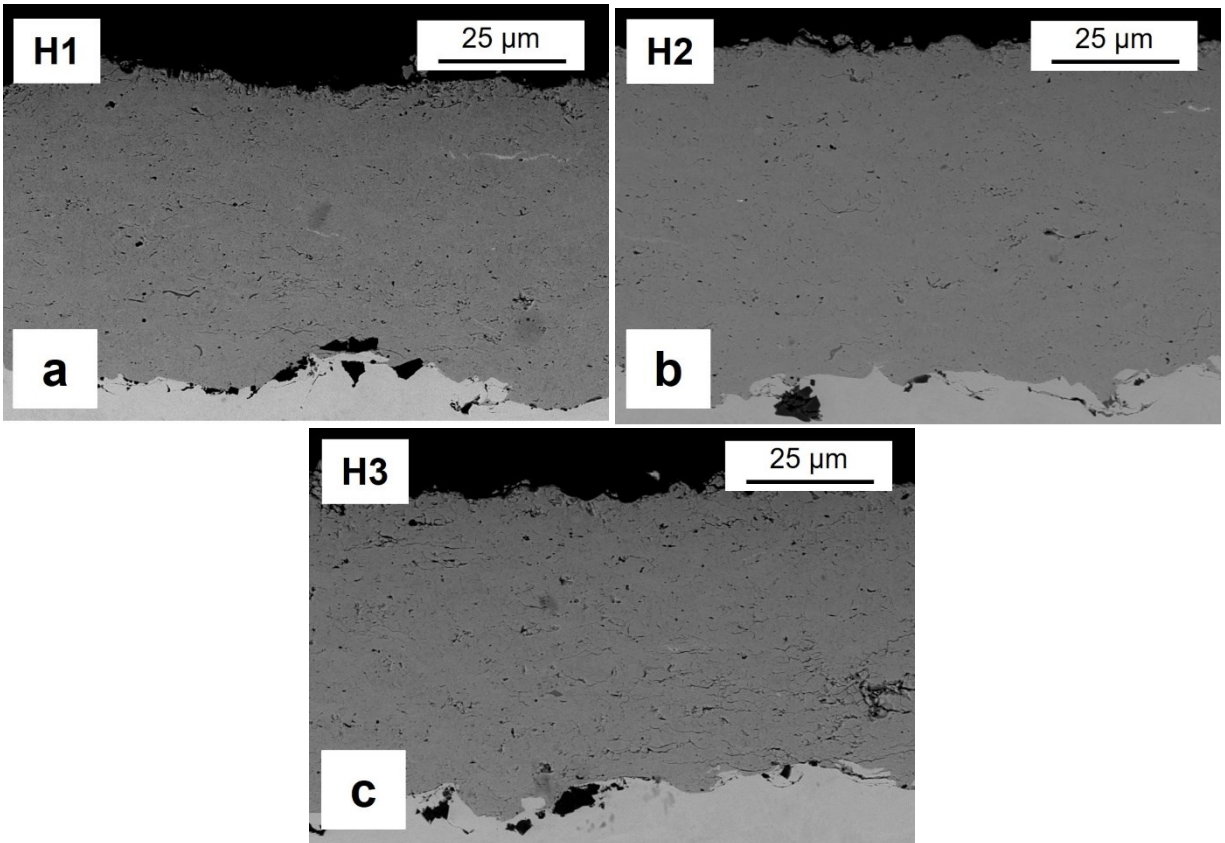


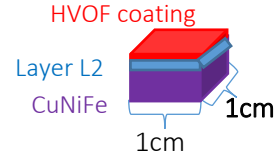
Figure S5.2. Cross-sectional SEM micrographs of coatings prepared in the first series of experiments using different HVOF gas compositions ranging.

A mass balance calculation was performed to determine the total amount of Fe and O atoms in Layer 1 and 2 of CoO coatings on Cu-rich substrate after heat treatment under argon:

	Thickness	Lattice parameter
HVOF coating (before HT)	$118 * 10^{-4}$ cm	$4.264 * 10^{-8}$ cm
HVOF coating (after HT)	$118 * 10^{-4}$ cm	$4.274 * 10^{-8}$ cm
Fe-poor layer	$50 * 10^{-4}$ cm	$3.60 * 10^{-8}$ cm

Cu-20Ni-15Fe in wt% = $\text{Cu}_{62.7}\text{Ni}_{20.9}\text{Fe}_{16.4}$ in at.%

If we consider the sample size is 1 cm * 1 cm =>



Before heat treatment:

Total oxygen in 118 μm thickness CoO:

If we consider the total coating volume is $0.0118 \text{ cm} * 1 \text{ cm} * 1 \text{ cm} = 0.0118 \text{ cm}^3$

CoO unit cell volume is: $(4.264 * 10^{-8} \text{ cm})^3 = 77.527 * 10^{-24} \text{ cm}^3$

In 0.0118 cm^3 there are: $0.0118 \text{ cm}^3 / 77.527 * 10^{-24} \text{ cm}^3 = 1.522 * 10^{20}$ CoO unit cells

Each CoO unit cell contains 4 atoms of O and 4 atoms of Co, therefore,

In this volume, there are $6.088 * 10^{20}$ atoms of oxygen.

Total Fe in 50 μm thickness of CuNiFe (Layer L2):

Cu-rich unit cell volume is: $(3.60 * 10^{-8} \text{ cm})^3 = 46.656 * 10^{-24} \text{ cm}^3$

If we consider the total substrate volume is $0.005 \text{ cm} * 1 \text{ cm} * 1 \text{ cm} = 0.005 \text{ cm}^3$

In 0.005 cm^3 there are: $0.005 \text{ cm}^3 / 46.656 * 10^{-24} \text{ cm}^3 = 1.071 * 10^{20}$ CuNiFe unit cells

Each CuNiFe unit cell (FCC) contains 4 atoms, 0.656 atoms Fe + 0.836 atoms Ni + 2.508 atoms Cu (Cu-20Ni-15Fe in wt% = $\text{Cu}_{62.7}\text{Ni}_{20.9}\text{Fe}_{16.4}$ in at.%).

So, there are totally $0.702 * 10^{20}$ atoms of Fe.

After heat treatment:

Total iron in 118 μm thickness of (Co,Fe)O:

If we consider the total coating volume is $0.0118 \text{ cm} * 1 \text{ cm} * 1 \text{ cm} = 0.0118 \text{ cm}^3$

(Co,Fe)O unit cell volume is: $(4.274 * 10^{-8} \text{ cm})^3 = 78.073 * 10^{-24} \text{ cm}^3$

In 0.0118 cm^3 there are: $0.0118 \text{ cm}^3 / 78.073 * 10^{-24} \text{ cm}^3 = 1.511 * 10^{20}$ CoO unit cells

Each (Co,Fe)O unit cell contains 4 (Co,Fe) atoms and 4 O atoms, 0.4 atoms Fe, 3.6 atoms Co [(Co_{0.4}Fe_{0.1})O].

Therefore, there are $0.604 * 10^{20}$ atoms of iron (Number of Fe atoms that diffused from L2 into CoO coating).

Remaining Fe atoms in L2 after HT:

#Fe atoms before HT - #Fe atoms diffused into CoO after HT:

$0.702 * 10^{20} - 0.604 * 10^{20}$ atoms of iron = $0.098 * 10^{20}$ atoms of iron

To oxidize all these Fe atoms (Fe₂O₃): $0.147 * 10^{20}$ atoms of oxygen is required.

Total O in CoO before HT was: $6.088 * 10^{20}$ atoms of oxygen.

2.414 at.% of O from CoO is required to oxidize the remaining Fe in L2.

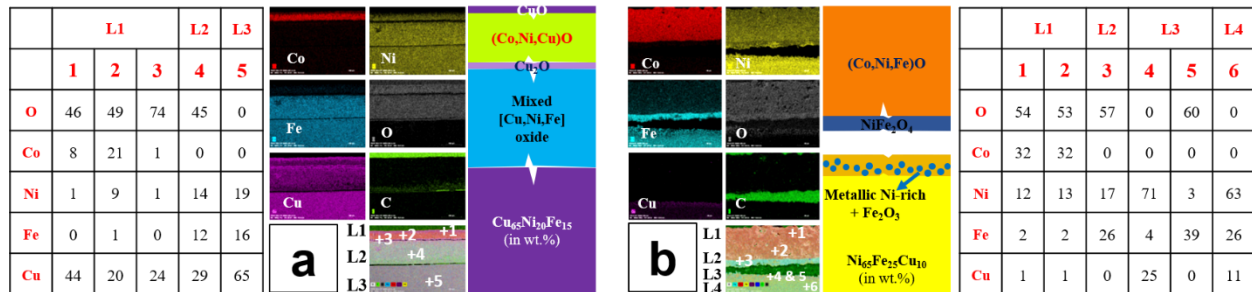


Figure S5.5. EDS analysis results and schematic illustration of $Co_{0.75}Ni_{0.25}O$ coating deposited on (a) Cu-20Ni-15Fe and (b) Ni-25Fe-10Cu substrate (sample S2 and S5, respectively), after 20 h of heat treatment at 1000 °C in static air. The source of carbon is the resin used for the sample preparation.

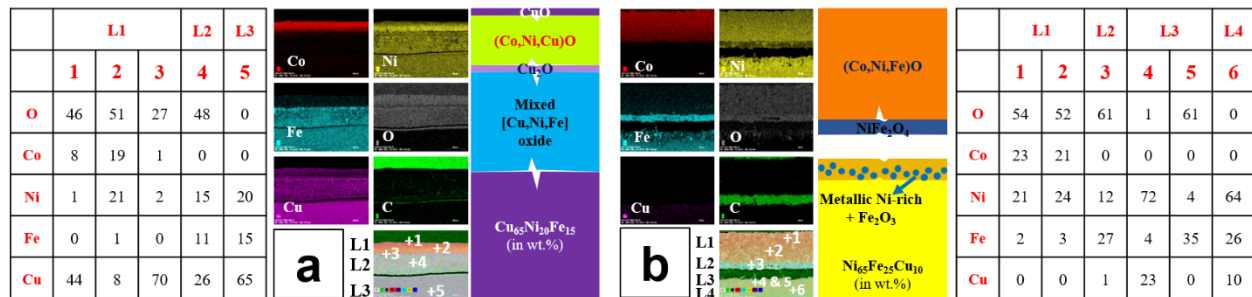


Figure S5.6. EDS analysis results and schematic illustration of $Co_{0.5}Ni_{0.5}O$ coating deposited on (a) Cu-20Ni-15Fe and (b) Ni-25Fe-10Cu substrate (sample S3 and S6, respectively), after 20 h of heat treatment at 1000 °C in static air. The source of carbon is the resin used for the sample preparation.

Appendix C

Impact of HVOF sprayed Ni-Cr and (Co,Ni)O coatings on the corrosion behaviour of Cu-Ni-Fe anodes for green aluminum production ⁵

Abstract

Cu-Ni-Fe alloys are promising O₂-evolving anode materials for green Al production but their corrosion-resistance needs to be improved. In the present work, (Co,Ni)O top-coats and Ni-Cr bond-coats are deposited by high-velocity oxy-fuel (HVOF) process on two Cu-Ni-Fe alloys (Cu-rich and Ni-rich). It is firstly shown that (Co,Ni)O materials have a low solubility in the alumina-saturated cryolitic bath at 1000 °C. Then, the impact of the coatings and substrate composition on their oxidation behaviour at 1000 °C in air and during Al electrolysis is studied. Although [Ni-Cr/(Co,Ni)O]-coating significantly increases the dry oxidation resistance of Cu-Ni-Fe alloys, the corrosion-resistance of the [Ni-Cr/(Co,Ni)O] coated Cu-Ni-Fe anodes is low due to the coating detachment during aluminum electrolysis. However, coating Cu-20Ni-15Fe anode with a single (Co,Ni)O layer increases its corrosion-resistance, prevents it from fluorination and leads to the rapid formation of a coherent protective NiFe₂O₄ layer beneath the (Co,Ni)O topcoat. Under the same conditions, the protective NiFe₂O₄ layer is not formed on the Ni-25Fe-10Cu anode.

Keywords: (Co,Ni)O coat, Ni-Cr bond-coat, Cu-Ni-Fe alloys, high-velocity oxygen fuel, inert anode, Al electrolysis.

C.1. Introduction

⁵ This appendix has been accepted for publication as an article in the *Metallurgical and Materials Transactions B*: S. Mohammadkhani, V. Jalilvand, A. Dolatabadi, C. Moreau, D. Guay, L. Roué.

Primary aluminum production by electrolysis is carried out by the Hall-Héroult process using consumable carbon anodes, which results in heavy CO₂ emissions [1]. The substitution of consumable carbon anodes emitting CO₂ with inert O₂-evolving anodes for the primary production of aluminum would reduce considerably the emissions of carbon dioxide and perfluorocarbons from this industry [1,2]. However, the design of inert anodes is a major challenge because of the severe aluminum electrolysis conditions that require materials with excellent resistance to corrosion and thermal shock, as well as adequate electrochemical properties. Inert anodes can also be of interest for other electrolytic process, such as the reduction of iron oxide to metallic iron. The use of inert anodes coupled with green sources of electricity will result in significant reduction of greenhouse gas emissions from extractive metal production [3,4]. Among the numerous materials studied so far [2,5], single-phase Cu-Ni-Fe alloys are promising materials for inert anodes due to their ability to form a protective nickel ferrite (NiFe₂O₄) layer upon Al electrolysis [6]. The nickel ferrite phase has low solubility in molten cryolite and good oxidation and corrosion resistance during Al electrolysis. However, this protective layer needs time to form at the surface of Cu-Ni-Fe alloys, during which fluorination can occur, causing premature degradation of the electrode [7-9]. It is therefore essential to increase the corrosion-resistance of Cu-Ni-Fe anodes with an appropriate fluorination barrier to allow the NiFe₂O₄ layer to form.

In a work by Nguyen and de Nora [10], it was shown that (Co,Ni)O solid solutions are promising protective coatings for metallic Ni-Fe anodes. In fact, CoO is an excellent fluorination barrier since the transformation of CoO to CoF₂ does not occur in aluminum electrolysis conditions. However, according to Co-O phase diagram, CoO converts to Co₃O₄ at ~960 °C in 1 bar O₂ [11]. The conversion of CoO to Co₃O₄ under Al electrolysis conditions is not desired since the O₂ evolution overpotential of n-type semiconductor Co₃O₄ is significantly higher than that of p-type semiconducting CoO [10]. Adding Ni atoms to CoO to form (Co,Ni)O solid solution can stabilize CoO and prevent its transformation to Co₃O₄ [10]. It was also shown that the required nickel content to form a stable (Co,Ni)O and avoid the formation of Co₃O₄ depends on temperature and oxygen pressure [12-14].

(Co,Ni)O coated Ni-Fe anodes were prepared through a two-step process by Nguyen and de Nora [10]. First, a Co-Ni alloy was electrodeposited on Ni-Fe alloy and then an oxidation treatment in air at high temperature was performed to favor the formation of (Co,Ni)O coating. With this procedure, it is very challenging to produce a crack-free oxide layer due to the

considerable change of densities that occurs upon oxidation of metallic Co-Ni alloy that could affect its long-term application for aluminum electrolysis. However, thermal spraying can be used as an alternative method to deposit oxide coatings directly through a single step and with a relatively high efficiency [15]. With thermal spray techniques, it is possible to produce thick crack-free coatings from materials with high melting points that are typically challenging to prepare using conventional methods such as sintering, electrodeposition and vacuum-based deposition methods [16,17]. Coatings for various applications such as thermal barrier coatings, wear and corrosion resistant coatings, biomaterials coatings, composite coatings and abradable coatings have been deposited with thermal spray techniques [18–20].

In our previous studies [21,22], protective $\text{Co}_x\text{Ni}_{1-x}\text{O}$ coatings with different compositions have been successfully deposited on Cu-Ni-Fe alloys by suspension plasma spray (SPS) and high velocity oxygen fuel (HVOF) methods. Adherent and non-porous $\text{Co}_x\text{Ni}_{1-x}\text{O}$ coatings were obtained using both SPS and HVOF techniques, however, the undesired reduction of NiO to Ni was observed during SPS process [21]. Dense, uniform, and single phase $\text{Co}_x\text{Ni}_{1-x}\text{O}$ coatings were deposited on two compositions of Cu-Ni-Fe alloys (Cu-20Ni-15Fe and Ni-25Fe-10Cu) using the HVOF process. Their oxidation behavior was studied at 1000 °C in air [22]. It was shown that the $\text{Co}_x\text{Ni}_{1-x}\text{O}$ coatings slow down both oxygen diffusion from the atmosphere to the substrate and copper diffusion from the Cu-rich substrate to the sample surface, and that this effect is accentuated as the Ni content of the $\text{Co}_x\text{Ni}_{1-x}\text{O}$ coatings is increased. On Ni-rich alloy, the formation of a NiFe_2O_4 scale was observed between the substrate and the coating, whose thickness decreases slightly as the Ni content of the $\text{Co}_x\text{Ni}_{1-x}\text{O}$ coatings increases. In all cases, a delamination of the $\text{Co}_x\text{Ni}_{1-x}\text{O}$ coatings was observed after 20 hours of oxidation.

To further increase the oxidation resistance of Cu-Ni-Fe alloys and to prevent coating delamination, the use of a Ni-Cr bond-coat between the Cu-Ni-Fe substrate and the (Co,Ni)O top-coat is here evaluated. The excellent resistance of nickel–chromium alloys to high temperature oxidation makes them widely used as thermally sprayed coatings in fossil fuel-fired boilers, waste incineration boilers, electric furnaces, etc. When heated, a thin layer of Cr_2O_3 will form at the surface of the coating which blocks the diffusion of oxygen into the underlying alloy and prevents the sample from further oxidation [23,24]. The formation of a Cr_2O_3 layer will also prevent the outward diffusion of elements from the substrate into the surface of the sample.

In the present study, Cu-Ni-Fe anodes (Cu-rich and Ni-rich alloys) are coated by HVOF with a single (Co,Ni)O coating or a combination of Ni-Cr + (Co,Ni)O coatings, and their behavior for dry oxidation and for Al electrolysis is presented. In addition, one of the main requirements in Al industry is to produce aluminum with a purity of more than 99.5-99.8% [2,25]. Hence, one of the most important characteristics for the materials used as anodes in aluminum electrolysis is low solubility in molten cryolite. The dissolution rate of NiO as a function of the composition of cryolite and time has been studied [26,27] but to our knowledge, the solubility of CoO and (Co,Ni)O in molten cryolite has never been measured. Here, the dissolution rate of $\text{Co}_x\text{Ni}_{1-x}\text{O}$ solid solutions in cryolite at 1000 °C is studied as well.

C.2. Experimental

C.2.1. (Co,Ni)O synthesis

$\text{Co}_x\text{Ni}_{1-x}\text{O}$ solid solutions with x varying from 0 to 1 were synthesized by mixing Co_3O_4 (purity $\geq 99.7\%$, -325 mesh, from Alfa Aesar) and NiO powders (purity $\geq 99\%$, 325 mesh, from Cerac) and heating the mixtures at 1200 °C for 12 h in an air atmosphere. CoO was also prepared by heating Co_3O_4 powder under argon flow at 1200 °C for 12 hours, followed by a rapid cooling to prevent the transformation of CoO to Co_3O_4 upon cooling. The single phase structure of the $\text{Co}_x\text{Ni}_{1-x}\text{O}$ solid solutions was confirmed from their X-ray diffraction (XRD) analysis as shown elsewhere [14].

C.2.2. Solubility measurements

To perform solubility measurements, sintered pellets of $\text{Co}_x\text{Ni}_{1-x}\text{O}$ were prepared. $\text{Co}_x\text{Ni}_{1-x}\text{O}$ ($x= 1, 0.75, 0.5, 0.25$ and 0) powders were mixed separately with an aqueous solution of polyvinyl alcohol (5 wt.% PVA in distilled water), then were cold-pressed under 50 MPa for 5 minutes. The obtained disc-shaped pellets of 10 mm diameter and ~5 mm thickness were left to dry in an oven at 100 °C overnight and then were sintered in a muffle furnace for 16 h in air at 1350 °C. Sintered CoO pellet was heated again in a tubular furnace at 950 °C under an argon flow for 3 h and was left to cool down under the argon flow to prevent its possible conversion to Co_3O_4 .

A pure CoO pellet was obtained, as confirmed by XRD. The apparent densities of all pellets were about 90% of their theoretical densities.

200 grams of cryolite-based electrolyte powders, composed of 82.15 wt.% Na_3AlF_6 + 9.85 wt.% AlF_3 + 8 wt.% Al_2O_3 (CR=2.3), were dried for 24 h in an oven at 150 °C prior to solubility measurements. Sintered pellets were put under the solid electrolyte powder mixture at the bottom of alumina crucibles. To perform the solubility measurements, cryolite-based electrolyte was heated at 1000 °C under an argon flow. After 3, 6, 8 and 9 h, ~2 grams of molten electrolyte were taken out using a graphite tube and left to cool down at room temperature. The obtained samples were crushed using a mortar and pestle and then analyzed by inductively coupled plasma atomic emission spectroscopy (ICP-AES). As a reference, 200 grams of electrolyte that was not put in contact with $\text{Co}_x\text{Ni}_{1-x}\text{O}$ pellets were heated at 1000 °C and ~2 grams of molten electrolyte were taken out and analyzed by ICP (blank sample).

C.2.3. High-velocity oxygen fuel (HVOF) coating

$\text{Co}_{0.75}\text{Ni}_{0.25}\text{O}$ powder was prepared in kg quantity with the same procedure as described above. Prepared (Co,Ni)O powder was sieved with -35 and +20 μm screens to obtain a flowable powder with appropriate particle size distribution for HVOF spraying. Commercially available Ni-20Cr (Metco 43VF-NS, Oerlikon Metco) powder was used to deposit a bond-coat layer between (Co,Ni)O and Cu-Ni-Fe alloys. Cu-20Ni-15Fe and Ni-25Fe-10Cu (in wt.%) substrates were produced by casting and were further homogenized by a heat-treatment under argon as explained in a previous work [28]. Cu-Ni-Fe substrates were cut into disc-shaped specimens of 15 mm diameter and ~7 mm thickness. Then, they were grit-blasted and cleaned by several rinsing in distilled water and acetone. Only one side of the disc-shaped samples was coated by HVOF and (Co,Ni)O coatings with ~150 μm thickness were prepared. In another series of experiments, first a ~50 μm thick Ni-Cr bond-coat was deposited, followed by a ~100 μm thick top-coat layer of (Co,Ni)O. The HVOF spraying parameters and HVOF setup are described in detail in our previous works [22,29].

C.2.4. Dry oxidation

The coated samples were heated at 1000 °C for 20 h in static air in a muffle furnace. The heating and cooling rates were 5 °C min⁻¹. Heat-treated samples were analyzed by XRD. Then, they were embedded in resin and polished by standard metallographic procedures to a final finish of 0.4 μm. Scanning Electron Microscopy / Energy Dispersive X-ray Spectroscopy (SEM-EDXS) observations of as-sprayed and heat-treated specimens were conducted using a Tescan Vega3 scanning electron microscope equipped with a Bruker XFlash® 6 | 10 Detector energy dispersive X-ray spectroscope. The SEM micrographs were acquired in the secondary electron mode at an operating voltage of 20 kV and a working distance of 15 mm.

C.2.5. Aluminum electrolysis

Disc-shaped anode (15 mm diam., ~7 mm thick), coated only on one side, was connected to a stainless steel 316 threaded rod which was placed inside an alumina tube. The anode was placed inside the electrolysis cell (5 cm above solid electrolyte), then the cathode, the anode and the electrolyte were heated slowly (2 °C.min⁻¹) up to the electrolysis temperature under argon atmosphere to prevent thermal shock into the coating layer. The anode was then inserted into the electrolyte and aluminum electrolysis started. A special electrochemical cell was designed to carry out the aluminum electrolysis and a schematic representation of the electrolysis cell is shown in Fig. C.1.

The electrolysis experiments were conducted at 1000 °C under argon at an anode current density of 0.5 A.cm⁻² for 5 h using a VMP3 potentiostat/galvanostat (Bio-Logic). The graphite crucible containing the electrolyte (~150 cm² in contact with the molten bath) was acting as the counter electrode. The electrolyte (~400 g) was composed of 82.15 wt.% Na₃AlF₆ + 9.85 wt.% AlF₃ + 8 wt.% Al₂O₃ (CR=2.3). The electrolyte powders were dried in an oven at 150 °C for at least 24 hours before the experiments. The alumina powder, which was dried with the same procedure, was periodically added to the electrolyte with an automatic feeder to keep the alumina concentration at saturation during the electrolysis.

After electrolysis, the anodes were taken out from the electrolyte and left to slowly cool down inside the electrolysis cell. Then, the anodes were detached from the stainless-steel threaded rod and were embedded in resin to prevent the delamination of the oxide layer from the anode

surface due to thermal and mechanical shocks. Samples were then polished using standard metallographic procedures and their cross-section was analyzed by SEM-EDXS.

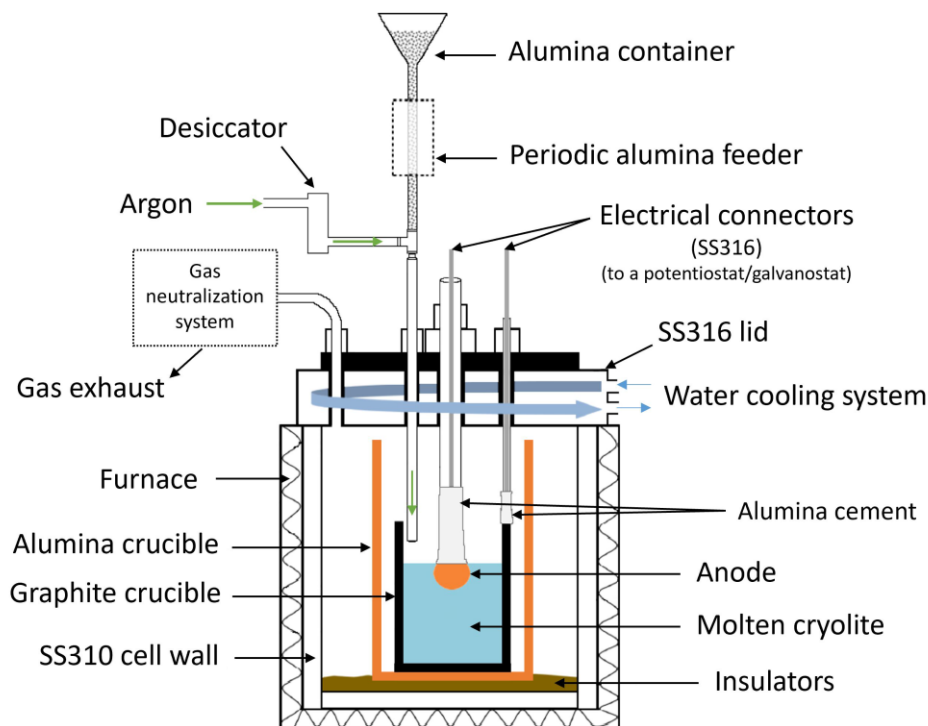


Figure C.1. Schematic illustration of aluminum electrolysis cell.

C.3. Results and discussion

C.3.1. Solubility measurements

Fig. C.2a-b shows the dissolution rates of cobalt and nickel from $\text{Co}_x\text{Ni}_{1-x}\text{O}$ pellets in cryolite-alumina bath at 1000 °C as a function of the immersion time. Cobalt and nickel contaminations in the as-received bath (blank sample) are 0.4 and 5 ppm, respectively. Increasing the immersion time from 3 to 8 h has a considerable effect on the concentration of cobalt and nickel in the electrolyte, but their concentrations do not change significantly when the immersion time increases from 8 to 9 h, suggesting that nearly steady-state concentrations were reached after 8-9 h of immersion. This is in accordance with the results obtained by DeYoung [30] who measured the solubility of nickel and iron oxides in cryolite-based baths, showing that 8 h of immersion is sufficient to achieve the equilibration of iron and nickel oxides with the melt. The amount of

dissolved Co from $\text{Co}_x\text{Ni}_{1-x}\text{O}$ solid solutions measured after 9 h of immersion varies from 16 ppm for $x = 0.25$ to 65 ppm for $x = 1$ (Fig. C.2a), while the amount of dissolved Ni varies from 9 ppm for $x = 0.75$ to 23 ppm for $x = 0$ (Fig. C.2b). Because of the higher dissolution rate of Co versus Ni, increasing the Co content in $\text{Co}_x\text{Ni}_{1-x}\text{O}$ solid solutions increases its global (Ni + Co) contamination, as shown in Fig. C.2c (after subtraction of the blank sample values). However, the total amount of dissolved (Ni + Co) from $\text{Co}_x\text{Ni}_{1-x}\text{O}$ solid solutions in cryolite-alumina bath at 1000 °C is below 70 ppm for all (Co,Ni)O compositions.

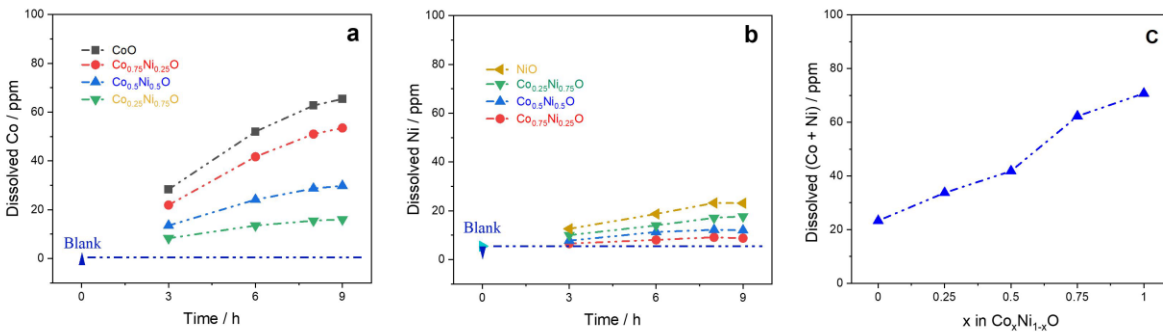


Figure C.2. Concentration of (a) Co and (b) Ni in cryolite-alumina bath at 1000 °C for $\text{Co}_x\text{Ni}_{1-x}\text{O}$ (with $x = 0, 0.75, 0.5, 0.25$ and 1) as a function of time and (c) as a function of x for $t = 9$ h.

A calculation was performed to determine the total thickness of $\text{Co}_{0.75}\text{Ni}_{0.25}\text{O}$ coatings that is likely to be dissolved during aluminum electrolysis experiments presented below. Note that the choice of this $\text{Co}_{0.75}\text{Ni}_{0.25}\text{O}$ coating composition was based on the De Nora's works, showing promising results with Ni-Fe-Cu anodes protected by a $\text{Co}_x\text{Ni}_{1-x}\text{O}$ coating with $x = 0.65-0.85$ [10]. Considering a constant volume of electrolyte, the size of disc-shape anode used for electrolysis and the saturation value for the dissolution of Co and Ni (57 ppm for $x = 0.75$ in Fig. C.2c), we find that a 25 μm layer of the (Co,Ni)O coatings is likely to be dissolved in the electrolyte. Details of these calculations are given in the supporting information section (refer to electronic supplementary material). All (Co,Ni)O coatings used for electrolysis had 100-150 μm thickness, thick enough to protect the underlying Cu-Ni-Fe substrate and not be completely dissolved for 5 h of Al electrolysis.

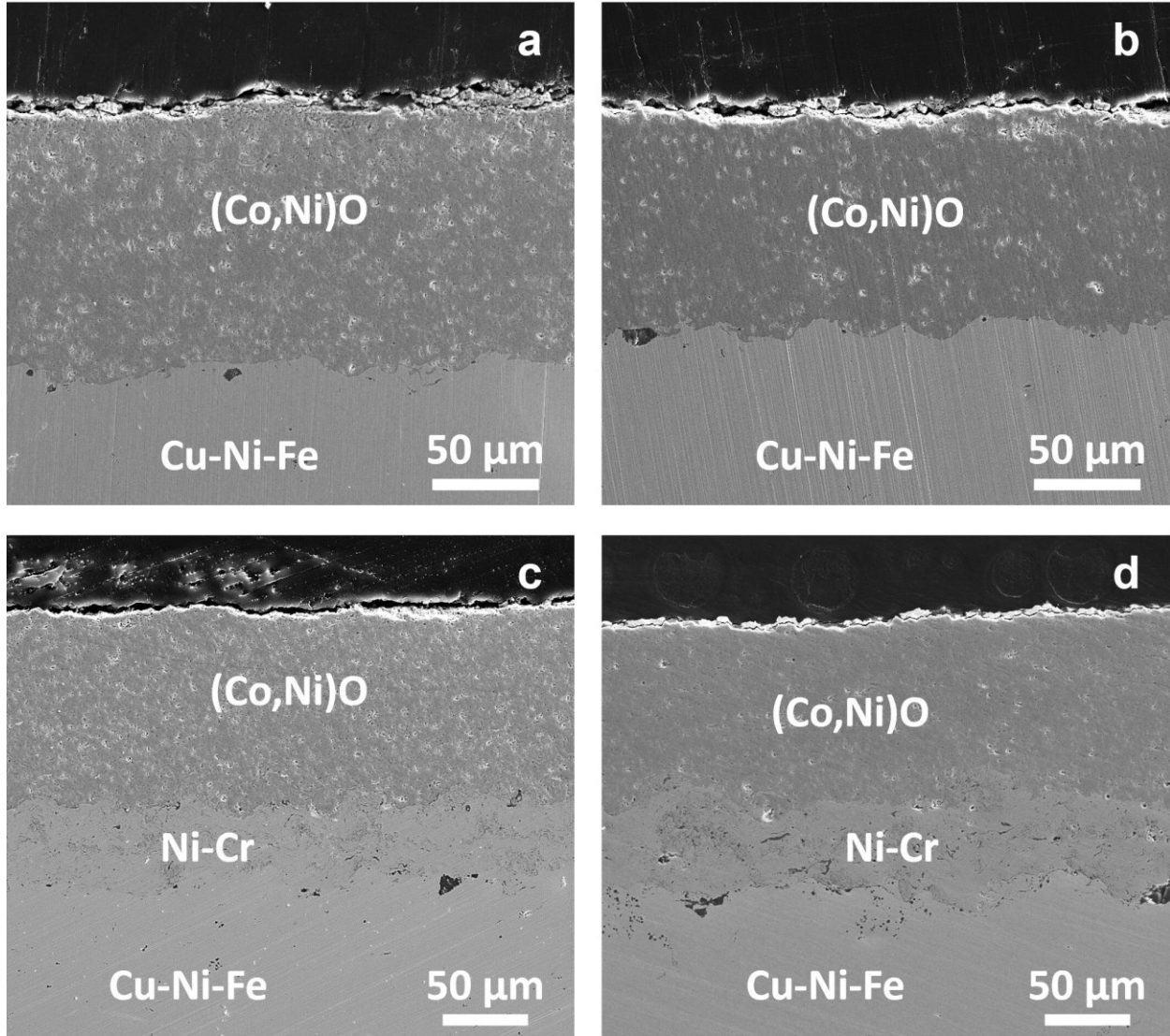


Figure C.3. Cross-sectional SEM micrographs of (a) (Co,Ni)O coating on Ni-25Fe-10Cu substrate, (b) (Co,Ni)O coating on Cu-20Ni-15Fe substrate, (c) [Ni-Cr + (Co,Ni)O] coatings on Ni-25Fe-10Cu substrate, and (d) [Ni-Cr + (Co,Ni)O] coatings on Cu-20Ni-15Fe substrate.

C.3.2. Heat treatment in air

Fig. C.3 shows the cross-sectional SEM micrographs of the as-sprayed samples. All coatings are uniform and crack-free with very low porosity. The surface of coatings is smooth, and the thickness of coatings for samples coated with a single (Co,Ni)O layer varies between 120 and 150 μm while for samples coated with [Ni-Cr + (Co,Ni)O] it is around 40-50 μm for the Ni-Cr bond layer and 100-110 μm for the (Co,Ni)O top layer. The composition of different regions

identified in the cross-sectional SEM micrographs shown in Fig. C.3, are determined using SEM/EDXS mapping (not shown here).

Fig. C.4 presents cross-sectional SEM micrographs and EDXS elemental mappings of Ni-rich substrates coated with only (Co,Ni)O as well as coated with [Ni-Cr + (Co,Ni)O] after a heat treatment in air at 1000 °C for 20 h.

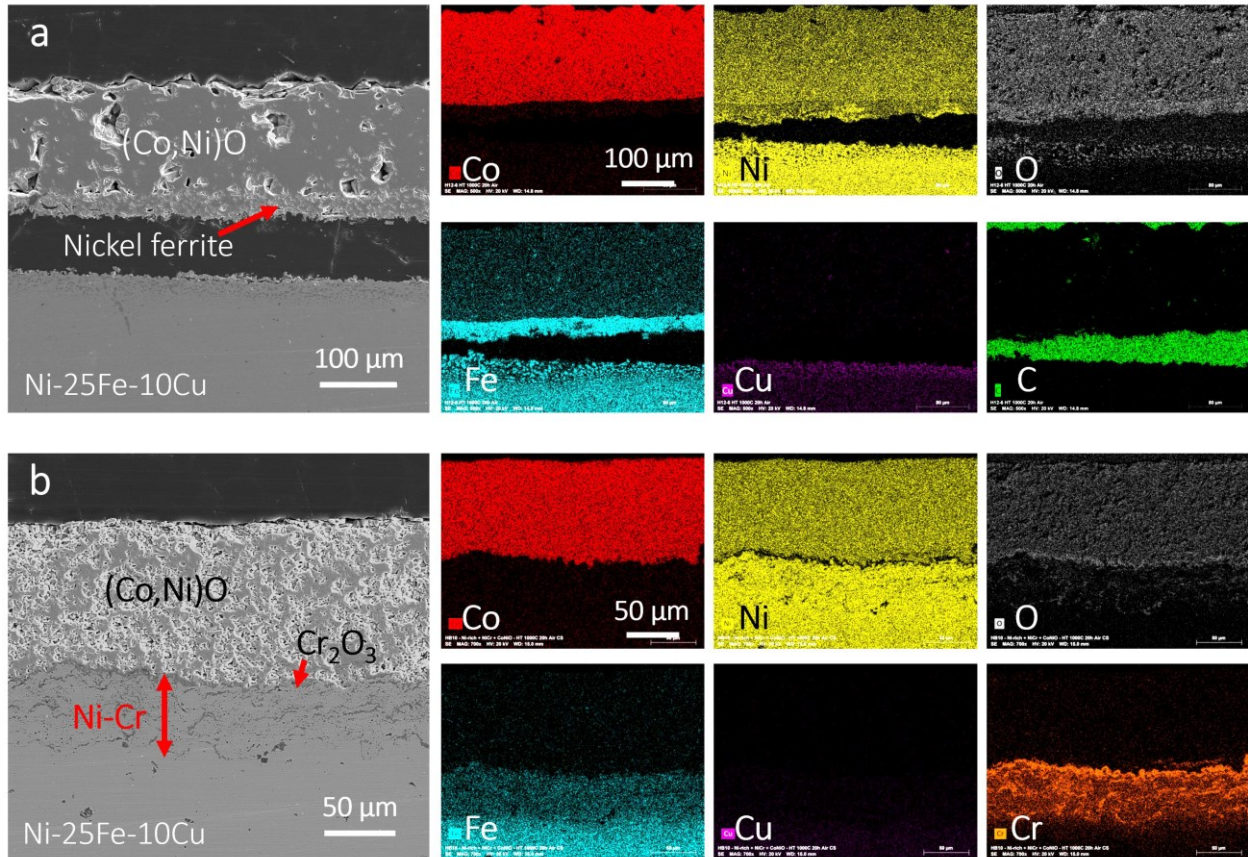


Figure C.4. Cross-sectional SEM images and EDXS elemental mappings of Ni-25Fe-10Cu coated by (a) (Co,Ni)O and (b) [Ni-Cr + (Co,Ni)O], after 20 h heat-treatment at 1000 °C in air.

On Ni-rich substrate coated with only (Co,Ni)O (Fig. C.4a), a thin inner layer ($\sim 30 \mu\text{m}$) of nickel ferrite was formed that is delaminated from the substrate but is still attached to the (Co,Ni)O coating. EDXS mappings also show that there is no outward diffusion of copper from the Ni-rich substrate to the (Co,Ni)O coating. However, small amount of iron ($\sim 4 \text{ at.}\%$) and nickel (6-10 at.%) were found in the (Co,Ni)O coating. As seen in the Cu elemental EDXS mapping, due to the outward diffusion of iron and nickel, a region richer in copper ($30 \mu\text{m}$ thick) is formed at the

surface of the Ni-rich alloy. Oxygen is also detected in this region (mainly as iron oxide inclusions), suggesting the inward diffusion of oxygen in the substrate was not fully blocked by the formation of the upper nickel ferrite layer, although it is possible that oxidation of the substrate occurred before the NiFe₂O₄ layer is fully formed.

On Ni-rich alloy coated with [Ni-Cr + (Co,Ni)O] (Fig. C.4b), both Ni-Cr bond-coat and (Co,Ni)O top-coat layers are well-attached to the Ni-rich substrate after the heat-treatment. The EDXS mappings show chromium and oxygen enrichment at the interface of the bond-coat/top-coat layers, indicating that a thin layer (~10 μm) of Cr₂O₃ was formed at the upper part of the Ni-Cr bond-coat. In contrast to the previous sample, NiFe₂O₄ layer was not formed at the coating/substrate interface, since the inward diffusion of oxygen is blocked by the formation of a continuous Cr₂O₃ layer. Also, as shown in EDXS mappings, Cu and Fe elements are detected in the Ni-Cr bond-coat at a concentration of about 4 and 8 at% respectively, while chromium is present (10 at%) in the first 10 μm of the substrate. Copper and iron atoms are not observed in the (Co,Ni)O top-coat, despite their minor diffusion from the substrate to the Ni-Cr bond-coat. It confirms the effectiveness of the Ni-Cr layer in acting as a diffusion barrier and preventing the outward diffusion of elements from the substrate to the surface of the sample.

Based on these observations, Fig. C.5 illustrates a schematic representation of the mechanisms responsible for the oxidation of coated Ni-rich alloys during the 20 h heat-treatment at 1000 °C in air. In Ni-rich alloy only coated by (Co,Ni)O (Fig. C.5a), oxygen atoms diffusing through the (Co,Ni)O coating and reaching the substrate, they are able to oxidize iron atoms in the Ni-rich substrate. Iron is the first element to oxidize, and iron oxide inclusions are formed and dispersed in a metallic matrix of Ni and Cu (rich in Ni) at the surface of the substrate. The preferential oxidation of iron is expected, because the standard Gibbs free energy of formation, ΔG°_f (at 1300 K) of iron oxides, Fe₂O₃ and Fe₃O₄ are -487 and -702 kJ mol⁻¹, respectively, lower compared to -74, -41 and -123 kJ mol⁻¹ for Cu₂O, CuO and NiO [31,32]. At the same time, nickel and iron atoms slightly diffuse and dissolve homogeneously into the (Co,Ni)O layer. The formation of iron oxide is followed by the oxidation of nickel (stage 2), which eventually results in the formation of a nickel ferrite phase at the coating/substrate interface, once the ratio between iron, nickel and oxygen atoms has the right value (stage 3). This nickel ferrite layer blocks further diffusion of oxygen, iron and nickel and prevents the underlying Ni-rich alloy from oxidation. When the sample is cooled down, the [NiFe₂O₄ + (Co,Ni)O] layer is delaminated due to the

difference in the thermal expansion coefficients of Ni-rich alloy and the oxide layers. The delamination occurred after the heat-treatment; otherwise, the Ni-rich substrate would be further oxidized after the detachment of the protective NiFe_2O_4 layer.

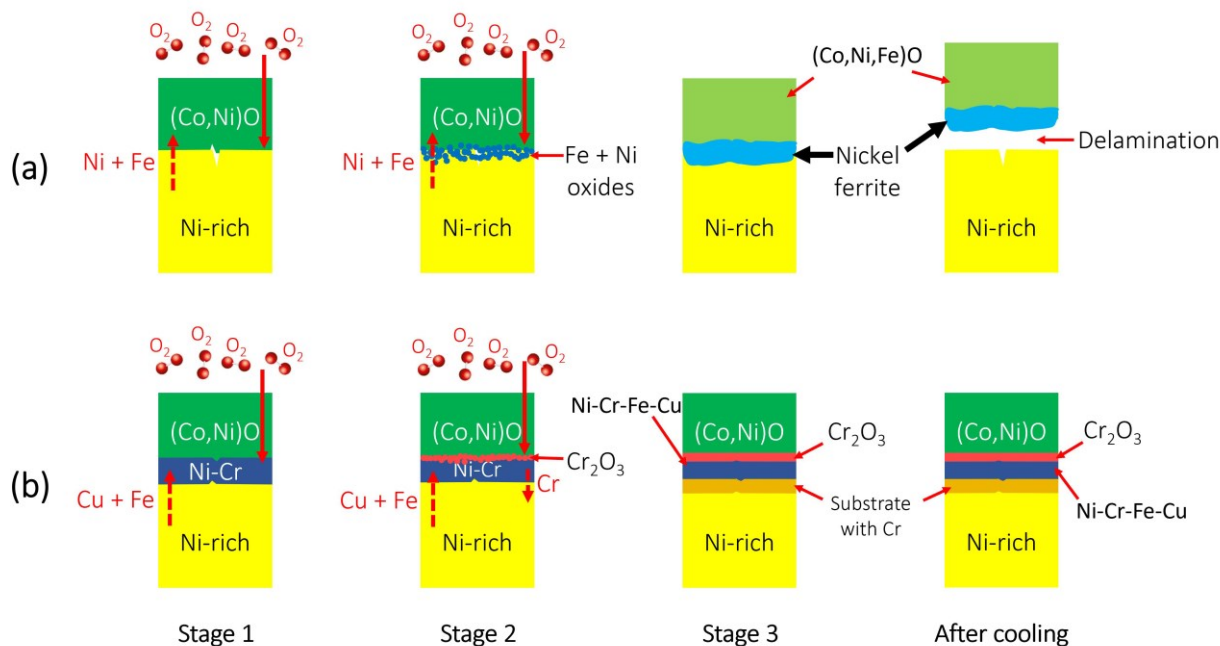


Figure C.5. Schematic representation of the oxidation stages of Ni-25Fe-10Cu coated by (a) $(\text{Co,Ni})\text{O}$ and (b) $[\text{Ni-Cr} + (\text{Co,Ni})\text{O}]$, during the 20 h heat-treatment at 1000 °C in air.

As shown in Fig. C.5b, in Ni-rich alloy coated with $[\text{Ni-Cr} + (\text{Co,Ni})\text{O}]$, due to the inward diffusion of oxygen through the $(\text{Co,Ni})\text{O}$ layer (stage 1), chromium is the first element to oxidize because chromium has a stronger affinity for oxygen than nickel, and the standard Gibbs free energy of formation, ΔG°_f (at 1300K) of Cr_2O_3 ($-840 \text{ kJ}\cdot\text{mol}^{-1}$) is much lower than that of NiO ($-123 \text{ kJ}\cdot\text{mol}^{-1}$) [33,34]. As a result, a chromium oxide layer is formed at the upper part of the Ni-Cr bond-coat. Also, Cu and Fe atoms slightly diffuse outward from the substrate to the Ni-Cr bond-coat, while chromium slightly diffuses to the substrate in the vicinity of the bond-coat/substrate interface (stage 2 and 3). Due to the formation of the Cr_2O_3 layer, no diffusion of oxygen into the substrate or that of Cu, Ni or Fe atoms into the $(\text{Co,Ni})\text{O}$ top-coat has taken place during the oxidation process. This explains the fact that no NiFe_2O_4 layer is formed at the interface with the substrate. When the sample is cooled down, the bond-coat and top-coat layers are still well-attached to the substrate and there is no sign of cracks, porosities or delamination. Indeed, the

continuous thin layer of Cr_2O_3 on the bond-coat works as a barrier for the diffusion of atoms into the top-coat, and protects the substrate from further oxidation. Also, the bond-coat layer increases the adherence of the oxide layers to the substrate and prevents their delamination when the sample is cooled down.

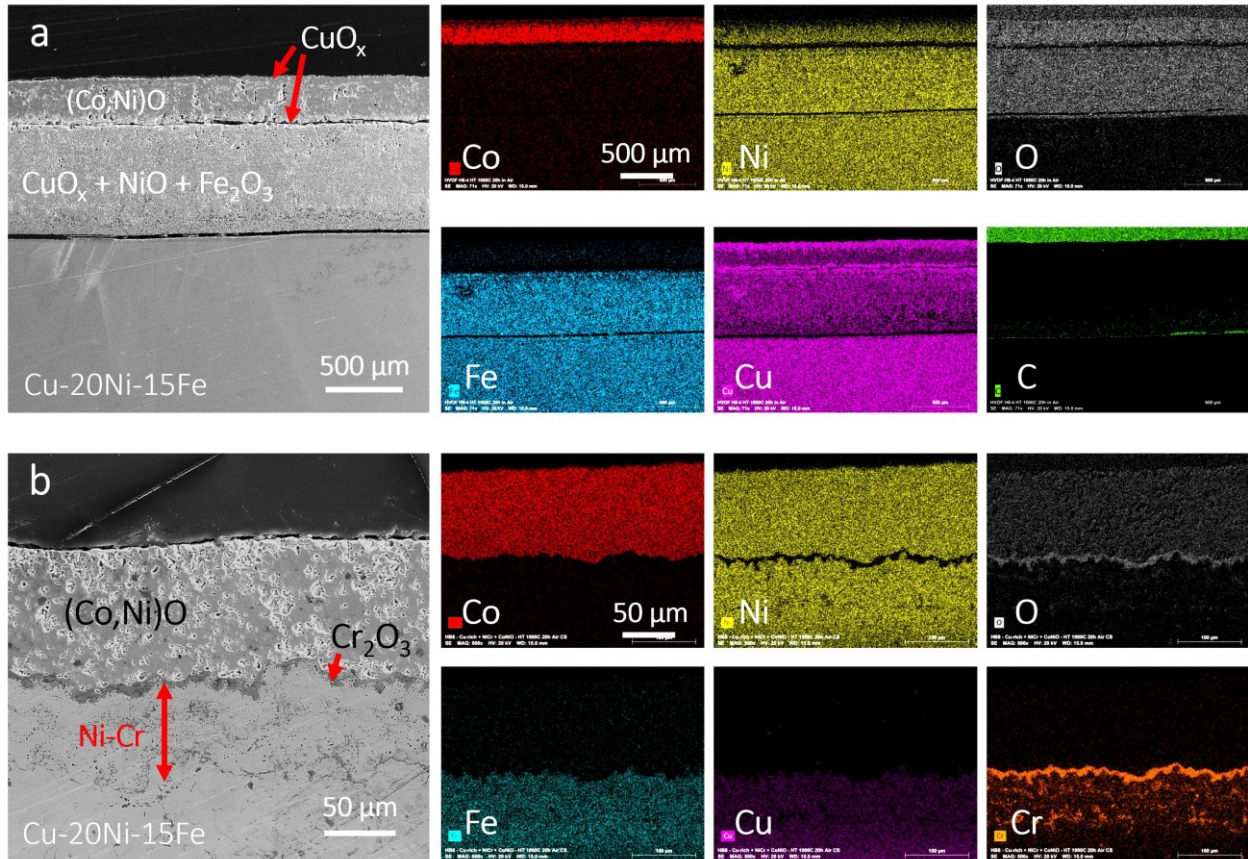


Figure C.6. Cross-sectional SEM images and EDXS mappings of Cu-20Ni-15Fe coated by (a) (Co,Ni)O and (b) [Ni-Cr + (Co,Ni)O], after 20 h heat-treatment at 1000 °C in air.

The dry oxidation behaviour of Cu-rich alloy substrate coated with (Co,Ni)O in air at 1000 °C is totally different from that of the Ni-rich alloy, as shown in Fig. C.6a. After heat treatment, the (Co,Ni)O coating is sandwiched between two layers of oxides, a copper oxide layer at the top and a very thick ($\sim 700 \mu\text{m}$) layer of [NiO + Fe₂O₃ + CuO_x] located between the (Co,Ni)O coating and the Cu-rich substrate, which results from the oxidation of the Cu-rich substrate. This last oxide layer does not have good adhesion to either the Cu-Ni-Fe substrate nor the (Co,Ni)O coating and is delaminated from both the (Co,Ni)O coating and the substrate. EDXS mappings in Fig. C.6a

confirm that there is no outward diffusion of nickel nor iron from the substrate, and unlike the Ni-rich alloy substrate coated by (Co,Ni)O, the continuous layer of nickel ferrite is not formed on the Cu-rich substrate.

The SEM-EDXS results in Fig. C.6b indicate that the behavior of the heat-treated Cu-rich substrate coated with [Ni-Cr + (Co,Ni)O] is comparable to that of the [Ni-Cr + (Co,Ni)O] coated Ni-rich substrate. Similarly, due to the formation of a protective Cr₂O₃ layer in the upper part of the Ni-Cr bond-coat, diffusion of elements into the (Co,Ni)O top-coat and oxidation of the Cu-rich substrate has been prevented. Thus, the formation of a copper oxide layer at the top and of a thick layer of [NiO + Fe₂O₃ + CuO_x] located between the (Co,Ni)O coating and the Cu-rich substrate are not observed, contrary to the Cu-rich alloy substrate coated with only (Co,Ni)O. As evident in EDXS mappings shown in Fig. C.6b, diffusion of copper and iron atoms from the Cu-rich substrate to the Ni-Cr bond-coat as well as a slight diffusion of Cr atoms from the bond-coat to the bond-coat/substrate interface are observed. Also, the coating layers are not detached after heat treatment.

Fig. C.7 illustrates the schematic representations of the oxidation stages of the coated Cu-rich alloy substrates during the 20 h heat-treatment at 1000 °C in air. The diffusion and mobility of Cu in Cu-rich alloy is a hundred times higher than that in Ni-rich alloy [35] and thus when heated in air, copper diffuses outward and is the first element to oxidize. In Cu-rich alloy coated with only (Co,Ni)O, the outward diffusion of Cu from the substrate through the (Co,Ni)O layer and the formation of a CuO_x layer at the surface of the sample, is accompanied by the inward diffusion of oxygen to the underlying alloy (stage 1 and 2 in Fig. C.7a). EDXS mappings in Fig. C.6a confirm that there is no outward diffusion of nickel nor iron from the substrate. Hence, the (Co,Ni)O coating is sandwiched between two layers of oxides. Unlike nickel ferrite, these CuO_x layers do not block the inward diffusion of oxygen or the outward diffusion of copper. As a result, the oxidation process continues and a thick [NiO + Fe₂O₃ + CuO_x] layer forms between the (Co,Ni)O and the Cu-rich substrate, its thickness increasing with heating time (stage 3). Here, the presence of CuO_x in large amount prevents the formation of NiFe₂O₄. When the sample is cooled down, the [NiO + Fe₂O₃ + CuO_x] layer is delaminated from both the Cu-rich substrate and the (Co,Ni)O coating.

The oxidation mechanism of Cu-rich substrates coated with [Ni-Cr + (Co,Ni)O] (Fig. C.7b) is similar to that of Ni-rich substrates coated with the same. When heated at 1000 °C in air, due to the inward diffusion of oxygen (stage 1), a thin layer of Cr₂O₃ is formed in the bond-coat layer,

which completely blocked further inward diffusion of oxygen (stage 2). Diffusion of Cu and Fe atoms from the Cu-rich substrate to the Ni-Cr bond-coat, as well as diffusion of Cr from the bond-coat to the Cu-rich substrate occurred during the heat-treatment (stage 2 and 3). Also, NiFe_2O_4 or $[\text{NiO} + \text{Fe}_2\text{O}_3 + \text{CuO}_x]$ layers are not formed and the coating layers are not delaminated when the sample is cooled down. The anodic behaviour of uncoated Cu-Ni-Fe alloys as well as coated with $(\text{Co},\text{Ni})\text{O}$ and $[\text{Ni-Cr} + (\text{Co},\text{Ni})\text{O}]$ are presented below.

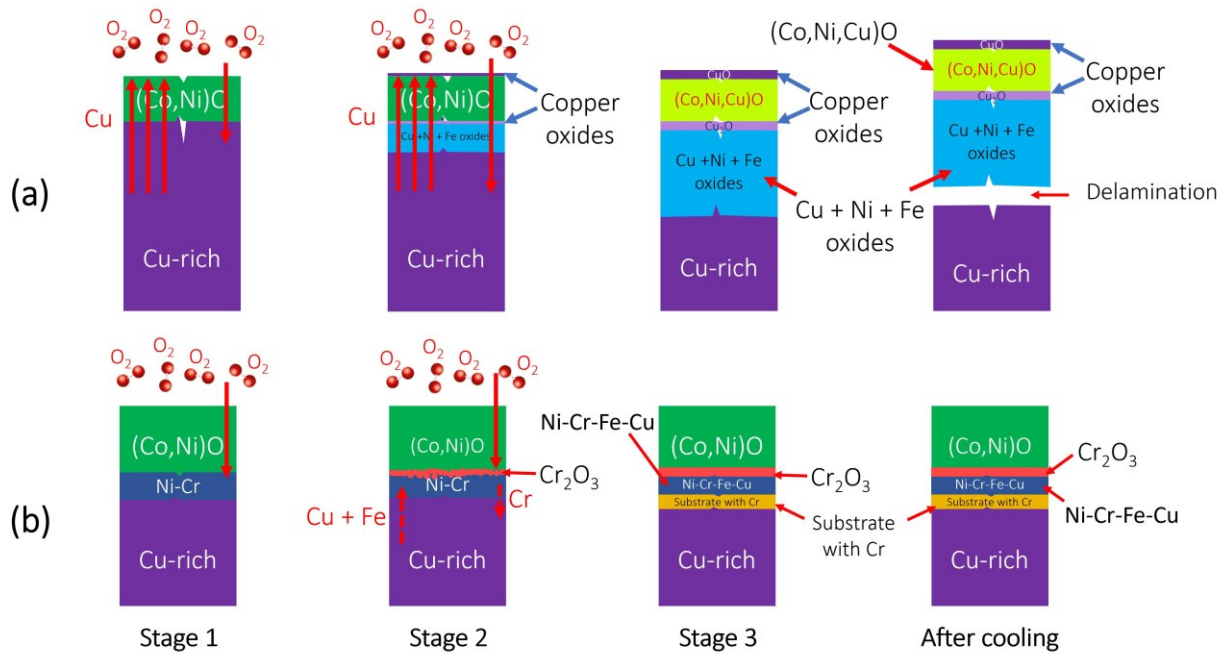


Figure C.7. Schematic representation of oxidation stages of (a) Cu-20Ni-15Fe coated by $(\text{Co},\text{Ni})\text{O}$ and (b) Cu-20Ni-15Fe coated by $[\text{Ni-Cr} + (\text{Co},\text{Ni})\text{O}]$, during the 20 h heat-treatment at 1000 °C in air.

C.3.3. Cell voltage evolution

Fig. C.8a-d shows the cell voltage evolution during the Al electrolysis performed at 1000 °C using the Ni-25Fe-10Cu and Cu-20Ni-15Fe anodes coated with $(\text{Co},\text{Ni})\text{O}$ and $[\text{Ni-Cr} + (\text{Co},\text{Ni})\text{O}]$. The cathode potential and the ohmic drop related to the electrolyte and electrical connections are expected to be stable and similar for different electrolysis experiments. Consequently, the variations of the cell voltage shown in Fig. C.8 are considered as indicative of the variation of the anode potential. It must however be noted that only one side of the disc shaped substrates was coated by HVOF, thus the variation of the cell voltage is representative of the

variation of the anode potential of both the coated and the uncoated sides of the Cu-Ni-Fe alloy substrates. The interpretation of these curves is therefore challenging.

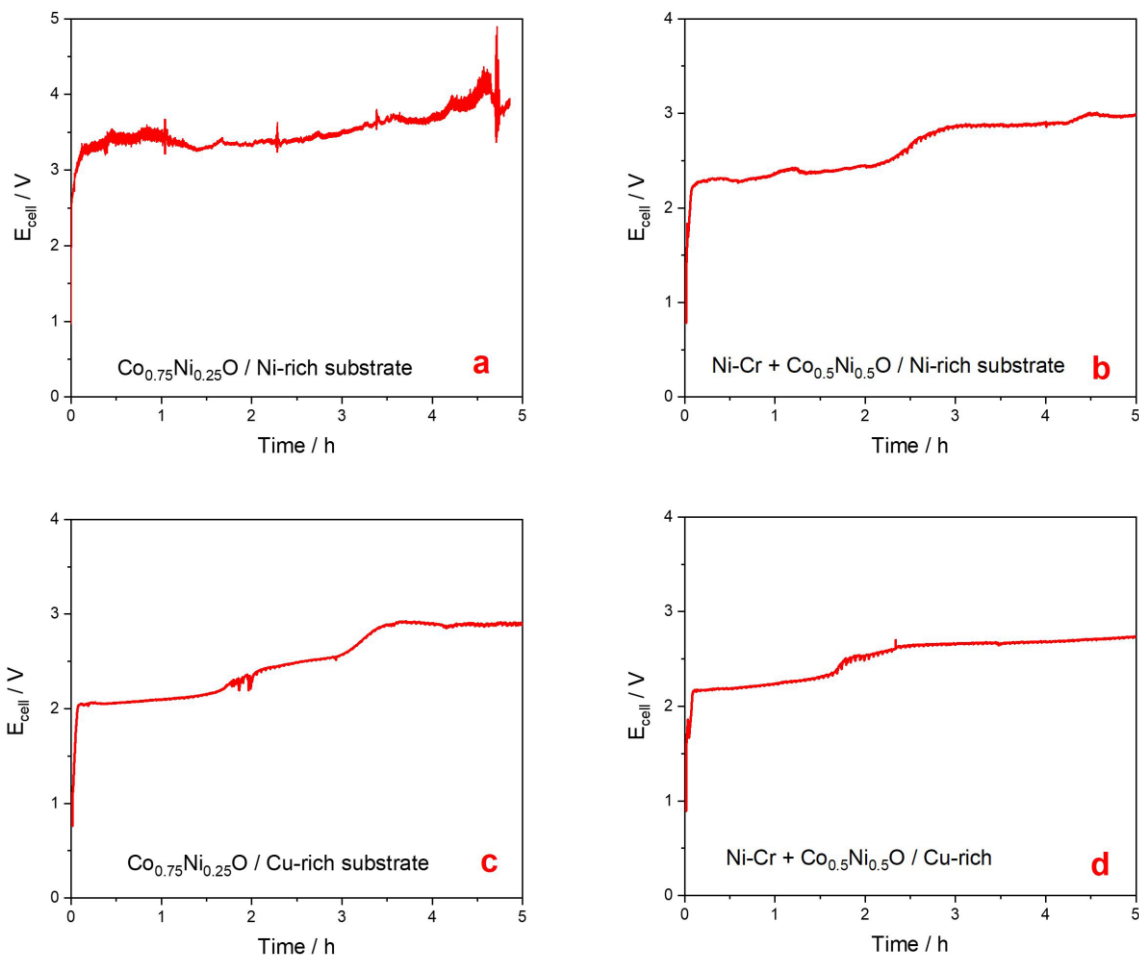


Figure C.8. Cell voltage vs. electrolysis time performed at 1000 °C for (a) Ni-rich anode coated with (Co,Ni)O, (b) Ni-rich anode coated with [Ni-Cr + (Co,Ni)O], (c) Cu-rich anode coated with (Co,Ni)O and (d) Cu-rich anode coated with [Ni-Cr + (Co,Ni)O].

For Ni-rich alloy coated with (Co,Ni)O (Fig. C.8a), the cell voltage reached 2.9 V at the beginning of electrolysis within few minutes followed by rapid fluctuations and a continuous increase of the cell voltage to reach about 4 V at the end of the electrolysis. This voltage instability suggests that the oxide layers formed on the anode are not chemically and/or mechanically stable and thus this anode is significantly degraded upon Al electrolysis. For the other anodes (Fig. C.8b-d), an increase of the cell voltage is also observed due to the anode oxidation. However, after about

2-3 h of electrolysis, a nearly steady state is reached with a cell voltage stabilized around 3 V associated with the oxygen evolution reaction.

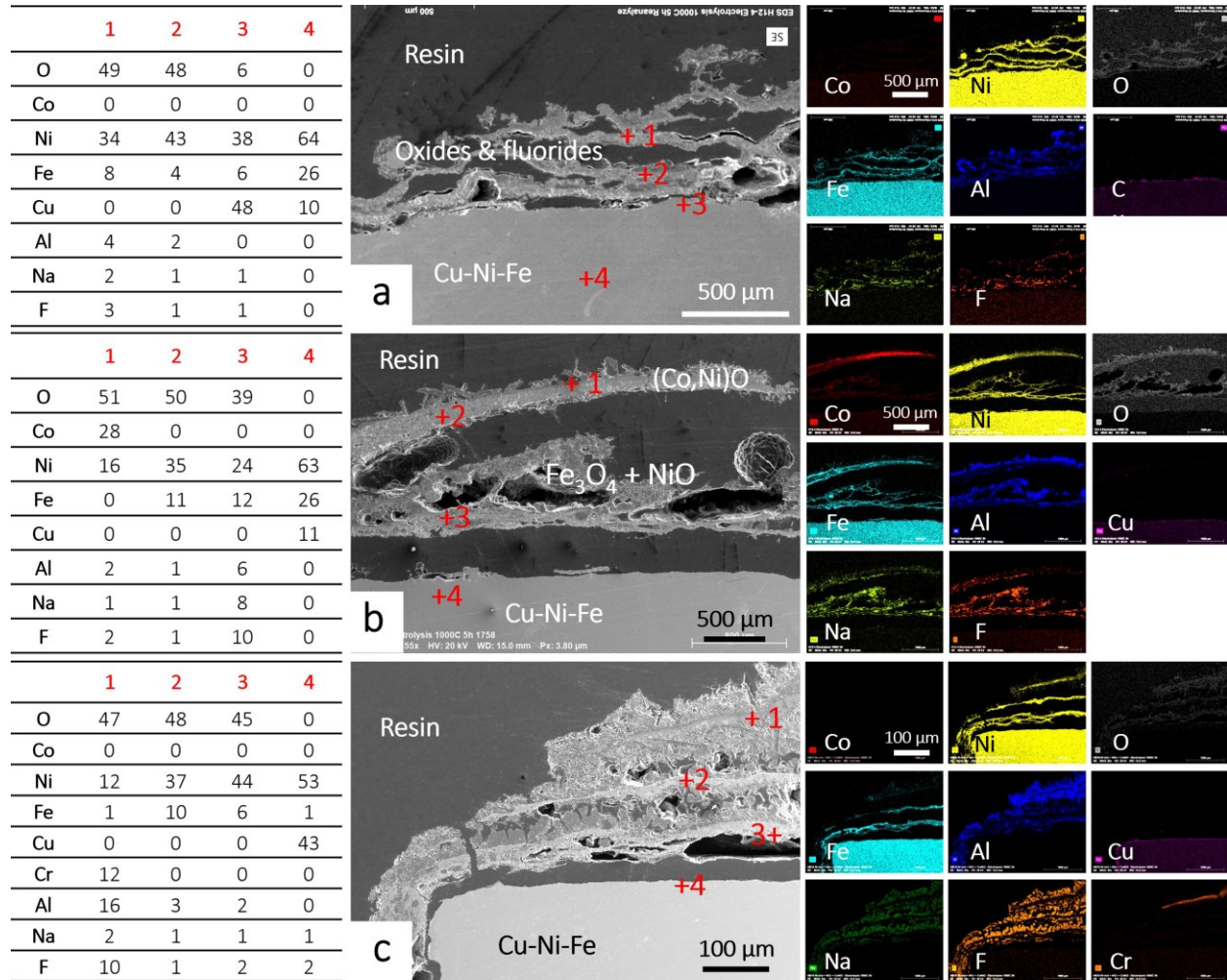


Figure C.9. Cross-sectional SEM images and EDXS analyses and mappings of Ni-25Fe-10Cu anodes (a) uncoated part, (b) coated with (Co,Ni)O and (c) coated with (Co,Ni)O + Ni-Cr after aluminum electrolysis at 1000 °C for 5 h.

C.3.4. Characterization of the anodes after Al electrolysis

Figs. C.9-10 show cross-sectional SEM micrographs as well as elemental EDXS analyses (in at.%) and mappings of the anodes after 5 h of aluminum electrolysis at 1000 °C. For both Ni-rich and Cu-rich anodes, cross-sectional SEM micrographs of uncoated, (Co,Ni)O and [Ni-Cr + (Co,Ni)O] parts of the anodes are presented.

On the uncoated parts of the Ni-rich anode, several thin delaminated layers of oxides are formed, as shown in Fig C.9a. These oxide layers are mixtures of nickel and iron oxides (richer in Ni). Electrolyte is infiltrated between these oxide layers and thus, a multilayered structure composed of a succession of thin layers of oxides separated by infiltrated electrolyte is formed. Due to the outward diffusion of iron and nickel, a very thin Cu-rich region is also formed at the surface of the substrate.

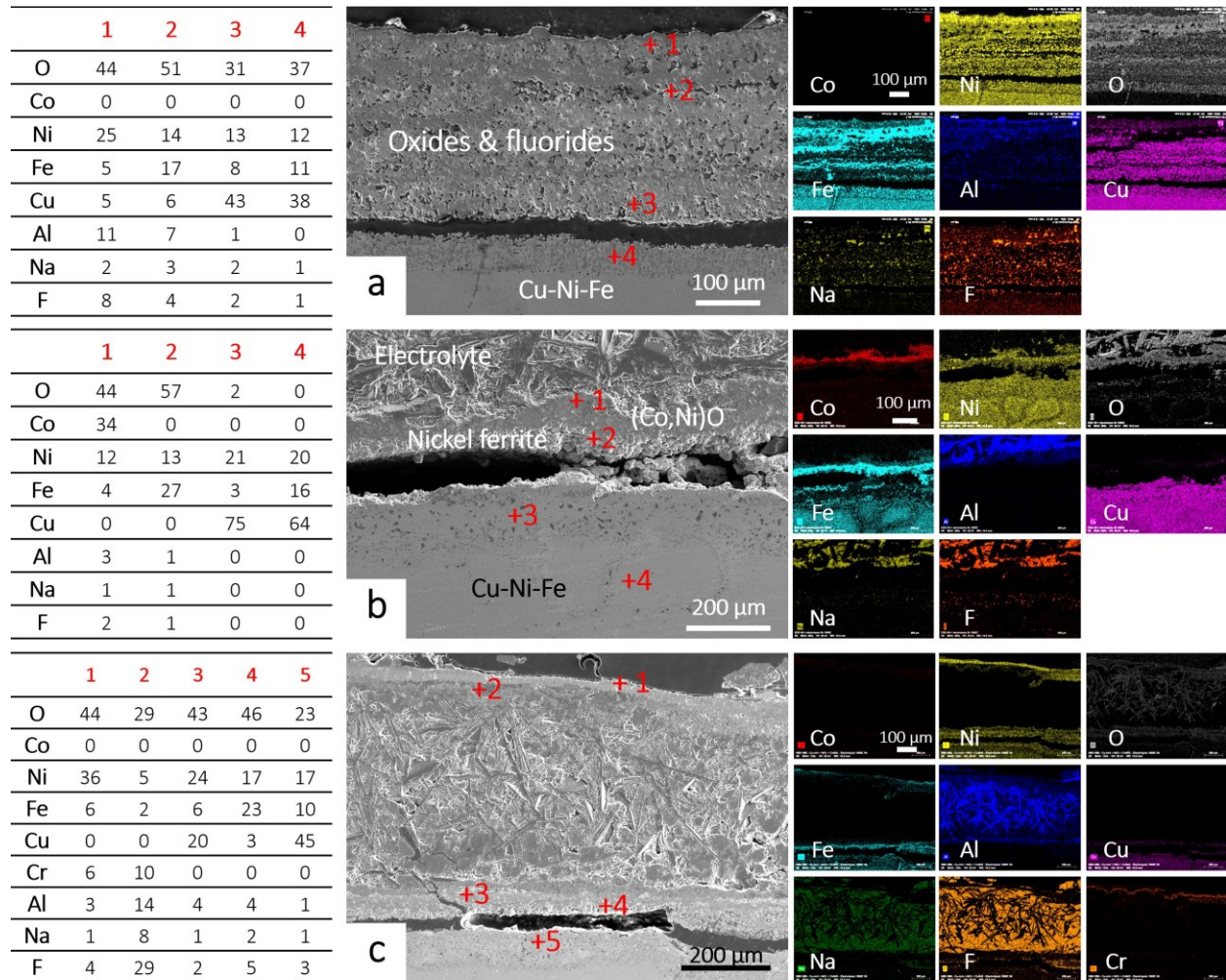


Figure C.10. Cross-sectional SEM images and EDXS analyses and mappings of Cu-20Ni-15Fe anodes (a) uncoated part, (b) coated with (Co,Ni)O and (c) coated with (Co,Ni)O + Ni-Cr after aluminum electrolysis at 1000 °C for 5 h.

On the Ni-rich anode coated with (Co,Ni)O (Fig C.9b), the (Co,Ni)O coating is delaminated and several detached thin layers (5 – 20 μm) of oxides are formed underneath the HVOF coating. Due to the infiltration of the electrolyte, these thin layers are composed of iron and

nickel oxides as well as components of the electrolyte, forming a multilayered structure composed of a succession of oxides and electrolyte, similar to that observed on the uncoated Ni-rich anode. The nickel and iron oxide scales are richer in nickel indicating that the Ni/Fe ratio was not optimal to favor the solid-state reaction yielding the formation of a nickel ferrite layer.

On the Ni-rich anode coated with [Ni-Cr + (Co,Ni)O] (Fig. C.9c), the (Co,Ni)O coating is no longer observed, *i.e.* it was completely delaminated, and the outermost oxide layer is a mixture of nickel and chromium oxides, formed as a result of the oxidation of the Ni-Cr layer, with a thickness ~ 40 μm and that detached from the substrate. A similar multilayered structure of several thin layers of oxides are formed beneath the Ni-Cr bond-coat that are delaminated as well. Similarly, these oxide layers are mixtures of nickel and iron oxides (richer in Ni). The electrolyte is infiltrated between these oxide layers and thus, a multilayered structure composed of a succession of thin layers of oxides separated by the infiltrated electrolyte is formed. At the surface of the alloy, a ~ 30 μm Cu-rich layer (very poor in iron) is formed.

These results indicate that on Ni-rich alloy substrate, the deposition of either (Co,Ni)O or [Ni-Cr + (Co,Ni)O] do not provide the required protection from oxidation and fluorination. This is most probably due to the premature delamination and detachment of these layers before a protective nickel ferrite layer could form at the surface of the Ni-rich alloy substrate. The difference in the behaviour of Ni-rich alloy during dry oxidation and electrolysis tests highlights the key role of the reactions with the electrolyte (e.g., dissolution, fluorination) on the anode degradation process. In addition, the mechanical action of the O₂ bubbles can likely induce the delamination of the oxide scales that form during electrolysis.

As mentioned earlier, in Ni-rich alloy substrate, iron is the first element to oxidize, followed by nickel. Thus, during electrolysis, it is expected that the oxidation of iron and nickel would lead to the formation of the nickel ferrite phase, similar to the results observed during the dry oxidation tests in air on the (Co,Ni)O coated sample. However, during aluminum electrolysis, the dissolution rate of iron oxide is higher than its oxidation rate. So, due to the higher solubility of iron oxide compared to nickel oxide in the molten electrolyte, that optimal Ni/Fe ratio for the formation of NiFe₂O₄ never occurs. The higher dissolution rate of iron oxide results in the formation of a Ni-rich scale that can react with the electrolyte and forms a poorly adherent NiAl₂O₄ layer. Also, the fluorination of Ni-rich alloys and the formation of NiF₂ and FeF₂ can happen, since the Ni-rich substrate is not protected by a protective oxide scale during Al electrolysis. As

mentioned earlier, the fluctuations in the cell potential observed when using Ni-rich alloy as an anode might be due to the continuous formation and dissolution of these iron and nickel oxides and fluorides.

Similar anodic behaviour was observed for uncoated Ni-rich alloy substrate during low temperature electrolysis at 700 °C in KF-based electrolyte, as investigated previously in our group [9]. After 10 h electrolysis at 700 °C, a multilayered structure composed of a succession of thin layers of oxides (~5 µm thick, mainly constituted of NiO and Fe₂O₃) separated by electrolyte layers (~10 µm thick) was formed at the surface of Ni-rich anode. Also, in that case, NiFe₂O₄ was not formed at the surface of Ni-rich anode, even after 10 hours of electrolysis at 700 °C. The thickness of this multilayered structure varied between 20 and 100 µm, indicating its partial delamination during Al electrolysis. The obtained results confirmed the inefficiency of the oxide scale formed on the Ni-25Fe-10Cu anode to prevent electrolyte infiltration and its spallation during Al electrolysis, resulting in an unstable cell voltage and a poor corrosion resistance.

Regarding the Cu-20Ni-15Fe based anodes (Fig. C.10), on the uncoated parts of the anode, a 300-400 µm thick layer of oxides and fluorides is formed, as shown in Fig. C.10a. This thick scale consists of nonhomogeneous regions of [CuO_x + Fe₂O₃ + NiO]. The composition of the oxides in different regions of this scale is not uniform and the relative CuO_x, Fe₂O₃ and NiO vary from point to point. Electrolyte has infiltrated into the porosities of the oxide scale, and metal fluorides are dispersed in this thick oxide layer. The upper part of the scale is a ~100 µm thick Cu-poor region, which is composed of an Ni-rich outer region (zone 1 in Fig. C.10a, SEM image) and an inner region composed of iron and nickel oxides (zone 2 in Fig. C.10a, SEM image). The inner part of the scale underneath this ~100 µm Cu-poor region, is richer in copper and is composed of [CuO_x + Fe₂O₃ + NiO] (~200 µm thick, zone 3 in Fig. C.10a, SEM image). Nickel ferrite is not formed on the uncoated parts of the anode yet and fluorination has occurred at the surface of the Cu-Ni-Fe alloy substrate underneath the thick porous oxide layer. Similar results were obtained in our previous work [9], where uncoated Cu-20Ni-15Fe alloy was used as an anode for low temperature electrolysis at 700 °C in KF-based electrolyte. It was shown that because of the higher solubility of Cu and Fe oxides compared to nickel oxide, a delaminated oxide scale mainly composed of NiAl₂O₄ was formed in the electrolyte near the anode surface. This phase is formed due to the reaction of NiO-rich surface scale with alumina from the electrolyte. After 20 h electrolysis at 700 °C, a CuO_x layer, an almost continuous NiFe₂O₄ layer (5-10 µm thick) and some

discontinuous $\text{NiO} + \text{Fe}_2\text{O}_3 + \text{CuO}_x$ regions were detected at the surface of Cu-rich alloy. Also, a nickel and iron fluoride layer was formed at the alloy/oxide interface and some electrolyte was detected in this area, indicating the partial fluorination of the Cu-rich alloy substrate despite the formation of the nickel ferrite layer.

On the Cu-rich anode coated with $(\text{Co,Ni})\text{O}$ (Fig. C.10b), the upper part of the scale is made of the $(\text{Co,Ni})\text{O}$ coating. A continuous and dense layer of nickel ferrite ($\sim 30 \mu\text{m}$) is formed on the inner side of the $(\text{Co,Ni})\text{O}$ coating. This oxide scale made of $(\text{Co,Ni})\text{O}$ and NiFe_2O_4 layers was detached from the Cu-rich alloy substrate. The delamination occurs after the electrolysis, when the anode was cooled down, because no electrolyte infiltration was detected in this area. Also, the Cu-rich substrate is not oxidized underneath the delaminated $[\text{NiFe}_2\text{O}_4 + (\text{Co,Ni})\text{O}]$ layer, confirming that their detachment occurred during cooling. The thickness of $(\text{Co,Ni})\text{O}$ layer is not uniform which suggests its partial delamination or dissolution during the aluminum electrolysis. This is in accordance with our calculation showing that a maximum of $\sim 25 \mu\text{m}$ of $(\text{Co,Ni})\text{O}$ coating would be dissolved in molten electrolyte.

On the Cu-rich anode coated with $[\text{Ni-Cr} + (\text{Co,Ni})\text{O}]$ (Fig. C.10c), the $(\text{Co,Ni})\text{O}$ coating is completely delaminated during aluminum electrolysis. The outermost oxide layer is a Ni-rich mixture of nickel, chromium and iron oxides with $\sim 40 \mu\text{m}$ thickness. This layer corresponds to the Ni-Cr bond-coat, in which iron atoms originating from the substrate have diffused and been oxidized. The inner part of this oxide layer is slightly richer in chromium. A delaminated 70-100 μm thick nonhomogeneous layer of $[\text{NiO} + \text{Fe}_2\text{O}_3 + \text{CuO}_x]$ is formed near the Cu-rich substrate, and the electrolyte has penetrated between this thicker oxide layer and the outermost thinner Ni-Cr-Fe oxide layer. A 120 μm thick layer of $[\text{NiO} + \text{Fe}_2\text{O}_3 + \text{CuO}_x]$ that is also formed at the surface of the Cu-rich alloy is observed that is still attached to the substrate. EDXS analysis of different parts of the oxide scale after electrolysis reveals that nickel ferrite is not formed at the surface of this anode and the $[\text{Ni-Cr} + (\text{Co,Ni})\text{O}]$ coating layer does not improve the resistance of the Cu-rich anode to oxidation and fluorination during Al electrolysis. As shown above, upon dry oxidation, there is not delamination of the $[\text{Ni-Cr} + (\text{Co,Ni})\text{O}]$ coating layers and oxidation of the substrate is prevented. On the contrary, during aluminum electrolysis, the $[\text{Ni-Cr} + (\text{Co,Ni})\text{O}]$ coating delaminates and thus does not protect the anode from oxidation. The mechanism under this delamination is presently unclear.

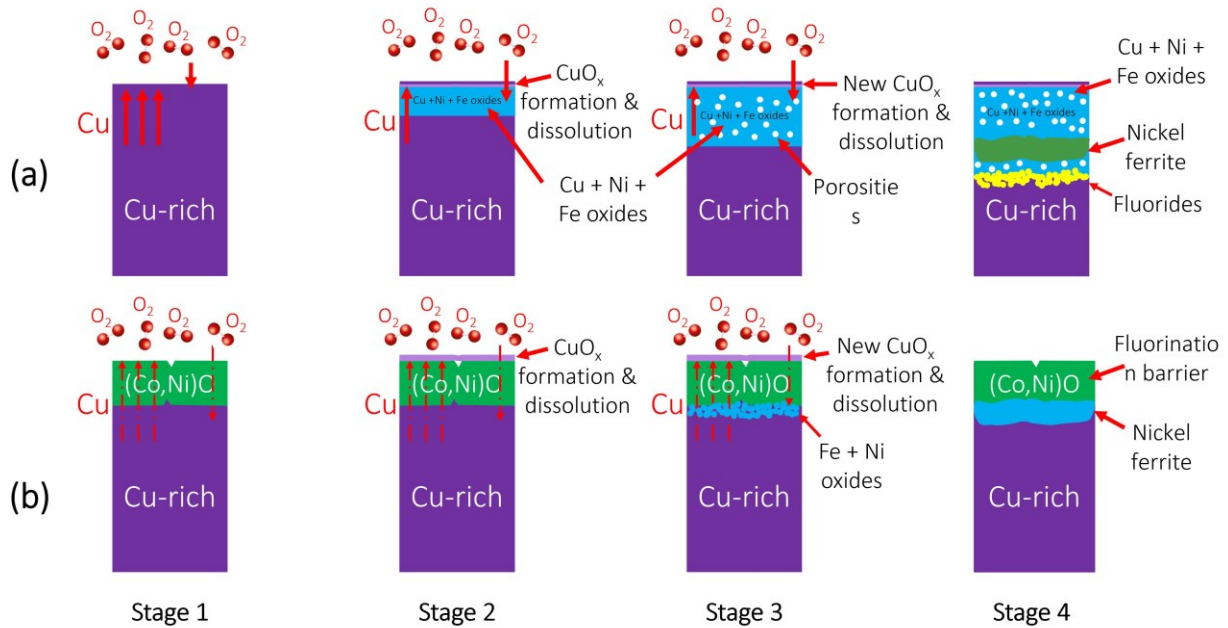


Figure C.11. Schematic representation of oxidation stages during Al electrolysis at 1000 °C of (a) Cu-20Ni-15Fe anode (a) without coating and (b) coated by (Co,Ni)O.

To understand better the Cu-rich anode oxidation and corrosion mechanisms during aluminum electrolysis, different stages of oxidation and corrosion on the (Co,Ni)O coated and uncoated sides of the anode are presented schematically in Fig. C.11. In uncoated Cu-rich alloy, similar to dry oxidation tests, in the first stage during aluminum electrolysis, the outward diffusion of copper occurs while nickel and iron do not diffuse outward, due to their lower mobility in the Cu-rich alloy (Fig. C.11a). Thus, a layer of copper oxide will form at the surface of the substrate in direct contact with the cryolitic media and a Cu-poor region will form underneath. At the same time, inward diffusion oxygen into the Cu-rich anode happens, resulting in the oxidation of iron, nickel and remaining copper substrate, underneath the outer copper oxide layer (stage 2). Since copper oxide has relatively high dissolution rate in molten electrolyte, the thin CuO_x layer formed at the surface of the anode dissolves and the outward diffusion of copper to the surface continues, forming another thin layer of CuO_x . Hence, the underlying alloy gets progressively poorer in copper. As shown in Fig. C.10b, the outermost part of the scale is rich in nickel and is poor in both copper and iron, while the inner parts contain higher contents of copper and iron. The relatively high solubility of copper and iron oxide in molten cryolite leads to their dissolution resulting the outermost part of the scale being richer in nickel. The thickness of $[\text{NiO} + \text{Fe}_2\text{O}_3 + \text{CuO}_x]$ scale

increases due to the continuous inward diffusion of oxygen, while some porosities are formed in this scale because of the outward diffusion of copper (stage 3). The formation and dissolution of copper oxide at the surface of the alloy continues until the ratio between NiO and Fe₂O₃ in the inner parts of the scale formed on the anode is such that NiFe₂O₄ is formed (stage 4). Nickel ferrite is expected to form from NiO and Fe₂O₃, whenever the correct ratio of NiO/Fe₂O₃ is available as the following equation:



However, it takes time for this nickel ferrite layer to form and the underlying Cu-rich alloy is not protected during this time. Since the scale on the uncoated Cu-rich anode is porous, electrolyte can infiltrate and fluorinate the alloy resulting in the formation of iron and nickel fluorides in the alloy (stage 4). The same behaviour was observed in a previous work in our group where an uncoated Cu-20Ni-15Fe alloy was used as anode for aluminum electrolysis in KF-based electrolyte at 700 °C [9].

As illustrated in Fig. C.11b, on the (Co,Ni)O coated side of the Cu-rich anode, similar to dry oxidation tests, (Co,Ni)O coating does not function as a barrier for the outward diffusion of copper and the inward diffusion of oxygen. The presence of the (Co,Ni)O coating only reduces their diffusion rates. Also, it was shown that nickel and iron do not diffuse as fast as copper due to their lower mobility in the Cu-rich alloy and the presence of a (Co,Ni)O coating. Thus, copper will diffuse through the (Co,Ni)O layer to the surface of the anode in direct contact with the cryolitic media, which results in the formation and dissolution of copper oxide (stage 2 in Fig. C.11b). At the same time, inward diffusion oxygen occurs into the underlying alloy. Due to the outward diffusion of copper, a Cu-poor region will form in the vicinity of the (Co,Ni)O/Cu-rich interface, and the inward diffusion of oxygen results in the oxidation of iron and nickel in a region that is continuously getting poorer in copper (stage 3). Consequently, [NiO + Fe₂O₃] are formed beneath the interface of (Co,Ni)O/Cu-rich and this process continues until eventually a nickel ferrite phase forms (stage 4). The dense (Co,Ni)O coating layer acts a fluorination/dissolution barrier and hence, prevents the underlying Cu-Ni-Fe alloy from fluorination/dissolution during the time required for the formation of NiFe₂O₄. The difference between the coated and uncoated sides of Cu-rich alloy indicates the key role of (Co,Ni)O coating in controlling the diffusion, oxidation and dissolution processes during aluminum electrolysis to favor the formation of a protective nickel ferrite layer.

C.4. Conclusion

The objective of this study was to evaluate the impact of (Co,Ni)O and [Ni-Cr + (Co,Ni)O] HVOF coatings on the degradation resistance of Cu-Ni-Fe anodes (Cu-rich and Ni-rich alloys) upon Al electrolysis at 1000 °C. In a first step, the low solubility of (Co,Ni)O materials in the alumina-saturated cryolitic bath was confirmed. Despite a great dry oxidation resistance of both Cu-Ni-Fe anodes coated with [Ni-Cr + (Co,Ni)O], their anodic behaviour is not improved compared to coating with only (Co,Ni)O. Indeed, during aluminum electrolysis, the [Ni-Cr + (Co,Ni)O] coating delaminates and does not protect the anode from oxidation. On the other hand, it was shown that coating Cu-20Ni-15Fe alloy with a (Co,Ni)O layer leads to a significant increase in the corrosion resistance of the substrate and a coherent NiFe₂O₄ layer was formed beneath the (Co,Ni)O layer. In comparison, a relatively thick layer of nonhomogeneous [NiO + Fe₂O₃ + CuO_x] was formed on the uncoated side of the Cu-20Ni-15Fe alloy substrate, with no sign of the formation of nickel ferrite layer after 5 hours electrolysis. This points to the critical role of the HVOF (Co,Ni)O coating in the formation of the protective nickel ferrite layer, as well as in preventing the fluorination of the Cu-Ni-Fe alloy substrate. Prolonged Al electrolysis experiments, *i.e.* up to the complete dissolution of the (Co,Ni)O coating layer, must be performed to confirm the long-term stability of the anode. It was also shown that the composition of the Cu-Ni-Fe alloy plays a key role in the formation of the protective NiFe₂O₄ layer since the latter was not observed on the (Co,Ni)O coated side nor on the uncoated side of the Ni-rich alloy substrate.

Supplementary information

A calculation was performed to determine the total thickness of Co_{0.75}Ni_{0.25}O coatings that is dissolved during aluminum electrolysis. The volume of electrolyte was considered to be constant during 5 h aluminum electrolysis. The saturation value for the dissolution of Co and Ni in molten sodium-based electrolyte (Fig. C.2c) was used in this calculation. The size and density of disc-shape coated anode used for electrolysis is given in the table below:

	Thickness	Density	Substrate diameter
(Co,Ni)O coating	120 * 10 ⁻⁴ cm	6.6975 g/cm ³	1.51 cm

$$\text{Coating volume} = \pi r^2 h = \pi \times 0.7552 \times 0.012 = 0.02149 \text{ cm}^3$$

$$\text{Coating weight} = 6.4975 \times 0.02149 = 0.1396 \text{ g}$$

(Co,Ni)O is composed of 78.6 wt.% of (Co + Ni) and 21.4 wt.% of O.

Total (Co + Ni) dissolution is 57 ppm = 0.057 g/kg of electrolyte

400 grams of electrolyte was used for electrolysis, so 0.0228 grams of (Co + Ni) can be dissolved, corresponding to $(0.0228/78.6) \times 100 = 0.0290$ grams of (Co,Ni)O.

The volume of (Co,Ni)O coating that can be dissolved is:

$$0.0290 \text{ g} / 6.4975 \text{ g/cm}^3 = 0.00446 \text{ cm}^3$$

Considering a disc-shape anode with 1.51 cm diameter, if a volume of 0.00486 cm³ of (Co,Ni)O coating is dissolved, the corresponding thickness of the coating will be dissolved is

$$h = V / \pi r^2 = 0.00486 / (\pi \times 0.7552) = 0.0025 \text{ cm (25 } \mu\text{m)}.$$

References

[1] H. Kvande, W. Haupin, Inert anodes for Al smelters: energy balances and environmental impact, JOM. 53 (2001) 29–33.

[2] I. Galasiu, R. Galasiu, J. Thonstad, Inert anodes for aluminium electrolysis, 1st ed., GmbH Aluminium-Verlag Market- ing & Komuunikation, Dusseldorf, 2007.

[3] H. Yin, D. Tang, H. Zhu, Y. Zhang, D. Wang, Production of iron and oxygen in molten K₂CO₃-Na₂CO₃ by electrochemically splitting Fe₂O₃ using a cost affordable inert anode. Electrochem. Commun. 13 (2011) 1521–1524.

[4] M. Esmaily, A.N. Mortazavi, N. Birbilis, A. Allanore, Oxidation and electrical properties of chromium–iron alloys in a corrosive molten electrolyte environment, Sci. Rep. 10 (2020) 14833.

[5] P. Sai Krishna, Y. Andrey S., P. Peter V., Progress of inert anodes in aluminium industry: Review, J. Sib. Fed. Univ. Chem. 11 (2018) 18–30.

[6] E. Gavrilova, G. Goupil, B. Davis, D. Guay, L. Roué, On the key role of Cu on the oxidation behavior of Cu–Ni–Fe based anodes for Al electrolysis, Corros. Sci. 101 (2015) 105–113.

- [7] G. Goupil, S. Jucken, D. Poirier, J.G. Legoux, E. Irissou, B. Davis, D. Guay, L. Roué, Cold sprayed Cu–Ni–Fe anode for Al production, *Corros. Sci.* 90 (2015) 259–265.
- [8] S. Jucken, M.H. Martin, E. Irissou, B. Davis, D. Guay, L. Roué, Cold-sprayed Cu-Ni-Fe anodes for CO₂-free aluminum production, *J. Therm. Spray Technol.* 29 (2020) 670–683.
- [9] S. Jucken, B. Tougas, B. Davis, D. Guay, L. Roué, Study of Cu-Ni-Fe alloys as inert anodes for Al production in low-temperature KF-AlF₃ electrolyte, *Metall. Mater. Trans. B.* 50 (2019) 3103–3111.
- [10] T. Nguyen, V. De Nora, De Nora oxygen evolving inert metallic anode, *TMS Light Met. In: Gallow* (2006) 385–390.
- [11] M. Chen, B. Hallstedt, L.J. Gauckler, Thermodynamic assessment of the Co-O system, *J. Phase Equilibria.* 24 (2003) 212–227.
- [12] R.J. Moore, J. White, Equilibrium relationships in the system NiO-CoO-O₂, *J. Mater. Sci.* 9 (1974) 1393–1400.
- [13] S. Kuboon, Y.H. Hu, Study of NiO–CoO and Co₃O₄–Ni₃O₄ solid solutions in multiphase Ni–Co–O systems, *Ind. Eng. Chem. Res.* 50 (2011) 2015–2020.
- [14] S. Mohammadkhani, E. Schaal, A. Dolatabadi, C. Moreau, B. Davis, D. Guay, L. Roué, Synthesis and thermal stability of (Co,Ni)O solid solutions, *J. Am. Ceram. Soc.* 102 (2019) 5063–5070.
- [15] P.L. Fauchais, J.V.R. Heberlein, M.I. Boulos, *Thermal spray fundamentals*, Springer US, Boston, MA, 2014.
- [16] D. Tejero-Martin, M. Rezvani Rad, A. McDonald, T. Hussain, Beyond Traditional coatings: a review on thermal-sprayed functional and smart coatings, *J. Therm. Spray Technol.* 28 (2019) 598–644.
- [17] M. Aghasibeig, F. Tarasi, R.S. Lima, A. Dolatabadi, C. Moreau, A Review on suspension thermal spray patented technology evolution, *J. Therm. Spray Technol.* 28 (2019) 1579–1605.
- [18] P.G. Lashmi, P.V. Ananthapadmanabhan, G. Unnikrishnan, S.T. Aruna, Present status and future prospects of plasma sprayed multilayered thermal barrier coating systems, *J. Eur. Ceram. Soc.* 40 (2020) 2731–2745.
- [19] D. Toma, W. Brandl, G. Marginean, Wear and corrosion behaviour of thermally sprayed cermet coatings, *Surf. Coatings Technol.* 138 (2001) 149–158.

- [20] H.I. Faraoun, T. Grosdidier, J.-L. Seichepine, D. Goran, H. Aourag, C. Coddet, J. Zwick, N. Hopkins, Improvement of thermally sprayed abrasible coating by microstructure control, *Surf. Coatings Technol.* 201 (2006) 2303–2312.
- [21] S. Mohammadkhani, V. Jalilvand, B. Davis, F. Ben Ettouil, A. Dolatabadi, L. Roué, C. Moreau, D. Guay, Suspension plasma spray deposition of $\text{Co}_x\text{Ni}_{1-x}\text{O}$ coatings, *Surf. Coatings Technol.* 399 (2020) 126168.
- [22] S. Mohammadkhani, V. Jalilvand, B. Davis, G.H. Gauthier, A. Dolatabadi, C. Moreau, L. Roué, D. Guay, High-temperature behaviour of HVOF (Co,Ni)O coated Cu-Ni-Fe anodes, *Corros. Sci.* 189 (2021) 109563.
- [23] T. Sundararajan, S. Kuroda, T. Itagaki, F. Abe, Steam Oxidation Resistance of Ni-Cr Thermal Spray Coatings on 9Cr-1Mo Steel. Part 2: 50Ni-50Cr., *ISIJ Int.* 43 (2003) 104–111.
- [24] T. Sundararajan, S. Kuroda, F. Abe, Steam oxidation of 80Ni-20Cr high-velocity oxyfuel coatings on 9Cr-1Mo steel: Diffusion-induced phase transformations in the substrate adjacent to the coating, *Metall. Mater. Trans. A.* 36 (2005) 2165–2174.
- [25] The Aluminum Association, Inert anode roadmap: A framework for technology development, Washington, 1998, (n.d.).
- [26] A.D. McLeod, J.-M. Lihmann, J.S. Haggerty, D.R. Sadoway, Selection and Testing of inert anode materials for Hall cells, *Light Met.* (1987) 357–365.
- [27] T.E. Jentoftsen, O.-A. Lorentsen, E.W. Dewing, G.M. Haarberg, J. Thonstad, Solubility of some transition metal oxides in cryolite-alumina melts: Part I. Solubility of FeO, FeAl_2O_4 , NiO, and NiAl_2O_4 , *Metall. Mater. Trans. B.* 33 (2002) 901–908.
- [28] S. Jucken, E. Schaal, B. Tougas, B. Davis, D. Guay, L. Roué, Impact of a post-casting homogenization treatment on the high-temperature oxidation resistance of a Cu-Ni-Fe alloy, *Corros. Sci.* 147 (2019) 321–329.
- [29] V. Jalilvand, S. Mohammadkhani, B. Davis, L. Roué, A. Dolatabadi, D. Guay, C. Moreau, The effect of bond coat on high-temperature behavior of HVOF-sprayed (Co,Ni)O coating on Cu-Ni-Fe anodes. *Surf. Coatings Technol.* 441 (2022) 128576.
- [30] D.H. DeYoung, Solubilities of oxides for inert anodes in cryolite-based melts, in: *Essent. Readings Light Met.*, Springer International Publishing, Cham, 2016: pp. 1073–1081.
- [31] M.W. Chase, A.I. of Physics., U. States., N.B. of Standards., A.C. Society., JANAF thermochemical tables, American Chemical Society and the American Institute of Physics for the National Bureau of Standards, [New York], 1985.

- [32] R.D. Holmes, H.S.C. O'Neill, R.J. Arculus, Standard Gibbs free energy of formation for Cu_2O , NiO , CoO , and Fe_xO : High resolution electrochemical measurements using zirconia solid electrolytes from 900–1400 K, *Geochim. Cosmochim. Acta.* 50 (1986) 2439–2452.
- [33] S.E. Ziemniak, L.M. Anovitz, R.A. Castelli, W.D. Porter, Thermodynamics of Cr_2O_3 , FeCr_2O_4 , ZnCr_2O_4 , and CoCr_2O_4 , *J. Chem. Thermodyn.* 39 (2007) 1474–1492.
- [34] F.H. Stott, Influence of alloy additions on oxidation, *Mater. Sci. Technol.* 5 (1989) 734–740.
- [35] S. V. Divinski, F. Hisker, C. Herzig, R. Filipek, M. Danielewski, Self- and Interdiffusion in Ternary Cu-Fe-Ni Alloys, *Defect Diffus. Forum.* 237–240 (2005) 50–61.